

Structural and Physical Properties of Rare-earth Chromium Oxides

by

Supriya Prabhakar Ughade
10PP17A26047

A thesis submitted to the
Academy of Scientific & Innovative Research
for the award of the degree of
DOCTOR OF PHILOSOPHY
in
SCIENCE

Under the supervision of
Dr. Pankaj Poddar



CSIR-National Chemical Laboratory, Pune

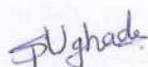


Academy of Scientific and Innovative Research
AcSIR Headquarters, CSIR-HRDC campus
Sector 19, Kamla Nehru Nagar,
Ghaziabad, U.P. – 201 002, India

February, 2023

Certificate

This is to certify that the work incorporated in this Ph.D. thesis entitled, "Structural and Physical Properties of Rare-earth Chromium Oxides", submitted by Supriya Prabhakar Ughade to the Academy of Scientific and Innovative Research (AcSIR), in partial fulfillment of the requirements for the award of the Degree of Doctor of Philosophy in Science, embodies original research work carried-out by the student. We further certify that this work has not been submitted to any other University or Institution in part or full for the award of any degree or diploma. Research material(s) obtained from other source(s) and used in this research work has/have been duly acknowledged in the thesis. Image(s), illustration(s), figure(s), table(s) etc., used in the thesis from other source(s), have also been duly cited and acknowledged.



(Signature of Student)

Supriya Prabhakar Ughade

13.02.2023



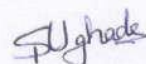
(Signature of Supervisor)

Dr. Pankaj Poddar

13.02.2023

STATEMENTS OF ACADEMIC INTEGRITY

I, Supriya Prabhakar Ughade, a Ph.D. student of the Academy of Scientific and Innovative Research (AcSIR) with Registration No. 10PPI7A26047 hereby undertake that the thesis entitled "Structural and Physical Properties of Rare-earth Chromium Oxides" has been prepared by me and that the document reports original work carried out by me and is free of any plagiarism in compliance with the UGC Regulations on "*Promotion of Academic Integrity and Prevention of Plagiarism in Higher Educational Institutions (2018)*" and the CSIR Guidelines for "*Ethics in Research and in Governance (2020)*".



Signature of the Student

Date: 13.02.2023

Place: Pune

It is hereby certified that the work done by the student, under my/our supervision, is plagiarism-free in accordance with the UGC Regulations on "*Promotion of Academic Integrity and Prevention of Plagiarism in Higher Educational Institutions (2018)*" and the CSIR Guidelines for "*Ethics in Research and in Governance (2020)*".



Signature of the Supervisor

Name: Dr. Pankaj Poddar

Date: 13.02.2023

Place: Pune

॥ श्री गणेशाय नमः ॥

*Dedicated to my Parents,
my In-laws, and
my Soulmate*

ACKNOWLEDGEMENTS

There are so many people whose support, inspiration, and encouragement are crucial to achieving meaningful life goals, mainly if they include parts of realizing one's most cherished aspirations. This thesis is a significant goal for me, and I am grateful to many individuals for their encouragement and well wishes as I travel this path. I would like to use this opportunity to express my gratitude to everyone who helped make the scientific work outlined in this thesis possible, directly or indirectly. I thank God for how good my life is, for providing me with this opportunity, and for giving me the ability to succeed.

First and foremost, I would like to thank my research supervisor, Dr. Pankaj Poddar, from the bottom of my heart for allowing me to work with him. He has been a tremendous help to me throughout my time as a Ph.D. student, and I want to thank him for that. His interest in science and holistic viewpoint has motivated me to work as a freelance researcher. I have learned throughout the years from his interactions how to approach a subject from all possible directions and find a solution at the most fundamental level. He continuously stresses the need to develop critical thought habits while teaching us the dos and don'ts of science and daily life. Aside from this, I appreciate his teaching style since he makes every issue incredibly plain and straightforward by beginning at a basic level and working his way up. I was highly amazed by his depth of knowledge in all subjects. Being a member of his study team and affiliated with him makes me feel fortunate and privileged.

I also want to express my gratitude to the members of my doctoral advisory committee, Dr. Nandini Devi, Dr. Suresh Bhat, Dr. Moneesha Furnandes, and Dr. D. S. Reddy, for their time, helpful advice, and support. I owe my external expert Dr. Surjeet Singh, IISER Pune, a great deal of respect and appreciation for assessing my work in my up-gradation meeting. I sincerely appreciate his time, insight, and conversation regarding my work.

I want to express my gratitude to Dr. Ashish Lele, the current director of the CSIR-NCL, and Dr. Ashwini Kumar Nangia, the previous director, for allowing me to work at this esteemed organization providing the resources I needed to do the research. For their generous assistance throughout the course of my Ph.D., I am incredibly grateful to Dr. T. Ajithkumar, Head of the Physical and Materials Chemistry Division, Dr. P. A. Joy (former HoD), and Dr. B. L. V. Prasad (former HoD). Many thanks to the division staff members who assisted me with the ordinary office tasks. I want to express my gratitude to the entire administrative and non-teaching personnel of CSIR-NCL for all of their help and support over the years.

I also want to express my gratitude to all the staff members at NCL's Center for Materials Characterization division who have helped me out over the years. I sincerely appreciate the prompt assistance provided by Mr. S. S. Deo, Mr. R. S. Gholap, Venkatesh, Sheetal, Chetan, Tushar, Medha, and Shurti for the XPS, TEM, HRTEM, FESEM, and SEM measurements. Special thanks to Medha ma'am and Chetan Sir for providing me with urgent slots on request. I also want to thank Dr. Suresh Gokhale and Dr. Rupali Waichal for granting me access to the Raman instrument. Many thanks to Dr. Tejas and Akshay for providing me with the XRD slots. My sincere gratitude goes out to Dr. Rajesh Gonnade for teaching the XRD topic in the coursework; the information he offered was excellent and aided me in conducting my research. Thank you for elaborating on the space groups. For his instruction on SAXS in the course work, Dr. Guruswamy Kumaraswamy of IIT Bombay has my sincere gratitude. Additionally, he gave me WAXS, which was helpful in the early stages of my Ph.D. research.

Dr. Sachin Agwane (NCL), Dr. Ravikumar Chaudhari (Shri Shiv Chhatrapati college Junnar) and Dr. Apurva Pawar (MDS Department of Pediatric and Preventive Dentistry), for giving me a chance to investigate the biophysics field, and Dr. Ganesh Kale (CSIR-NEERI), for the engineering field, are my collaborators who first introduced me to multidisciplinary science.

I appreciate that the DST-INSPIRE Fellowship gave me the fellowship I needed to conduct research at NCL.

I would also like to thank my lab's senior researchers, Dr. Preeti Padhye, Dr. Preeti Gupta, Dr. Mousumi Sen, and Dr. Puneet Khandelwal. They were no longer at NCL when I joined the lab, but the unexpected encounters with them have motivated me to succeed in research. They have shared experiences with me that I will never forget, and I intend to keep in touch with them.

Additionally, I'd like to express my gratitude to Dr. Geeta Sharma, Dr. Chiti Tank, Dr. Manorama lakhe, Dr. Subodh Gautam (with a special thanks to bhaiya for giving me the best Ph.D. advice, helping with my reactions, and teaching me how furnaces work), and Dr. Bhavana Joshi (with a special thanks to di for supporting me in my work) for the stimulating discussions. A special thanks to Shubhra di for her wonderful support throughout my trip, as well as to Dinesh and Manisha for fostering a friendly and conducive work environment in the lab.

Without mentioning my lovely senior cum friend Dr. Monika Malik Dhadwal, from whom I have gained so much research knowledge, this essay would fall short. She introduced me to all the chemical ideas and provided me with presentation slides for outside samples. Di, I appreciate your help. Monika, my lab partner, roommate, closest friend, and my support, I appreciate you always being there

for me, reprimanding me, making me go out, and cheering me on when the challenges of my Ph.D. seemed unresolvable. I will never forget the masti and dance activities we engaged in over the past five years, including our joint conferences, travels, and birthday parties. I appreciate your love, attention, and company. I want to express my gratitude to Gaurav for the last six years of companionship, support, and shared memories. My sincere gratitude to you three for making my dream a reality.

I'd want to thank all of my NCL friends, including Amrita (thank you for looking after me, Ammu), Himanshu, Ravi Ranjan, Indronil, Vinita, Lakshmi, Rohit, Inderjeet, and Umasharan (for XRD slots) as well as my girls Priya, Priyanka (thanks for your help in TGA slot), Pooja, Kalyani, Manali, Anuradha (thanks for your help in XRD slot), and Kranti. Many thanks to Chandan, Kritika, Rajni, Soumya, Smita, Surya, and Neha. Thank you very much, Tubai and Debu (for all masti). Thank you to the following seniors for their contributions to my life at NCL: Betsy di, Abha di, Ragini di, Bhawana di, Reshma di, Monika Mathur di, Shailja di, Pavan bhaiya, Aakash bhaiya, Ambarish bhaiya (thank you so much bhaiya all your support), Ram bhaiya, Arun bhaiya (thanks for XRD slots), Abhijit bhaiya, Govind bhaiya, Ashish bhaiya, Ruchi di, Reddy Anna, and Anupam bhaiya. Thanks, Sujeet and Chotu bhaiya, for giving me the best meals during the last four years. Thanks to my MSc buddies Oma (special thanks to omdi for always being with me), Pushpendra (Bhai), Rahul, Sonu (Trusha), Shalu, and Sarang for listening to me. Thanks to my schoolmates Arti, Bhagyashri, Roshani, Vaishali, Kalyani, and Trupti. Special thanks to Gedam Sir and Sudhir Sir for their support throughout this journey.

I want to sincerely thank my parents, Mummy (Sunanda Ughade) and Papa (Prabhakar Ughade), for their unending love and unwavering support throughout my life. In every aspect of my life, you two have served as a consistent source of encouragement. I appreciate your believing in me and being patient with me. In addition, I want to thank my little sisters (Shitu (thanks for always supporting me and being with me), Prerana, Samiksha, Mahi, Pooja di, brother (Vaibhav), jiju (Raj jiju), Bavaji, Aaji, and my dashing hero Mahir for their unwavering moral support, care, and love. I thank my mother-in-law (Shobha Aai), father-in-law (baba), Aapaji, Aaji, and Dadi for their encouragement, continued support over the years, and enthusiasm as I neared my goal. I also thank Nilam tai, Rutu tai, Prajot jiju, and Ashu da for supporting me and my little girls Aastha, Yastika, and Aashvi for their unconditional love. Above all, I thank them all for trusting me when I most needed it. Finally, I want to express my deep gratitude to my life partner Saurabh for always being there for me and his understanding, support, love, and care. His extraordinary capacity to maintain composure, faith, and patience in the face of tragedy has made it feasible to complete a dissertation. You have understood when

I am irritated and impatient, you cheer with me when even the smallest things go right, and you are always available to listen simply. You have been my best tutor, holding my hand and pointing me in the proper direction. I appreciate you providing special meals for me, dinner, and other small favors. I want to thank all my teachers, from elementary school through graduate school, for instilling good morals and knowledge in me. I could not have completed my research without the support of all these wonderful people!

Supriya Ughade

Table of Contents

Chapter 1: Introduction

1.1 Fundamentals of magnetism...	3
1.1.1 Ferromagnetism	3
1.1.2 Antiferromagnetism	5
1.2 Exchange interaction	6
1.2.1 Direct exchange	7
1.2.2 Indirect exchange	8
❖ Superexchange interaction.....	8
❖ Double exchange interaction	10
1.3 Magnetocaloric effect... ..	11
1.4 Ferroelectric effect	12
1.5 Synthesis methods... ..	14
1.5.1 Solid state synthesis.....	14
1.5.2 Sol-gel synthesis method.....	14
1.5.3 Hydrothermal synthesis	15
1.6 Rare earth chromium oxides... ..	17
1.6.1 Chromates (RCrO ₄).....	17
1.6.1.1 Crystal structure	17
❖ Zircon-type structure.....	17
❖ Monazite-type structure	18
❖ Scheelite-type structure.....	19
1.6.1.2 Phase transition in RCrO ₄	19

1.6.1.3 Properties of RCrO_4	20
❖ Magnetic Properties... ..	20
❖ Magnetocaloric effect in RCrO_4	22
❖ Ferroelectric effect RCrO_4	23
1.6.2 Chromites (RCrO_3)... ..	24
1.6.2.1 Crystal structure.....	24
❖ Perovskite structure.....	24
1.6.2.2 Properties of RCrO_3	25
❖ Magnetic Properties... ..	25
❖ Magnetocaloric effect in RCrO_4	26
1.7 Lanthanides.....	27
1.8 Why is rare earth chromium oxide (R-Cr-O) so interesting?.....	29
1.9 Thesis objective.....	30
1.10 Thesis outline.....	31
1.11 References.....	32
Chapter 2: Formation of zircon-type DyCrO_4 and its magnetic properties	
2.1 Introduction.....	43
2.2 Experimental... ..	47
2.3 Results and discussion... ..	50
2.3.1 Formation mechanism... ..	50
2.3.1.1 Acidic medium... ..	50
2.3.1.2 Basic medium.....	53
2.3.2 X-ray diffraction study.....	56

2.3.2.1 Ammonia Solution (NH ₄ OH)...	57
2.3.2.2 Oxalic acid (C ₂ H ₂ O ₄)	58
2.3.2.3 Citric acid (C ₆ H ₈ O ₇).....	59
2.3.2.4 EDTA (C ₁₀ H ₁₆ N ₂ O ₈)	60
2.3.3 Electron Microscopy imaging and diffraction study	63
2.3.4 X-ray photoelectron spectroscopy analysis... ..	68
2.3.5 Magnetic measurements.....	71
2.4 Conclusion... ..	74
2.5 References.....	75
 Chapter 3: A systematic study of rare-earth ions size-dependent structural phase transition from monazite to zircon-type in rare earth chromates using Raman spectroscopy	
3.1 Introduction.....	81
3.2 Experiment.....	84
3.3 Results and discussion... ..	85
3.3.1 X-ray diffraction analysis... ..	85
3.3.2 Room temperature Raman spectra	88
3.4 Conclusions.....	99
3.5 References.....	100
 Chapter 4: Shape tunable synthesis of perovskite DyCrO₃ at a low temperature by varying primary reaction conditions	
4.1 Introduction.....	104
4.2 Experimental.....	109
4.3 Results and discussion... ..	111

4.3.1 Reaction mechanism.....	111
4.3.1.1 With identical KOH amounts but different reaction temperatures	112
4.3.1.2 With different KOH amounts added in two steps during the reaction.....	112
4.3.1.3 With different crystal growth duration	118
4.3.1.4 With different Chromium precursors.....	119
4.3.1.5 With the addition of surfactants CTAB and PVA	121
4.4 Raman Study of single phase DyCrO ₃	129
4.5 Conclusions.....	131
4.6 References.....	132

Chapter 5: Summary and Future Scope

5.1 Summary of the thesis.....	138
5.2 Future scope	142

Abstract

List of publications

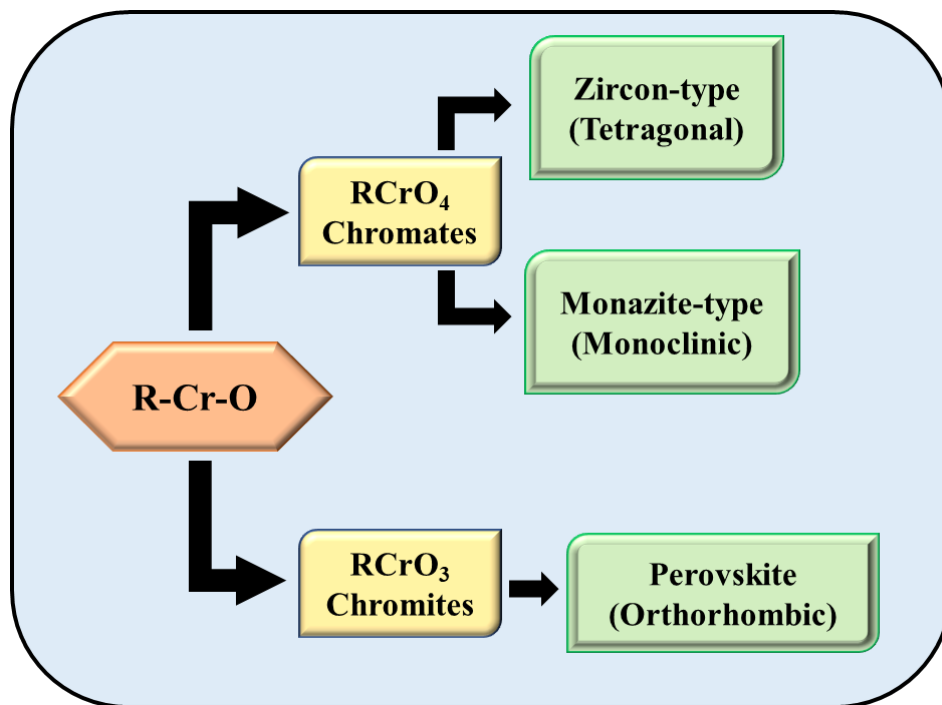
List of Abbreviations

1. Paramagnetic	PM
2. Ferromagnetic	FM
3. Antiferromagnetic	AFM
4. Curie temperature	T_c
5. Neel temperature	T_N
6. Interatomic distance	r_{ab}
7. Radius	r_d
8. Superexchange	SE
9. Magnetocaloric effect	MCE
10. Adiabatic temperature change	T_{ad}
11. Isothermal entropy change	S_M
12. Room temperature	RT
13. Rare-earth chromium oxides	R-Cr-O
14. Chromate	$RCrO_4$
15. Chromite	$RCrO_3$
16. Rare earth element	R
17. Spin reorientation	SR
18. Specific heat capacity	C_p
19. Refrigeration capacity	RC
20. Ethylenediaminetetraacetic acid	EDTA, E
21. Anderson-Goodenough-Kanemori	AGK
22. Oxalic acid	O
23. Citric acid	C
24. Acidic	A

25. Basic	B
26. X-ray diffraction	XRD
27. thermogravimetric analysis	TGA
28. Transmission Electron Microscope	TEM
29. Field emission scanning electron microscopy	FESEM
30. Energy Dispersive X-ray Analysis	EDAX
31. X-ray Photoelectron Spectrometer	XPS
32. Nanoparticles	NPs
33. Superconducting quantum interference device- based vibrating sample magnetometer	SQUID-VSM
34. Magnetization <i>versus</i> magnetic field	M–H
35. Magnetization <i>versus</i> temperature	M–T
36. Field-cooled	FC
37. Zero-field cooled	ZFC
38. Crystallite size	<i>d</i>
39. full width at half maxima	FWHM
40. Bright-field	BF
41. Dark-field	DF
42. Selected Area Electron Diffraction	SAED
43. Temperature	T
44. Translational	T
45. Rotational	R
46. Cetyltrimethylammonium bromide	CTAB
47. Polyvinyl alcohol	PVA
48. Chromium	Cr

Chapter 1

Introduction



Outline

This chapter serves as the thesis's introduction. It begins by describing the inspiration for the research done and then gives a general summary of the fundamentals of magnetism. The concluding section of this chapter examines the characteristics of chromites (RCrO_3) and chromates (RCrO_4). The reasoning behind the focus on RCrO_4 and RCrO_3 , which are rare-earth chromium oxides, is also covered in detail. In-depth descriptions of the crystal structure and its properties, including magnetism and magnetocaloric effect, are given. We have provided the thesis work outline toward the end of this chapter.

1.1 Fundamentals of magnetism

A free atom has two contributions to its magnetic moment. The orbital angular momenta of electrons moving around the nucleus behave like a flowing electric current, placing a magnetic moment. Whereas each electron's "spin" results in another contribution to its magnetic moment. So, the magnetic moment detected results from the interaction between the orbital angular and spin momenta. These two moments finally evolved in the different types of magnetism in the materials.^{1,2} Diamagnetism and paramagnetism (PM), which make up most of the elements listed in the periodic table at ambient temperature, are the two prevalent types of magnetism. These substances are typically described as non-magnetic, while those considered magnetic are ferromagnetic (FM). Antiferromagnetism (AFM) is another type of magnetism that may be seen in pure elements at ambient temperature.^{2,3}

Furthermore, magnetic materials may also be categorized as ferrimagnetic, despite the fact that this property is not seen in any pure elements and may only be found in compounds like the mixed oxides recognized as ferrites. The property name ferrimagnetic was itself from ferrites.^{2,3} The magnetic susceptibility value for each type of material falls into a specific range, as shown in **Table 1.1**.

1.1.1 Ferromagnetism

Around 600 BC, magnetite was discovered as the first material to exhibit magnetism.⁴ Materials become PM due to the random alignments of unpaired spins, and FM results from parallel orientation. The FM materials have a significant magnetic field response as well as spontaneous magnetization. The Curie and Weiss theory⁵ and the Stoner band theory⁶ are two phenomenological ideas that potentially explain FM.

Many PM materials follow the Curie-Weiss law, which predicts a more widespread temperature dependency rather than the Curie law. *Equation (1)* shows the Curie-Weiss

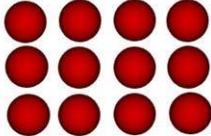
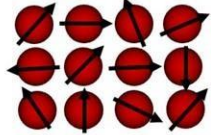
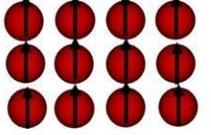
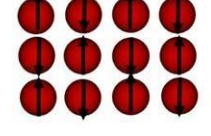
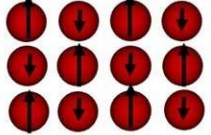
Types of magnetism	Atomic and molecular behaviour		Examples
Diamagnetism	Atoms have no net magnetization. Susceptibility is small and negative, -10^{-6} to -10^{-5}		Inert gases; many metals e.g. Au, Cu, Hg; non-metallic elements e.g. B, Si, P, S; many ions e.g. Na^+ , Cl^- & their salts; diatomic molecules e.g. H_2 , N_2 ; H_2O ; most organic compounds
Paramagnetism	Atoms have randomly oriented magnetic moments and net magnetization. Susceptibility is small and positive, $+10^{-5}$ to $+10^{-3}$		Some metals, e.g. Al; some diatomic gases, e.g. O_2 , NO; ions of transition metals and rare earth metals, and their salts; rare earth oxides.
Ferromagnetism	Atoms have parallelly aligned magnetic moments. Susceptibility is large (below T_c) and positive.		Transition metals Fe, H, Co, Ni; rare earths with $64 \leq Z \leq 69$; alloys of ferromagnetic elements; some alloys of Mn, e.g. MnBi, Cu_2MnAl .
Antiferromagnetism	Atoms have antiparallelly aligned magnetic moments. Susceptibility is small & positive, $+10^{-5}$ to $+10^{-3}$		Transition metals Mn, Cr & many of their compound, e.g. MnO, CoO, NiO, Cr_2O_3 , MnS, MnSe, CuCl_2 .
Ferrimagnetism	Atoms have antiparallelly aligned magnetic moments with unequal magnitude. Susceptibility is large (below T_c)		Fe_3O_4 (magnetite); $\gamma\text{-Fe}_2\text{O}_3$ (maghemite); mixed oxides of iron and other elements such as Sr ferrite.

Table 1.1: a list of the several categories of magnetic behavior.³

Equation: χ is susceptibility, C is the Curie constant, T is absolute temperature, and θ is the Weiss constant in temperature dimensions.

$$\chi = \frac{C}{T - \theta} \quad (1)$$

Underneath the Curie temperature (T_c), i.e., a critical temperature, PM material becomes FM and obeys the Curie-Weiss Equation by spontaneously rearranging the spins in the direction parallel to externally applied magnetic field. The assumption made in the derivation of the Curie law is that the localized atomic magnetic moments only undergo slight reorientation as a result of the applied magnetic field. Weiss proposed an intrinsic connection between the localized moments, which he named a "molecular field," in order to explain the Curie-Weiss phenomenon that had been seen. Besides speculating that his molecular field is the result of the

mutual interaction of electrons, which prefers to arrange the dipole moments parallel to one another, he made no other assumptions about its origin. A positive value of θ in Curie-Weiss Equation means that the molecular field is working in the same direction as the external magnetic field, tends to align the elementary magnetic moments in parallel with the applied field and with one another, which will be the case in FM material. PM materials behave like FM below the critical temperature, T_c . The destruction of the FM ordering occurs above T_c , where thermal energy dominates. The interaction energy at T_c must therefore be equivalent to the thermal energy.⁷

Whereas the Stoner band theory states that at temperature lower than T_c , an uneven up-and-down spin counts will reach in net magnetization, but temperature above T_c , an equal up-and-down spin counts will reach in no net magnetization.⁵

1.1.2 Antiferromagnetism

In AFM materials, the interaction of magnetic moments' tries to position nearby moments direction antiparallel to one another. AFM ordering in magnetic systems was found by Louis Néel⁸. First magnetic ions set spontaneously becomes magnetized at a temperature below a critical temperature (known as Neel temperature (T_N)). In contrast, the other set of magnetic ions spontaneously becomes magnetized in a reverse way by a similar amount. AFM, as a result, lower net spontaneous magnetization, and at a constant temperature, their reaction to external applied fields is comparable with that of PM materials. Specifically, the magnetization is linear in the external applied field, and the susceptibility is positive and minimal. Just above T_N , the susceptibility has a temperature dependency comparable to PM materials, while below T_N , the susceptibility gets weaker with rising temperature.⁹

When Shull and Smart¹⁰ acquired the neutron diffraction spectrum of manganese oxide, MnO, in 1949, they gave the first direct proof for the existence of antiferromagnetic ordering. Their findings demonstrated that there are two sets of spins on Mn^{2+} ions, one of which is

antiparallel with the other. Before this discovery, the only proof that antiferromagnetism existed was that the Curie-Weiss theory's predicted curves and the observed temperature dependence of the susceptibility agreed.⁹

Based on the coupling, the AFM ordering in metal oxides is divided into three groups (Figure 1.1).¹¹

- 1) A-type: AFM for interplane coupling and FM for intraplane coupling.
- 2) C-type: AFM is used for the intraplane coupling and FM for the interplane.
- 3) G-type: AFM is used for both intraplane and interplane connections.

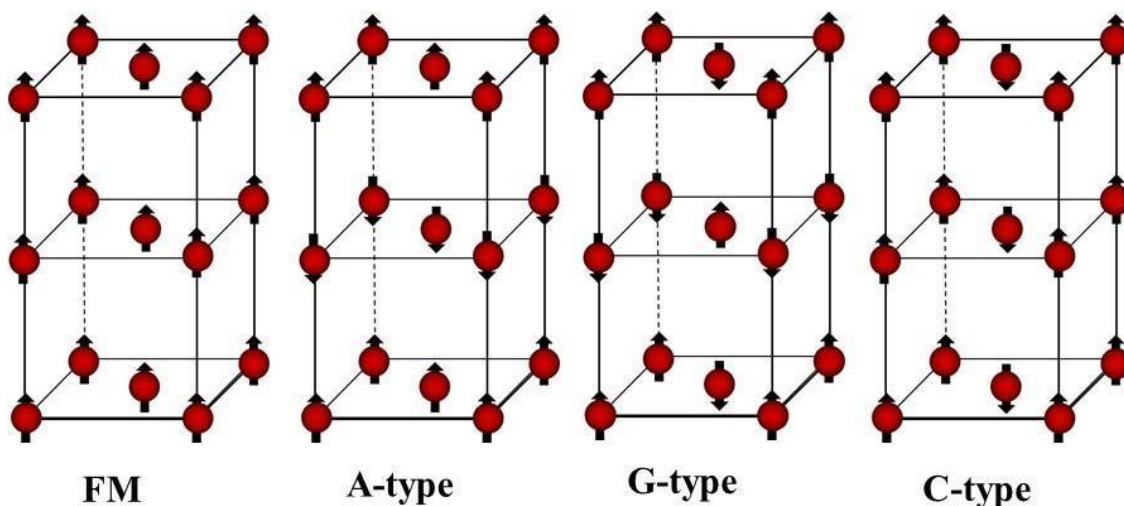


Figure 1.1: Classification of AFM ordering.¹¹

1.2 Exchange interaction

The spin-spin, and spin-lattice interactions serves as the foundation for current magnetic theories. Due to the intricacy of exchange interactions as well as the existence of a wide range of magnetic substances and structures, the universal condition for FM is exceptionally challenging to express. Strong electron-electron interactions are the microscopic cause of FM. Due to Pauli's exclusion principle, parallel-spin electrons have a tendency to avoid one another

spatially. The quantum theory of magnetism states that this results in exchange interactions, which in turn cause magnetic phenomena.^{12, 13}

1.2.1 Direct exchange

Direct exchange happens when the confined orbitals of electrons on nearby magnetic ion sites directly overlap (**Figure 1.2**). a Bethe-Slater curve which explains why some metals show FM nature and other shows AFM nature shown in **Figure 1.3**. The differences in exchange energies of transition metals are explained as resulting from the interatomic separation ratio to the radius of the $3d$ electron shell in the Bethe-slater curve, on the assumption that magnetism operates according to the Heisenberg model.¹⁴

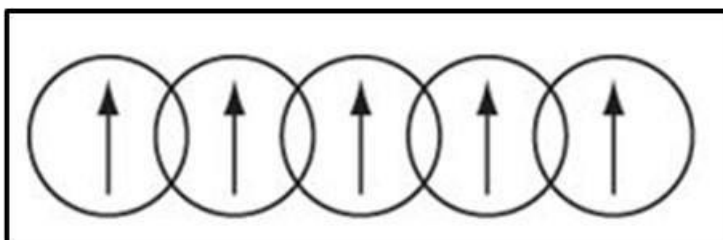


Figure 1.2: Schematic illustration of direct exchange interaction.¹²

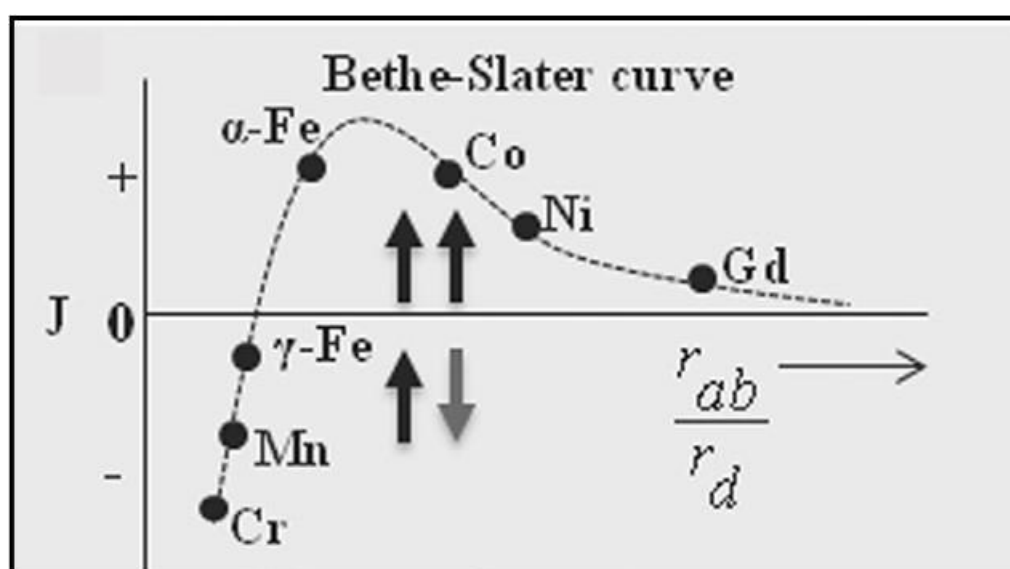


Figure 1.3: A Bethe-Slater curve showing the interatomic distance (r_{ab}) and radius (r_d) of an atom's unfilled d -shell in relation to the strength of direct exchange coupling.¹²

The relationship between exchange energy and interatomic separation was first put forth in 1930 by John C. Slater and represented as a curve on a graph in 1933 by Sommerfeld and Bethe.^{15,16,17}

Since electrons spend majority of their time in between atoms when the interatomic distance is minimal, principal of Pauli's exclusion results in development of the AFM order. However, due to a significant interatomic distance, the FM order is created when the electrons spend most of their time apart from one another. As a result, different models have been developed to explain magnetic states seen in the materials when internuclear separations are relatively significant.¹²

1.2.2 Indirect exchange

❖ Superexchange interaction

Superexchange (SE) interaction involves a non-magnetic ion or ligand that separates localised electrons by indirect exchange. Their shared non-magnetic ion/ligand mediates the localised electrons' orbital overlap with the magnetic sites. As the magnetic ions oxidation states are precisely the same/varied by two during a SE interaction, there isn't electron transfer from one magnetic site to another. Hendrik Kramers proposed SE first in 1934.¹⁸ Kramers' model was later improved by Phillips Anderson in 1950.¹⁹ Further, John B. Goodenough and Junjiro Kanamori created a set of semi-empirical norms for interaction ordering in the 1950s.^{20, 21, 22} **Figure 1.4** schematically depicts the SE interaction in MnO.

Shull identifies the magnetic spin pattern in the MnO crystal below T_N in neutron diffraction, as mentioned in the above section.¹⁰ MnO has a face-centered cubic lattice structure with spins antiparallel to each other. The T_N for the MnO crystal was reported as 122 K.¹⁹ In **Figure 1.5**, the crystal structure is displayed which depicts the strongly coupled Mn^{2+} ions that were separated by a supposedly non-magnetic oxygen (O) ion directly between them.¹⁹

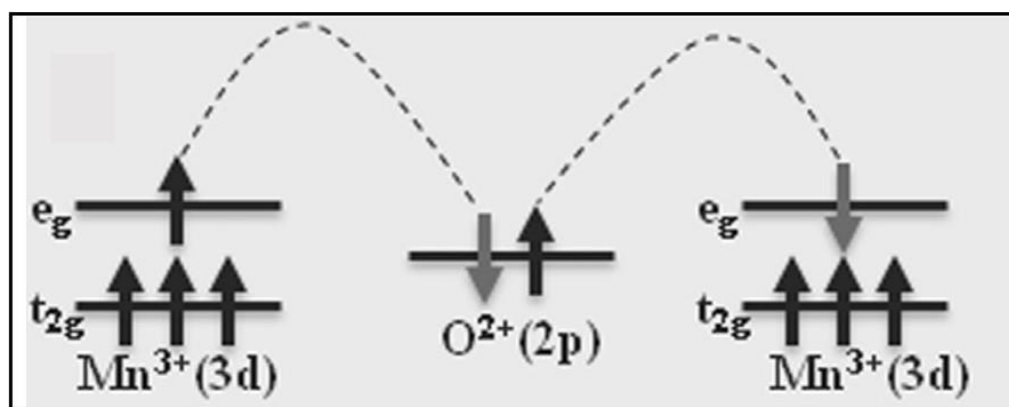


Figure 1.4: Superexchange interactions in the MnO system.¹²

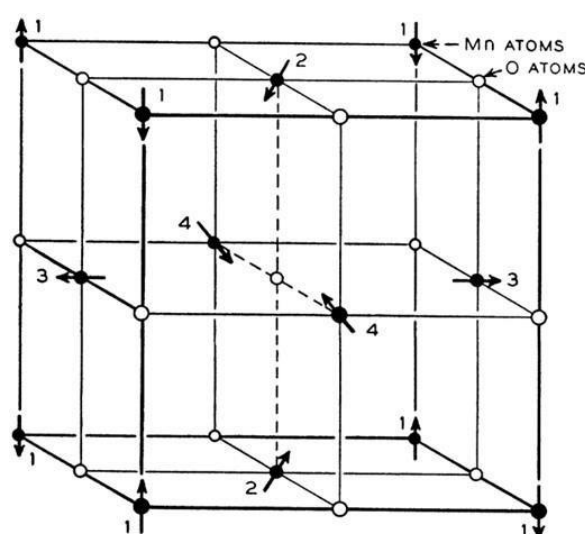


Figure 1.5: AFM Pattern for the MnO structure recorded by neutron diffraction.¹⁹

The existence of insulating FM compounds is explained by the SE interaction, even though the majority of FM materials now known are metallic. SE, which results from the magnetic electrons orbital overlapping with their intermediate ligands through O inside oxide materials, is the primary reason for exchange interaction in magnetic insulators.¹⁹ The critical element in determining the strength and sign of SE interaction is the occupancy and orbital degeneracy of the $3d$ states. There are numerous scenarios to take into account, as well as the Goodenough-Kanamori guidelines provide an overview of the findings.^{20, 21, 22, 23, 24} Anderson simplified these rules as follows:

1. The exchange is strong and AFM ($J < 0$) when two cations have lobes of singly occupied $3d$ orbitals that point in the same direction. For $120^\circ - 180^\circ$ M-O-M bonds, this is typically the situation.
2. When two cations have a symmetry-constrained overlap integral between individually occupied $3d$ orbitals of zero, the exchange is FM and very weak. This is for 90° M-O-M bonds situation.
3. The exchange is FM again when two cations overlap between singly occupied $3d$ orbitals and vacant or doubly occupied orbitals of the same kind, although relatively weak. As the overlap integrals are more likely to be greater than zero, SE is more frequently AFM than FM.

❖ **Double exchange interaction:**

The SE interaction is comparable to the double exchange interaction. In double exchange interactions, electrons can transfer from a magnetic ion another simply because the oxidation states of two magnetic ion that are closest to one another differ by one, as shown in **Figure 1.6**. This interaction was proposed by Clarence Zener²⁵ first; hence, a double exchange interaction has another name a Zener exchange interaction. It is predicated on the idea that localised spin and delocalized spin display strong intraatomic exchange interactions, causing the latter's spins to align parallel to the former continuously. This double exchange interaction model might accurately predict metallic manganite's ferromagnetic phase.¹²

Assume the 180° interaction between Mn, O, and Mn, where the Mn " e_g " orbitals come in direct contact with the $O2p$ orbitals, and one of the Mn ions seems to have more electrons than the other. The electrons on each Mn ion in the ground state are arranged in accordance with Hund's rule, which states that if O wants to give up its up-spin electron to Mn^{4+} , afterward, an electron from Mn^{3+} can supply its vacant orbital. In this process, electron maintained its spin

and traveled between the nearby metal ions. The double-exchange concept states that if the electrons do not have to change their spin direction to respect to Hund's rules when they belong to the accepting species, the transfer of electrons across species will become more effortless. Hopping (delocalization) reduces kinetic energy. Consequently, the overall energy savings may result in the ferromagnetic alignment of nearby ions.²⁶

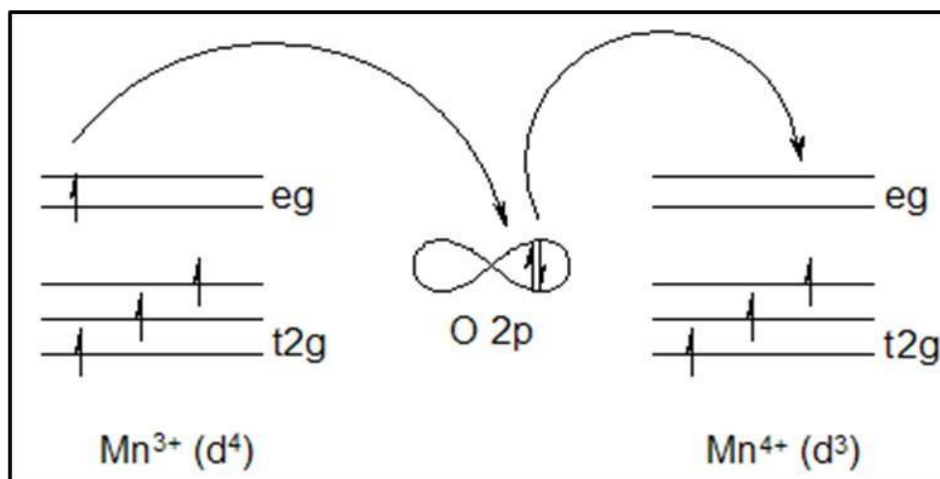


Figure 1.6: Double exchange interaction in the MnO system.²⁶

1.3 Magnetocaloric effect

The term magnetocaloric (MCE) effect refers to a magnetic substance being heated or cooled as a result of the application of an external magnetic field. Even though this phenomenon represents a real-world application of the MCE in magnetic materials, this process has long been known as adiabatic demagnetization.^{27,28} Warburg's observation of MCE in iron in 1881 led to its discovery²⁹. Debye³⁰ and Giauque³¹ each explained the MCE's inception. They also proposed the first application of the MCE, which was utilized to achieve temperatures lower than liquid helium, which had been the lowest temperature that could be reached experimentally. There is a lot of interest in employing the MCE as an alternate method of refrigeration, from ambient temperature to the temperatures at which hydrogen and helium liquefy (~20 - 4.2 K). As an alternative to the prevalent vapor-cycle refrigeration technology

now in use, magnetic refrigeration promises to be both energy-efficient and environmentally beneficial^{32, 33}.

MCE is an inherent property of all magnetic materials. However, the strength of the effect varies depending on the characteristics of each material. As a result of the magnetic sublattice's coupling to the external magnetic field, that is the physical source of the MCE, the magnetic component to the solid's entropy changes. MCE is often described as adiabatic temperature change (T_{ad}) or isothermal entropy change (S_M) that occurs when a system is subjected to a magnetic field.³⁴ By adiabatically demagnetizing PM salts, MCE was first utilized to reach temperatures below Kelvin.^{35, 36} The development of room temperature (RT) MCE materials like Gd (10.2 J/kg K at 294 K) and Gd₅Si₂Ge₂ (18.4 J/kg K at 276 K) has pushed research toward producing ambient condition MCE cooling rather than the current approach for compression-expansion of gas.^{36, 37} The current focus of MCE research is to find novel materials with substantial entropy changes (S_M) and controllable operating temperatures. Therefore, systems with higher MCE at RT would benefit technological applications requiring ambient conditions. In contrast, systems with low temperature regimes below Kelvin are desirable for operations like space science and liquefaction of hydrogen in the fuel business, among others.³⁶ Intermetallic materials with first-order magnetic transitions, like LaFe_{13-x}Si_x, MnAs_{1-x}Sb_x, and MnFeAs_{1-x}P_x-based compounds, also exhibit RT MCE in addition to Gd-based compounds.³⁸⁻⁴⁰ However, their employment in MCE refrigeration is hampered by their high magnetic hysteresis and weak corrosion and oxidation resistance.

1.4 Ferroelectric effect

A ferroelectric material is a substance that undergoes a phase change from a high-temperature, conventional dielectric phase to a low-temperature phase that exhibits spontaneous polarisation. The direction of the applied electric field can change the spontaneous polarization's direction.^{41, 42} The first ferroelectric material was discovered in 1921 when

Valasek noticed nonlinear electrical features in sodium tartrate tetrahydrate, also known as Rochelle salt ($\text{KNaC}_4\text{H}_4\text{O}_6\cdot 4\text{H}_2\text{O}$). He later verified that hydrogen bonds inside the materials cause the ferroelectricity of the materials.⁴³⁻⁴⁵ Ferroelectricity in KH_2PO_4 was identified in 1930, and phase transition theory was created.⁴⁶

Barium titanate, also known as BaTiO_3 , is ferroelectric material that has multiple ferroelectric phases.⁴⁷⁻⁵⁰ **Figure 1.7** shows the lattice geometries of perovskite BaTiO_3 . Ferroelectric materials have unique physical characteristics that make them useful for various applications, including data storage devices, capacitors, transducers, and actuators because of their hysteresis loop and high dielectric permittivity. Ferroelectricity is produced by the deformed perovskite structure's off-centering of titanium ions.⁵¹ It is now well understood why perovskite structures like BaTiO_3 prefer ferroelectricity. The cause is the ligand field stabilization energy, in which the oxygen $2p$ orbital donates its electron density to the empty d orbital. The titanium atom becomes off-centered by the transition metal cation, which causes the B site Ti ions to shift from their centrosymmetric orientations and produce a net polarization and ferroelectricity.⁵¹ For the ferroelectric phase to be stabilized, unoccupied d orbitals of transition metal ions with the proper energy range are therefore necessary.

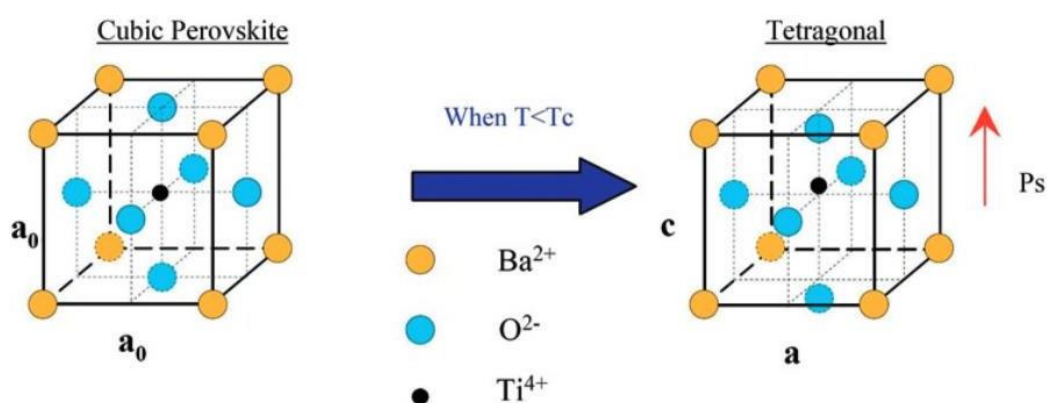


Figure 1.7: Lattice geometries of the high-temperature paraelectric phase (left) and low-temperature ferroelectric phase (right) of perovskite BaTiO_3 .⁵¹

1.5 Synthesis methods

1.5.1 Solid state synthesis

Solid state reaction, sometimes referred to as shake and bake, is a process of synthesis in which the raw components are combined before being heated in an oven. The majority of these reactions require high temperatures, often in the hundreds of degrees Celsius range, to speed up the reaction and ensure that it happens in enough time.⁵² The simplest and most popular method of creating reactions is solid-state reactions, which do not require expensive equipment. As most of the compounds are stable under typical settings, obtaining solid-form reactants for reactions is not challenging. This technique is also adaptable at industrial and lab scales. The synthesis compounds include mixed metal oxides, sulphides, nitrides, aluminosilicates, and many more materials.⁵³

The primary issue with the solid-state reaction approach is dispersion in solid materials. The reaction is still limited by molecular diffusion between the constituents in the solid state, even after the materials have been ground and shaped into pellets. The majority of these reactions take a long time and demand high temperatures. Utilizing high temperatures for extended periods will also require large amounts of energy, which could raise the expense of applying this technique. Most of the reaction mechanisms are yet unknown, which is another issue. Furthermore, it was challenging to eliminate the contaminants in the finished product.⁵²

1.5.2 Sol-gel synthesis method

The wet-chemical process known as sol-gel synthesis method is widely applied in the creation of materials. A range of premium oxide materials are produced using this approach. This procedure is called a sol-gel method because, during the creation of the metal-oxide, the liquid precursor is transformed into a sol, which is then transformed into a network structure called a gel.⁵⁴ In order to hydrolyze the metal oxide and produce a sol, either water or alcohol are used. Condensation occurs next, increasing the solvent's viscosity to create porous

structures that can oxidize. Metal-hydroxo- (M-OH-M)/ metal-oxo- (M-O-M) bonds develop in condensation or polycondensation process, leading to the creation of metal-hydroxo-/ metal-oxo-polymers in the solution.^{55, 56} A polycondensation continues due to age, altering the material's structure, characteristics, and porosity. Aging causes the porosity to diminish and spacing between colloidal particles to widen. The gel is dried after the ageing process, which entails taking out the water and other organic solvents. Later on the process of calcination is completed. The type of precursor, the rate of hydrolysis, the amount of time the product is aged, the pH, and the molar ratio of the precursor to water are all variables that affect the final product made using the sol-gel process.^{57, 58}

Sol-gel chemistry, one of these methods, offers some unique advantages since it can create solid-state materials from chemically homogenous precursors. One must be able to synthesize complex inorganic compounds like ternary as well as quaternary oxides at relatively lower temperature range with smaller formation time by capturing "randomness of the solution state"⁵⁹ and therefore maintaining mixing of reagents at atomic level. Sol-gel chemistry must also make it possible to have more command over particle size and morphology. Numerous sol-gel approaches were developed for preventing phase segregation during formation because, in reality, producing a homogeneous precursor at room temperature does not guarantee reaction homogeneity.⁶⁰

1.5.3 Hydrothermal synthesis

The hydrothermal approach is an intriguing low-temperature synthesis route, as it is an energy-efficient, environmentally friendly, as well as very flexible method during synthesizing a wide range of materials.⁶¹⁻⁶⁴ The hydrothermal approach involves a reaction in a sealed, heated vessel called an autoclave. The hydrothermal approach boosts the solubility of the solid and speeds up the reaction between the solids in autoclaves by using a solvent above its critical

point. Autoclaves are typically steel cylinders used to conduct chemical processes over extended periods at high pressure and temperature.⁶⁵

In hydrothermal synthesis, superheated water acts as a powerfully polarising agent at temperatures between 100 °C and 200 °C, providing favourable conditions for reactions, suitable to promote solubility, crystallization, and diffusion. The following factors affect hydrothermal route of synthesis: a) temperature, b) pH level, and c) reaction time. The molar ratios of the reactants are crucial in figuring out the level of supersaturation, which affects the speed at which crystals develop. Supersaturation may be brought about by adding complexing agent to solution. The complexing agent needs to be stable enough and available inside an acceptable concentration to improve solubility but not solidify. The experiment's temperature significantly affects the generation of autogenous pressure inside the autoclave. Aqueous solution growth aims to supersaturate the solution without triggering nucleation spontaneously, which would compromise the final crystalline result. Water encourages the density of the materials it can dissolve and has a higher diffusivity. This lower viscosity makes mass transfer easier and has a high compressibility that simplifies changing density and dissolving power. Under high pressure, water speeds up chemical reactions.⁶⁶⁻⁷⁰ High reactant reactivity, ease of controlling solution/ interface reactions, create metastable and distinctive condensed phases, reduced energy use, and reduced air pollution are all benefits of hydrothermal synthesis. In this technique, the solvent permits controlling the kinetics of growth while preventing agglomeration. However, the drawbacks of this process include the requirement for autoclaves and the inability to see the growth of nanocrystals. The crystallinity of the generated NPs using this method is often excellent.⁷¹

1.6 Rare earth chromium oxides (R-Cr-O)

A rare earth chromium oxide (R-Cr-O) system combined and formed two compounds, named chromates (RCrO_4) and chromites (RCrO_3). These compounds' structural and physical properties differ from those discussed as follows:

1.6.1 Chromates (RCrO_4)

1.6.1.1 Crystal structure

The phase stability of lanthanide chromates (RCrO_4) depends upon the radius of rare earth elements (R). Most of the chromates crystallized in the zircon-type structure.⁷² However, with increasing radius, Ln^{3+} ions show a strong tendency towards the monazite-type structure. The details about the crystallized structures and their coordination between the elements are discussed as follows:

❖ Zircon-type structure

RCrO_4 (R = Pr, Gd, Nd, Tm, Pm, Tb, Eu, Ho, Dy, Yb, Er) compounds at ambient conditions crystallize in tetragonal zircon-type phase (space group $I4_1/amd$).^{72, 73} The zircon phase mainly consists of two fundamental building blocks, CrO_4 tetrahedra and RO_8 bisdisphenoid polyhedral. As opposed to aligning with the CrO_4 units in the third direction, RO_8 units join along the two crystallographic axes that share $O-O$ edges.⁷⁴⁻⁷⁶ **Figure 1.8 (a1)** illustrates how units of CrO_4 are spatially segregated by units of RO_8 , and the atomic arrangement in the structure is depicted in **Figure 1.8 (a2)**. Careful analysis of the structure reveals the possible pathways of the interaction. This structure provides exciting SE interaction between magnetic ions R^{3+} and Chromium (Cr^{5+}) via O , which are often extended like $\text{Cr}-O-\text{R}-O-\text{Cr}$ or $\text{R}-O-\text{Cr}-O-\text{R}$.⁷⁷ The reflection condition in the zircon-type structure written as, $h+k = 2n$; $l = 0$, $h+k = 2n$; $h = 0$, $k+l = 2n$; and $h = k$, $2h+l = 4n$. The atoms occupy the following position in zircon-type chromates: R^{3+} in $4a$ sites (0, 3/4, 1/8), Cr^{5+} in $4b$ sites (0, 1/4, 3/8), and O in $16h$ (0, y , z). The size of the RO_8 bisdisphenoid polyhedron gradually declines, and the

size of the CrO_4 tetrahedra increases when the size of the R^{3+} ion drops from Pr^{3+} to Yb^{3+} . Consequently, the $Cr-O$ bond length increases, which means the bonds become weaker along with the $RCrO_4$ series of oxides. In contrast, the $R-O$ bond length gets shorter along the series resulting in stronger bonds showing a more acidic Lewis character having more affinity for the electrons.⁷⁸⁻⁸⁰

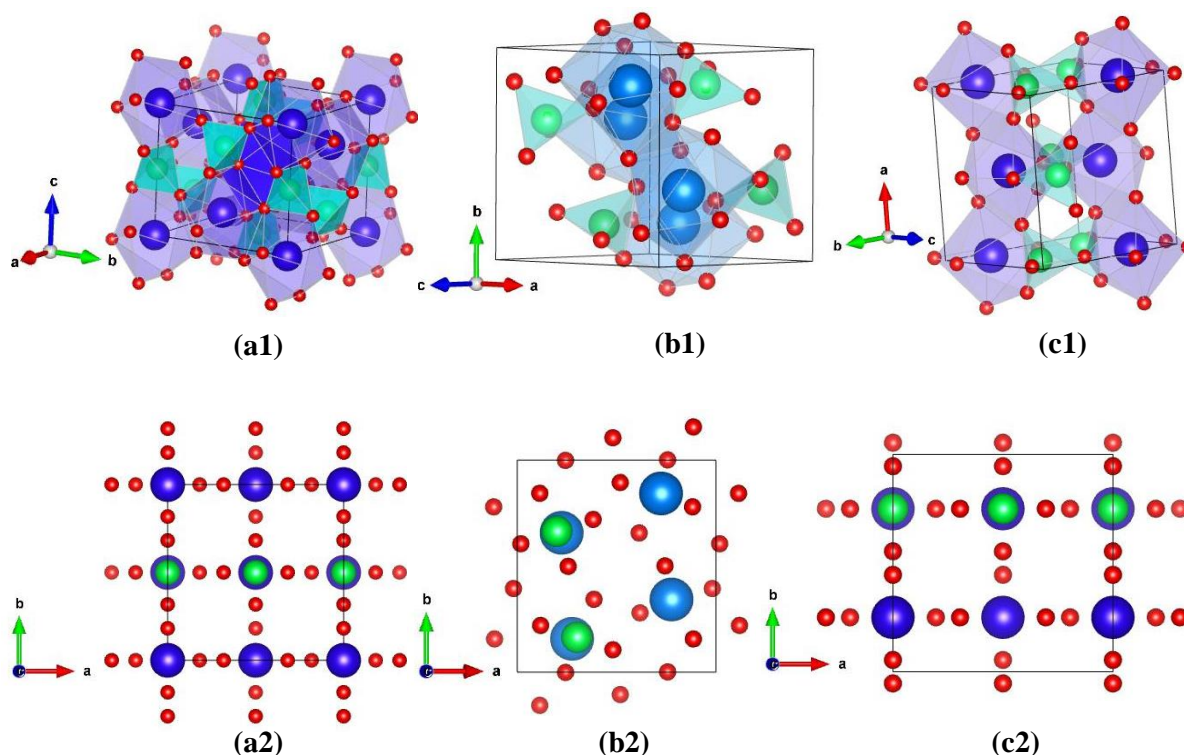


Figure 1.8: shows the crystal structure of $RCrO_4$: (a1 & a2) for zircon-type phase, (b1 & b2) monazite-type phase and (c1 & c2) scheelite-type phase. The R atom (blue), Cr atom (green), and O atoms are shown as small red circles. The perspective projection of CrO_4 tetrahedra (Cr green in the center) and RO_8 polyhedra (R blue in the center) are shown in the (a1) and (c1) structure, whereas in (b1) CrO_4 tetrahedra and RO_9 polyhedra (R blue in the center) are shown.

❖ Monazite-type structure

$R = La$ and Pr , in the $RCrO_4$, crystallizes in a monoclinic monazite-type structure due to a larger ionic radius of La^{3+} ion with space group $P2_1/n$. This structure has two fundamental

building blocks, CrO_4 tetrahedra, and RO_9 polyhedra, which are edge-shared with CrO_4 tetrahedra along the c-axis; therefore, the coordination number is 9 in the monazite-type structure. The $PrCrO_4$ compound crystallizes in dimorphic form, i.e., both zircon-type as well as monazite-type phases. But the most stable phase for $PrCrO_4$ is the zircon-type phase.⁷⁹⁻⁸⁷

Fig. 1.8 (b1 & b2) shows the structure view and atom position for the monazite-type $RCrO_4$ compound.

❖ Scheelite-type structure

The scheelite-type phase has a tetragonal symmetry with space group $I4_1/a$. The fundamental building blocks in this structure are the same as that of zircon-type structure; CrO_4 tetrahedra as well as RO_8 polyhedra. But the linkage between both the polyhedrons was different as in the zircon-type structure. There is no edge-sharing between both polyhedral RO_8 and CrO_4 , as shown in **Fig. 1.8 (c1 & c2)**, which shows the structural view and atomic position in the scheelite-type phase. In scheelite-type phase, RO_8 basisphenoid of different chains form dimers of R_2O_{14} composition, whereas the CrO_4 tetrahedra are aligned along the a-axis.^{76, 88-90} Scheelite-type structure has been reported with a minimal difference in the two types of $R-O-Cr$ bond angle as compared to the zircon-type structure.⁷³ For this the reflection conditions were written as: $h+k+l = 2n$; $l = 0$, $h, k = 2n$; and $h = k = 0$, $l = 4n$ with the position of atoms: R^{3+} at $(0, 1/4, 5/8)$ on the $4b$ Wyckoff sites, Cr^{5+} at $(0, 1/4, 1/8)$ on the $4a$ Wyckoff sites, O at (x_2, y_2, z_2) on the $16f$ Wyckoff sites, where x_2 , y_2 , and z_2 are internal parameters.^{78, 91}

1.6.1.2 Phase transition in the $RCrO_4$

The $RCrO_4$ compounds are affected by external pressure and temperature. When pressure and temperature were applied externally, the zircon phase changed into the tetragonal scheelite phase. In contrast, high-temperature sintering (under ambient pressure) changed the zircon type to the orthorhombic perovskite phase. Many research groups explored these phase transitions. The phase transition of $RCrO_4$ ($R = Pr, Nd, Sm-Lu$, and Y) has so far been explored.

Most frequently, this transition was seen at temperatures between 773 K - 873 K and pressures between 6 GPa - 8 GPa.^{76, 90} Scheelite-type phases have a 10% higher density and more-efficient structural packing than zircon-type phases due to a simple shearing mechanism and slight rotations of the CrO_4 tetrahedral unit during the phase transition. The zircon to scheelite phase transition is both reconstructive and first-order. The $Cr-O$ and $R-O$ lengths are not much altered during this transition; however, there has been a notable shift in bond angles.^{73, 90} For the $YCrO_4$ compound, the optimal phase transition pressure and temperature from zircon-to-scheelite-type phase imply 8–10 GPa with 350 °C –400 °C. During the transition, the c/a lattice-axis ratio and theoretical density in scheelite phase grew by around 156% and 10.7%, respectively.⁷⁸

In the $RCrO_4$, the valence state of Cr^{5+} is very rare. A high enough temperature will cause the complex to break into a refractory $RCrO_3$ perovskite because of its peculiar ionic state, which is sensitive to heat. The zircon phase changed into the perovskite phase, which contains Cr in the most stable state, Cr^{3+} , at high temperature and ambient pressure. In order to analyze the phase transition in $DyCrO_4$, low-temperature neutron diffraction was used. This comprehensive diffraction investigation results show that the unit cell volume does not significantly alter throughout the crystal structural phase transition from tetragonal $I41/amd$ to orthorhombic $Imma$ symmetry, which occurs between 27 K and 40 K. The tetragonal phase transforms into orthorhombic at temperatures higher than 600 °C. At 700 °C and ambient pressure, the monazite-type $LaCrO_4$ phase transforms into $LaCrO_3$.^{73, 92, 93}

1.6.1.3 Properties of $RCrO_4$

❖ Magnetic properties

The exceptionally high chemical valence of Cr, i.e., Cr^{5+} , in $RCrO_4$ compounds has led to research into their intriguing magnetic characteristics. This system has the contrast magnetic

RCrO₄ compounds	Structure, Symmetry, Space group	Magnetic nature	Transition temperature (T_N/T_C) (K)
LaCrO₄	Monazite-type, Monoclinic, P2 _{1/n}	Antiferromagnetic	25
PrCrO₄	Zircon-type, tetragonal, I4 _{1/amd}	Antiferromagnetic	9
NdCrO₄	Zircon-type, tetragonal, I4 _{1/amd}	Antiferromagnetic	25
SmCrO₄	Zircon-type, tetragonal, I4 _{1/amd}	Antiferromagnetic	15
GdCrO₄	Zircon-type, tetragonal, I4 _{1/amd}	Ferromagnetic	21-22
TbCrO₄	Zircon-type, tetragonal, I4 _{1/amd}	Ferromagnetic	22
DyCrO₄	Zircon-type, tetragonal, I4 _{1/amd}	Ferromagnetic	23
HoCrO₄	Zircon-type, tetragonal, I4 _{1/amd}	Ferromagnetic	18
ErCrO₄	Zircon-type, tetragonal, I4 _{1/amd}	Ferromagnetic	14.9
TmCrO₄	Zircon-type, tetragonal, I4 _{1/amd}	Ferromagnetic	19
YbCrO₄	Zircon-type, tetragonal, I4 _{1/amd}	Antiferromagnetic	25
LuCrO₄	Zircon-type, tetragonal, I4 _{1/amd}	Antiferromagnetic	9

Table 1.2: Listed out the transition temperature and nature of the magnetic transition of the monazite and zircon-type RCrO₄ compounds.

order put forth. The presence of R elements affects the magnetic properties of RCrO_4 compounds. RCrO_4 of the zircon type (R= Nd, Sm, Yb, and Lu) exhibits an AFM transition, but RCrO_4 of the zircon-type (R= Gd, Ho, Tb, Er, Dy, and Tm) exhibits an FM nature, depending on the R-O distance.^{72, 77, 78, 80, 90, 91, 94-100} Crystal structure and magnetic nature with the reported transition temperature for the RCrO_4 compound were tabulated in **Table 1.2**. According to the *et.al.*, R^{3+} and Cr^{5+} sublattices are ordered at a relatively lower temperature.^{72,}
¹⁰¹ Due to the involvement of multiple potential SE pathways, DyCrO_4 's magnetic origin is quite complicated.^{73, 95} Since numerous interactions must unavoidably be considered, the SE processes are highly complicated. The O ions are present in all of the routes, which comprise the sequences $\text{Cr}^{5+} - \text{O} - \text{O} - \text{Cr}^{5+}$, $\text{Cr}^{5+} - \text{O} - \text{R}^{3+}$, and $\text{R}^{3+} - \text{O} - \text{Cr}^{5+} - \text{O} - \text{R}^{3+}$. The magnetic characteristics of monazite-type PrCrO_4 have not yet been investigated.^{79, 80, 84}

❖ Magnetocaloric effect in RCrO_4

RCrO_4 compounds, which have both sublattices $3d$ and $4f$ order collinearly and concurrently at a common temperature, are the ideal system for investigating $3d-4f$ spin interaction and the low-temperature MCE effect. The ordering of these sublattices has been investigated using neutron diffraction analysis and magnetic measurements. The MCE effect was researched in zircon-type RCrO_4 with R = Gd, Ho, Er, and Dy.^{75, 89} GdCrO_4 and HoCrO_4 display a negative entropy change close to the magnetic transition temperature due to a field-induced metamagnetic transition. This transition provides the more considerable MCE parameters for moderate field strength applicable in low-temperature magnetic refrigeration. The DyCrO_4 has also been demonstrated to undergo the significant magnetic entropy change associated with the FM transition. This could be due to the intense rivalry between FM and AFM SE contacts, which renders the system a prospective magnetic refrigerant material for hydrogen liquefaction.^{74, 75, 89}

The investigation continues with the composite material of GdCrO_4 and ErCrO_4 , as these compounds exhibit MCE action. The Curie transition temperatures for the second-order magnetic transition in both compounds are 22.0 K and 14.9 K, respectively, and this combined magnetic contribution exhibits a significant entropy decrease. The transition temperature of the composite material is close to 20.3 K, which is within the range of the liquid hydrogen temperature. Consequently, we can employ this compound to store liquid hydrogen as well.¹⁰²

❖ **Ferroelectric effect in RCrO_4**

The research demonstrates that RCrO_4 is a novel multiferroic compound. According to ab initio calculations, the Cr^{5+} tetrahedral coordination causes a high bandgap in the YCrO_4 and RCrO_4 . YCrO_4 was shown to be a reliable insulator through experimentation. The monazite-type and zircon-type oxides are typically known as insulators. Still, they are n-type semiconductors in RCrO_4 compounds.

A few members of the RCrO_4 series (R= Sm, Ho, Dy, Gd) and YCrO_4 were examined for ferroelectric ordering. The ferroelectric ordering of these compounds is driven by the centrosymmetric $I41/amd$ to non-centrosymmetric $I42d$ structural transition, which takes place above their magnetic ordering temperature. The considerable spontaneous electric polarisation value of YCrO_4 ($\sim 590 \mu\text{C}/\text{m}^2$) indicates that the presence of rare earth cations has no impact on this value.⁷² The distortion of the CrO_4 tetrahedra served as the primary catalyst for the emergence of the polar order and spontaneous electric polarisation. Experimental results were shown that the ferroelectric ordering temperatures for RCrO_4 (R = Sm, Ho, Gd, Dy) and YCrO_4 at 103 K, 108 K, 98 K, 97 K, and 100 K are substantially higher than that for their magnetic ordering temperatures 15 K, 22 K, 18 K, 23 K, and 9 K, respectively.^{72,103,104}

1.6.2 Chromite (RCrO_3)

1.6.2.1 Crystal structure

❖ Perovskite structure

A large class of compounds known as "perovskites" share crystal structures with the perovskite mineral CaTiO_3 . There are numerous diverse types of compounds in the perovskite structure. This compound class has various physical properties because it can retain a wide range of ions. The family of oxides known as perovskites has likely been the subject of most research. The vast and always unexpected range of properties exhibited by compounds with this family of crystal structures and their adaptability to accommodate practically all of the periodic system's elements are what draw people's interest in them. In the 1920s, Goldschmidt et al.¹⁰⁵ did ground breaking structural research on perovskites, the foundation for subsequent studies of the perovskite family of chemicals.¹⁰⁵

In ABO_3 , the B ion is octahedrally coordinated by six O ions, whereas two B cations & four A cations coordinate the O anions, and 12 O anions surround the A cation in a dodecahedral environment. 3D cubic network of corner-sharing BO_6 octahedra is the typical description of the perovskite structure. According to the definition, a cation is located in the middle of a cube with eight units that share a corner. There are numerous known compounds with perovskite or similar structures due to the perovskite structure's well-known flexibility and the ability to vary the A and B ions. In addition to the mineral perovskite itself being slightly deformed, the perfect cubic perovskite structure is not particularly common. Perovskites have a cubic system in their ideal state, but several structural aberrations are possible, giving perovskites a wealth of physical features. Perovskite materials have a variety of crystal forms, including cubic, tetragonal, orthorhombic, rhombohedral, monoclinic, and triclinic¹⁰⁶. Reduced symmetry in distorted perovskites is crucial to their magnetic and electric characteristics.

Rarely can a single consequence be linked to a distortion of a specific perovskite molecule? Usually, the structure is affected by several things. Three mechanisms might lead to variations from the ideal perovskite structure: octahedra distortions, displacements of cation inside the octahedra, and tilting of octahedra. The electronic instability of the metal ion leads to octahedral distortions and cation displacements inside them.¹⁰⁷ Perovskites are very important in industry because of these characteristics, especially the ferroelectric tetragonal form of BaTiO_3 . BaTiO_3 is a complex material that undergoes four phase changes when heated: rhombohedral ($R3m$), orthorhombic (Amm_2), tetragonal ($P4mm$), and cubic ($Pm-3m$).^{108, 109}

Figure 1.9 shows the perovskite crystal structure.

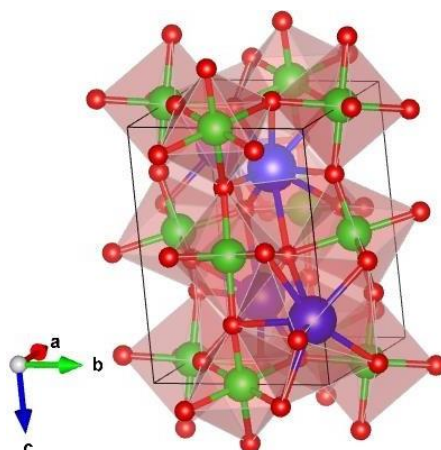


Figure 1.9: Perovskite crystal structure for RCrO_3 . The R atom (blue), Cr atom (green), and O atoms are shown as small red circles.

1.6.2.2 Properties of RCrO_3

❖ Magnetic properties

Orthorhombic rare earth manganites and rare earth ferrites are isostructurally related to RCrO_3 . Orthochromites typically have T_N values between ~ 110 K and ~ 210 K and are G-type AFMs.¹¹⁰⁻¹¹² G-type configurations with the ideal Γ_1 , Γ_2 , and Γ_4 orthochromites are used to represent them (**Figure 1.10**).^{113, 114} Orthochromites can have a magnetic structure of either Γ_4

or Γ_2 , depending on the magnetic properties of the R-site element.^{113, 114} Some orthochromites, such as (Er, Sm, Gd, and Nd) CrO₃, display spin reorientation (SR) transitions, which change from a spin structure of two to one, as a result of the magnetic interaction between the canted Cr³⁺ spins and the R³⁺ spins at low temperatures.^{111, 112, 115-117}

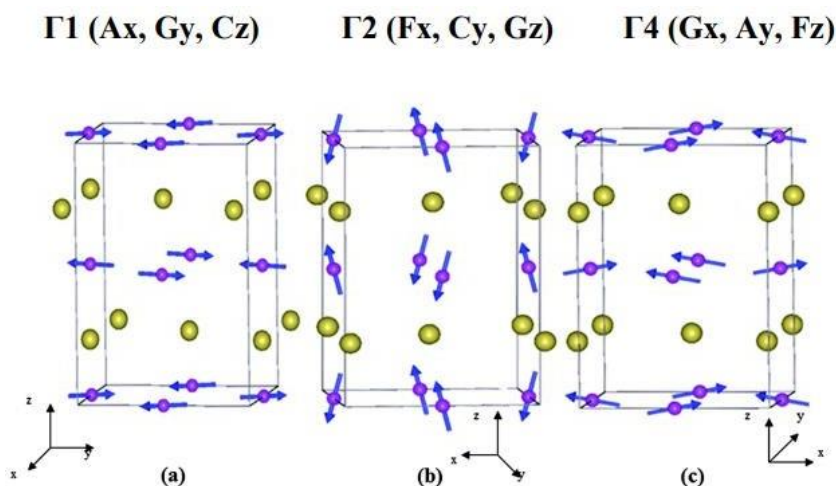


Figure 1.10: G-type AFM configuration having Γ_1 , Γ_2 , and Γ_4 spin structure with $Pbnm$ symmetry.^{113, 114}

❖ Magnetocaloric effect in RCrO₃

Since R spins are ordered at low temperatures, RCrO₃ materials are also thought to exhibit the MCE, offering them a suitable option for MCE refrigeration applications requiring low temperatures. Like manganites, RCrO₃ was primarily investigated for their multiferroic behavior, although the genesis of FE is still up for question, and much of the study was focused on figuring it out.^{118, 113, 111} As a result, their reduced specific heat capacity (C_p) values (~ 95 – 109 J/mol/K), which promote more significant ΔT_{ad} , the RCrO₃ family of compounds, have recently come to light as possible MCE materials. *McDannald et al.*¹¹⁹ investigated the MCE in bulk DyCrO₃ as well as discovered a significant entropy change of 8.1 J/Kg K at a temperature of ~ 12 K with a relative cooling power (RCP) of ~ 196 J/Kg in a 3 T applied magnetic field. In a similar vein, the reported magnetic entropy for single crystals of GdCrO₃

is 31.6 J/Kg K.¹²⁰ The magnetic nanoparticles, as opposed to their bulk equivalents, offer better magnetocaloric refrigeration performance.^{121, 122} Nanoparticles' refrigeration capacity (RC) is enhanced, making them suitable for commercial use. Nanoparticles were distinctive in features, such as distribution of particle size and interparticle interactions, which broaden the entropy change over a wide range of temperature.^{121, 123, 124} A magnetic refrigerant that operates inbetween 10 K and 80 K at a low applied field is generally ideal.¹¹⁹

1.7 Lanthanides

The lanthanides, which stand between the *s* and *d* block elements, are electropositive metals. Their inner cores are xenon ion-configured with [Xe] $4f^n 5d^1 6s^2$ or [Xe] $4f^n 6s^2$ electronic configurations. The lanthanides were previously referred to as rare earth elements because scientists thought that only trace amounts of these elements were present in the earth's crust. The first element in this family, lanthanum, inspired the word "lanthanides," which was later used. The majority of lanthanides are found in the earth's crust; however, they are not exceptionally rare. Today, all of the lanthanides—aside from promethium—have abundances equivalent to numerous other elements in the periodic table.¹²⁵

Over 150 years of research leading up to the lanthanide's discovery were conducted. Due to the abundance of lanthanides in the same minerals and their similar chemical properties—including equal ionic radii, the same dominant oxidation state (+3), and minor variations in complex formation and solubility—separation of the elements proved to be difficult for scientists.¹²⁵ Nevertheless, the discovery of lanthanide ions was made possible thanks to significant efforts by researchers worldwide and the spectroscope's development.

Atomic no.	Name, symbol	Electronic configuration	Ln 3+ Electronic configuration
58	Cerium, Ce	[Xe] 4f ¹ 5d ¹ 6s ²	[Xe] 4f ¹
59	Praseodymium, Pr	[Xe] 4f ³ 6s ²	[Xe] 4f ²
60	Neodymium, Nd	[Xe] 4f ⁴ 6s ²	[Xe] 4f ³
61	Promethium, Pm	[Xe] 4f ⁵ 6s ²	[Xe] 4f ⁴
62	Samarium, Sm	[Xe] 4f ⁶ 6s ²	[Xe] 4f ⁵
63	Europium, Eu	[Xe] 4f ⁷ 6s ²	[Xe] 4f ⁶
64	Gadolinium, Gd	[Xe] 4f ⁷ 5d ¹ 6s ²	[Xe] 4f ⁷
65	Terbium, Tb	[Xe] 4f ⁹ 6s ²	[Xe] 4f ⁸
66	Dysprosium, Dy	[Xe] 4f ¹⁰ 6s ²	[Xe] 4f ⁹
67	Holmium, Ho	[Xe] 4f ¹¹ 6s ²	[Xe] 4f ¹⁰
68	Erbium, Er	[Xe] 4f ¹² 6s ²	[Xe] 4f ¹¹
69	Thulium, Tm	[Xe] 4f ¹³ 6s ²	[Xe] 4f ¹²
70	Ytterbium, Yb	[Xe] 4f ¹⁴ 6s ²	[Xe] 4f ¹³
71	Lutetium, Lu	[Xe] 4f ¹⁴ 5d ¹ 6s ²	[Xe] 4f ¹⁴

Table 1.3: The electronic configurations of lanthanides and lanthanide ions, along with their ground state term symbols.¹²⁷

Ytterby, a small Swedish hamlet, had a quarry where Arrhenius made the rare mineral discovery known as ytterite in 1787. Finn Johan Gadolin investigated ytterite for seven years before coming to the conclusion that it contains yttria, an impure form of yttrium oxide. In 1800, the mineral ytterite was renamed gadolinite in Johan Gadolin's honor. This ore was subsequently used to produce nine new elements: ytterbium, erbium, terbium, holmium, thulium, scandium, gadolinium, dysprosium, and lutetium.¹²⁶ In terms of the lanthanide series

of elements, cerium was the first to be discovered, which came from the ceria oxide ore in the second half of the 18th century.¹²⁷

The electrons in the $4f$ orbitals are filled as we transition from La^{3+} to Lu^{3+} . The lanthanide atom has a Xe atom configuration with three outer electrons ($4f^n 6s^2$ or $4f^n 6s^2 5d^1$ if $n > 14$), with a change in the f electrons, in its ground state electronic configuration. During ionization, the $6s^2 5d^1$ electrons stripped from lanthanide atoms result in Ln^{3+} ions with the structure $[\text{Xe}] 4f^n$. The most stable ionization state for lanthanides is the trivalent state.¹²⁸ The $5s^2 5p^6$ subshells outside of the $4f$ shells have a wider radial expansion, which acts to shield the levels from the effects of the environment and shield the $4f$ orbitals. **Table 1.3** lists the ground state term symbols for the electronic configurations of the Ln and Ln^{3+} ions.¹²⁷

1.8 Why is rare earth chromium oxide (R-Cr-O) so interesting?

Rare earth chromium oxides (R-Cr-O) in different combinations give us two types of structures chromates RCrO_4 and Chromites RCrO_3 . RCrO_4 has a unstable state of Cr i.e., Cr^{+5} . The structural symmetry of these compounds depends on the R element present in the compound. For larger atomic radii elements like La and Pr, it crystallized in a monazite-type structure. In comparison, it gives a zircon-type structure for smaller atomic radii elements such as Nd, Dy, Eu, Ho, Sm, Er, Gd, Tm, Yb, and Lu.^{72, 73, 79-87}

Further on, external temperature and pressure application show the phase transition to scheelite-type and perovskite structure.^{73, 76, 78, 90, 92, 93} Again depending on the rare earth involved in the structure, it gives the different magnetic properties for RCrO_4 .^{72, 77, 78, 80, 90} It is a perfect system to explore the $3d-4f$ interaction since the lattice elements R^{3+} and Cr^{5+} are ordered at low temperatures. This property made it a potential candidate for MCE at low temperatures, which was used in the application field of hydrogen liquification and cryogenics.^{75, 89, 102} We chose to experiment with RCrO_4 compounds due to the structural phase shift and the opportunity to thoroughly study new synthesis techniques. It is possible to study

this structural distortion in the phases caused by the alteration of the bond distances between $R-O$ and $Cr-O$ when shifting R from La-Yb, utilizing various measuring techniques.

The other compounds, which together created $RCrO_3$, crystallized in perovskites, which are known for their many characteristics. The negative magnetization and exchange bias of chromites, which have important technological implications for memory and spintronics, are two intriguing features that our group previously discovered in chromites.^{111, 129, 130, 131-135} Due to the fact that magnetic properties depend on the size and form of the particles, we are intrigued to work with $RCrO_3$ compounds by examining several synthesis techniques, which provide us the unique morphology at low temperatures.

1.9 Thesis objective

As a part of ternary metal oxides, the $R-Cr-O$ system has different structural and physical properties. The physical properties of the compounds were changed due to shape, size, and different chemical environments. The synthesis route followed to get a single phase also plays a vital role during the investigation. The complete knowledge of the formation mechanism involved during the synthesis made understanding the properties easy. And the confirmation of the single phase of the compounds gives confidence in the studied properties. For these, we need to choose the appropriate synthesis method. A deep understanding of the material's formation process can only help control the pure compound. There is a lot of work to be done to refine the material property.

Thus, this thesis noticed the critical role of used formation processes while getting the single phases of $DyCrO_4$ and $DyCrO_3$ compounds. During synthesis processes, the role of complexing agents such as oxalic acid, citric acid, EDTA, CTAB, and PVA, the role of pH, and the importance of R elements has also been described in this thesis.

So, the aim of the work presented in this thesis is as follows:

1. Investigating and proposing the formation mechanism involved in the used synthesis pathway while synthesizing zircon-type DyCrO_4 and perovskite DyCrO_3 in different environments by using various complexing agents.
2. Studying the rare earth-dependent structural phase transition from monazite to zircon-type in RCrO_4 .
3. Observing the effect of different reaction parameters such as synthesis duration, synthesis temperature, synthesis time, precursors, and additional agents on the shape of the particles.

1.10 Thesis outline

In **Chapter 1**, we have provided the basics of magnetism, followed by the involvement of exchange interaction. Additionally, the principles of the numerous physical properties have been shown. The RCrO_4 and RCrO_3 structures are also addressed, along with their structures, phase transition, and summary of the investigated properties. This chapter talks about the significance of R-Cr-O compounds in terms of their fundamental and technological relevance. The last discussion is about the thesis's scope.

In **Chapter 2**, we have completely examined and proposed the formation mechanism for the hydrolytic sol-gel synthesis of DyCrO_4 in acidic and basic environments after carefully reviewing the intermediate samples obtained throughout the reaction. In order to determine the crystallization temperature for single-phase DyCrO_4 with the least amount of impurities, the impact of complexing agents was also investigated. The magnetic characteristics of DyCrO_4 produced in a basic solution with oxalic acid were then analyzed.

In **Chapter 3**, we have covered the impact of changing rare earth elements on structural phase transition from monazite to zircon-type in RCrO_4 compounds using Raman scattering. The single-phase polycrystalline monazite-type LaCrO_4 , intermediate PrCrO_4 , zircon-type RCrO_4 ($R = \text{Nd, Sm, Gd, Dy, Ho, Er, Tm, and Yb}$), and YCrO_4 has been synthesized using sol-gel synthesis method. Further, the scope of the investigation is extended by comparing Raman

modes for different crystal structures and rare-earth (Dy, La) and non-rare-earth (Y) elements in the structure.

Chapter 4 looked into the hydrothermal synthesis technique for producing perovskites at low temperatures. In-depth research has also been done on the reaction mechanism while varying reaction parameters like synthesis time, temperature, and duration. There has also been discussion on the function and results of adding the precursors in order.

Lastly, in **Chapter 5**, we summarized the studies described in the thesis. Additionally, the scope of this work will be given in this chapter.

1.11 References

1. W.F. Brown, *IEEE Trans. Magn.* (1984), 20: 112.
2. Nicola A. Spaldin, *Magnetic materials, fundamentals and applications* (2011), second edition, Chapter 3, PP-22.
3. Tomas Scepka, *Noninvasive control of magnetic state in ferromagnetic nanodots by Hall probe magnetometry*, thesis (2016), Chapter 4, PP 14-19.
4. M.A. H, *The Physical Principles of Magnetism*, Wiley, Newyork, (1965).
5. P. Weiss, *J. Phys.* (1907), 6, 661.
6. E.C. Stoner, *Philos. Mag.* (1933), 15, 1018.
7. Nicola A. Spaldin, *Magnetic materials, fundamentals and applications*, (2011), second edition, Chapter 5, PP 52-54.
8. L. Néel, Propriétés Magnétiques Des Ferrites; Férrimagnétisme et Antiferromagnétisme, *Annales de Physique (Paris)*, (1948).
9. Nicola A. Spaldin, *Magnetic materials, fundamentals and applications*, (2011), second edition, Chapter 8, PP 96-98.
10. G. Shull and J.S. Smart. *Phys. Rev.*, (1949), 76:1256.
11. E.O. Wollan and W.C. Koehler, *Phys. Rev.* (1955), 100, 545.

12. Ranber Singh, *J. Magn. Magn. Mater.* (2013), 346, 58–73.
13. N. Majlis, *The Quantum Theory of Magnetism*, 2nd edition, World Scientific Publishings Co. Pte. Ltd., Singapore, (2007).
14. R.E. Hummel, *Electronic Properties of Materials*, 3rd edition, Springer Science+Business Media, Inc., New York, NY, USA, (2005).
15. Slater, J. C., *Phys. Rev.* (1930), **35** (5): 509–529.
16. Slater, J. C., *Phys. Rev.* (1930), **36** (1): 57–64.
17. Sommerfeld, A., Bethe, H., Geiger, H., Scheel, K. (eds.). *Elektronentheorie der Metalle*. Handbuch der Physik (in German) (1933), Vol. 24/2. Springer Berlin, Heidelberg. p. 595.
18. H. Kramers, *Phys.* (1934), 1, 182–192.
19. P.W. Anderson, *Phys. Rev.* (1950), 79, 350–356.
20. J. B. Goodenough, *Phys. Rev.* (1955), 100 (2): 564.
21. John B. Goodenough, *J. Phys. Chem. Solids* (1958) **6** (2–3): 287.
22. J. Kanamori, *J. Phys. Chem. Solids* (1959), **10** (2–3): 87.
23. J. M. D. Coey, *Magnetism and magnetic materials*, United States of America by Cambridge University Press, New York (2010), chapter 5 , pp 135-144.
24. https://abinit14.sciencesconf.org/data/program/lecture_May_16_bousquet_magnetism.pdf.
25. C. Zener, *Phys. Rev.* (1951), 82, 403–405.
26. Pierre-Gilles de Gennes, *Phys. Rev.* (1960), **118** (1), 141.
27. A. M. Tishin, in *Handbook of Magnetic Materials*, edited by K. H. J. Buschow (North Holland, Amsterdam, (1999), Vol. 12, pp. 395-524.
28. V. K. Pecharsky and K. A. Gschneidner, Jr., *J. Magn. Magn. Mater.* (1999), 200, 44.
29. E. Warburg, *Ann. Phys.*(1881), 13, 141.

30. P. Debye, *Ann. Phys.*(1926), 81, 1154.
31. W. F. Giaouque, *J. Amer. Chem. Soc.*(1927), 49, 1864.
32. V. K. Pecharsky and K. A. Gschneidner, Jr., *J. Appl. Phys.* (1999), 85, 5365.
33. K. A. Gschneidner, Jr. and V. K. Pecharsky, *Annu. Rev. Mater. Sci.* (2000), 30, 387.
34. K. Das, T. Paramanik, and I. Das, *J. Magn. Magn. Mater.* (2015), 374, 707.
35. N. Pavan Kumar and P. Venugopal Reddy, *Mater. Lett.* (2014), 132, 82.
36. K. Gschneidner, V.K. Pecharsky, and O. Tsokol, *Reports Prog. Phys.* (2005), 68, 1479.
37. V.K. Pecharsky and K. a Gschneidner, *Phys. Rev. Lett.* (1997), 78, 3.
38. M. Balli, P. Fournier, S. Jandl, and M.M. Gospodinov, *J. Appl. Phys.* (2014), 115, 173904.
39. H. Wada, T. Takahara, K. Katagiri, T. Ohnishi, K. Soejima, and K. Yamashita, *J. Appl. Phys.* (2015), 117, 172606.
40. O. Tegus, E. Brück, K.H.J. Buschow, and F.R. de Boer, *Nature* (2002), 415, 150.
41. Hill, N. A., *J. Phys. Chem. B* (2000), 104, (29), 6694-6709.
42. Cohen, R. E., *Nature* (1992), 358, (6382), 136-138.
43. Valasek, J., *Phys. Rev.* (1921), 17, 475-481.
44. Fugiel, B., *Physica B Condens.Matter* (2003), 325, (1-4), 256-258.
45. Konsin, P., *Phys Status Solidi B Basic Res* (1975), 70, (2), 451-459.
46. Slater, J. C., *J. of Chem. Phys.* (1941), 9, (1), 16-33.
47. Debretteville, A., *Phys. Rev.* (1955), 98, (5), 1563-1563.
48. Jaynes, E. T., *Phys. Rev.* (1950), 79, (6), 1008-1009.
49. Danielson, G. C.; Matthias, B. T.; Richardson, J. M., *Phys. Rev.* (1948), 74, (8), 986-987.
50. Richardson, J. M.; Matthias, B. T., *Phys. Rev.* (1948), 74, (8), 987-988.
51. Wang, K. F.; Liu, J. M.; Ren, Z. F., *Adv. Phys.* (2009), 58, (4), 321-448.

-
52. Anthony R. West, *Solid State Chemistry and its Applications*, Student edition (2nd edition) (2013), pp. 407.
53. D.D Sarma, A new class of magnetic materials: Sr FeMoO₆ and related compounds, 2 *Cur Opin Solid State Mater* (2001), Vol. 5 (4), pp. 261-268.
54. A. E. Danks, S. R. Hall and Z. Schnepp, *Mater. Horiz.* (2016), 3, 91–112.
55. T. K. Tseng, Y. S. Lin, Y. J. Chen and H. Chu, *Int. J. Mol. Sci.* (2010), 11, 2336–2361.
56. M. Parashar, V. K. Shukla and R. Singh, *J. Mater. Sci.: Mater. Electron.* (2020), 31, 3729–3749.
57. C. de Coelho Escobar and J. H. Z. dos Santos, *J. Sep. Sci.* (2014), 37, 868–875.
58. Nadeem Baig, Irshad Kammakakam, and Wail Falath, *Mater. Adv.* (2021), 2, 1821–1871.
59. M. Kakihana, *J. Sol-Gel Sci. Technol.* (1996), 6, 7–55.
60. A. E. Danks, S. R. Hallb and Z. Schnepp, *Mater. Horiz.* (2016), 3, 91—112.
61. Spoooren, J., Rumpelcker, A., Millange, F., Walton, *R. I. Chem. Mater.* (2003), 15, 1401.
62. Feng, S., Wang, D., Yu, R., Na, L. *Proceedings of the International Symposium on SolvoHydro-Thermal Processes* (1997), 12.
63. Feng, S., Li, G, Zhao, C., Wang, G., Wang, D., Mao, Y. Proc. 2nd Int. Conf. Solvothermal Reactions; *Org. Comm. Solvothermal Tech. Res.:* Takamatsu, Japan (1996), 101.
64. Hagrman, P. J., Hagrman, D., Zubieta, J., *Angew. Chem., Int. Ed.* (1999), 38, 2638.
65. M. Haase and H. Schäfer, *Angew. Chemie Int. Ed.* (2011), 50, 5808–5829.
66. Batten, S. R.; Robson, R. *Angew. Chem., Int. Ed.* (1998), 37, 1460.
67. Janiak, C. *Angew. Chem., Int. Ed. Engl.* (1997), 36, 1431.
68. West, A.R. *Solid State Chemistry* (1984), John Wiley & Sons USA.
69. Laudise, R.A. *The growth of single crystals* (1970), Prentice Hall USA.
-

-
70. Wu, N. C, Shi, E. W., Zheng Y. Q., Li, W. J. J., *Amer. Cer. Soc.* (2002), 85, 2462.
 71. Hensch, H.K. *Crystal in Gels and Liesegang Rings* (1988), CUP. Britain.
 72. A. Indra, K. Dey, J. K. Dey, S. Majumdar, U. Rütt, O. Gutowski, M. v. Zimmermann, and S. Giri, *Phys. Rev. B* (2018), 98, 014408.
 73. Youwen Long, Qingqing Liu, Yuxi Lv, Richeng Yu, and Changqing Jin, *Phys. Rev. B* (2011) 83, 024416.
 74. A. Midya, N. Khan, D. Bhoi, and P. Mandal, *J. Appl. Phys.* (2014), 115, 17E114.
 75. A. Midya, N. Khan, D. Bhoi, and P. Mandal, *Appl. Phys. Lett.* (2013), 103, 092402.
 76. Avijeet Ray and Tulika Maitra, *J. Phys.: Condens. Matter* (2015), 27, 105501 (9pp).
 77. A. Morales-Sánchez and F. Fernández, *J. Alloys Compd.* (1993), 201, 161-165.
 78. Y. W. Long, L. X. Yang, Y. Yu, F. Y. Li, R. C. Yu, and C. Q. Jin, *Phys. Rev. B* (2007), 75, 104402.
 79. E. Jimenez, J. Isasi, R. Saez-Puche, *J. Alloys Compd.* (2001), 323–324, 115–118.
 80. E. Jimenez, J. Isasi, and R. Saez-Puche, *J. Solid State Chem.* (2002), 164, 313–319.
 81. S. G. MANCA and E. J. BARAN, *J. Appl. Cryst.* (1982), 15, 102-103.
 82. Yoshitaka Aoki, Hidetaka Konno, Hiroto Tachikawa and Michio Inagaki, *Bull. Chem. Soc. Jpn.* (2000), 73, 1197-1203.
 83. Hidetaka KONNO, Hiroto TACHIKAWA, Atsushi FURUSAKI and Ryusaburo FURUICHI, *Anal Sci.* (1992), VOL. 8
 84. S. G. MANCA and E. J. BARAN, *J. Phys. Ch. Solids* (1981) Vol. 42. No. 10,99.
 85. Nicolas Clavier, Renaud Podor, Nicolas Dacheux, *J. Eur. Ceram Soc.* (2011), 31, 941–976.
 86. Daniel Errandonea, *Phys. Status Solidi B* (2017), 254, No. 5, 1700016.
 87. Yoshitaka Aoki, Hidetaka Konno and Hiroto Tachikawa, *J. Mater. Chem.* (2001), 11, 1214–1221.
-

-
88. Huaiyong Li, Hyeon Mi Noh, Byung Kee Moon, Byung Chun Choi, Jung Hyun Jeong, *J Alloys Compd* (2014), 582, 151–156.
89. E. Palacios, C. Tomasi, R. Saez-Puche, A. J. Dos santos-García, F. Fernandez-Martínez, and R. Burriel, *Phy. Rev. B* (2016), 93, 064420.
90. R. Sáez Puche, J. M. Gallardo, J. Romero de Paz, N. Taira and E. Climent-Pascual, *J. Argent. Chem. Soc.* (2009), 97(1), 90-101.
91. Linyan Li, Wen Yu, and Changqing Jin, *Phy. Rev. B* (2006), 73, 174115.
92. Y.W. Long, Q. Huang, L.X. Yang, Y. Yu, Y.X. Lv, J.W. Lynn, Ying Chen, C.Q. Jin, *J Magn. Mater.* (2010), 322, 1912–1916.
93. J. D. Carter, H. U. Anderson, M. G. Shumsky, *J. Mater Sci.* (1996), 31, 551- 557.
94. Esteban Climent-Pascual, Julio Romero de Paz, José Manuel Gallardo-Amores, Regino Sáez-Puche, *Solid State Sci.* (2007), 9, 574-579.
95. Keitaro Tezuka and Yukio Hinatsu, *J Solid State Chem.* (2001), 160, 362-367.
96. Keitaro Tezuka, Yoshihiro Doi and Yukio Hinatsu, *J. Mater. Chem.* (2002), 12, 1189–1193.
97. E. Jimenez, J. Isasi, R. Saez-Puche, *J Alloys Compd* (2000), 312, 53–59.
98. R. Sáez-Puche, E. Jiménez, J. Isasi, M.T. Fernández-Dí and J.L. García-Munoz, *J Solid State Chem.* (2003), 171, 161–169.
99. E. Jimenez-Melero, N.H. van Dijk, W.H. Kraan, P.C.M. Gubbens, J. Isasia, R. Saez-Puche, *J Magn. Mater.* (2005), 288, 1–14.
100. E. Climent Pascual, J. M. Gallardo Amores, and R. Sáez Puche, *Phys. Rev. B* (2010), 81, 174419.
101. E Jimenez-Melero, P C M Gubbens, M P Steenvoorden, S Sakarya, A Goosens, P Dalmas de Reotier, A Yaouanc, J Rodríguez-Carvajal, B Beuneu, J Isasi, R Sáez-Puche, U Zimmerman and J L Martínez, *J. Phys.: Condens. Matter* (2006), 18, 7893–7904.
-

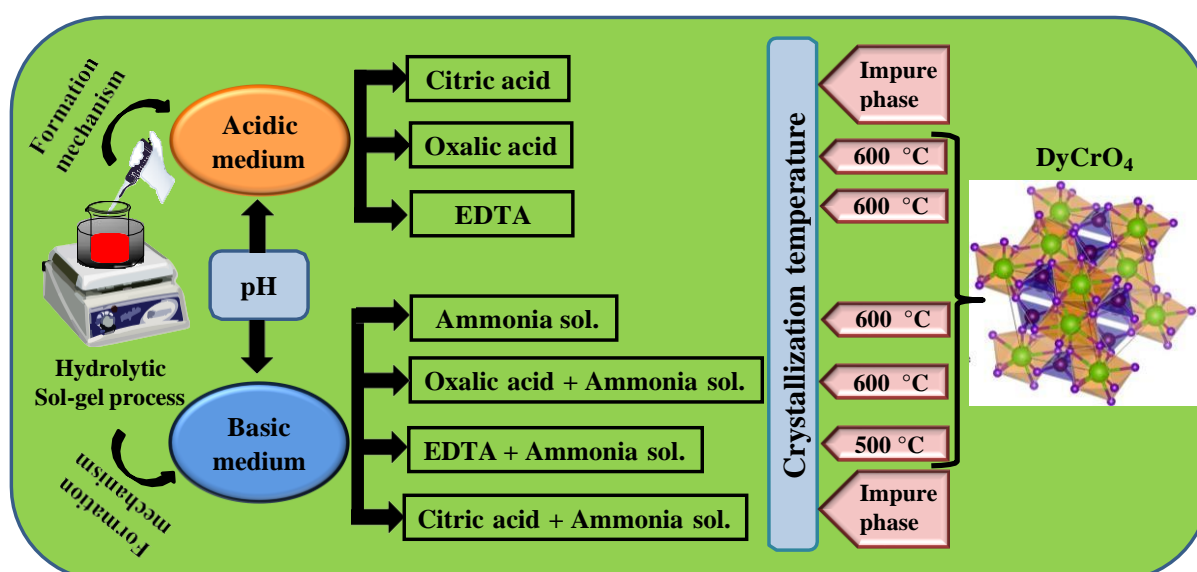
-
102. Q. Y. Dong, Y. Ma, Y. J. Ke, X. Q. Zhang, L. C. Wang, B. G. Shen, J. R. Sun, and Z. H. Cheng, *Mater. Lett.* (2015), V-161, 669-673.
103. A. Indra, S. Giri, *J. Magn. Magn. Mater.* (2019), 489, 165467.
104. Xudong Shen, Long Zhou, Yisheng Chai, Yan Wu, Zhehong Liu, Yunyu Yin, Huibo Cao, Clarina Dela Cruz, Young Sun, Changqing Jin, Angel Muñoz, JoséAntonio Alonso and Youwen Long, *NPG Asia Materials* (2019), 11:50.
105. A.S. Bhalla, R. Guo and R. Roy, *Mat. Res. Innovat.* (2000), 4, 3-26.
106. Aleksandrov, K. S.; Bartolome, *J. Phase Transitions* (2006), 74, 255.
107. Woodward, P. M. *Acta Cryst. B* (1997), 53, 32.
108. A.F. Wells, *Structural Inorganic Chemistry*, Oxford Science publications (1995).
109. U. Müller, *Inorganic Structural Chemistry*, Wiley & Sons Ltd (1993).
110. K. Sardar, M.R. Lees, R.J. Kashtiban, J. Sloan, and R.I. Walton, *Chem. Mater.* (2011), 23, 48.
111. A. Jaiswal, R. Das, K. Vivekanand, T. Maity, P.M. Abraham, S. Adyanthaya, and P. Poddar, *J. Appl. Phys.* (2010), 107, 013912.
112. H. Cooke, D.M. Martin, and M.R. Wells, *J. Phys. C Solid State Phys.* (1974), 7, 3133.
113. R. Saha, a. Sundaresan, and C.N.R. Rao, *Mater. Horizons* (2014), 1, 20.
114. B. Rajeswaran, D.I. Khomskii, K. Zvezdin, C.N.R. Rao, and Sundaresan, *Phys. Rev. B - Condens. Matter Mater. Phys.* (2012), 86, 1.
115. G. Gorodetsky, R.M. Hornreich, S. Shaft, B. Sharon, Shaulov, and B.M. Wanklyn, *Phys. Rev. B* (1977), 16, 515.
116. X. Qian, L. Chen, S. Cao, and J. Zhang, *Solid State Commun.* (2014), 195, 21.
117. R.M. Hornreich, Y. Komet, R. Nolan, B.M. Wanklyn, and I. Yaeger, *Phys. Rev. B* (1975), 12, 5094.
-

-
118. J.R. Sahu, C.R. Serrao, N. Ray, U. V. Waghmare, and C.N.R. Rao, *J. Mater. Chem.* (2007), 17, 42.
119. McDannald, L. Kuna, and M. Jain, *J. Appl. Phys.* (2013), 114.
120. L.H. Yin, J. Yang, X.C. Kan, W.H. Song, J.M. Dai, and Y.P. Sun, *J. Appl. Phys.* (2015), 117, 133901.
121. P. Poddar, J. Gass, D.J. Rebar, S. Srinath, H. Srikanth, S. a. Morrison, and E.E. Carpenter, *J. Magn. Magn. Mater.* (2006), 307, 227.
122. P. Poddar, S. Srinath, J. Gass, B.L. V Prasad, and H. Srikanth, *J. Phys. Chem. C* (2007), 111, 14060.
123. S. Srinath, P. Poddar, R. Das, D. Sidhaye, B.L.V. Prasad, J. Gass, and H. Srikanth, *Chem Phys Chem* (2014), 15, 1619.
124. V. Franco, a. Conde, D. Sidhaye, B.L. V Prasad, P. Poddar, S. Srinath, M.H. Phan, and H. Srikanth, *J. Appl. Phys.* (2010), 107, 1.
125. S. Cotton, *Lanthanide and Actinide Chemistry*, John Wiley & Sons, Ltd, Chichester, UK, (2006).
126. M. H. V. Werts, *Sci. Prog.* (2005), 88, 101–131.
127. D. R. Lide, G. Baysinger, L. I. Berger, R. N. Goldberg, H. V Kehiaian, K. Kuchitsu, D. L. Roth and D. Zwillinger, *Handbook of Chemistry and Physics*, CRC Press (2003).
128. J.-C. G. Bünzli and S. V. Eliseeva, in *Lanthanide Luminescence: Photophysical, Analytical and Biological Aspects*, Springer-Verlag Berlin Heidelberg (2010), vol. 2, pp. 1–45.
129. K. Yoshii, *Appl. Phys. Lett.* (2011), 99, 142501.
130. K. Yoshii, *Mater. Res. Bull.* (2012), 47, 3243.
131. T. Bora and S. Ravi, *J. Magn. Magn. Mater.* (2014), 208, 358-359.
132. P.K. Manna and S.M. Yusuf, *Phys. Rep.* (2014), 535, 61.
-

133. S.M. Yusuf, A. Kumar, and J. V. Yakhmi, *Appl. Phys. Lett.* (2009), 95, 182506.
134. A. Kumar and S.M. Yusuf, *Phys. Rep.* (2015), 556, 1.
135. Preeti Gupta, Richa Bhargava and Pankaj Poddar, *J. Phys. D: Appl. Phys.* (2015), 48 025004.

Chapter 2

Formation of zircon-type DyCrO_4 and its magnetic properties



Outline

The formation mechanism of hydrolytic sol-gel synthesized DyCrO_4 with a complexing agent in acidic and basic mediums is thoroughly studied. The role of complexing agents and pH on phase formation temperature is also investigated. The formation temperature for DyCrO_4 is ~ 500 °C in the absence and presence of complexing agents such as oxalic acid and ethylenediaminetetraacetic acid (EDTA) at pH 10. Whereas, when citric acid is used, the formation of DyCrO_4 along with Cr_2O_3 is observed. The crystallite size in the presence of a complexing agent in the basic medium is ~ 55 nm which is small compared to only ammonia solution. The various reaction modes lead to tetragonal zircon-type DyCrO_4 at ~ 500 °C, transforming into orthorhombic perovskite DyCrO_3 at 800 °C. The magnetization curve shows the ferromagnetic behaviour of DyCrO_4 below transition temperature $T_c \sim 21$ K.

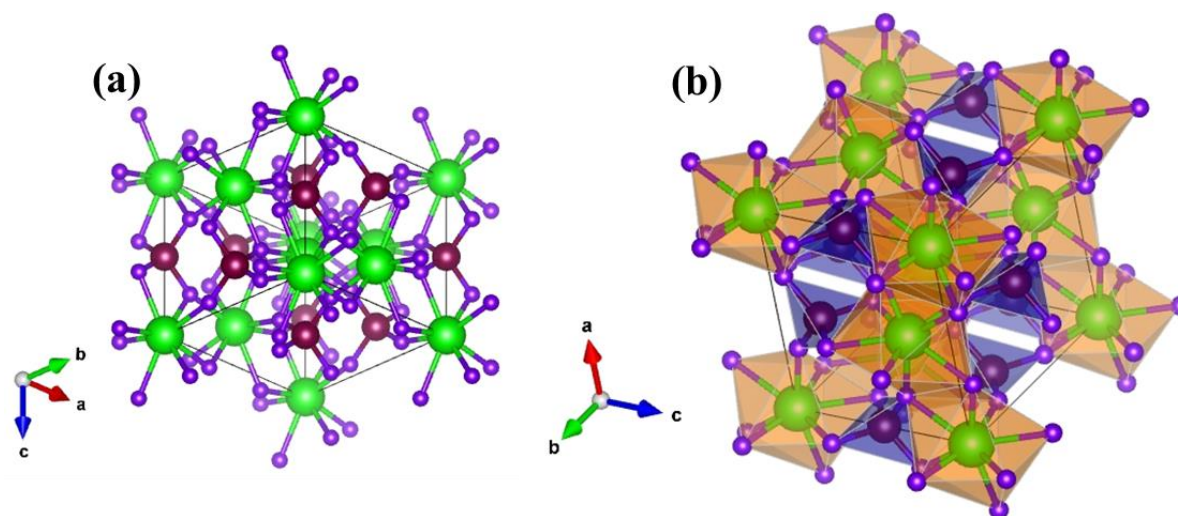
2.1 Introduction

The mixed-metal oxides such as chromites, manganites, and ferrites have gained tremendous attention due to their large-scale structural, magnetic, and transport properties, potentially being used in optoelectronic and magnetoelectric devices.¹⁻⁶ The R-Cr-O (R - rare earth element) combination in mixed-metal oxides was crystallized in chromates (RCrO_4) and chromites (RCrO_3). The RCrO_4 compounds were found in a tetragonal zircon-type structure (for R= Pr, Nd, Sm, Eu, Gd, Tb, Dy, Ho, Er, Tm, Yb, Lu) with space group $I4_1/amd$ and monoclinic monazite-type structure (for R= La, Ce) with space group $P2_1/n$, while R=Pr shows both types of structures.⁷⁻¹⁷ The RCrO_4 compounds were sensitive to external parameters like temperature and pressure. On the application of external pressure, the zircon-type RCrO_4 structure changes to another tetragonal scheelite-type structure with space group $I4_1/a$. This irreversible phase transition exhibits a volume contraction of close to 10%, denoting first-order phase transition. This phase transition results in volume change without changing the basic units of the parent structure.¹⁸⁻²³ The difference in crystal structure directly affects the properties of RCrO_4 . Hence, selecting an appropriate synthesis process for RCrO_4 becomes very important.

The magnetic interaction in RCrO_4 compounds depends on R^{3+} - R^{3+} interchain spacing. In RCrO_4 , when R= Nd, Sm, Eu, Yb, Lu shows AFM ordering, whereas R= Gd, Er, Tm, Dy, Ho settled for FM ordering because of the shortening of the R^{3+} - R^{3+} inter-chain distances.⁸⁻¹⁵ As pointed out by the Anderson-Goodenough-Kanemori (AGK) empirical rules, the SE interaction results in AFM ordering for $\sim 180^\circ$ interaction and FM for 90° interaction.²⁴⁻²⁶ Morales-Sanchez *et al.* reported the Sm-Sm distance for the SmCrO_4 was $\sim 7.248 \text{ \AA}$, larger than that along the c-axis, with the most favorable angle Sm-O-Cr of 180° that will enhance the interactions along the a-axis.¹⁰ So, SmCrO_4 shows AFM nature. The RCrO_4 structures are also ideal for studying the $3d$ - $4f$ spin interaction. The magnetism shown by these structures was due

to the interplay of spin interactions in rare-earth and transition metal-sublattices. This interplay generates one exciting property in the material, namely the magnetocaloric effect (MCE). This technology is not related to any harmful chemicals, and that's why environment friendly. Initially, MCE was only used for cryogenic refrigeration, but now it is used in applications where cryogenic temperatures are required, such as hydrogen liquefaction, magnetic measurements, etc.²⁷⁻²⁹

Among RCrO_4 compounds, zircon-type DyCrO_4 was studied for their unusual metamagnetism driven by coexisting ferromagnetic and antiferromagnetic interactions.⁶ The large angular momentum of Dy^{3+} plays a significant role in tuning the magnetic properties of RCrO_4 . **Scheme 2.1 (a) & (b)** shows the crystal structure for zircon-type DyCrO_4 . The DyCrO_4 structure was drawn with the VESTA software (version: 3.1.0) using CIF-COD ID: 1008138.



Scheme 2.1: Crystal structure of zircon-type DyCrO_4 plotted using VESTA software (3.1.0 version) using CIF – COD ID: 1008138. (a) Dy, Cr, and O atoms were represented by green, magenta, and blue spheres, respectively. (b) The basic units of the zircon-type structure are DyO_8 polyhedra (Dy atom is situated at the center of an orange polyhedron) and CrO_4 tetrahedra (Cr atom is situated at the center of a blue tetrahedron).

The DyCrO₄ structure consists of two basic units, namely CrO₄ tetrahedra and DyO₈ bidisphenoid polyhedra. DyO₈ polyhedra connect along the two crystallographic axes sharing O-O edges along the x-axis and y-axis, whereas it alternatively aligns with the CrO₄ tetrahedra along the third direction (z-axis). So CrO₄ tetrahedra were spatially isolated by DyO₈ polyhedra. It provides the superexchange pathways between Dy⁺³ ions through the direct linkage of polyhedra (Dy⁺³-O²⁻-Dy⁺³) or the CrO₄ tetrahedra (Dy⁺³-O²⁻-Cr⁺³-O²⁻-Dy⁺³), which was responsible for the magnetic properties in these compounds.⁶ The rare-earth sublattices of Dy⁺³ were ordered antiferromagnetically at low temperatures (< 25 K), whereas transition metal Cr⁺³ was ordered at relatively high temperatures.^{4,6} The low-temperature ordering in the Dy sublattices was due to the complex orbital configuration of *f*-electrons compared to transition metal *d*-electrons and magnetic interactions between *f-f* and *d-f* electrons.⁸

In tetragonal zircon-type DyCrO₄ (*I4₁/amd*), both Cr and Dy sublattices are ordered collinearly and simultaneously at a common transition temperature (24 K), making the magnetocaloric effect possible at low temperatures.⁸ MCE is related to the magnetic entropy change in the adiabatic process when applying a magnetic field. This entropy change is associated with the angular momentum 'J'. The J value for a rare and unstable Cr⁺⁵ (3d¹4s⁰) is large enough in RCrO₄ compared to the other isostructural RXO₄ (X= P, As, V) compounds. Such a large J value of Cr⁺⁵ may be responsible for the large entropy change near the transition temperature of these compounds.^{19, 30-33} On the other hand, Cr⁺³ in orthorhombic perovskite DyCrO₃ (*Pbnm*) hardly contributes to the magnetocaloric effect at low temperatures due to the different ordering temperatures of Dy⁺³ and Cr⁺³.⁵

The synthesis of DyCrO₄ compounds was consistently reported by the solid-state methods.³⁴⁻³⁵ However, materials synthesized by the solid-state technique are bulk and have poor control over particle size, crystallinity, and morphology. The solid-state synthesis involves the multiple sintering sequences for a longer time (~4 h -11 h) in an oxygen

environment to achieve the single-phase of the RCrO_4 compound.^{9-12, 14} Whereas, the solution-based sol-gel method offers good control over morphology and particle size. It produces complex inorganic ternary and quaternary oxides at comparatively lower sintering temperatures and in a shorter synthesis time than the solid-state method. The aqueous hydrolysis chemistry of the metal ions in the sol-gel synthesis can be modified by complexing agents. This modification gives pure phases and nanoparticles that can tune magnetic properties.³⁶⁻³⁷

In this work, the nanocrystalline DyCrO_4 synthesis was carried out using sol-gel and complexing agents. Further, the formation mechanism involved in the hydrolytic sol-gel process was intensively investigated and proposed for the first time in zircon-type DyCrO_4 . These samples were synthesized in two different mediums; acidic (in oxalic acid) and basic (in ammonia solution), and the formation mechanism was carried out thoroughly by analyzing the intermediate samples collected in between the reactions. The steps consisting of the formation of complex, gel, and specific structures at sintering temperatures were discussed. It was observed that complexing agents like oxalic acid, citric acid, and EDTA affects the crystallization temperature of zircon-type DyCrO_4 . The comparative study between the complexing agent for different mediums (acidic and basic) was done to understand which suitable complexing agent with a reaction medium will form the single phase of DyCrO_4 with minimal impurity. To the best of our knowledge, the sol-gel method for synthesizing DyCrO_4 is rarely reported, and not much information is available on the formation mechanism. Further, morphology changes and surface valence state of the Dy, Cr, and O with the used reaction mediums for different complexing agents were investigated. The magnetic properties of sol-gel synthesized DyCrO_4 in oxalic acid were also studied and compared to the earlier reported solid-state prepared bulk DyCrO_4 .

2.2 Experimental

2.2.1 Sample preparation

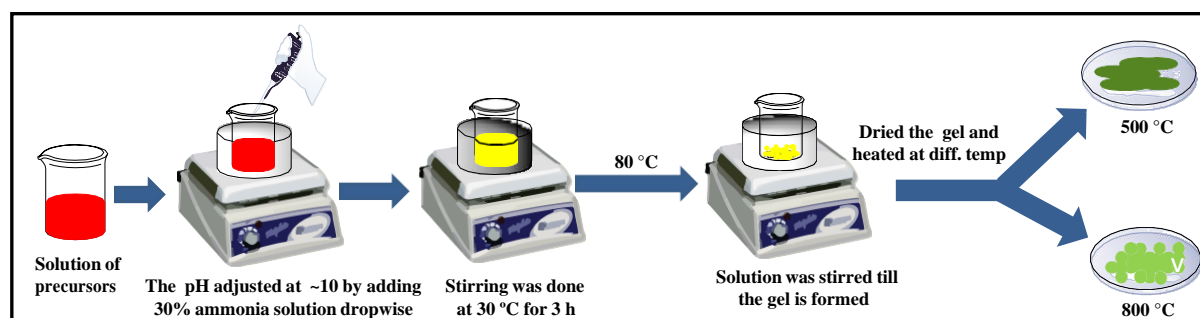
A hydrolytic sol-gel method was used to synthesize the polycrystalline zircon-type DyCrO_4 . The reaction sequence is explained in **Scheme 2.2**. The mechanism of phase formation was studied by (i) changing the reaction medium, i.e., acidic and basic (depending on the pH of the precursor solution in the reaction), and (ii) in the absence and presence of a complexing agent. Oxalic acid ($\text{H}_2\text{C}_2\text{O}_4 \cdot 2\text{H}_2\text{O}$, Merck, 99.5%), citric acid ($\text{C}_6\text{H}_8\text{O}_7$, Merck, 99.5%), and EDTA ($\text{C}_{10}\text{H}_{16}\text{N}_2\text{O}_8$, Thomas Baker, 99.0%) were used as complexing agents. The homogeneous solution was prepared for two different reaction mediums, acidic (A) and basic (B).

The dysprosium(III) nitrate hydrate ($\text{Dy}(\text{NO}_3)_3 \cdot x\text{H}_2\text{O}$, Aldrich, 99.9% metal basis), chromium trioxide (CrO_3 , Thomas Baker, 99.9%) were dissolved in deionized water in the molar ratio- Dy: Cr -1.3: 1, without using any complexing agent called hereafter as precursor solution. The precursor solution was kept on stirring for 3h at $\sim 30^\circ\text{C}$, which resulted in a sol formation. The pH of the precursor solution was observed to be ~ 0.4 . Further, without adjusting the pH, the precursor solution, when heated at 80°C , resulted in sticky gel adhering to the beaker's bottom that was difficult to collect and use for the calcination. For comparison, sol was formed by adding 30% ammonia solution dropwise to adjust the pH to ~ 10 . The obtained sol with pH 10 was heated at 80°C , which initially forms a gel, and then dried powder can be collected for further calcination process and denoted as $\text{DyCrO}_{4(\text{B})}$.

The formation mechanism was studied using the intermediate samples between the reactions in acidic (in the presence of oxalic acid) and basic (in ammonia solution) mediums for characterization. At the same time, the effect of a complexing agent was also studied by adding an aqueous solution of oxalic acid to the precursor solution. The pH of the precursor solution with oxalic acid was ~ 0.24 . As mentioned earlier, the acidic sol was heated and dried

to collect the powder. Also, for basic sol with oxalic acid, the pH was adjusted to 10 by the dropwise addition of 30% ammonia solution and dried to collect the powder. The oxalic acid derived acidic and basic powders were named $\text{DyCrO}_{4(\text{OA})}$ and $\text{DyCrO}_{4(\text{OB})}$, respectively.

Further, the powders were calcined at 500 °C, 600 °C, 700 °C, and 800 °C for 2h to find the accurate crystallization temperature of the phases. Citric acid and EDTA were also used as complexing agents in the other two reactions. The whole reaction was carried out with citric acid, and EDTA using the same reaction sequence mentioned for oxalic acid in acidic and basic medium and denoted as $\text{DyCrO}_{4(\text{CA})}$, $\text{DyCrO}_{4(\text{CB})}$, $\text{DyCrO}_{4(\text{EA})}$, $\text{DyCrO}_{4(\text{EB})}$. (C= citric acid, E=EDTA, A= acidic and B=basic)



Scheme 2.2: The reaction sequence followed in the hydrolytic sol-gel method to synthesize DyCrO_4 in different reaction mediums depending on the pH of the precursor's solution using complexing agents.

2.2.2 Characterization techniques

Powder X-ray diffraction (XRD) patterns of the synthesized samples were recorded using a PANalytical X'PERT PRO instrument in the 2θ range of 10° – 80° with iron-filtered $\text{Cu K}\alpha$ radiation ($\lambda = 1.54 \text{ \AA}$) and step size of 0.013° . HR-800 Raman spectrophotometer (Jobin Yvon-HORIBA, France) was used for bond analysis equipped with He–Ne laser (633 nm), operated at 20 mW with the accuracy of $\pm 1 \text{ cm}^{-1}$. The Raman spectra were recorded with thermoelectrically cooled (with Peltier junctions), multichannel, spectroscopic grade CCD detector (1024×256 pixels of $26 \mu\text{m}$). An objective of 50 XLD magnification was used to

focus and collect the signal from the powder sample dispersed on a glass slide. The thermal decomposition study was done using the thermogravimetric analysis (TGA) model DTG-60H of Shimadzu instrument at a heating rate of 10 °C/ min in an air atmosphere. Transmission Electron Microscope (TEM) (FEI Tecnai T20) was used to characterize the morphology and particle size at an accelerating voltage of 200 keV. Field emission scanning electron microscopy (FESEM: Hitachi S-4200) was used to analyze the particle size. Also, Energy Dispersive X-ray Analysis (EDAX) was done to determine the elemental composition of synthesized samples. The X-ray Photoelectron spectra for Dy, Cr, and O were recorded on Thermo Fisher Scientific X-ray Photoelectron Spectrometer (XPS) K-Alpha+. The monochromatic Al K α ($h\nu = 1486.6$ eV) as the X-ray source was operated with a beam current of 6 mA and voltage of 12 kV coupled with a Physical Electronics 04-548 dual Mg/Al anode and in an ultra-high vacuum system with a base pressure of $\leq 5 \times 10^{-9}$ Torr. The spot size of 400 μm was used during the XPS measurement. The recorded XPS data were deconvoluted using XPS PEAK 4.123. The XPS measurements were done on the exposed surface of the nanoparticles (NPs) prepared with a different complexing agent for acidic and basic pH without any surface treatment. All measurements mentioned above were performed at a laboratory temperature of ~ 30 °C. A superconducting quantum interference device-based vibrating sample magnetometer (SQUID-VSM, Quantum Design) was used to measure the magnetic properties of DyCrO₄. The precisely weighed powder sample was taken and packed inside a plastic sample holder. It was fitted into a brass specimen holder provided by Quantum Design Inc., contributing to an overall magnetic signal. The magnetization *versus* magnetic field (M–H) loops was collected at a different temperature in a field sweep ± 60 kOe. The magnetization *versus* temperature (M–T) measurements at standard field-cooled (FC) and zero-field cooled (ZFC) sequences was performed at a temperature sweep from 5 to 300 K in a field of 100 Oe.

2.3 Results and discussion

2.3.1 Formation mechanism

In order to study the effect of acidic and basic mediums on the phase formation temperature of DyCrO_4 , the formation mechanism of the sol-gel reaction was intensively examined by collecting intermediate samples. The details involved in the mechanism were discussed in this work.

2.3.1.1 Acidic medium

The DyCrO_4 was synthesized using oxalic acid (pH ~ 0.24) using the hydrolytic sol-gel method. The dissolution of CrO_3 in water resulted in the formation of chromic acid (H_2CrO_4) and $\text{Dy}(\text{NO}_3)_3$ in the aqueous medium dissociated in Dy^{3+} and $(\text{NO}_3)^{3-}$ ions (**Scheme 2.3(1, 2)**). So, at 30 °C, the precursor solution contains H_2CrO_4 , Dy^{3+} , and $(\text{NO}_3)^{3-}$. The addition of oxalic acid in the precursor solution made the complex with Dy^{3+} , resulting in dysprosium oxalate hydrate ($\text{Dy}_2(\text{C}_2\text{O}_4)_3 \cdot \text{H}_2\text{O}$) (**Scheme 2.3(3)**) as seen in the powder XRD pattern (JCPDS card number 21-0315, **Figure 2.1a(i)**) and Raman spectra (**Figure 2.1b(iv)**). Whereas the highlighted portions of the Raman spectra in Figure 1b at $\sim 890 \text{ cm}^{-1}$ and 365 cm^{-1} also gave the presence of CrO_4 unit for the chromic acid solution and $< 200 \text{ cm}^{-1}$ (denoted by *) confirming the presence of Dy-O .³⁸⁻⁴⁰ At 80 °C, after 1h, the XRD peaks of dysprosium oxalate hydrate disappeared due to its conversion from crystalline to an amorphous form, as observed in **Figures 2.1a(i & ii)**. The Raman spectra also showed changes in the bonding at 80 °C compared to the precursor solution at 30 °C (**Figure 2.1b(v)**). After the complete gelation, the XRD in **Figure 2.1a(iii)** revealed the traces of crystalline dysprosium oxalate hydrate. **Figure 2.1b(vi)** shows a slight shift in peak at $\sim 890 \text{ cm}^{-1}$ of Raman spectra supporting linkage formation in the gel. The peaks at $\sim 890 \text{ cm}^{-1}$ and $\sim 357 \text{ cm}^{-1}$ gave evidence for CrO_4 unit, which was also present in the single phase of DyCrO_4 (**Figure 2.1b(vii)**).³⁸⁻⁴⁰

The phase transformation of dysprosium oxalate hydrate and chromic acid from dried gel to crystalline DyCrO₄ during the sintering from 30 °C to 500 °C was also studied by TGA. Initially, TGA of precursor CrO₃ and dysprosium oxalate hydrate synthesized for reaction were studied individually to identify the decomposition temperature. The TGA curve of only the CrO₃ precursor depicts the decomposition at ~357 °C for the pyrolysis of CrO₃ forming Cr₂O₅

(a) Acidic medium (in presence of oxalic acid):

1. $\text{CrO}_3 + \text{H}_2\text{O} \rightarrow \text{H}_2\text{CrO}_4$
2. $\text{Dy}(\text{NO}_3)_3 + \text{H}_2\text{O} \rightarrow \text{Dy}^{3+} + (\text{NO}_3)^{3-}$
3. $\text{H}_2\text{CrO}_4 + \text{Dy}^{3+} + (\text{NO}_3)^{3-} + (\text{COOH})_2 \rightarrow \text{Dy}_2(\text{C}_2\text{O}_4)_3 \cdot \text{H}_2\text{O} + \text{H}_2\text{CrO}_4$
4. $2 \text{H}_2\text{CrO}_4 \rightarrow 2 \text{CrO}_3 + 2 \text{H}_2\text{O} \uparrow \rightarrow \text{Cr}_2\text{O}_5 + \frac{1}{2} \text{O}_2 \uparrow \rightarrow \text{Cr}_2\text{O}_3 + \text{O}_2 \uparrow$
5. $2 \text{Dy}_2(\text{C}_2\text{O}_4)_3 \cdot \text{H}_2\text{O} \rightarrow 2 \text{Dy}_2(\text{C}_2\text{O}_4)_3 + \text{H}_2\text{O} \uparrow \rightarrow 2 \text{Dy}_2\text{O}_3 + 6 \text{CO}_2 \uparrow + 6 \text{CO} \uparrow$
6. $\text{Cr}_2\text{O}_3 + \text{Dy}_2\text{O}_3 + \text{O}_2 \rightarrow 2 \text{DyCrO}_4$
7. $2 \text{DyCrO}_4 \rightarrow 2 \text{DyCrO}_3 + \text{O}_2 \uparrow$

(b) Basic medium (in presence of ammonium solution only):

8. $\text{H}_2\text{CrO}_4 + \text{Dy}^{3+} + (\text{NO}_3)^{3-} + \text{NH}_4\text{OH} \rightarrow (\text{NH}_4)_2\text{CrO}_4 + (\text{NH}_4)_2\text{Cr}_2\text{O}_7 + \text{Dy}(\text{OH})_3 + \text{NH}_4(\text{NO})_3$
9. $2 (\text{NH}_4)_2\text{CrO}_4 \rightarrow (\text{NH}_4)_2\text{Cr}_2\text{O}_7 + 2 \text{NH}_3 \uparrow + \text{H}_2\text{O} \uparrow$
10. $3 (\text{NH}_4)_2\text{Cr}_2\text{O}_7 \rightarrow 3 (\text{Cr}_2\text{O}_5, \text{NH}_3) + \text{N}_2 \uparrow + 6 \text{H}_2\text{O} \uparrow + \text{NH}_3 \uparrow \rightarrow [(\text{CrO}_2)_6(\text{H}_2\text{O})] + \text{N}_2 \uparrow + 2 \text{H}_2\text{O} \uparrow + \text{NH}_3 \uparrow \rightarrow 6 \text{CrO}_2 + \text{H}_2\text{O} \uparrow \rightarrow 3 \text{Cr}_2\text{O}_3 + 2 \text{O}_2 \uparrow$
11. $\text{Dy}(\text{OH})_3 \rightarrow \text{DyOOH} + \text{H}_2\text{O} \uparrow$
12. $2 \text{DyOOH} \rightarrow \text{Dy}_2\text{O}_3 + \text{H}_2\text{O} \uparrow$

Scheme 2.3: Proposed formation mechanism of the DyCrO₄ compound in (a) acidic (in presence of oxalic acid) and (b) basic (in presence of ammonia solution) mediums.

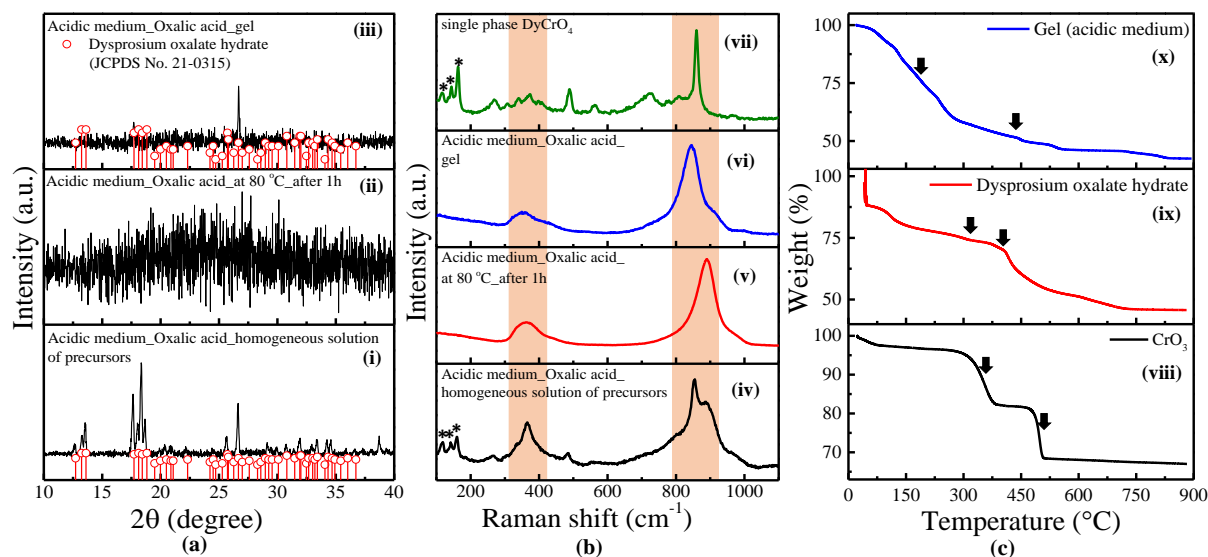


Figure 2.1: (a) XRD patterns (b) Raman spectra for the samples taken during the reaction for acidic medium in the presence of oxalic acid as a small molecule. (i) & (iv) Crystalline nature and bonding for the homogeneous solution of precursors at 30 °C. (ii) & (v) Amorphous nature and Raman spectra for the sample collected during the reaction at 80 °C after one hour. (iii) & (vi) crystallinity and bonds in the gel form. (vii) The structural bonding in single-phase DyCrO₄. The highlighted portion in the Raman graphs shows the presence of CrO₄ units (~890 cm⁻¹ and ~365 cm⁻¹) for the higher frequency region. In comparison, at lower frequency region < 200 cm⁻¹, asterisks show the presence of rare earth element Dy. (c) The TGA plots of (viii) CrO₃ precursor, (ix) synthesized dysprosium oxalate hydrate (x) dried gel of the sample, in air atmosphere. The arrows in the graphs denote the decomposition point in the corresponding compounds.

(Figure 2.1c(viii)). The second decomposition step shows the conversion of Cr₂O₅ to Cr₂O₃ at ~499 °C. The steps for converting CrO₃ to Cr₂O₃ well matched with the reported data studied in N₂ and O₂ that had shown similar results in both the atmosphere.⁴¹ The thermal decomposition of only dysprosium oxalate hydrate shows a loss of water at ~112 °C. The formation of anhydrous oxalate can be traced by weight loss occurring between ~112 °C to 304

°C. Further, the anhydrous oxalate rapidly decomposes to give Dy_2O_3 at ~ 416 °C, as shown in **Figure 2.1c(ix)**; the arrows in the plot show the decomposition temperatures.⁴²

The thermal decomposition of gel containing dysprosium oxalate hydrate and chromic acid exhibits similar transition temperatures starting from the evaporation of water molecule at ~ 82 °C along with the conversion of chromic acid to CrO_3 (**Figure 2.1c(x)**). Further, the CrO_3 loses oxygen to form Cr_2O_5 at ~ 238 °C and Cr_2O_3 at ~ 450 °C, as shown in **Scheme 2.3(4)**.⁴¹ The gel's transition temperatures are lower for Cr_2O_5 and Cr_2O_3 than the individual transition temperature of CrO_3 to Cr_2O_3 , as the gel also contains dysprosium oxalate hydrate. The second component of the gel form, dysprosium oxalate hydrate ($Dy_2(C_2O_4)_3 \cdot H_2O$), transforms to anhydrous oxalate ($Dy_2(C_2O_4)_3$) in the first step between 133 °C- 283 °C, and rapidly decomposes to Dy_2O_3 between 283 °C- 450 °C in the second step, as the anhydrous oxalate was very unstable (**Scheme 2.3(5)**).⁴² So, in the temperature range of 400 °C – 450 °C, the Cr_2O_3 and Dy_2O_3 phases are present during the gel sintering process, which further converts to $DyCrO_4$ at ~ 500 °C as confirmed by XRD presented later (**Figure 2.3b**). The $DyCrO_4$ then decomposes to $DyCrO_3$ at ~ 700 °C as observed by slight weight loss in TGA Figure 1c(x). The same reactions are also presented in **Scheme 2.3(6,7)**. The similar formation mechanism might also apply to the citric acid and EDTA.

2.3.1.2 Basic medium

In order to carry out the reaction in the basic medium, the 30% ammonia solution (NH_4OH) was added to the precursor solution containing chromic acid (H_2CrO_4), Dy^{3+} , and $(NO_3)^{3-}$ ions (**Scheme 2.3(1, 2)**). After the addition of NH_4OH in the precursor solution, it resulted in ammonium chromate ($(NH_4)_2CrO_4$ (JCPDS card number [75-1578]), ammonium dichromate ($(NH_4)_2Cr_2O_7$ (JCPDS card number [25-0029]), and NH_4NO_3 (JCPDS card number [89-2829]), as shown in **Figure 2.2a(i)** and **Scheme 2.3(8)**. The Raman peak at ~ 860 cm^{-1} showed a CrO_4 unit, as reported for single-phase $DyCrO_4$ (**Figure 2.2b(iv & vii)**).³⁸

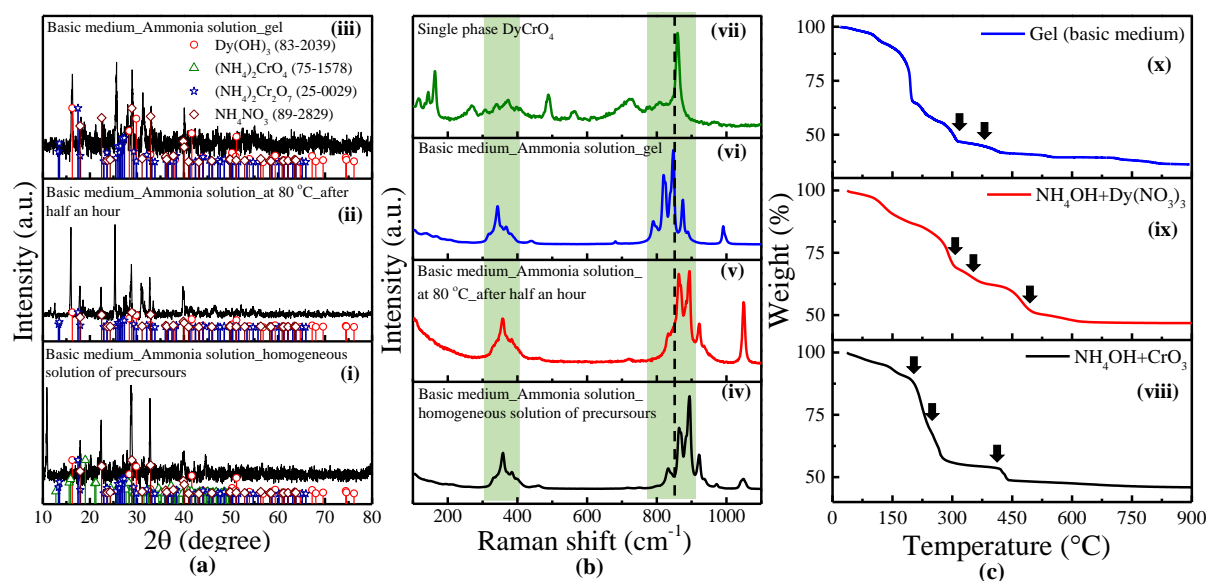


Figure 2.2: (a) XRD patterns for the samples taken during the reaction for basic medium in the presence of ammonia solution: (i) homogeneous solution of precursors at 30 °C, (ii) sample taken at 80 °C after one hour, (iii) gel form, revealed the presence of (NH₄)₂Cr₂O₇, NH₄NO₃ and Dy(OH)₃. (b) Raman spectra show the bonding in the samples collected during the basic medium reaction (in the presence of ammonia solution): (iv) homogeneous solution of precursors at 30 °C, (v) sample taken at 80 °C after one hour, (vi) gel form. (vii) Raman bonding in single-phase DyCrO₄. The highlighted portion and dotted line in the Raman spectra show the peak at ~ 358 cm⁻¹, and ~860 cm⁻¹ denoted the presence of the CrO₄ unit. (c) Thermal decomposition curve in presence of air: (viii) CrO₃ and (ix) Dy(NO₃)₃ precursors mixed with 30% ammonia solution, (x) dried gel of the sample. Decomposition points for the corresponding compounds denoted by arrows.

The shift in CrO₄ frequency from 890 cm⁻¹ (acidic medium -(H₂CrO₄)) to 860 cm⁻¹ (basic medium) confirms the formation of the complex (NH₄)₂CrO₄ due to the addition of NH₄OH. The shift to the lower frequency is due to the higher mass of (NH₄)₂CrO₄ compared to H₂CrO₄. The highlighted portion in **Figure 2.2b** shows the bending of CrO₄ at ~358 cm⁻¹.⁴⁰ For the gel formation, the homogeneous solution was heated at 80 °C. The intermediate sample

was collected after 1h at 80 °C, which shows the presence of $(\text{NH}_4)_2\text{Cr}_2\text{O}_7$, NH_4NO_3 , and $\text{Dy}(\text{OH})_3$ (JCPDS card number [83-2039]) as shown in XRD pattern **Figure 2.2a(ii)** and **Scheme 2.3(9)**.⁴³ After the formation of gel, the phases remain consistent, as confirmed by XRD (**Figure 2.2a(iii)**). The bonding in Raman spectra (**Figure 2.2b(v and vi)**) also remains unchanged.

The phases formed during the sintering temperature were investigated by thermal decomposition using TGA of the dried gel obtained in the reaction; further phases were confirmed by thermal decomposition of CrO_3 and $\text{Dy}(\text{NO}_3)_3$ mixed with 30% ammonia. The CrO_3 mixed with 30% ammonia solution, when dried at 80 °C, forms $(\text{NH}_4)_2\text{Cr}_2\text{O}_7$. The TGA investigated this ammonium dichromate, as shown in **Figure 2.2c(viii)**. The decomposition steps were observed at ~224 °C (conversion of Cr(VI) to Cr(V) with the partial loss of ammonia), ~253 °C to 265 °C (approached Cr(IV) from Cr(V), with the loss of rest of ammonia) and at ~430 °C (complete decomposition to Cr_2O_3) (Scheme 1(10)).⁴⁴ The thermal decomposition of NH_4NO_3 and $\text{Dy}(\text{OH})_3$ formed as a product of a mixture of $\text{Dy}(\text{NO}_3)_3$ with 30% ammonia was also studied using TGA (**Figure 2.2c(ix)**). The decomposition of the mixture observed at ~292 °C reveals the presence of DyOOH , which converts to Dy_2O_3 at 345 °C- 474 °C (**Scheme 2.3(11,12)**).⁴⁵ In the same temperature range, the NH_4NO_3 decomposed to gases, as reported by Chaturvedi *et al.*⁴⁶ Further, in **Figure 2.2c(x)**, the TGA of gel containing $(\text{NH}_4)_2\text{Cr}_2\text{O}_7$, NH_4NO_3 , and $\text{Dy}(\text{OH})_3$ were also investigated. The decomposition temperatures of gel observed to be: ~110 °C, ~227 °C, ~253 °C, ~306 °C- 411 °C corresponds to the loss of water; transformation of Cr(VI) to Cr(V), with loss of half of the ammonia; conversion of Cr(V) to Cr (IV) followed by the formation of Cr_2O_3 , respectively (**Scheme 2.3(10)**).⁴⁴ The remaining two components of the gel NH_4NO_3 and $\text{Dy}(\text{OH})_3$ were decomposed in the gases and formed DyOOH from $\text{Dy}(\text{OH})_3$ at ~306 °C. Further, Dy_2O_3 formation occurs at ~ 411 °C.^{45- 46} Based on the comparison of decomposition of only ammonium dichromate

and $\text{Dy}(\text{OH})_3$, it can be concluded that in sintered gel, Cr_2O_3 and Dy_2O_3 both are present at an altered temperature of $\sim 411^\circ\text{C}$ that can be further converted to DyCrO_4 at $\sim 500^\circ\text{C}$ (**Scheme 2.3(5)**) as confirmed by XRD (**Figure 2.4a**). The proposed scheme suggests the formation of Cr_2O_3 and Dy_2O_3 . However, the phase formation could not be observed in XRD and Raman but can be illustrated by TGA. The DyCrO_4 was transformed to DyCrO_3 above $\sim 700^\circ\text{C}$ by removing oxygen, as shown in **Scheme 2.3(5)**.

The same reactions were carried out using the complexing agent (oxalic acid, citric acid, and EDTA), followed by adding ammonia solution to increase the solution's pH by ~ 10 . The oxalic acid reacts with Dy^{3+} to form Dy-oxalate hydrate, and further addition of $(\text{NH}_4)\text{OH}$ forms $(\text{NH}_4)_2\text{CrO}_4$. These complex molecules may form Dy_2O_3 and Cr_2O_3 via the intermediate reactions as discussed by the proposed mechanism in acidic and basic mediums during the sintering process. Further, sintering of Dy_2O_3 and Cr_2O_3 up to 600°C forms single-phase DyCrO_4 . Similar reactions can also elaborate the formation mechanism when citric acid and EDTA are used with ammonia solution. The advantages of the sol-gel reactions carried out in this work suggest the formation of Dy_2O_3 and Cr_2O_3 via intermediate steps. These Dy_2O_3 and Cr_2O_3 forms nano-sized DyCrO_4 during the sintering process (as confirmed from XRD). Such controls over the size are difficult to achieve in the solid-state reaction, which is generally used for DyCrO_4 synthesis.

2.3.2 X-ray diffraction study

The gel form of DyCrO_4 precursors synthesized using only a complexing agent (acidic medium), only ammonia solution (basic medium), and complexing agents with the ammonia solution (pH ~ 10) were sintered at different temperatures 500°C - 800°C . Further, the XRD measurements were carried out to understand the role of the complexing agent in altering the sintering temperature and achieving single-phase DyCrO_4 and its transformation to DyCrO_3 , as discussed below. The molecular structure of used complexing agents were shown in the **Figure**

2.3.

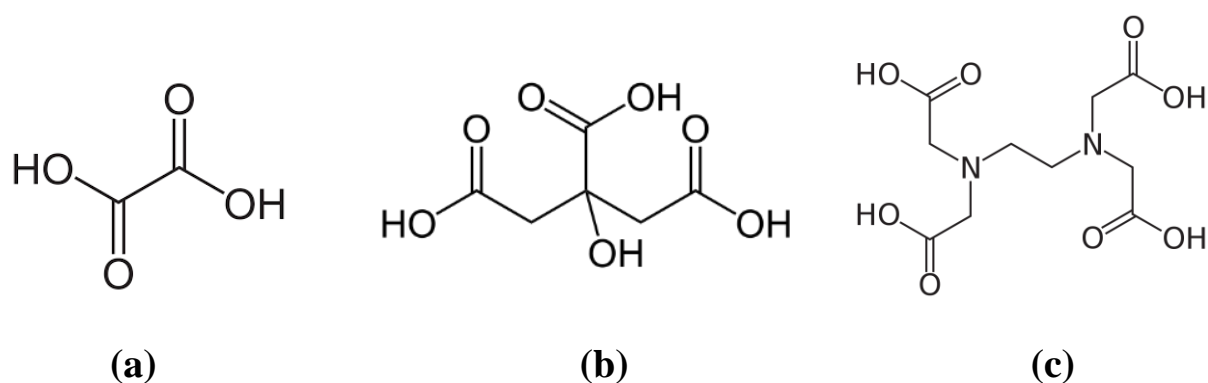


Figure 2.3: Molecular structure for different complexing agents used in the reaction: (a) Oxalic acid, (b) Citric acid, (c) EDTA.

2.3.2.1 Ammonia solution (NH_4OH)

The zircon-type $\text{DyCrO}_{4(\text{NB})}$ was obtained by sintering the intermediate gel forms of Dy, and Cr precursors formed using only NH_4OH . The phase formation is studied by XRD at different temperatures to get DyCrO_4 and DyCrO_3 . **Figure 2.4(a)** revealed zircon-type DyCrO_4 , obtained at 500 °C and 600 °C, that decomposes to DyCrO_3 at 700 °C and 800 °C by the removal of the oxygen from DyCrO_4 . The phases well matched the reported JCPDS card numbers [74-1249] and [74-2196] of zircon-type DyCrO_4 and perovskite DyCrO_3 compounds, respectively.

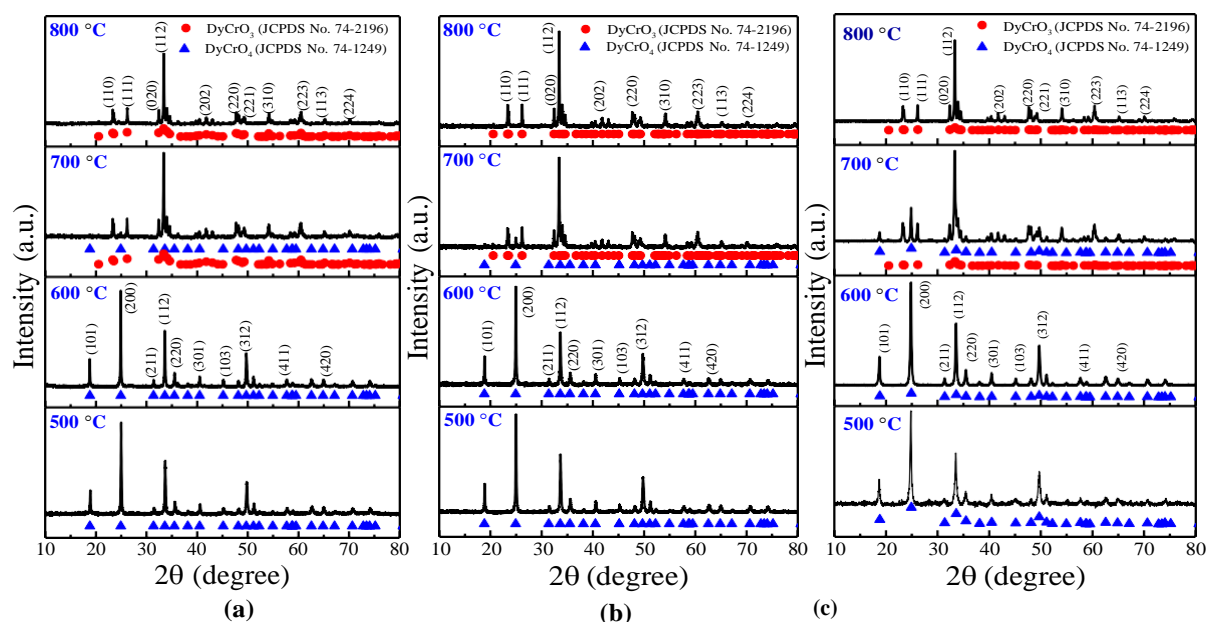


Figure 2.4: The phase transformation of the dysprosium chromium oxide system from DyCrO_4 phase to DyCrO_3 with increasing heating temperatures from 500 °C to 800 °C. The DyCrO_4 phase decomposes to DyCrO_3 at higher temperatures when any of these conditions are met: (a) in the absence of complexing agents /small molecules, and at basic pH, (b) in presence of oxalic acid (acidic medium), and (c) in presence of oxalic acid (basic medium—pH~10 adjusted by the addition of ammonia solution).

2.3.2.2 Oxalic acid ($\text{C}_2\text{H}_2\text{O}_4$)

Oxalic acid (bidentate ligand) crystallized the phases for both acidic ($\text{DyCrO}_{4(\text{OA})}$) and basic ($\text{DyCrO}_{4(\text{OB})}$) mediums at 500 °C, similar to phases crystallized for $\text{DyCrO}_{4(\text{NB})}$, as shown in **Figure 2.4(b) and 2.4(c)**. In acidic and basic mediums, at 500 °C and 600 °C, the zircon-type DyCrO_4 phase was obtained and well-matched with the JCPDS card number [74-1249]. Further, calcination at higher temperatures of 700 °C and 800 °C, the DyCrO_4 phase started to deform in the DyCrO_3 perovskite phase with the removal of oxygen from the structure. The phase obtained at 800 °C was well-matched with the JCPDS card number [74-2196]. At 700 °C, both phases, DyCrO_4 and DyCrO_3 , were observed. The same trend for the phase formation

temperature was noticed in $\text{DyCrO}_{4(\text{OA})}$ and $\text{DyCrO}_{4(\text{OB})}$, as oxalic acid controls the decomposition profile of the nitrates to form pure phase DyCrO_4 in basic and acidic mediums.³⁸

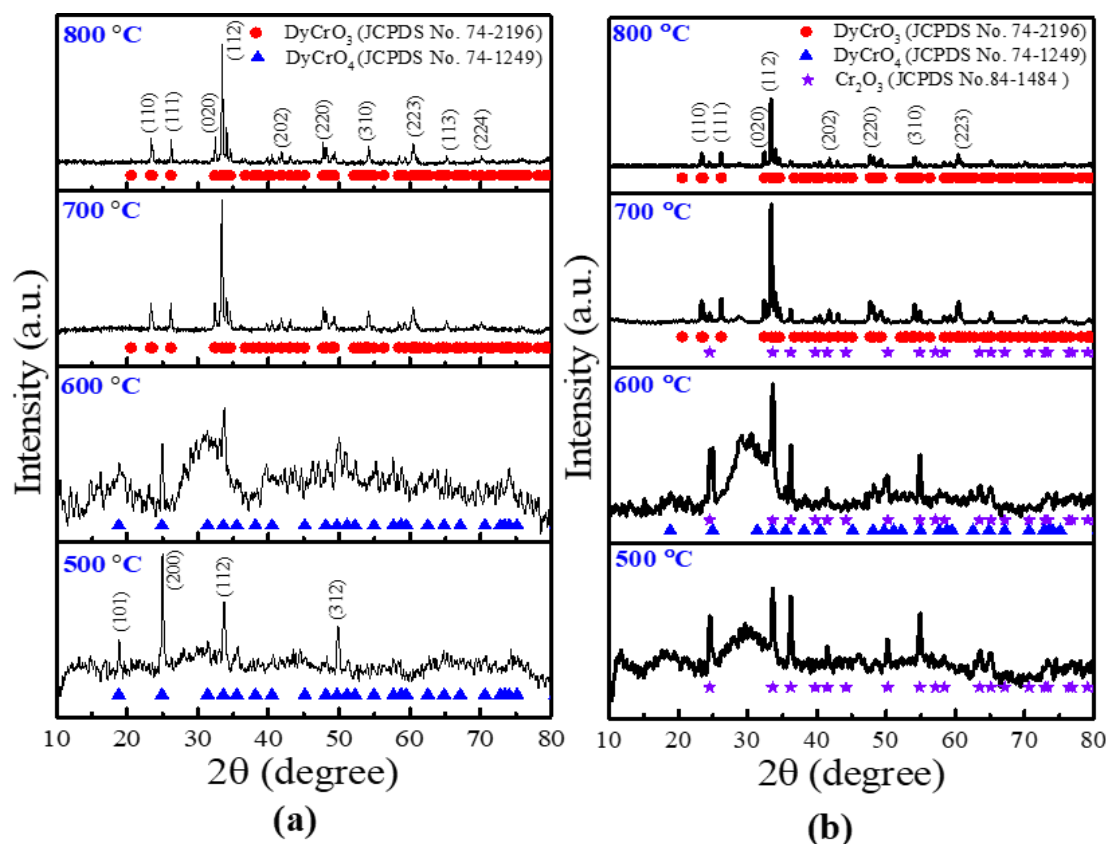


Figure 2.5: The temperature-dependent XRD patterns of dysprosium chromium oxide in presence of citric acid over the heating temperature range of 500 °C to 800 °C. For (a) lower pH (acidic) gives DyCrO_4 phase (not fully crystalline) at 500 °C, and 600 °C which was converted to DyCrO_3 at 700 °C and 800 °C, and (b) pH~10 (basic) by addition of ammonia solution to the precursor's solution shows hump at $\sim 30^\circ$ with the presence of Cr_2O_3 phase for 500 °C and 600 °C which was converted to DyCrO_3 at higher temperature 700 °C and 800 °C.

2.3.2.3 Citric acid ($\text{C}_6\text{H}_8\text{O}_7$)

The tridentate ligand, citric acid, decomposes the phases differently from other ligands. The citrate sol-gel method is more popular for the synthesis of nanoparticles of the perovskites like DyCrO_3 , SmCrO_3 , and YbCrO_3 . The pH-dependent homogeneity and stability of metal citrate solutions were studied previously.⁵ The present work observed that the citrate sol-gel

method decomposes the phases differently over the calcination in acidic and basic mediums. $\text{DyCrO}_{4(\text{CA})}$ shows the DyCrO_4 phase at 500 °C and 600 °C with some impurities in an acidic medium. The phase was not entirely crystallized over the temperature range up to 600 °C. It was converted to DyCrO_3 perovskite phase at 700 °C and 800 °C. The hump near 30° in the XRD graphs shown in **Figure 2.5(a)** for 600 °C heating temperature may be due to the individual hydroxide in the sample. However, in the basic medium (**Figure 2.5(b)**) for $\text{DyCrO}_{4(\text{CB})}$, at 500 °C found, the presence of Cr_2O_3 with the hump at 30°. $\text{DyCrO}_{4(\text{CB})}$ shows the presence of DyCrO_4 at 600 °C with Cr_2O_3 impurity phase, and over the heating temperature of 700 °C and 800 °C, the phase decomposed to DyCrO_3 . It was observed that the citrate sol-gel method did not give the single phase of DyCrO_4 in the basic condition at pH 10, which means it favors the formation of Cr^{+3} ionic state to form the DyCrO_3 .

2.3.2.4 EDTA ($\text{C}_{10}\text{H}_{16}\text{N}_2\text{O}_8$)

EDTA (hexadentate ligand) crystallized the phases relatively at a lower temperature in the basic medium ($\text{DyCrO}_{4(\text{EB})}$) as compared to the acidic medium ($\text{DyCrO}_{4(\text{EA})}$), as shown in **Figures 2.6(a) and 2.6(b)**. The DyCrO_4 phase was obtained for calcination temperatures of 500 °C and 600 °C in a basic medium, whereas $\text{DyCrO}_{4(\text{EA})}$ was found at 600 °C. At 700 °C and 800 °C, a DyCrO_3 was obtained for $\text{DyCrO}_{4(\text{EA})}$ and $\text{DyCrO}_{4(\text{EB})}$. At calcination of 600°C, $\text{DyCrO}_{4(\text{EB})}$ exhibits mix phase of DyCrO_4 and DyCrO_3 . Comparing the two reaction mediums for EDTA, the basic medium completes the hydrolysis process earlier than the acidic. Hence, the DyCrO_4 phase was crystallized at a lower temperature in a basic medium than in an acidic medium. The early completion of hydrolysis steps provides more condensation sites; thus, the phase was formed at a lower temperature.³⁸

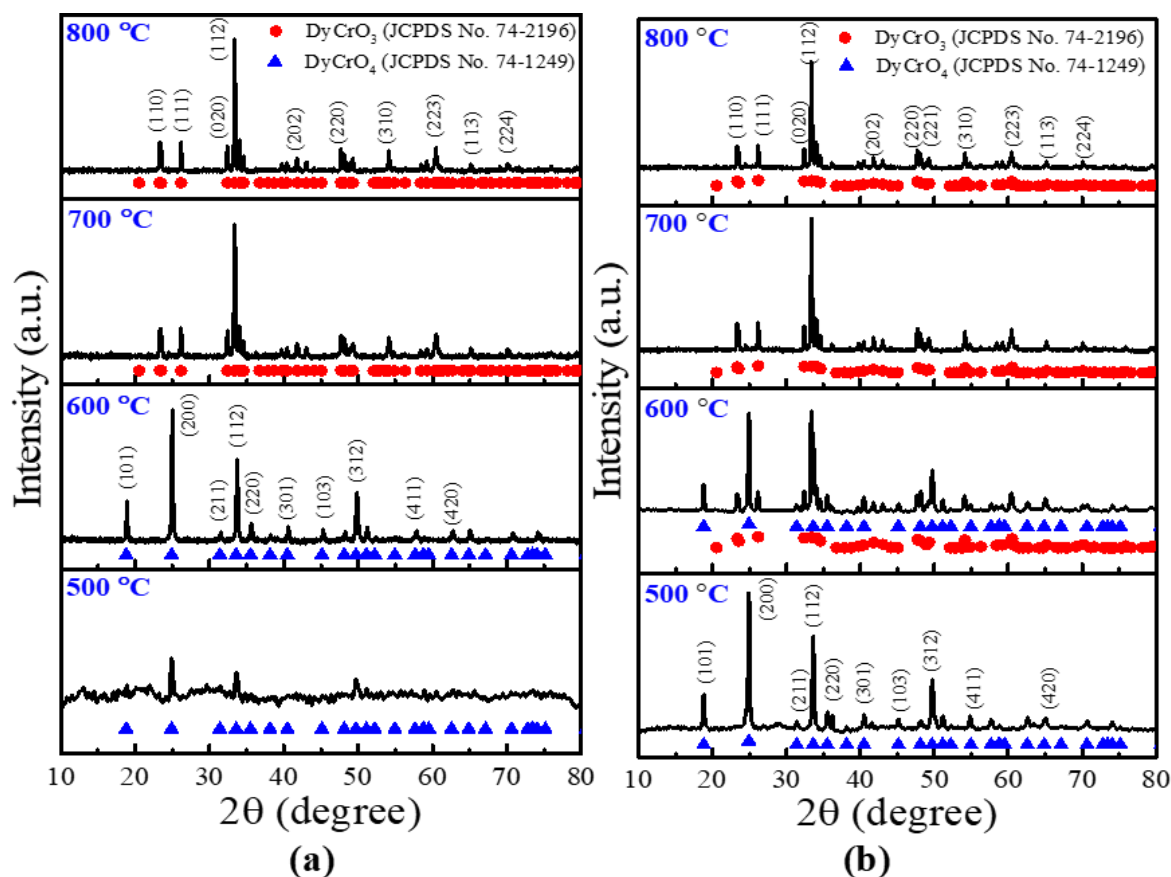


Figure 2.6: The XRD patterns of dysprosium chromium oxide system in the presence of EDTA over the heating temperature range 500 °C – 800 °C when the reaction is performed at (a) lower pH (acidic), (b) higher pH ~10 (basic).

Based on the overall XRD analysis of the phases obtained at different heating temperatures with various complexing agents in acidic and basic mediums, oxalic acid and EDTA formed the single DyCrO_4 phase, as shown in **Table 2.1**. The crystallite size (d) for the single-phase DyCrO_4 prepared using a complexing agent in different reaction mediums depending on the solution's pH was calculated using the Debye-Scherrer equation 1 for the highest intensity (200) plane tabulated in **Table 2.2**. The formula used to calculate the crystallite size along the hkl plane (hkl are the Miller indices of the plane) from the measured width of their diffraction curves are given as:

$$d = K\lambda / B \cos \theta \text{ ----- (1)}$$

Here, B represents the width of the diffraction curve at an intensity equal to half the maximum intensity called full width at half maxima (FWHM), measured in radians. The λ is the wavelength of the incident X-rays of source Cu K_{α} ($\lambda \sim 1.54 \text{ \AA}$), θ is the Bragg angle associated with hkl plane, and K is the numerical constant, considered as 0.94 since the shape of particles is random as observed in FESEM. Without taking the B values directly from peak broadening, it is corrected from standard data using equation 2.

$$B^2 = B_M^2 - B_S^2 \text{ ----- (2)}$$

B_M and B_S are the measured widths (FWHM) of the diffraction peaks of synthesized materials and standard samples, resulting in deducting the instrumental errors from the peak broadening.

Reaction temperature (°C)	Reaction medium	Liq. ammonia	Oxalic acid	Citric acid	EDTA
500	Acidic (pH not adjusted)	-	DyCrO ₄	DyCrO ₄	DyCrO ₄
600		-	DyCrO ₄	Impurity+ DyCrO ₄	DyCrO ₄
700		-	DyCrO ₄ + DyCrO ₃	DyCrO ₃	DyCrO ₃
800		-	DyCrO ₃	DyCrO ₃	DyCrO ₃
500	Basic (pH~10 adjusted using liq. ammonia)	DyCrO ₄	DyCrO ₄	Cr ₂ O ₃	DyCrO ₄
600		DyCrO ₄	DyCrO ₄	Cr ₂ O ₃ + DyCrO ₄	DyCrO ₄ + DyCrO ₃
700		DyCrO ₃ + DyCrO ₄	DyCrO ₃ + DyCrO ₄	Cr ₂ O ₃ + DyCrO ₃	DyCrO ₃
800		DyCrO ₃	DyCrO ₃	DyCrO ₃	DyCrO ₃

Table 2.1: The obtained phases of dysprosium chromium oxide system with increasing temperatures in presence of different small molecules in lower (acidic) and higher (basic) pH solution.

The $\text{DyCrO}_4(\text{OA})$ and $\text{DyCrO}_4(\text{EA})$ has crystallite size of ~ 63 nm and ~ 77 nm, respectively. However, in the basic medium, the crystallite size was reduced to ~ 56 nm ($\text{DyCrO}_4(\text{OB})$) and ~ 54 nm ($\text{DyCrO}_4(\text{EB})$), which was nearly the same for both the complexing agent. The crystallite size of ~ 218 nm was observed for $\text{DyCrO}_4(\text{NB})$. It was concluded from the calculation that the DyCrO_4 synthesized with the complexing agent in basic medium favor the synthesis of smaller crystallite size. The crystallite size for $\text{DyCrO}_4(\text{CA})$ and $\text{DyCrO}_4(\text{CB})$ was not calculated, as the single-phase DyCrO_4 was not obtained.

Reaction medium		Crystallite size (nm) for (200) plane
Basic	Liq. ammonia	218 ± 10
	Oxalic acid + liq. ammonia	56 ± 5
	EDTA+ liq. ammonia	54 ± 5
Acidic	Oxalic acid	63 ± 5
	EDTA	77 ± 5

Table 2.2: The crystallite size for the pure phase of DyCrO_4 for the (200) plane.

2.3.3 Electron microscopy imaging and diffraction study

The morphology of the DyCrO_4 samples for different reaction mediums in the presence of a complexing agent was investigated using TEM. The TEM images show the hydroclathrus-like morphology with unevenly sized holes for the DyCrO_4 phase synthesized using a complexing agent and extended sheet-like structure in the absence of a complexing agent. The bright-field (BF) TEM image in **Figure 2.7(a)** reveals the extended sheet-like structure for $\text{DyCrO}_4(\text{NB})$. The size of morphology well corresponds to the listed crystallite size of

DyCrO₄(NB). BF- images **Figure 2.7(c) and 2.7(e)** shows the TEM images for DyCrO₄(OA) and DyCrO₄(OB). The acidic medium has a hydrocathrus-like morphology with larger holes but

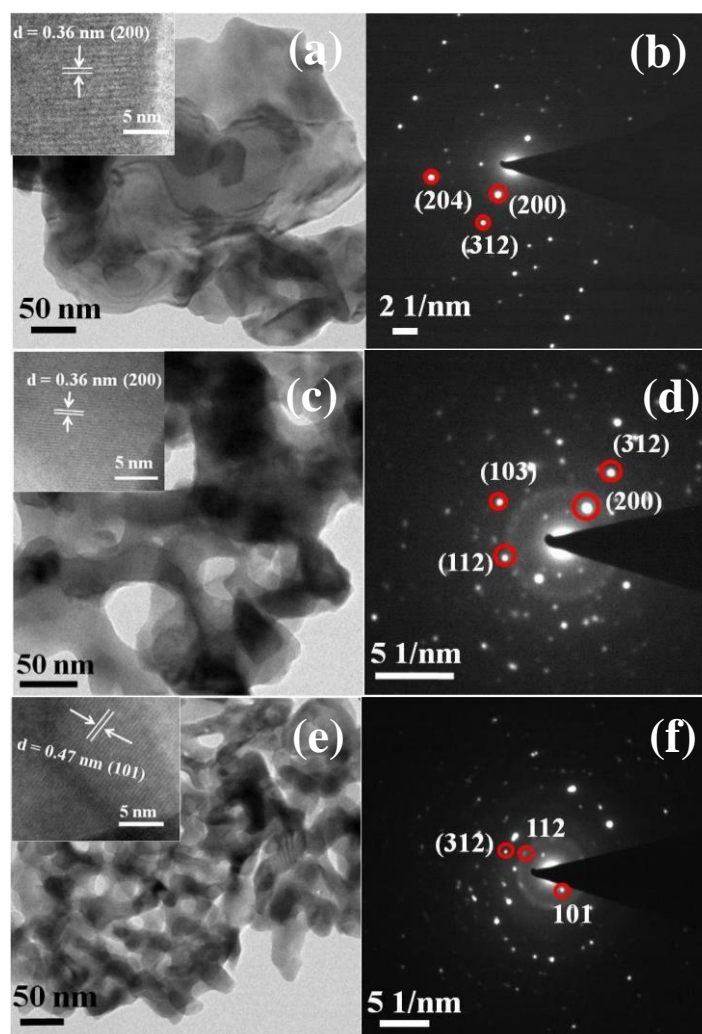


Figure 2.7: BF-TEM images of synthesized DyCrO₄ shown in (a), (c), and (e). (a) Extended sheet-like morphology for basic medium in absence of small molecules. The d-spacing for the sample 0.36 nm (200) is shown in the inset of (a). DF-TEM image shows the crystalline nature of the DyCrO₄ in SAED. (c) and (e) shows hydrocathrus-like morphology for DyCrO₄ prepared in acidic and basic mediums in the presence of oxalic acid, respectively. Inset of (c) shows the lattice fringes spacing of 0.36 nm corresponds to (200) plane. Inset (e): lattice fringes spacing of 0.47 nm represent (101) plane. (d) and (f) SAED pattern reveals the level of crystallinity for the DyCrO₄. (BF-bright field and DF- dark field)

connected sheets. Whereas, in the basic medium the sheet like morphology has smaller particles and comparatively smaller holes than that of the acidic medium. Following the same trend, the calculated crystallite size was smaller in basic medium. Inset of **Figure 2.7(a)**, **2.7(c)**, and **2.7(e)** shows the lattice fringes spacing of 0.36 nm for (200) plane of $\text{DyCrO}_{4(\text{NB})}$ and, $\text{DyCrO}_{4(\text{OA})}$ whereas 0.47 nm for (101) plane of $\text{DyCrO}_{4(\text{OB})}$. Darkfield images (DF) in **Figure 2.7(b)**, **2.7(d)**, and **2.7(f)**, shows the selected area electron diffraction (SAED) pattern, confirmed the crystalline nature of the synthesized $\text{DyCrO}_{4(\text{NB})}$, $\text{DyCrO}_{4(\text{OA})}$, $\text{DyCrO}_{4(\text{OB})}$ respectively.

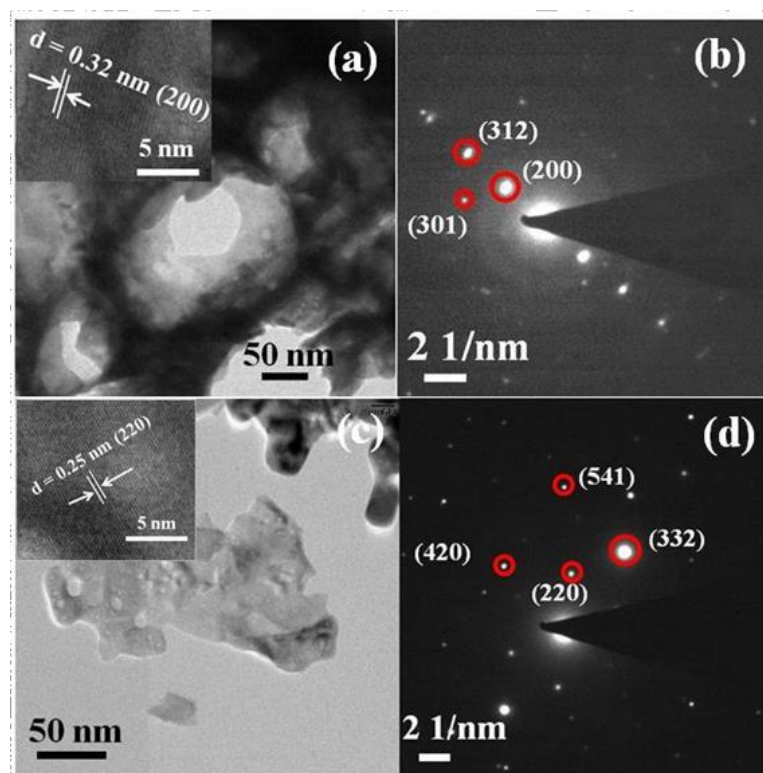


Figure 2.8: Hydroclathrus-like morphology of DyCrO_4 shown in BF- TEM images (a) for lowerpH and (b) for higher pH, in the presence of citric acid. Inset of (a) and (c) shows the lattice fringes spacing of 0.32 nm and 0.25 nm corresponds to (200) and (220) planes, respectively. DF-TEM images show SAED patterns, revealing the crystallinity level for DyCrO_4 (b) In the acidic medium and (d) in the basic medium, with citric acid.

The $\text{DyCrO}_{4(\text{CA})}$ shows the hydroclathrus-like morphology having larger holes (**Figure 2.8(a)**) with a d-spacing of 0.32 nm (inset **Figure 2.8(a)**). The crystalline nature of the prepared $\text{DyCrO}_{4(\text{CA})}$ was confirmed by the SAED pattern, as shown in **Figure 2.8(b)**. The TEM-image and SAED pattern of $\text{DyCrO}_{4(\text{CB})}$ heated at 600 °C was shown in **Figures 2.8(c) & 2.8(d)**. At 600 °C, $\text{DyCrO}_{4(\text{CB})}$ sample attains the DyCrO_4 phase with the impurity of Cr_2O_3 . The d-spacing of 0.25 nm is shown in inset **Figure 2.8(c)** may correspond to the (220) plane of the Cr_2O_3 phase. The sample's crystallinity was again confirmed from the SAED pattern in **Figure 2.8(d)**.

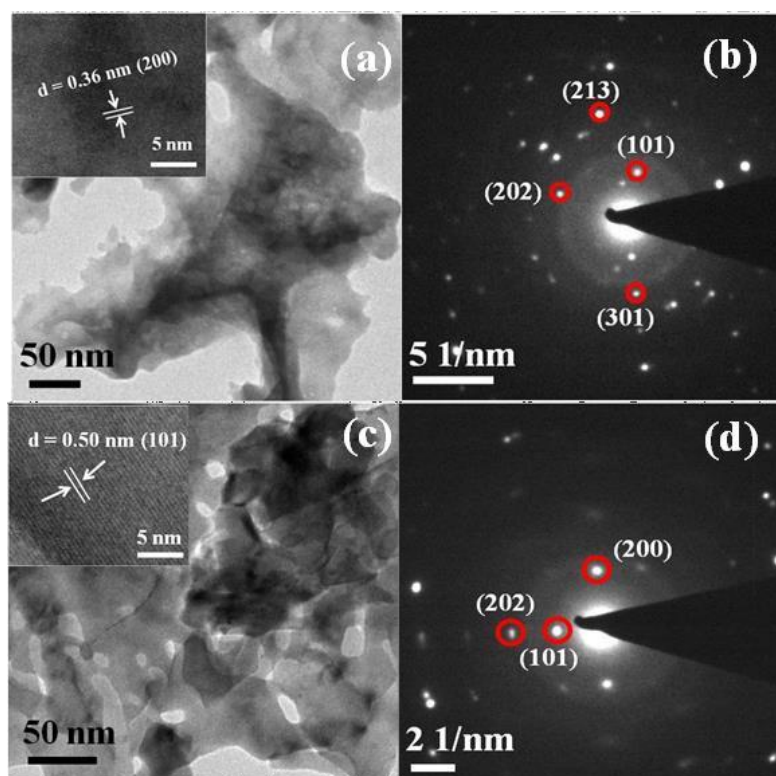


Figure 2.9: (a) and (c) BF-TEM images show the hydroclathrus-like morphology for DyCrO_4 prepared using EDTA in both acidic and basic mediums. The lattice fringes spacing of 0.36 nm corresponds to (200) plane (inset (a)) and 0.50 nm present (101) plane (inset (c)). (b) and (d) DF-TEM images reveal the SAED patterns showing crystalline nature of DyCrO_4 in acidic and basic mediums with EDTA, respectively.

The $\text{DyCrO}_{4(\text{EA})}$ and, $\text{DyCrO}_{4(\text{EB})}$ show the same morphology as that of $\text{DyCrO}_{4(\text{OA})}$ and, $\text{DyCrO}_{4(\text{OB})}$, as presented in **Figure 2.9(a) & 2.9(c)**. SAED pattern shows the crystalline nature

of the $\text{DyCrO}_4(\text{EA})$ and $\text{DyCrO}_4(\text{EB})$ samples in **Figures 2.9(b) and 2.9(d)**. Inset of **Figure 2.9(a) and 2.9(c)** shows the lattice fringes spacing of 0.36 nm ($\text{DyCrO}_4(\text{EA})$) and 0.50 nm ($\text{DyCrO}_4(\text{EB})$). The size of morphology in TEM images are consistent with the calculated crystallite size of synthesized DyCrO_4 using a complexing agent in the different reaction mediums from XRD measurements.

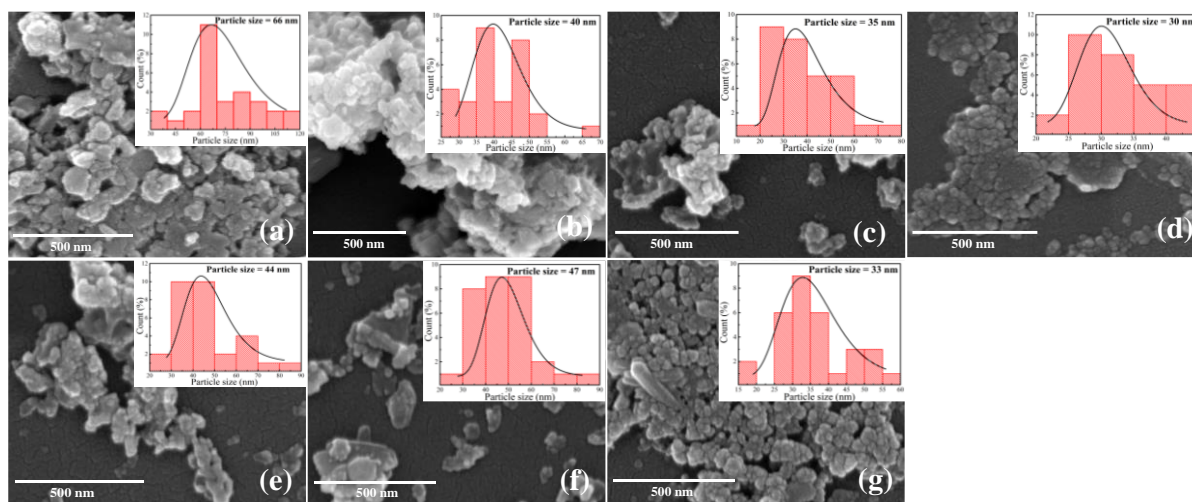


Figure 2.10: FESEM images with the size distribution histograms for DyCrO_4 compounds synthesized in (a) ammonia solution, (b) oxalic acid, (c) citric acid, and (d) EDTA for basic medium, (e) oxalic acid, (f) citric acid (g) EDTA in acidic medium. The black lines represent the results of Gaussian fitting.

After sintering, the FESEM measurements were done for the single-phase DyCrO_4 to calculate the particle size. All the FESEM images show the random morphology of DyCrO_4 particles suggesting their crystallization. The histogram was calculated for 30 particles in each case. **Figure 2.10** shows the FESEM images with the calculated histogram. The particle size is in nm, as mentioned in **Figure 2.10**. Further, the EDAX analysis was done as presented in **Table 2.3**, which confirms the presence of Dy, Cr, and O in sintered single-phase DyCrO_4 samples.

Reaction mediums	Complexing agents	Atomic percentage of elements (%)		
		Dy	Cr	O
Basic (in ammonia solution)	Ammonia solution	5	6	89
	Oxalic acid	5	7	88
	Citric acid	3	4	93
	EDTA	4	5	91
Acidic	Oxalic acid	3	5	92
	Citric acid	4	4	92
	EDTA	2	4	94

Table 2.3: EDAX data of the DyCrO₄ compounds formed in basic and acidic reaction mediums with different complexing agents.

2.3.4 X-ray photoelectron spectroscopy analysis:

XPS spectra for the DyCrO₄ synthesized using a complexing agent at different reaction mediums were recorded at room temperature to reveal the surface valence states of the Dy, Cr, and O atoms. The core-level binding energy was aligned with the carbon binding energy of ~ 284.8 eV. **Figure 2.11(a)** represents the XPS spectra of DyCrO_{4(NB)} without a complexing agent. The Cr 2p_{3/2} peak for DyCrO_{4(NB)} resolved into three peaks at ~ 576 eV, ~ 578 eV, ~ 579 eV corresponding to Cr⁺³, Cr⁺⁵, and Cr⁺⁶. At the same time, the Cr 2p_{1/2} resolved into two peaks, ~ 586 eV and 588 eV.⁴⁷⁻⁴⁸ **Figures 2.11(d)** and **2.11(g)** show the Cr 2p XPS binding energy spectra for DyCrO_{4(OA)} and DyCrO_{4(OB)}, respectively. The spectra contain two spin-orbit split peaks of 2p_{1/2} and 2p_{3/2} were located at ~ 588 and 580 eV for DyCrO_{4(OA)}, whereas for DyCrO_{4(OB)} at ~ 588 and 579 eV. The deconvolution of peaks further resolved the Cr 2p_{3/2} peak of DyCrO_{4(OA)} in three peaks situated at ~ 577 eV (Cr⁺³), ~ 578 eV (Cr⁺⁵), ~ 580 eV (Cr⁺⁶).⁴⁷⁻
⁴⁸ However, the Cr 2p_{1/2} peak divides into ~ 582 and 588 eV. It is well known that the binding

energy of Cr^{+6} and Cr^{+5} has nearly the same value, so it is difficult to distinguish them. Cr is in a +5-oxidation state that contains one unpaired electron in its valence band, contributing to the different valency states of Cr. The XPS spectra of Cr $2p_{3/2}$ for $DyCrO_4(OB)$ fitted peaks show the three peaks at ~ 577 eV (Cr^{+3}), ~ 578 eV (Cr^{+5}), ~ 579 eV (Cr^{+6}), and Cr $2p_{1/2}$ at ~ 585 , and 588 eV. The binding energy for the surface elements present in $DyCrO_4(OA)$ and $DyCrO_4(OB)$ was nearly the same. It contains +3, +5, and +6 valence states of Cr.

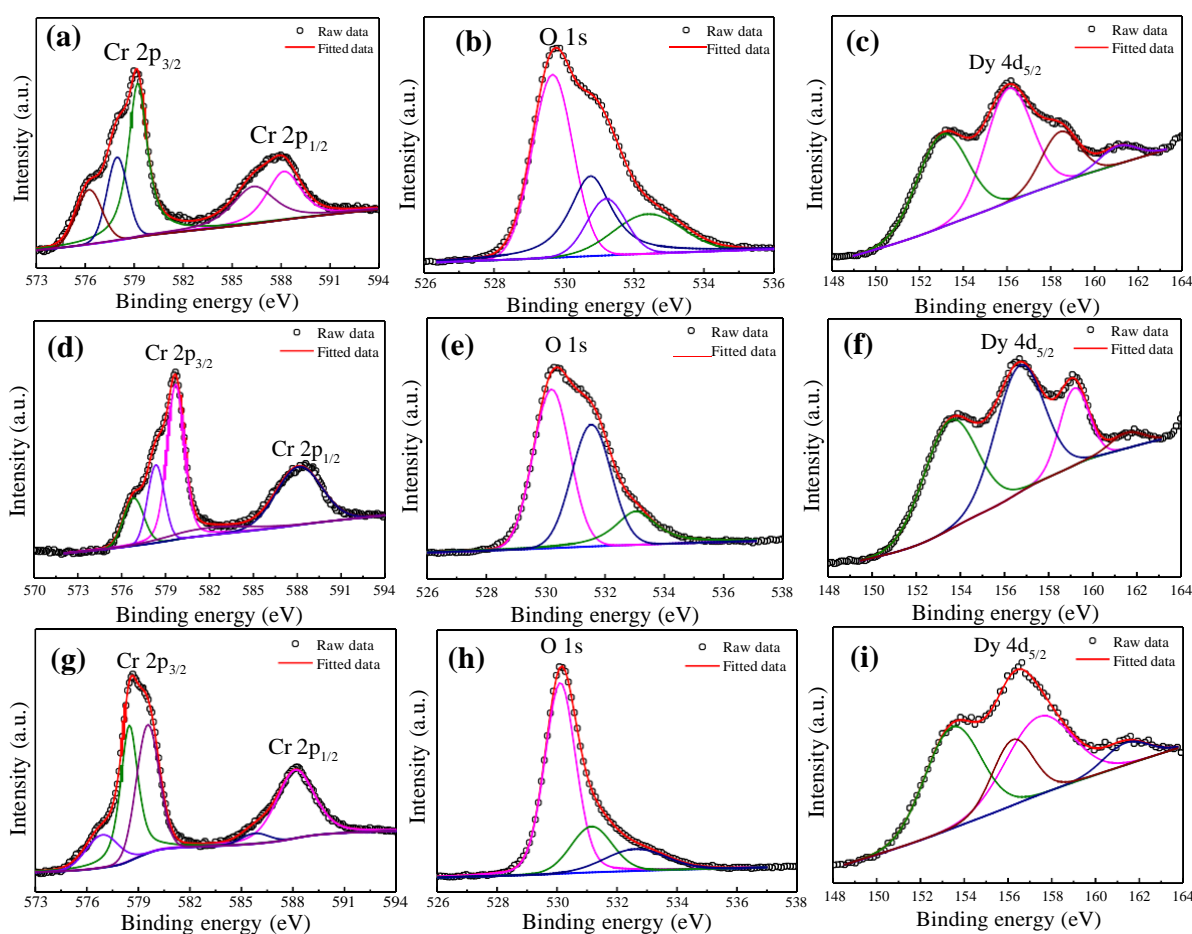


Figure 2.11: XPS derived Cr 2p, O 1s, Dy 4d core levels electron binding energy spectra for $DyCrO_4$ synthesized in the absence of small molecule in basic medium ((a)-(c)), in the presence of oxalic acid in acidic medium ((d)-(f)), and oxalic acid in basic medium ((g)-(i)) to conclude the valence state of elements.

The fixed spherical size of the oxygen ion is approximated, but in reality, the valence electronic shell of the oxygen ion is no longer uniform but polarized when placed between covalent cations. The O1s spectra of $\text{DyCrO}_{4(\text{NB})}$ (**Figure 2.11(b)**) fitted with four peaks ~ 529 eV (Cr-O , metal oxide), ~ 530 eV (O^{2-}), ~ 531 eV (surface absorbed oxygen in $-\text{OH}$ form), ~ 532 eV (chemically absorbed oxygen in the form of water).⁴⁹⁻⁵⁰ **Figure 2.11(e) and 2.11(h)** also show the similar deconvolution peaks of O1s spectra for $\text{DyCrO}_{4(\text{OA})}$ and $\text{DyCrO}_{4(\text{OB})}$. Thus, the XPS spectra of oxygen indicate the carboxyl and hydroxyl groups of the oxalic acid.

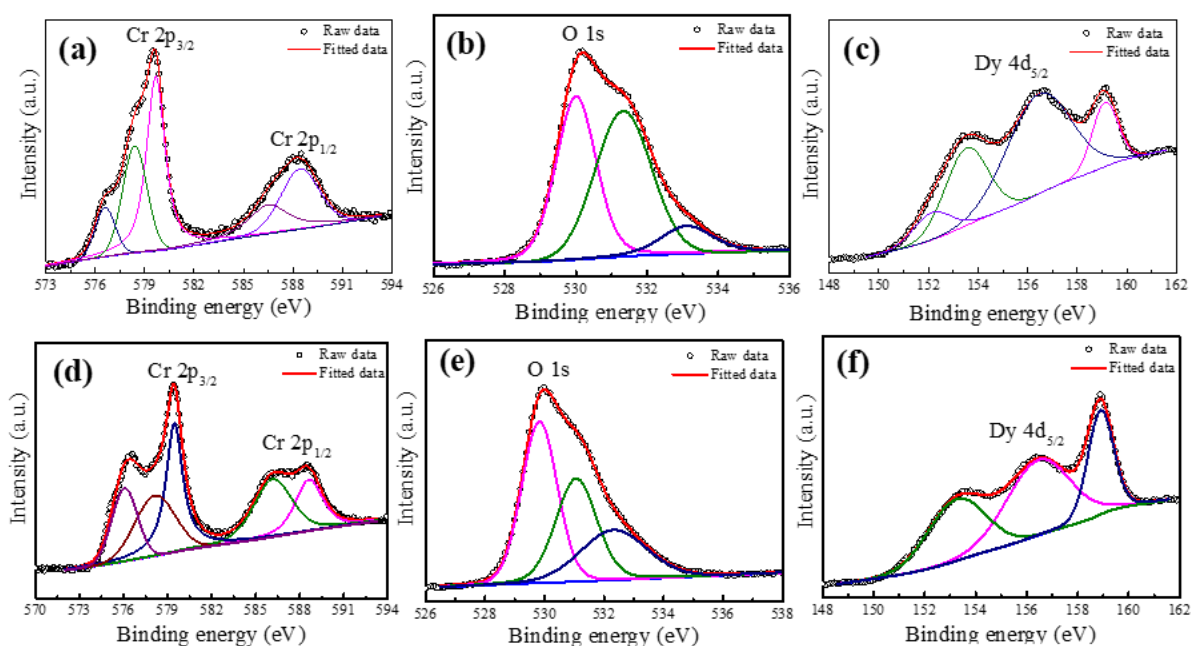


Figure 2.12: Electron binding energy spectra obtained from XPS for Cr 2p, O 1s, Dy 4d core-levels of the DyCrO_4 prepared using EDTA as a small molecule for acidic ((a)-(c) $\text{pH} < 7$), and basic ((d)-(f) $\text{pH} > 7$) mediums.

Figure 2.11(f) and 2.11(i) shows the deconvoluted Dy 4d core-level spectra for $\text{DyCrO}_{4(\text{OA})}$ and, $\text{DyCrO}_{4(\text{OB})}$, respectively. The Dy 4d spectra have the four peaks at ~ 153 eV, ~ 156 eV, ~ 159 eV, ~ 161 eV for $\text{DyCrO}_{4(\text{OA})}$ and ~ 153 eV, ~ 156 eV, ~ 157 eV, ~ 161 eV for $\text{DyCrO}_{4(\text{OB})}$. The peaks at ~ 153 eV correspond to the Dy-Cr bond. The Dy-O -related peak was positioned at ~ 156 and 157 eV. In contrast, the highest binding energy peaks at ~ 161 eV of

Dy 4d were revealed for the Dy^{3+} ionic state.⁵¹⁻⁵⁷ The same correspondence for the peak binding energy was also observed in $DyCrO_{4(NB)}$, with the peaks at ~ 153 eV ($Dy-Cr$), ~ 156 eV ($Dy-O$), ~ 158 , and 161 eV (Dy^{3+}) in **Figure 2.11(c)**.

The surface valance state of $DyCrO_{4(EA)}$ and $DyCrO_{4(EB)}$ was also studied. The Cr 2p, O 1s, and Dy 4d core-level XPS spectra for $DyCrO_4$ synthesized using EDTA were shown in **Figure 2.12(a)-(c)** for acidic medium and **Figure 2.12(d)-(f)** for basic medium. The deconvoluted peaks positioned at ~ 576 eV, ~ 578 eV, ~ 579 eV in both $DyCrO_{4(EA)}$ and $DyCrO_{4(EB)}$ corresponds to Cr 2p_{3/2}. The peaks related to Cr⁺³ ionic states were positioned at ~ 576 eV. While ~ 578 eV reveals Cr^{+5} , and ~ 579 eV shows the presence of Cr^{+6} ionic form.⁴⁷⁻⁴⁸ Peaks at ~ 586 eV and ~ 588 eV show Cr 2p_{1/2} for $DyCrO_4$ prepared in the presence of EDTA only and EDTA at pH 10. The deconvoluted O 1s spectra resolved into three peaks in both the mediums located at ~ 530 eV ($Cr-O$, due to metal oxide), ~ 531 eV (surface absorbed oxygen), and ~ 533 eV (chemically absorbed oxygen in the form of water) for $DyCrO_{4(EA)}$ and $DyCrO_{4(EB)}$.⁴⁹⁻⁵⁰ The core-level XPS spectrum of Dy 4d shows the presence of Dy^{3+} , $Dy-Cr$, and $Dy-O$. The peaks at ~ 152 and 159 eV of $DyCrO_{4(EA)}$ correspond to Dy^{3+} . The same binding energy peak was observed in $DyCrO_{4(EB)}$ at ~ 159 eV. The peak at ~ 153 and 156 eV reveals $Dy-Cr$ and, $Dy-O$ bonds, respectively, for $DyCrO_{4(EA)}$ and $DyCrO_{4(EB)}$.⁵¹⁻⁵⁷ The XPS spectra for the samples prepared with citric acid in both the pH condition $pH < 7$ and $pH > 7$ were not recorded as the phases got for these reaction conditions have some impurity of Cr_2O_3 . So, the XPS spectra reveal the chemical composition and state of the surface atoms in all synthesized samples under different reaction conditions.

2.3.5 Magnetic measurements

The magnetic measurement was carried out only for $DyCrO_{4(OB)}$, as both the mediums crystallized the zircon phase at the same temperature of 500 °C. The M-H measurements resulted in the straight line passing through origin without any hysteresis for temperatures 300

K to 50 K, corresponding to the PM state (**Figure 2.13(a)**) of DyCrO_{4(OB)}. Whereas, for 20 K and 10 K, the curve shows the hysteresis loop was depicting the soft ferromagnetic nature of DyCrO_{4(OB)}, as shown in **Figure 2.14 (zoom view)**. At 10 K, the M-H curve shows the coercivity ~ 752 Oe and remanence ~40 emu/g; however, the values are smaller than permanent magnetic materials such as ferrites and magnetic alloys.^{58, 59} The soft ferromagnetic behavior at low temperature in the DyCrO₄ was due to the *f-f* orbital superexchange interactions, as *f* orbitals have complex interactions. A similar, soft ferromagnetic curve was also observed in the case of solid-state derived DyCrO₄ due to the temperatures only. This weak ferromagnetic super exchange coupling gives rise to opening up of hysteresis loop below 20 K with decreasing temperature.

Superexchange mechanism:

Weak ferromagnetic interaction between Dy-O-Cr below 20 K.

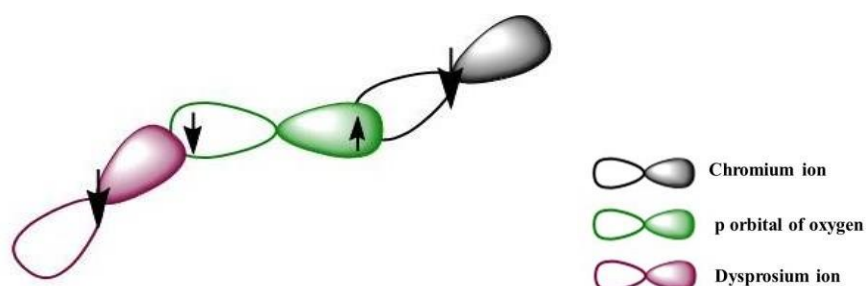


Figure 2.13(b) shows the temperature dependence of ZFC and FC magnetization measured at a field of 100 Oe for the determination of transition temperature (T_c) of DyCrO_{4(OB)}. The ZFC and FC curve does not separate in the paramagnetic state and increases monotonically with decreasing temperature (T). It was observed that in the ZFC curve of DyCrO_{4(OB)}, the magnetization value sharply increases as the temperature goes to ~ 21 K (T_c) due to PM-FM transition.

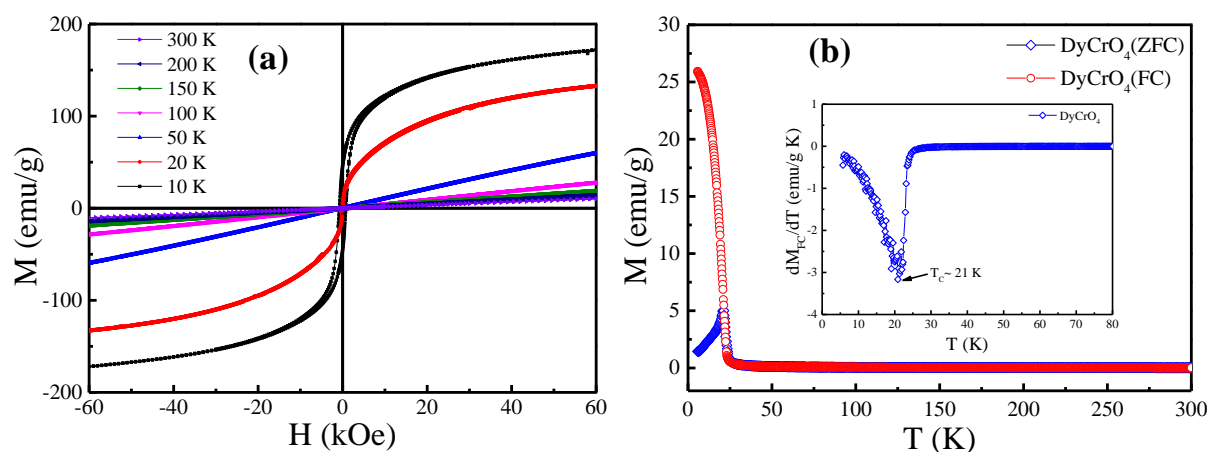


Figure 2.13: Magnetic nature of the DyCrO_4 synthesized using oxalic acid in a basic (pH~10) medium. (a) The magnetization versus magnetic field behavior of the sample over the temperature range 10 K – 300 K. At 300 K, DyCrO_4 shows a paramagnetic nature, whereas 10 K, the DyCrO_4 , shows a weak ferromagnetic nature. (b) Field-cooled and zero-field cooled measurements for the DyCrO_4 at a magnetic field of 100 Oe. Inset shows dM_{FC}/dT curve to conclude the transition temperature, at ~ 21 K.

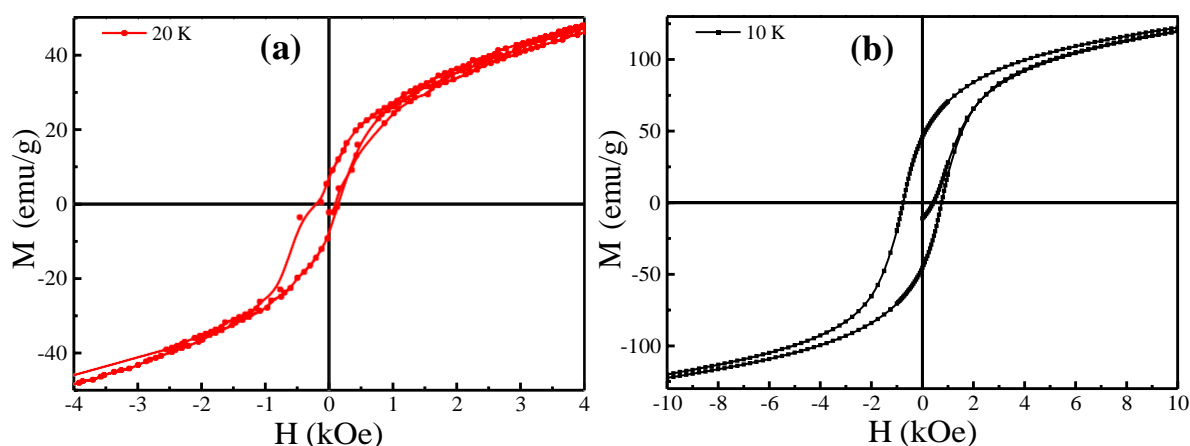


Figure 2.14: Magnetic behavior for zircon-type DyCrO_4 synthesized in a basic medium using oxalic acid (a) at 20 K and (b) at 10 K.

A similar PM-FM transition was reported by Long *et al.* in solid-state derived bulk DyCrO_4 at 23 K.⁶ For bulk DyCrO_4 , the neutron diffraction study also shows the transition temperature at 23 K.⁸ The ZFC and FC magnetization vs temperature curves separation shows the domain wall pinning effect. The domain can align along the external field direction or in a local anisotropy field direction if the sample is cooled down from the high temperature with or

without field. Inset of **Figure 2.13(b)** shows the derivative of FC magnetization concerning temperature reveals the transition temperature T_c of ~ 21 K, which is lower than the reported for the solid-state synthesized bulk DyCrO_4 .^{27, 60} The lowering in the transition temperature in sol-gel synthesized nanocrystalline DyCrO_4 was related to the small size effect of the particles; as the particle size decreases, the surface-to-volume ratio increases, which results in a larger number of surface electron spins per unit volume. The electron spin fluctuations became more prominent in nanocrystalline particles, causing disordered spin alignments, leading to the reduction in transition temperature as well as magnetization.⁶¹

2.4 Conclusion

The process involved in the synthesis of zircon-type DyCrO_4 by hydrolytic sol-gel method in acidic (using oxalic acid) and basic (using ammonium solution) mediums was thoroughly discussed. The formation mechanism shows the presence of Cr_2O_3 and Dy_2O_3 in the gelation step of sol-gel as concluded by TGA. After sintering, this Cr_2O_3 and Dy_2O_3 form nanocrystalline DyCrO_4 , validating the advantage of sol-gel over solid-state reaction. When only ammonia solution was used for gel formation, the DyCrO_4 phase crystallized at 500°C , which further converted to the DyCrO_3 at 800°C . The gel formed with only oxalic acid and oxalic acid with pH 10 crystallizes to DyCrO_4 at the same temperature of 500°C . In the case of EDTA, the acidic medium gel crystallized the DyCrO_4 at 600°C , whereas EDTA with pH 10 forms DyCrO_4 at 500°C , which is lower than that of the acidic medium. The citric acid in the acidic as well as in the basic medium gives crystalline DyCrO_4 along with Cr_2O_3 as an impurity at a sintering temperature of 500°C . The DyCrO_4 phase decomposed to the DyCrO_3 for all complexing agents with increased sintering temperature. The crystallite size of DyCrO_4 formed using oxalic acid and EDTA at pH 10 was determined to be ≈ 55 nm. TEM shows the hydrocathrus-like morphology for the DyCrO_4 samples. The binding energy of the valence state of elements present in the DyCrO_4 differs due to the different surroundings of complexing

agents used in the acidic and basic mediums during the sol-gel synthesis. The magnetic measurements of single-phase DyCrO₄ synthesized using oxalic acid at pH 10 showed ferromagnetic nature below the transition temperature of 21 K, which is less than the previously reported bulk DyCrO₄ by solid-state synthesis. Thus, the nanocrystalline DyCrO₄ synthesized at a lower sintering temperature (500 °C) and in a shorter duration (2 h), can be suitable for cryogenic applications such as hydrogen liquefaction owing to its lower transition temperature of 21 K.

2.5 References

1. M.B. Salamon, M. Jaime, *Rev. Mod. Phys.* (2001), 73, 583–628.
2. P.A. Lee, N. Nagaosa, X.G. Wen, *Rev. Mod. Phys.* (2006) 78.
3. Y.W. Long, N. Hayashi, T. Saito, M. Azuma, S. Muranaka, Y. Shimakawa, *Nature*. (2009), 458, 60–63.
4. P. Gupta, R. Bhargava, R. Das, P. Poddar, *RSC Adv.* (2013), 3, 26427–26432.
5. P. Gupta, R. Bhargava, P. Poddar, *J. Phys. D: Appl. Phys.* (2015), 48, 25004.
6. Y. Long, Q. Liu, Y. Lv, R. Yu, C. Jin, *Phys. Rev. B - Condens. Matter Mater. Phys.* (2011), 83, 4–9.
7. H. Li, H.M. Noh, B.K. Moon, B.C. Choi, J.H. Jeong, *J. Alloys Compd.* (2014), 582, 151–156.
8. Y.W. Long, Q. Huang, L.X. Yang, Y. Yu, Y.X. Lv, J.W. Lynn, Y. Chen, C.Q. Jin, *J. Magn. Mater.* (2010), 322, 1912–1916.
9. K. Tezuka, Y. Hinatsu, *J. Solid State Chem.* (2001), 160, 362–367.
10. A. Morales-Sánchez, F. Fernández, R. Sáez-Puche, *J. Alloys Compd.* (1993), 201, 161–165.
11. R. Sáez-Puche, E. Jiménez, J. Isasi, M.T. Fernández-Díaz, J.L. García-Muñoz, *J. Solid State Chem.* (2003), 171, 161–169.
12. E. Climent-Pascual, J. Romero de Paz, J.M. Gallardo-Amores, R. Sáez-Puche, *Solid State*

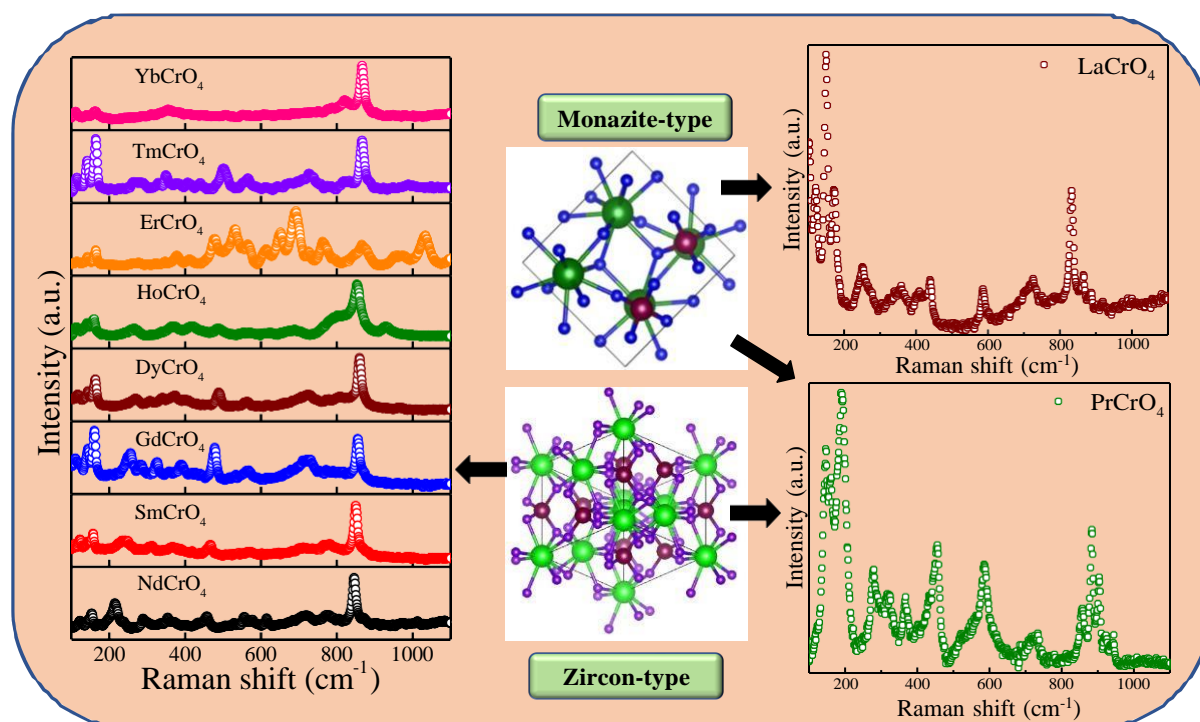
- Sci.* (2007), 9, 574–579.
13. K. Tezuka, Y. Doi, Y. Hinatsu, *J. Mater. Chem.* (2002), 12, 1189–1193.
 14. E. Jiménez, J. Isasi, R. Sáez-Puche, *J. Solid State Chem.* (2002), 164, 313–319.
 15. E. Jiménez, J. Isasi, R. Sáez-Puche, *J. Alloys Compd.* (2000), 312, 53–59.
 16. S.G. Manca, E.J. Baran, *J. Appl. Crystallogr.* (1982), 15, 102–103.
 17. S.G. Manca, E.J. Baran, *J. Phys. Chem. Solids.* (1981), 42, 923–925.
 18. L. Li, W. Yu, C. Jin, *Phys. Rev. B - Condens. Matter Mater. Phys.* (2006), 73, 1–6.
 19. A. Ray, T. Maitra, *J. Phys. Condens. Matter.* (2015), 27, 105501.
 20. R. Sáez Puche, J.M. Gallardo, R.J. de Paz, N. Taira, E. Climent-Pascual, *J. Argentine Chem. Soc.* (2009), 97, 90–101.
 21. Y.W. Long, L.X. Yang, Y. Yu, F.Y. Li, R.C. Yu, C.Q. Jin, *Phys. Rev. B - Condens. Matter Mater. Phys.* (2007), 75.
 22. A.J. Dos Santos-García, E. Climent-Pascual, J.M. Gallardo-Amores, M.G. Rabie, Y. Doi, J. Romero De Paz, B. Beuneu, R. Sáez-Puche, *J. Solid State Chem.* (2012), 194, 119–126.
 23. E. Climent Pascual, J.M. Gallardo Amores, R. Sáez Puche, M. Castro, N. Taira, J. Romero De Paz, L.C. Chapon, *Phys. Rev. B - Condens. Matter Mater. Phys.* (2010), 81, 1–7.
 24. P.W. Anderson, Antiferromagnetism. *Phys. Rev.* (1950), 79, 350–356.
 25. J.B. Goodenough, *Phys. Rev.* (1955), 100, 564–573.
 26. J. Kanamori, *J. Phys. Chem. Solids.* (1959), 10, 87–98.
 27. A. Midya, N. Khan, D. Bhoi, P. Mandal, *Appl. Phys. Lett.* (2013), 103.
 28. E. Palacios, C. Tomasi, R. Sáez-Puche, A.J. Dos Santos-García, F. Fernández-Martínez, R. Burriel, *Phys. Rev. B.* (2016), 93, 1–8.
 29. Q.Y. Dong, Y. Ma, Y.J. Ke, X.Q. Zhang, L.C. Wang, B.G. Shen, J.R. Sun, Z.H. Cheng, , *Mater. Lett.* (2015), 161, 669–673.
 30. A. Gschneidner, V.K. Pecharsky, A.O. Tsokol, *Reports Prog. Phys.* (2005), 68, 1479–1539.

-
31. B.F. Yu, Q. Gao, B. Zhang, X.Z. Meng, Z. Chen, *Int. J. Refrig.* (2003), 26, 622–636.
 32. A. Midya, S.N. Das, P. Mandal, S. Pandya, V. Ganesan, *Phys. Rev. B - Condens. Matter Mater. Phys.* (2011), 84, 1–10.
 33. M. Shao, S. Cao, S. Yuan, J. Shang, B. Kang, B. Lu, J. Zhang, *Appl. Phys. Lett.* (2012), 100, 1–5.
 34. X. Shen, L. Zhou, Y. Chai, Y. Wu, Z. Liu, Y. Yin, H. Cao, C. Dela Cruz, Y. Sun, C. Jin, A. Muñoz, J.A. Alonso, Y. Long, *NPG Asia Mater.* (2019), 11.
 35. A. Midya, N. Khan, D. Bhoi, P. Mandal, *J. Appl. Phys.* (2014), 115, 2012–2015.
 36. E. Jiménez-Melero, P.C.M. Gubbens, M.P. Steenvoorden, S. Sakarya, A. Goosens, P.D. De Réotier, A. Yaouanc, J. Rodríguez-Carvajal, B. Beuneu, J. Isasi, R. Sáez-Puche, U. Zimmerman, J.L. Martínez, *J. Phys. Condens. Matter.* (2006), 18, 7893–7904.
 37. H. Schmidt, Fraunhofer-Institut für Siliciumforschung Würzburg Fed. Rep. Germany, (1988), 100, 51–64.
 38. A.E. Danks, S.R. Hall, Z. Schnepf, *Mater. Horizons.* (2016), 3, 91–112.
 39. Y.W. Long, L.X. Yang, Y. Yu, F.Y. Li, Y.X. Lu, R.C. Yu, Y.L. Liu, C.Q. Jin, *J. Appl. Phys.* (2008), 103.
 40. M.A. Vuurman, D.J. Stufkens, A. Oskam, J.A. Moulijn, F. Kapteijn, *J. Mol. Catal.* (1990), 60, 83–98.
 41. S.A.A. Sajadi, M. Khaleghian, *J. Therm. Anal. Calorim.* (2014), 116, 915–921.
 42. W.W. Wendlandt, *Anal. Chem.* (1958), 30, 58–61.
 43. S. Rajam, A.K. Galwey, *J. Chem. Soc. Faraday Trans. 1 Phys. Chem. Condens. Phases.* (1982), 78, 2553–2561.
 44. B. Mahieu, D.J. Apers, P.C. Capron, *J. Inorg. Nucl. Chem.* (1971), 33, 2857–2866.
 45. J. Jin, Y. Ni, W. Huang, C. Lu, Z. Xu, *J. Alloys Compd.* (2013), 553, 333–337.
 46. S. Chaturvedi, P.N. Dave, *J. Energ. Mater.* (2013), 31, 1–26.
-

-
47. K. Jagannathan, A. Srinivasan, C.N.R. Rao, *J. Catal.* (1981), 69, 418–427.
 48. D.L. Hoang, A. Dittmar, M. Schneider, A. Trunschke, H. Lieske, K.W. Brzezinkab, K. Witke, *Thermochim. Acta.* (2003), 400, 153–163.
 49. D.A. Pawlak, M. Ito, M. Oku, K. Shimamura, T. Fukuda, *J. Phys. Chem. B.* (2002), 106, 504–507.
 50. L.Q. Wu, Y.C. Li, S.Q. Li, Z.Z. Li, G.D. Tang, W.H. Qi, L.C. Xue, X.S. Ge, L.L. Ding, *AIP Adv.* (2015), 5.
 51. P. Wu, C. Cai, *Electroanalysis.* (2005), 17, 1583–1588.
 52. Y.T. Tsai, T.C. Chang, W.L. Huang, C.W. Huang, Y.E. Syu, S.C. Chen, S.M. Sze, M.J. Tsai, T.Y. Tseng, *Appl. Phys. Lett.* (2011), 99, 2009–2012.
 53. K. Thirumalai, M. Shanthi, M. Swaminathan, *RSC Adv.* (2017), 7, 7509–7518.
 54. R. Tholkappian, K. Vishista, *Nanosci. Nanotechnol. Lett.* (2015), 7, 469–475.
 55. D. Barreca, A. Gasparotto, A. Milanov, E. Tondello, A. Devi, R.A. Fischer, *Surf. Sci. Spectra.* (2007), 14, 52–59.
 56. A.P. Milanov, R.W. Seidel, D. Barreca, A. Gasparotto, M. Winter, J. Feydt, S. Irsen, H.W. Becker, A. Devi, *Dalt. Trans.* (2011), 40, 62–78.
 57. F. Zhang, M. Wen, M. Cheng, Q. Wu, X. Meng, *J. Mater. Chem.* 20 (2010) 7661–7668.
 58. Asuka Namai, Marie Yoshikiyo, Kana Yamada, Shunsuke Sakurai, Takashi Goto, Takayuki Yoshida, Tatsuro Miyazaki, Makoto Nakajima, Tohru Suemoto, Hiroko Tokoro & Shin-ic, *Nat. Commun.* (2012).
 59. Pratap K. Deheri, Viswanathan Swaminathan, Shekhar D. Bhame, Zhongwu Liu, and Raju V. Ramanujan, *Chem. Mater.* (2010), 6509–6517.
 60. G.A. Stewart, J.M. Cadogan, W.D. Hutchison, D.H. Ryan, *AIP Adv.* (2019), 9.
 61. Bashar Issa, Ihab M. Obaidat, Borhan A. Albiss, Yousef Haik, *J. Mol. Sci.* (2013), 14, 21266-21305.
-

Chapter 3

A systematic study of rare-earth ions size-dependent structural phase transition from monazite to zircon-type in rare earth chromates using Raman spectroscopy



Outline

Rare earth chromates (RCrO_4) undergo monazite to zircon-type structural phase transition due to a decreased rare-earth ion size. They also exhibit an intermediate mixed phase. However, there is no systematic study on the influence of structural distortion on their phononic behavior, which is quite sensitive to subtle environmental variations. A change in the room temperature phononic spectrum was studied in the family of RCrO_4 compounds where R was varied from La to Yb using Raman modes. With an increase in the atomic number from Nd to Yb for zircon-type phases, the external translational and rotational modes were observed to shift towards lower and higher frequencies, respectively. At the same time, all internal vibrational modes shifted towards higher phonon energies. A comparison between Raman modes for monazite, intermediate, and zircon-type RCrO_4 phases showed a gradual shift in the internal modes towards a higher wavenumber. The confirmation of the change in Raman modes with the decreasing radius was found by comparing the rare-earth elements in DyCrO_4 and LaCrO_4 with non-rare-earth elements in YCrO_4 .

3.1. Introduction

Rare earth chromates (RCrO_4 , here R = rare earth element) was crystallized in two different polymorphs depending on the R involved in the crystal structure. With the increasing lanthanide radius, the first R element 'La' formed a monazite-type structure with monoclinic symmetry belonging to space group $\text{P}2_1/\text{n}$ (C_{2h}^5). The monazite-type structure has four number of molecules per unit cell ($Z = 4$). The other R elements, such as Nd, Sm, Eu, Gd, Tb, Dy, Ho, Tm, Yb, and Lu, crystallized in a tetragonal zircon-type crystal structure with $\text{I}4_1/\text{amd}$ space group (D_{4h}^{19} , $Z = 4$). R = Pr exhibits both monazite-type and zircon-type structures for RCrO_4 compounds. Many groups tried to obtain PrCrO_4 in any single-phase form; however, crystallization of PrCrO_4 in any single phase was very difficult.¹⁻⁴ The stability of the phases in rare earth chromates depends on the R element radius in the crystal structure.²

The crystal structure of monazite-type has two basic units: RO_9 edge-shared polyhedra and CrO_4 tetrahedra. In contrast, a tetragonal zircon-type structure has been observed with basic units of RO_8 dodecahedra or polyhedra and CrO_4 tetrahedra.³⁻⁷ The crystal structures for both monazite-type and zircon-type RCrO_4 compounds are shown in **Figures 3.1(a)** and **3.1(b)**, drawn using VESTA software (version: 3.1.0). The monoclinic monazite-type crystal structure had a larger oxygen coordination number which is 9 than the tetragonal zircon-type structure, with an oxygen coordination number of 8.⁸⁻¹⁵ monazite and zircon-type structures were observed to have strong sensitivity toward the externally applied pressure and temperature. With external pressure, the zircon-type structure deforms into other tetragonal scheelite-type structures having larger density and lower symmetry. The zircon to scheelite transition only involved a noticeable change in the bond angles. However, with the application of external temperature, an orthorhombic perovskite structure was formed for both the monazite and zircon-type structures.¹

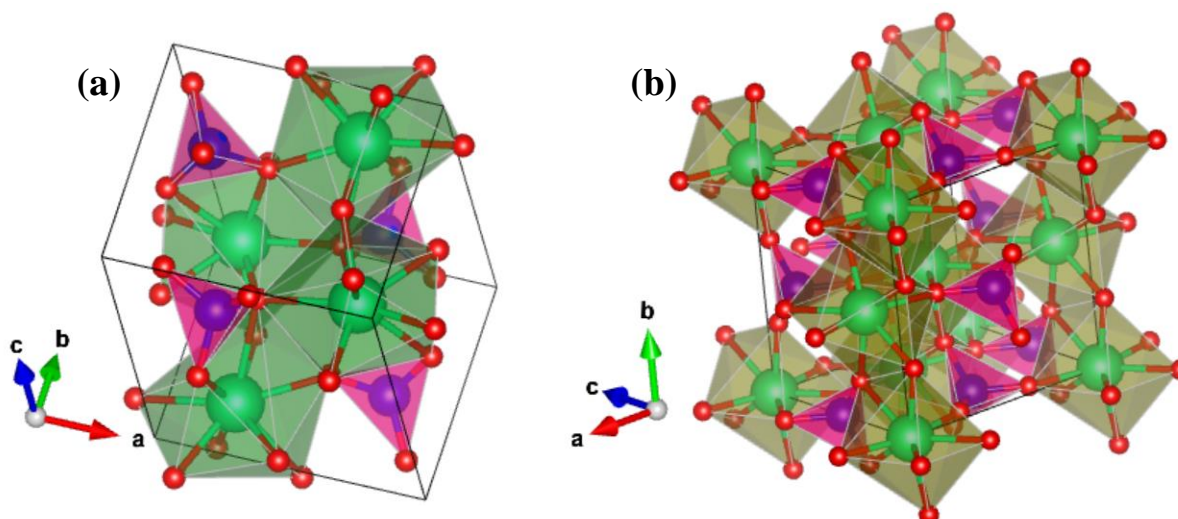


Figure 3.1. Perspective view of (a) monazite-type and (b) zircon-type crystal structure (plotted using VESTA software) of RCrO_4 , showing R, Cr, and O atoms by green, blue, and red spheres, respectively (R = rare earth). The CrO_4 unit is denoted by the tetrahedra (pink color) for both the structures, whereas the RO_9 (in monazite-type) and RO_8 (in zircon-type) appeared in polyhedra (green color).

The exhibiting physical and chemical properties in the different materials mainly depend on the inbuilt crystallographic structure, which results in importance of phase control of these materials. An extensive investigation of the magnetic properties of most of the RCrO_4 compounds was studied by considering the rare valence state of chromium "+5".^{1-3, 8, 9, 13, 16-18} The RCrO_4 compounds were good candidates to study $3d-4f$ interaction and magnetocaloric effect (MCE) at low temperatures as both the sublattices are ordered at this temperature.¹⁻⁵ The co-structural compounds such as RPO_4 and RVO_4 were studied for the structural changes using Raman modes at room temperature and with pressure variation. Firstly, the RPO_4 compounds were studied for the lattice vibration in the structure. The structural packing of $(\text{PO}_4)^{3-}$ ions was observed in these compounds for the lanthanide series. However, the same closer packing of $(\text{VO}_4)^{3-}$ ion was also studied in the RVO_4 compounds.^{19, 20} Aoki *et al.*¹¹ conducted the initial Raman study at room temperature with LaCrO_4 and NdCrO_4 . LaCrO_4 has a monoclinic

monazite-type structure, and NdCrO_4 has a tetragonal zircon-type structure. The vibrational structures of these compounds were analyzed using Raman spectroscopy which was affected due to the CrO_4 tetrahedra symmetry. Further, with pressure-dependent Raman spectra, Y. Long *et al.*²¹ reported the Raman study at room temperature for DyCrO_4 and NdCrO_4 . They observed eight Raman modes in their work. The phase transition from the zircon-type to the scheelite-type crystal structure was investigated with Raman modes.²¹ The rest of the RCrO_4 compounds (except $\text{R} = \text{La}$, Nd , and Dy) have not been studied yet. The R-site element in RCrO_4 compounds determines the crystallization structure. So, the different R-site elements create structural changes in these compounds, which have not been investigated so far. The reported synthesis method for these compounds was a solid-state reaction method with the drawback of having an impurity phase in the obtained mixture. Thus, there is a need to synthesize the single-phase RCrO_4 compounds and re-investigate their physical and chemical properties.^{1, 4, 5, 22, 23}

The present study shows the room-temperature Raman spectra for monoclinic monazite-type LaCrO_4 , both polymorph (monazite-type and zircon-type) containing PrCrO_4 , tetragonal zircon-type RCrO_4 compounds ($\text{R} = \text{Nd}$, Sm , Gd , Dy , Ho , Er , Tm , and Yb). The effect of the R-site element on the Raman modes of RCrO_4 compounds was investigated. The comparative study for the Raman spectra of different structures as well as Dy , La as rare earth elements, and Y as non-rare earth elements present at the R-site in RCrO_4 compounds was also observed. Y was the next adjacent element to lanthanide from the d -block (group 3). It has similar chemical properties as that of lanthanides, but the radius contraction may differ in this element. So, YCrO_4 was introduced in the Raman study along with the RCrO_4 compounds to determine the contraction effect on the structure.

Further, the Raman study extended to changes in the Raman modes of DyCrO_4 by substituting Dy with Sm in some percentages forming the $\text{Sm}_x\text{Dy}_{1.3-x}\text{CrO}_4$ system. The Sm has

a larger atomic radius and smaller atomic number than Dy. So, the effect of a larger atomic radius element substitution in place of a smaller one was investigated in this system.

3.2. Experiment

3.2.1 Sample preparation

The powder samples of the monazite-type LaCrO_4 and zircon-type RCrO_4 ($\text{R} = \text{Pr, Nd, Sm, Gd, Dy, Ho, Er, Tm, Yb}$) and YCrO_4 were synthesized using a hydrolytic sol-gel synthesis method. As mentioned in our previous work, the reaction sequence was followed to prepare RCrO_4 compounds.²⁴ The starting materials of R (III) nitrate hydrate ($\text{R}(\text{NO}_3)_3 \cdot \text{H}_2\text{O}$, Aldrich, 99.9% metal basis), chromium nitrate ($\text{Cr}(\text{NO}_3)_3$, Aldrich, 99.9%), and oxalic acid ($\text{H}_2\text{C}_2\text{O}_4 \cdot 2\text{H}_2\text{O}$, Merck, 99.5%) were used. The ratio of the precursors was taken as $\text{R} : \text{Cr} = 1 : 1$ except for $\text{R} = \text{Dy}$. The DyCrO_4 single phase was found with a higher concentration of $\text{Dy}(\text{NO}_3)_3$ as compared to other R elements. Firstly to synthesize LaCrO_4 , the precursor's $\text{La}(\text{NO}_3)_3$, $\text{Cr}(\text{NO}_3)_3$, and oxalic acid were dissolved in de-ionized water separately. The homogeneous solution was obtained by mixing all three aqueous solutions in one beaker with stirring. The pH of the homogeneous solution was raised to ~ 10 by adding 30% ammonia solution drop-wise. The mixture was then stirred at $\sim 30^\circ\text{C}$ for 3h, which resulted in a sol formation. The obtained sol was heated at 80°C and formed the gel. The gel form of the sample is heated, so the water gets evaporated and converted into the dried gel. The dried gel was sintered at 600°C for 2h to obtain the expected phase. The same procedure was repeated to prepare zircon-type RCrO_4 ($\text{R} = \text{Nd, Sm, Gd, Dy, Ho, Er, Tm, Yb}$) and YCrO_4 , mixed (zircon and monazite-type) PrCrO_4 and $\text{Sm}_x\text{Dy}_{1.3-x}\text{CrO}_4$ system by taking respective precursor salts. Further, to observe the effect of the longer atomic radius of Sm in place of the smaller atomic radius of Dy on Raman scattering, the samples were prepared by substituting Sm in place of Dy in DyCrO_4 . Sm concentration was taken as $x = 0.3, 0.7$, and 1 for the replacement of Dy in

$\text{Sm}_x\text{Dy}_{1.3-x}\text{CrO}_4$, as the single-phase of DyCrO_4 was obtained with a molar ratio of 1.3:1 (Dy:Cr).

3.2.2 Characterisation techniques

The crystallinity and phase purity of the samples was confirmed by X-ray diffraction (XRD) using a PANalytical X'PERT PRO instrument. The X-ray source was the iron-filtered Cu $K\alpha$ radiation of wavelength 1.54 Å with a diffraction angle (2θ) varied in the range of 10° – 80° with a step size of 0.013° . Room-temperature Raman spectra were obtained from HR-800 Raman spectrophotometer (Jobin Yvon-Horiba, France) with a He-Ne laser of wavelength 633 nm, of 20 mW power. The Raman instrument was equipped with a thermoelectrically cooled (with Peltier junctions), multi-channel, spectroscopic-grade CCD detector (1024×256 pixels of 26 microns). An objective of 50 XLD magnification was used to focus and collect the signal from the powder sample dispersed on a glass slide.

3.3. Results and discussion

3.3.1. X-ray diffraction analysis

The XRD patterns show that at a sintering temperature of 600°C , LaCrO_4 crystallized in a monazite-type structure, as shown in **Figure 3.2** (JCPDS card number [89-0448]). However, PrCrO_4 (sintered at 600°C) shows the coexistence of both zircon [JCPDS card number 74-1243] and monazite [JCPDS card number 35-1289] phases (**Figure 3.2**), with the zircon phase forming the major fraction. Even after optimization of reaction conditions, the efforts to obtain the single-phase PrCrO_4 didn't get success with the hydrolytic sol-gel method. The other RCrO_4 phases ($R = \text{Nd, Sm, Gd, Dy, Ho, Er, Tm, Yb}$) and YCrO_4 crystallized in the zircon-type after sintering at 600°C (**Figure 3.2**). The Rietveld refinement using FullProf software also confirms the single phase, as shown in **Figure 3.3**. When the JCPDS data of the zircon-type structures of RCrO_4 compounds were piled together, it showed

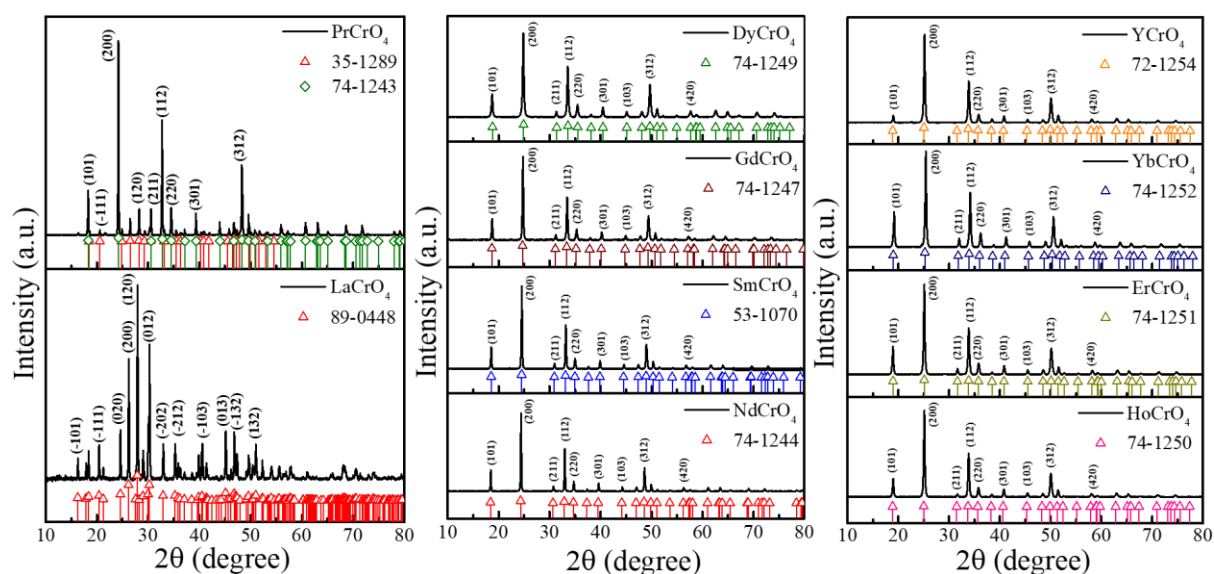


Figure 3.2. XRD patterns for monazite-type LaCrO_4 , mixed monazite and zircon-type PrCrO_4 (showing both polymorphs), and zircon-type RCrO_4 compounds ($\text{R} = \text{Nd}, \text{Sm}, \text{Gd}, \text{Dy}, \text{Ho}, \text{Er}, \text{Yb}$), and YCrO_4 . The JCPDS data matched with the synthesized compounds showing single phases of the RCrO_4 compounds.

a systematic shift in the 2θ position (**Figure 3.4 (a)**) towards higher angles while going from NdCrO_4 to YbCrO_4 , which shows the decrease in the lattice parameters. A similar shift in the 2θ position was also observed in XRD data of as-synthesized samples, as shown in **Figure 3.4 (b)**. The shift in the 2θ towards the higher values shows the contraction in the lattice.^{27, 28} The lattice gets contracted with the increasing atomic number and decreasing atomic size (radius). The RCrO_4 structure is affected by changing the R-site from Nd to Yb in the zircon-type structure. The powder XRD measurements on $\text{Sm}_x\text{Dy}_{1.3-x}\text{CrO}_4$ series, with $x = 0.3, 0.7,$ and 1 (**Figure 3.5**), show that no structural phase transition was observed when the ratio Sm/Dy was altered from the parent structures (SmCrO_4 and DyCrO_4) which both crystallize in the zircon-type structure.

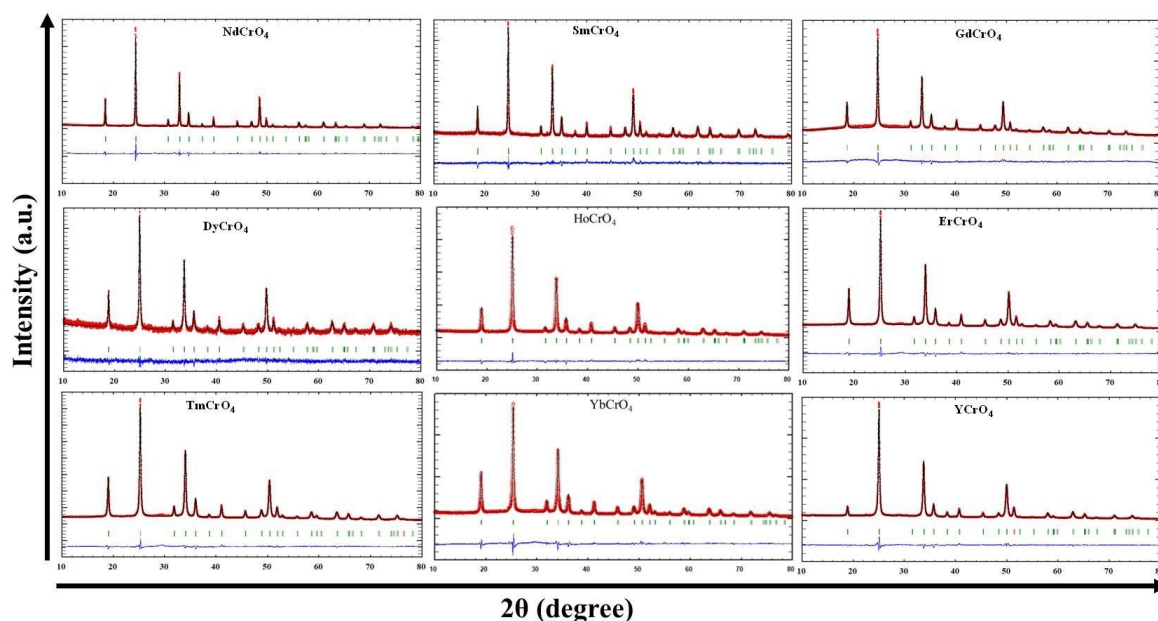


Figure 3.3: X-ray diffraction patterns fit zircon-type RCrO_4 compounds ($R = \text{Nd, Sm, Gd, Dy, Ho, Er, Tm, Yb}$) and YCrO_4 . The observed and calculated peaks are denoted in red marks and solid lines (black), respectively. The vertical lines in the middle (green color) show Bragg reflection positions. The line in the blue color in the lower part of the graph reveals the difference in the calculated and observed intensities.

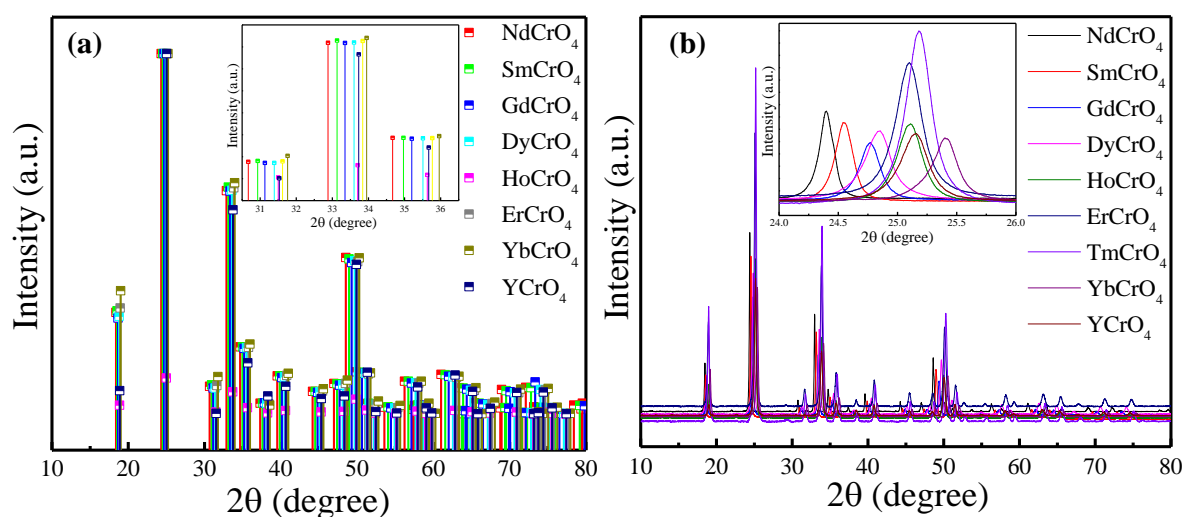


Figure 3.4: The shift in the XRD pattern (a) JCPDS files from Nd-Yb, and Y in zircon-type RCrO_4 compounds. Inset: zoom view of the graph. And (b) recorded for synthesized zircon-

type RCrO_4 compounds ($R = \text{Nd, Sm, Gd, Dy, Ho, Er, Yb}$) and YCrO_4 . The inset shows the zoom view of the graph.

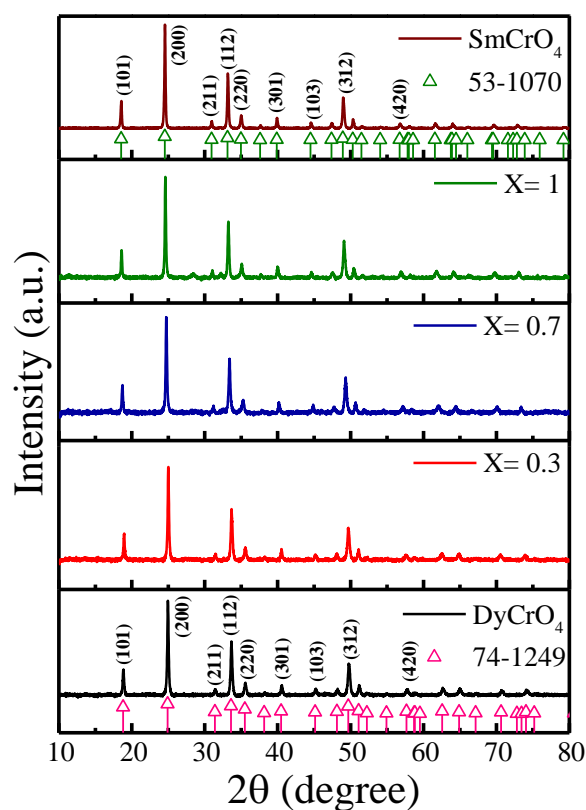


Figure 3.5: XRD patterns for Sm substituted zircon-type $\text{Sm}_x\text{Dy}_{1.3-x}\text{CrO}_4$ ($x= 0.3, 0.7, 1$) system and single-phase DyCrO_4 and SmCrO_4 .

3.3.2 Room temperature Raman spectra

According to group theory analysis, the monoclinic monazite-type structure exhibits 69 optical modes represented as ^{27, 28}

$$\Gamma = 16B_u + 17A_u + 18A_g + 18B_g.$$

Among that, 36 modes are Raman active, and 33 modes are IR-active:

$$\Gamma = 18A_g + 18B_g$$

$$\Gamma = 16B_u + 17A_u.$$

The tetragonal zircon-type structure has 33 optical modes from group theory prediction.

Among these 33 optical modes, 12 are Raman active. ^{19-21, 27, 29}

$$\Gamma = A_{1g}(v_1, v_2) + B_{1g}(2T, v_3, v_4) + B_{2g}(v_2) + E_g(2T, R, v_3, v_4).$$

A vibrational spectra of monazite and zircon-type structures were divided into two modes: (i) internal modes (v_1 – v_4), which are associated with CrO_4 tetrahedron and can be further divided into bending and stretching modes, and (ii) external modes can be classified as translational (T)- and rotational (R)-like modes that involves the movement of both R element and CrO_4 ions.^{27, 28}

In this experiment, eleven modes with measurable intensity were observed in the Raman spectra (recorded at room temperature) of the monazite-type $LaCrO_4$ (**Figure 3.6**). Out of the eleven modes listed in **Table 3.1**, ten modes were correlated with the previously reported $LaCrO_4$ structure.^{11, 27} Due to the overlap of several A_g and B_g modes and their low Raman scattering cross-section, other Raman modes may not have been present. The mixed zircon and monazite-type $PrCrO_4$ show fourteen measurable intensity peaks, but only eight vibrational modes were correlated with the reported constructs (**Figure 3.6**).²⁸

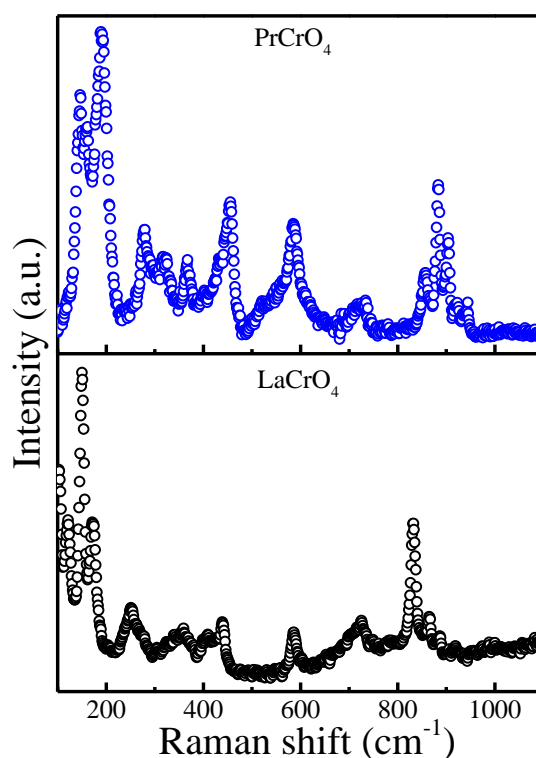


Figure 3.6: The room temperature Raman spectra for monazite-type $LaCrO_4$, mixed monazite, and zircon-type $PrCrO_4$ in the frequency range 100 cm^{-1} - 1100 cm^{-1} .

These assigned modes show the zircon-type as well as the monazite-type structure of PrCrO_4 . The maximum modes were related to the zircon-type structure, which means the zircon phase was the major one in the mixture of PrCrO_4 . One external ($\text{R}(\text{E}_g)$) and five internal ($\nu_2(\text{B}_{1g})$, $\nu_2(\text{A}_{1g})$, $\nu_4(\text{B}_{1g})$, $\nu_3(\text{B}_{1g})$, $\nu_1(\text{A}_{1g})$) modes were observed for the zircon-type PrCrO_4 , at the same

LaCrO ₄ (Monazite-type)		PrCrO ₄ (Monazite-type and zircon-type)	
Frequency (cm ⁻¹)	Raman modes	Frequency (cm ⁻¹)	Raman modes
109	A _g	147	A _g
121	B _g	160	R(E _g)/A _g
150	A _g	191	$\nu_2(\text{B}_{1g})/\text{A}_g$
173	B _g	279	$\nu_2(\text{A}_{1g})/\text{A}_g$
252	A _g	321	-
359	A _g	366	-
439	A _g	456	$\nu_4(\text{B}_{1g})$
586	-	585	-
725	A _g	724	$\nu_3(\text{B}_{1g})$
832	A _g /B _g	857	-
865	A _g	883	$\nu_1(\text{A}_{1g})$
		903	-
		923	-
		945	A _g /B _g

Table 3.1: Listed Raman modes for monazite-type LaCrO_4 and mixed zircon and monazite-type PrCrO_4 compounds.

time four A_g modes were listed in the monazite-type PrCrO_4 . The Raman frequencies assigned with the modes for LaCrO_4 and PrCrO_4 are listed out in **Table 3.1**.

Figure 3.7(a) shows room temperature Raman spectra for zircon-type RCrO_4 ($R = \text{Nd, Sm, Gd, Dy, Ho, Er, Tm, and Yb}$) compounds from $100 - 1100 \text{ cm}^{-1}$ frequency range. The external modes for zircon-type RCrO_4 compounds were reported from the $100 \text{ cm}^{-1} - 200 \text{ cm}^{-1}$ frequency range. Three external modes were observed in this lower frequency region, as shown in **figure 3.7(b)**. The external translational ($T(E_g)$) and rotational ($R(E_g)$) modes split into two separate modes as the atomic radius of the R (r_R) decreased in zircon-type RCrO_4 . The two translational $T(B_g)$ and $T(E_g)$ modes shifted to lower frequency towards the left side as the atomic radius decreased and the atomic number increased from Nd-Yb. This tendency was ostensibly compensated for as a mass effect (harmonic approximation remains valid). In comparison, the $R(E_g)$ mode shifted to the higher frequency related to the lanthanide contraction.^{19,20} The shift in the external modes was denoted by the dotted line in **Figure 3.7(b)**. As even the atomic number rises, the energy of the R -atomic ion's orbital drops. Consequently, the stronger the interaction force constant between R and CrO_4 is, the smaller the energy difference is, which accounts for the shift in frequency of the internal modes and the decline in the R - O bond distance.^{19,20}

A internal vibrational modes for RCrO_4 compounds were recorded from 200 cm^{-1} to 1000 cm^{-1} . The first two internal modes $\nu_2(B_{2g})$ and $\nu_2(A_{1g})$, symmetric bending modes were observed in the frequency range of $200 \text{ cm}^{-1} - 400 \text{ cm}^{-1}$ (**Figure 3.8(a)**). The antisymmetric bending mode $\nu_4(B_{1g})$ was located at $\sim 456 \text{ cm}^{-1}$ for the NdCrO_4 , which was shifted to the right towards a higher frequency region with the increasing atomic number and decreasing atomic radius, as shown in **Figure 3.8(b)**. The antisymmetric stretching ($\nu_3(B_{1g})$ and $\nu_3(E_g)$) with symmetric stretching ($\nu_1(A_{1g})$) modes were observed in the higher frequency region from $700 \text{ cm}^{-1} - 1000 \text{ cm}^{-1}$, shown in **Figure 3.8(b)**.

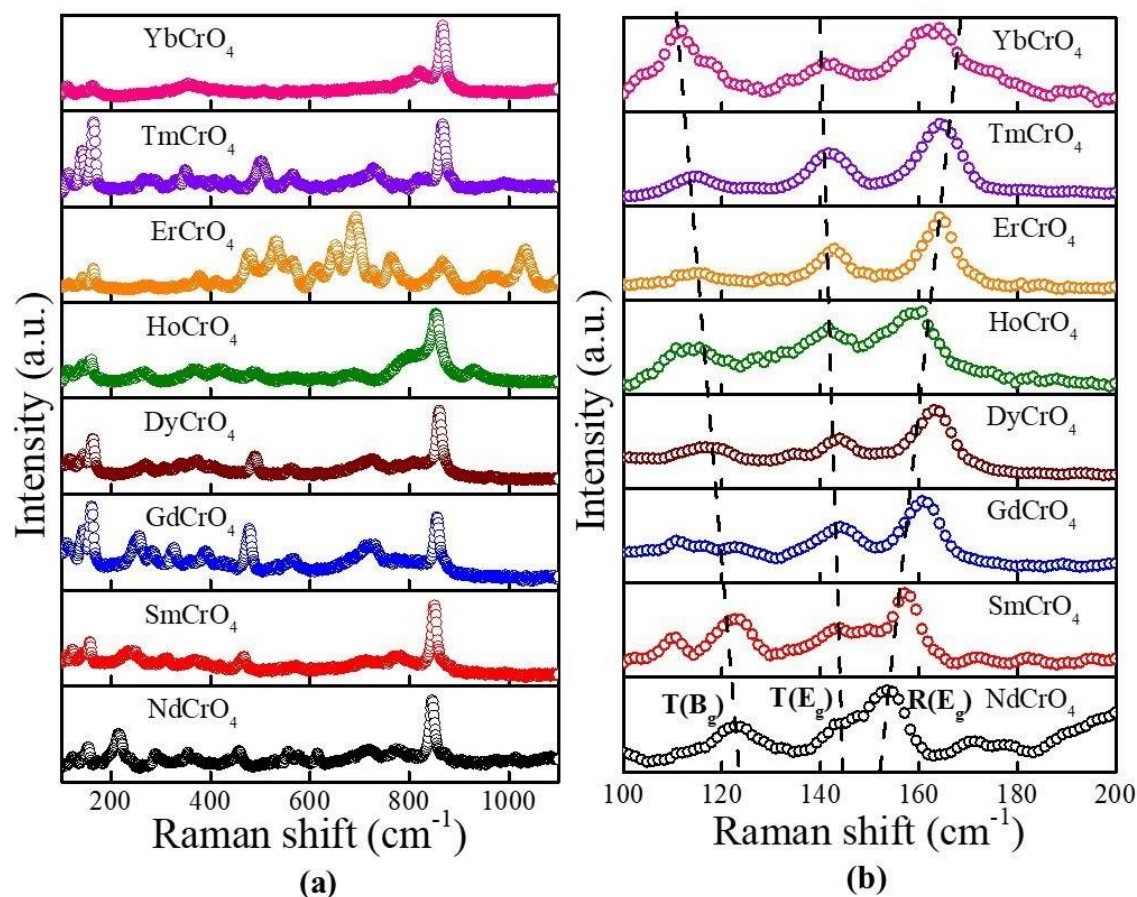


Figure 3.7: (a) The Raman spectra at room temperature from the frequency range 100 cm^{-1} - 1100 cm^{-1} , and (b) external vibrational modes of Raman spectra for zircon-type RCrO_4 compounds ($R = \text{Nd, Sm, Gd, Dy, Ho, Er, Tm, Yb}$) in 100 cm^{-1} - 200 cm^{-1} frequency range. The dotted line shows the shift in the Raman modes.

All observed internal modes in zircon-type RCrO_4 compounds were shifted to a higher frequency (right shift) as the atomic number increased (r_R decreases) from Nd to Yb (shown in the dotted line in **Figure 3.8**). This tendency was attributed towards the lanthanide contraction, which causes the lanthanide atomic radii to shrink as the lanthanide atomic number grows and the energy of the atomic orbital to drop starting with Nd-Yb. The interaction force constant across R and CrO_4 is correlated with this energy differential. The stronger interaction force constant is produced as a result of the lower energy differential. Additionally, this causes the R - O bond length to decrease and the frequency of a internal modes to increase.^{19, 20} The RCrO_4

compounds show many peaks in the Raman spectra. The modes were assigned to RCrO_4 combinations by correlating with the reported vibrational spectra of RVO_4 and RPO_4 . This work observed nine, ten, eight, eight, eight, four, six, and five Raman modes for NdCrO_4 , SmCrO_4 , GdCrO_4 , DyCrO_4 , HoCrO_4 , ErCrO_4 , TmCrO_4 , and YbCrO_4 , respectively. In addition, some weak modes probably overlapped in the compounds, which is why we cannot discern them in our work. The modes observed for ErCrO_4 in the higher frequency region from 200-1000 cm^{-1} cannot be assigned as the peaks are not matched with the reported data.

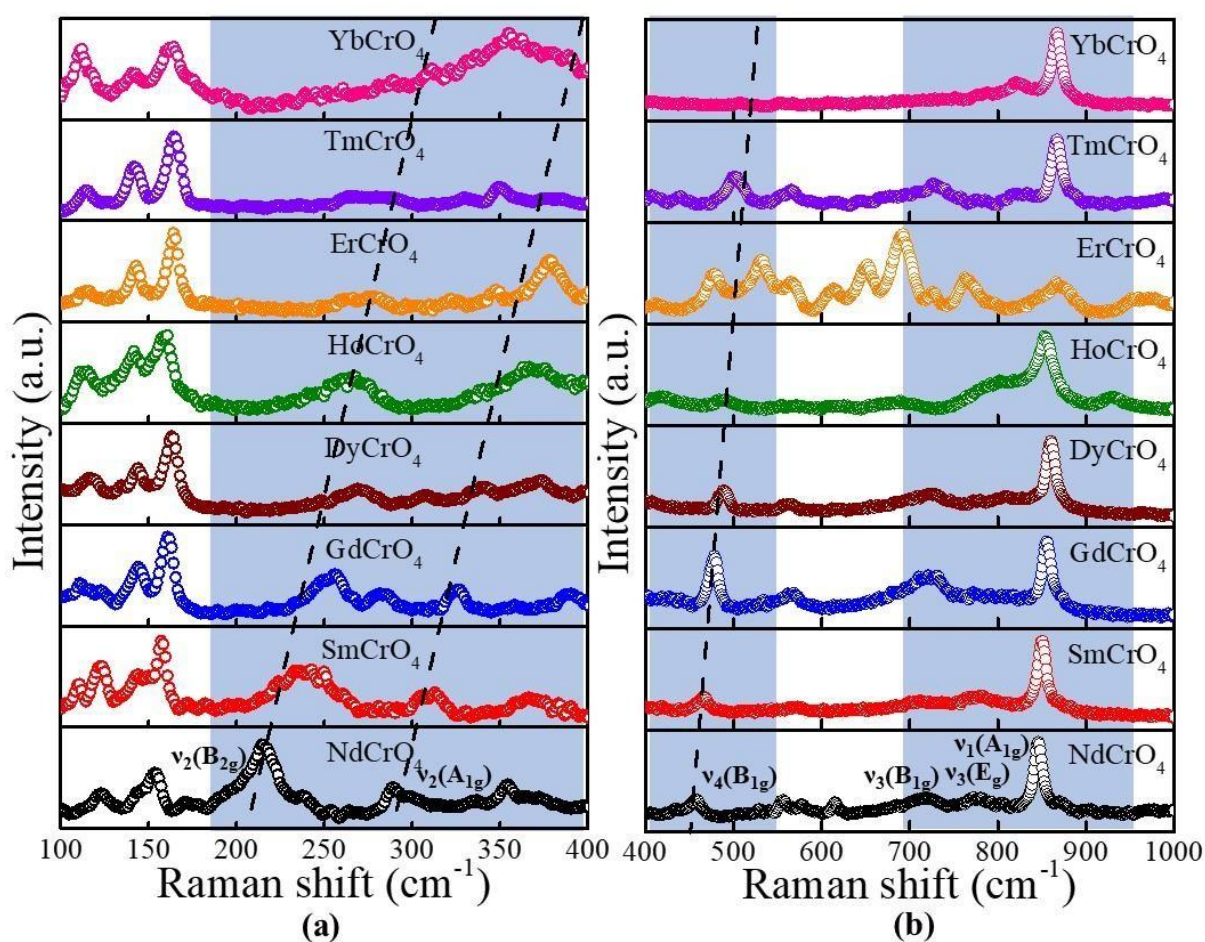


Figure 3.8: Internal vibrational modes of Raman spectra recorded at room temperature in zircon-type RCrO_4 ($\text{R} = \text{Nd}, \text{Sm}, \text{Gd}, \text{Dy}, \text{Ho}, \text{Er}, \text{Tm}, \text{Yb}$) compounds in the frequency range (a) $100 \text{ cm}^{-1} - 400 \text{ cm}^{-1}$, (b) $400 \text{ cm}^{-1} - 1000 \text{ cm}^{-1}$. The shaded portion and dotted line reveal the Raman frequencies and shift in the Raman modes.

Compounds	External modes (cm ⁻¹)					Internal modes (cm ⁻¹)						
	E _g	B _{1g}	E _g	E _g	B _{1g}	v ₂ (B _{2g})	v ₂ (A _{1g})	v ₄ (B _{1g})	v ₃ (B _{1g})	v ₂ (B _{1g})	v ₃ (E _g)	v ₁ (A _{1g})
NdCrO ₄	-	123	144	152	-	215	289	456	717	-	776	846
SmCrO ₄	110	122	143	157	-	238	311	466	712	-	780	850
GdCrO ₄	111	-	142	160	-	255	326	478	720	-	-	855
DyCrO ₄	-	117	142	163	-	268	340	489	810	-	-	860
HoCrO ₄	-	114	141	158	-	266	367	489	805	-	-	853
ErCrO ₄	-	114	141	163	-	-	377	-	-	-	-	-
TmCrO ₄	-	114	142	165	-	-	-	501	826	-	-	868
YbCrO ₄	-	111	141	161	-	-	-	-	821	-	-	867
YCrO ₄	-	150	186	278	-	-	337	488	805	-	-	856

Table 3.2: At room temperature, internal and external Raman modes are listed for zircon-type RCrO₄ (R = Nd, Sm, Gd, Dy, Ho, Er, Tm, and Yb) and YCrO₄.

The R³⁺ ions inside the RO₈ dodecahedron gradually shrink from Pr³⁺ to Yb³⁺ as the size of the rare earth increases. The size of a CrO₄ tetrahedra also grows concurrently. When a result, as the RCrO₄ series of oxides grows, the Cr-O bond length expands and the bonds weaken. The stronger bonds, on the other hand, have a more acidic Lewis character and have a greater attraction for electrons since the R-O bond length decreases during the course of the series. Due to the lanthanide contraction in zircon-type RCrO₄ compounds, the ionic radii of the rare earth is reduced from Pr to Yb, which causes a linear decline in the a and c lattice parameters of these phases.^{8, 9, 30}

The Raman measurements further extend to the comparative study between rare-earth (Dy, La) and non-rare earth (Y) elements in RCrO_4 at R-site and for different structures such as zircon, monazite, and mixed RCrO_4 compounds. The comparison between rare-earth and Y in RCrO_4 combinations shows the shift in the Raman peaks, as shown in **Figure 3.9(a)**. The highlighted portion in **Figure 3.9(a)** shows the peak position for $\nu_1(\text{A}_{1g})$ mode. The intense high rise of symmetric stretching mode $\nu_1(\text{A}_{1g})$ (internal mode related to motion in CrO_4 tetrahedra) for zircon-type DyCrO_4 is located at $\sim 860 \text{ cm}^{-1}$. The same mode was positioned at $\sim 832 \text{ cm}^{-1}$ for monazite-type LaCrO_4 and $\sim 856 \text{ cm}^{-1}$ for zircon-type YCrO_4 . So, comparing the Dy, La (rare earth), and Y (non-rare earth) elements in the structure, the highest intensity mode $\nu_1(\text{A}_{1g})$ is located at a lower frequency in YCrO_4 due to the larger Y-O bond length than

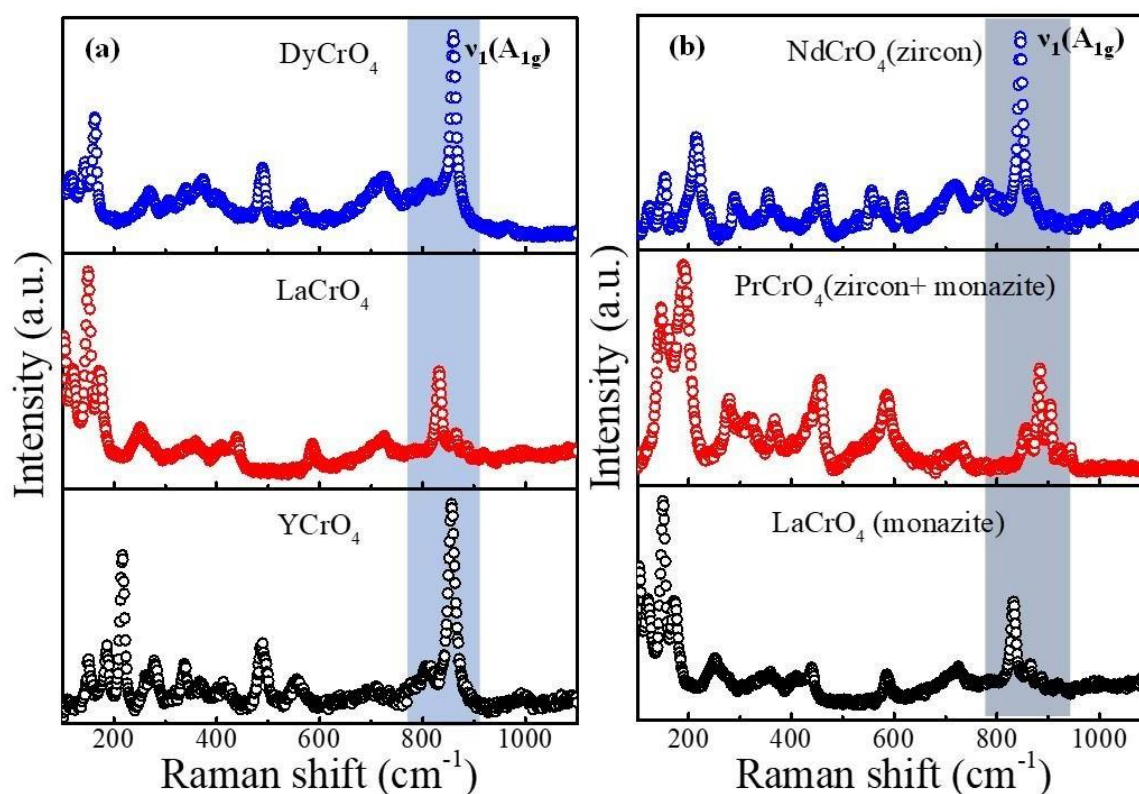


Figure 3.9: Raman spectra for (a) rare-earth-based RCrO_4 ($R = \text{Dy}, \text{La}$) and non-rare earth-based YCrO_4 compounds, (b) rare-earth-based RCrO_4 compounds with the different crystal structures (zircon-type and monazite-type). Highlighted portion in both figures shows the peak position of $\nu_1(\text{A}_{1g})$ mode.

Dy-O in the zircon-type DyCrO_4 structure. In contrast, $\nu_1(\text{A}_{1g})$ mode in the LaCrO_4 is located at the middle position as that of DyCrO_4 and YCrO_4 , as the crystal structure changes the frequency of Raman modes.

Figure 3.9(b) compares the Raman modes in the different crystal structures. The $\nu_1(\text{A}_{1g})$ mode of monazite-type LaCrO_4 (at $\sim 832 \text{ cm}^{-1}$) is lower than that of zircon-type NdCrO_4 (at $\sim 846 \text{ cm}^{-1}$). The $\nu_1(\text{A}_{1g})$ mode is related to the CrO_4 unit in monazite-type and zircon-type crystal structures. The comparison between the common modes gives us the distortion in the structure related to the R-O bond distance. The PrCrO_4 containing monazite and zircon-type structures shows various modes in the 800 cm^{-1} - 1000 cm^{-1} frequency range associated with the CrO_4 bonding.^{27, 28}

The internal modes at lower frequency range were apparently associated to the Sm or Dy motion, based on group theory analysis, in which a simplified zircon-type structure is thought to be formed of two sublattices of Sm or Dy and CrO_4 "molecules."^{27, 28} In comparison, CrO_4 motion was connected to the latter modes at a greater frequency range (external modes). Raman spectroscopy is a useful instrument for examining the consequences of structural abnormalities, as was already mentioned. The first-order Raman phonon spectrum of a perfect crystal is composed of small lines that correlate to the Raman-allowed zone centre and that follow specific polarisation selection rules. However, in the case of disordered crystals, the phonon spectrum is expected to exhibit the following characteristics: (i) a broadening of the first-order Raman lines; (ii) the activation of prohibited Raman phonons; (iii) the emergence of broad Raman bands indicating the phonon density of states; (iv) frequency shifting of certain peaks proportional to the amount of the dopant element (i.e., one-phonon-like (i.e., two-phonon like behavior).^[31]

In this study, the newly synthesized materials were studied using Raman measurements. The Dy was substituted with Sm in zircon-type DyCrO_4 , and the effect of substitution was

studied using Raman spectra (**Figure 3.10**). The zircon-type DyCrO_4 was substituted with $x = 0.3, 0.7, 1$ and compared with single-phase DyCrO_4 and SmCrO_4 . The Raman peaks intensity for samples $x = 0.3$ and 0.7 was greater as compared to the other samples. The Raman spectra observed extra peaks for $x = 0.3$ and 0.7 .

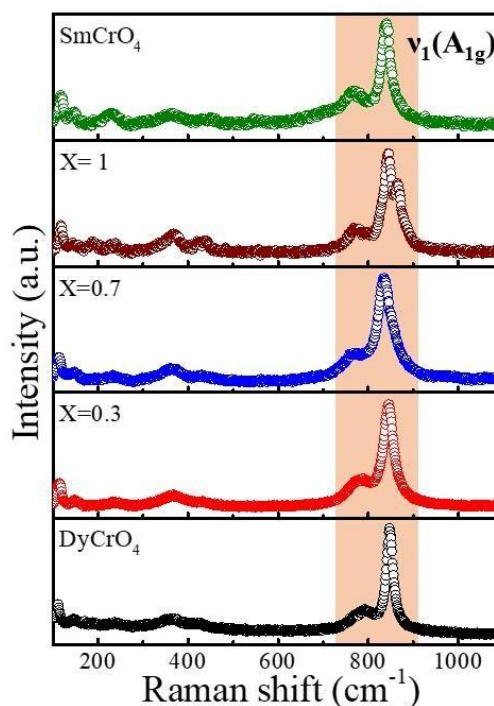


Figure 3.10: Recorded Raman spectra for Sm substituted zircon-type $\text{Sm}_x\text{Dy}_{1.3-x}\text{CrO}_4$ ($x = 0.3, 0.7, 1$) comparing with single phases of DyCrO_4 and SmCrO_4 . The shaded portion shows the Raman frequency for $\nu_1(\text{A}_{1g})$ in the $\text{Sm}_x\text{Dy}_{1.3-x}\text{CrO}_4$ system.

The most intense $\nu_1(\text{A}_g)$ peak for pure DyCrO_4 was found at $\sim 847 \text{ cm}^{-1}$, which is somewhat at the lowest frequency as the previously measured DyCrO_4 . The peak position shift was observed when Dy was substituted in zircon-type DyCrO_4 by Sm. The intense peak $\nu_1(\text{A}_g)$ shifted to a lower frequency for $\text{Sm}_x\text{Dy}_{1.3-x}\text{CrO}_4$ ($x=0.7$), with a broadening in the line width. However, for $x=1$, the $\nu_1(\text{A}_g)$ mode splits into two peaks. The peak position may relate to the single-phase SmCrO_4 and DyCrO_4 , which reveals the vibration of the CrO_4 group in both

Modes	Frequency (cm ⁻¹) DyCrO ₄	Frequency (cm ⁻¹) (X = 0.3)	Frequency (cm ⁻¹) (X = 0.7)	Frequency (cm ⁻¹) (X = 1)	Frequency (cm ⁻¹) SmCrO ₄
T (B _{1g})	110	114	113	117	116 120
T (E _g)	144	149	146	Weak	147
ν_2 (B _g)	236	234	233	Weak	233
ν_2 (A _g)	361	365	361	365	363
ν_4 (B _g)	-	431	429	-	-
ν_3	784	780	769	767	770
ν_1 (A _g)	847	845	834	844 865	839
-	-	994	980	-	925

Table 3.3: Raman modes listed for room temperature Raman spectra of zircon-type Sm_xDy_{1.3-x}CrO₄ (x = 0.3, 0.7, 1) and single-phase DyCrO₄ and SmCrO₄.

Structures, indicating two phonons-like behavior. The substitution of Sm with x = 0.3 and x = 1 shows the lower shift in the ν_1 (A_g) mode compared to the Sm substitution with x = 0.7. The broadening of the Raman peaks was observed in the Sm_xDy_{1.3-x}CrO₄ system as the percentage of Sm substitution was raised. And that's why it is difficult to record the phonon frequency of the samples accurately. Internal ν_2 (B_g), ν_4 (B_g), ν_1 (A_g), and ν_3 modes shifted to lower wavenumber because of the effects of lanthanide contraction as discussed for the zircon-type RCrO₄ compounds. At the same time, the external mode T(B_{1g}) shifted to a higher wavenumber. Whereas T (E_g) shows randomly increased and decreased Raman frequency. The

shifting in the higher wavenumber confirmed the mass effect—validation of harmonic approximation.^{19, 20} The same trend for external and internal modes was observed with the zircon-type RCrO_4 compounds changing with the R-site from Nd -Yb. The frequencies assigned to the Raman modes are listed in **Table 3.3**.

3.4 Conclusion

The entire series of compounds -RCrO_4 (R = La, Pr, Nd, Sm, Gd, Dy, Ho, Er, Tm, Yb) and YCrO_4 were synthesized using the hydrolytic sol-gel method. The RCrO_4 (R = Nd, Sm, Gd, Dy, Ho, Er, Tm, Yb) and YCrO_4 crystallized in zircon-type, while LaCrO_4 forms monazite-type. On the other hand, PrCrO_4 showed the coexistence of both the polymorphs, i. e. zircon-type and monazite-type structures at 600 °C. The Raman study of zircon-type RCrO_4 compounds concludes that the external Raman modes $\text{T}(\text{B}_g)$ and $\text{T}(\text{E}_g)$ shifted to a lower frequency from Nd-Yb. However, $\text{R}(\text{E}_g)$ and internal modes moved to higher energy as the atomic radius decreased and the atomic number increased from Nd-Yb. A comparison between DyCrO_4 , LaCrO_4 (rare-earth), and YCrO_4 (non-rare earth) shows the lower frequency of ν_1 (A_{1g}) mode for YCrO_4 compared to the other two compounds. The structural comparison reveals the ν_1 (A_{1g}) mode at a lower frequency in the monazite-type structure than in the zircon-type structure. The substitution of Sm in the DyCrO_4 host shifted the internal Raman modes (ν_2 (B_{1g}), ν_2 (A_{1g}), ν_4 (B_{1g}), ν_3 , ν_1 (A_{1g})) to the lower frequency region. The shift towards the higher frequency is related to the mass effect, whereas the lower frequency shift counters the lanthanide contraction in the samples going from Nd-Yb in the RCrO_4 system.

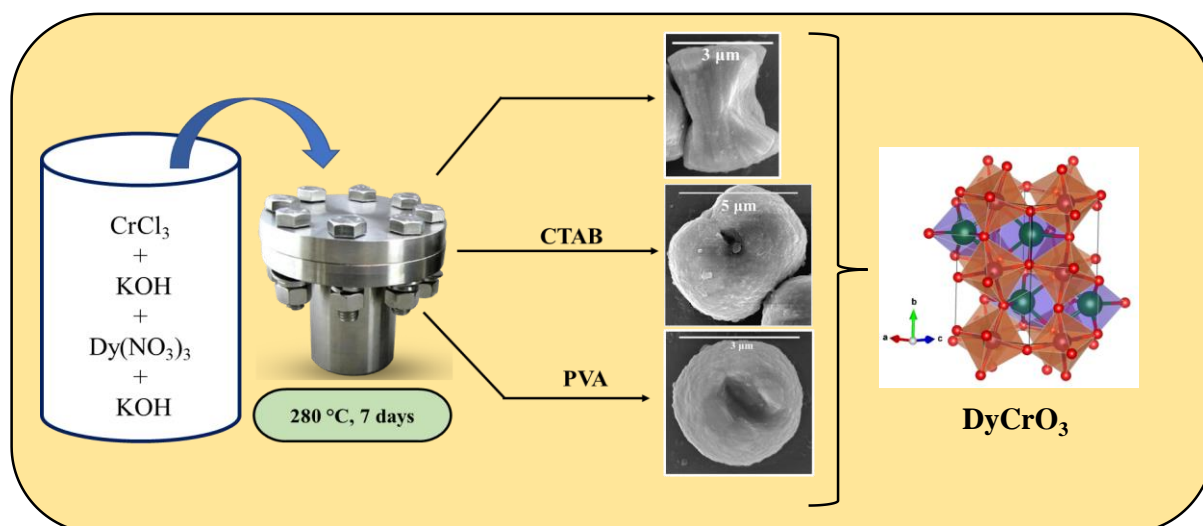
3.4. References

1. Y. Long, Q. Liu, Y. Lv, R. Yu, C. Jin, *Phys. Rev. B - Condens. Matter Mater. Phys.* (2011), 83, 4.
2. A. Indra, K. Dey, J. K. Dey, S. Majumdar, U. Rütt, O. Gutowski, M. V. Zimmermann, S. Giri, *Phys. Rev. B* (2018), 98, 14408.
3. Y. Aoki, H. Konno, H. Tachikawa, *J. Mater. Chem.* (2001), 11, 1214.
4. A. Midya, N. Khan, D. Bhoi, P. Mandal, *J. Appl. Phys.* (2014), 115, 2012.
5. A. Midya, N. Khan, D. Bhoi, P. Mandal, *Appl. Phys. Lett.* , DOI:10.1063/1.4819768.
6. A. Ray, T. Maitra, *J. Phys. Condens. Matter* (2015), 27, 105501.
7. A. Morales-Sánchez, F. Fernández, R. Sáez-Puche, *J. Alloys Compd.* (1993), 201, 161.
8. E. Jimenez, J. Isasi, *J. Alloys Compd.* (2000), 312, 53.
9. E. Jiménez, J. Isasi, R. Sáez-Puche, *J. Solid State Chem.* (2002), 164, 313.
10. S. G. Manca, E. J. Baran, *J. Appl. Crystallogr.* (1982), 15, 102.
11. Y. Aoki, H. Konno, H. Tachikawa, M. Inagaki, *Bull. Chem. Soc. Jpn.*, (2000), 73, 1197–1203.
12. H. Konno, H. Tachikawa, A. Furusaki, R. Furuichi, *Anal. Sci.* **1992**; VOL. 8.
13. S. G. Manca, E. J. Baran, *J. Phys. Chem. Solids* (1981), 42, 923.
14. N. Clavier, R. Podor, N. Dacheux, *J. Eur. Ceram. Soc.* (2011), 31, 941.
15. D. Errandonea, *Phys. Status Solidi Basic Res.* , DOI:10.1002/pssb.201700016.
16. E. Jiménez-Melero, P. C. M. Gubbens, M. P. Steenvoorden, S. Sakarya, A. Goosens, P. D. De Réotier, A. Yaouanc, J. Rodríguez-Carvajal, B. Beuneu, J. Isasi, R. Sáez-Puche, U. Zimmermann, J. L. Martínez, *J. Phys. Condens. Matter* (2006), 18, 7893.
17. E. Climent-Pascual, J. Romero de Paz, J. M. Gallardo-Amores, R. Sáez-Puche, *Solid State Sci.* (2007), 9, 574.
18. K. Tezuka, Y. Hinatsu, *J. Solid State Chem.* (2001), 160, 362.
19. C. C. Santos, E. N. Silva, A. P. Ayala, I. Guedes, P. S. Pizani, C. K. Loong, L. A. Boatner, *J. Appl. Phys.* , DOI:10.1063/1.2437676.
20. G. M. Begun, G. W. Beall, L. A. Boatner, W. J. Gregor, *J. Raman Spectrosc.* (1981), 11, 273.

-
21. Y. W. Long, L. X. Yang, Y. Yu, F. Y. Li, Y. X. Lu, R. C. Yu, Y. L. Liu, C. Q. Jin, *J. Appl. Phys.* , DOI:10.1063/1.2909202.
 22. E. Palacios, C. Tomasi, R. Sáez-Puche, A. J. Dos Santos-García, F. Fernández-Martínez, R. Burriel, *Phys. Rev. B* (2016), *93*, 1.
 23. Q. Y. Dong, Y. Ma, Y. J. Ke, X. Q. Zhang, L. C. Wang, B. G. Shen, J. R. Sun, Z. H. Cheng, *Mater. Lett.* (2015), *161*, 669.
 24. S. Ughade, B. Joshi, P. Poddar, *Ceram. Int.* (2022), DOI:10.1016/j.ceramint.2022.05.113.
 25. P. Barpanda, N. Recham, J. N. Chotard, K. Djellab, W. Walker, M. Armand, J. M. Tarascon, *J. Mater. Chem.* (2010), *20*, 1659.
 26. M. Ginting, S. Taslima, K. Sebayang, D. Aryanto, T. Sudiro, P. Sebayang, *AIP Conf. Proc.* , DOI:10.1063/1.4991166.
 27. X. Cheng, D. Guo, S. Feng, K. Yang, Y. Wang, Y. Ren, Y. Song, *Opt. Mater. (Amst.)*. (2015), *49*, 32.
 28. E. N. Silva, A. P. Ayala, I. Guedes, C. W. A. Paschoal, R. L. Moreira, C. K. Loong, L. A. Boatner, *Opt. Mater. (Amst.)*. (2006), *29*, 224.
 29. I. Guedes, Y. Hirano, M. Grimsditch, N. Wakabayashi, C. K. Loong, L. A. Boatner, *J. Appl. Phys.* (2001), *90*, 1843.
 30. Y. W. Long, L. X. Yang, Y. Yu, F. Y. Li, R. C. Yu, C. Q. Jin, *Phys. Rev. B - Condens. Matter Mater. Phys.* , DOI:10.1103/PhysRevB.75.104402.
 31. M. R. Moura, A. P. Ayala, I. Guedes, C. K. Loong, L. A. Boatner, *J. Appl. Phys.* (2004), *96*, 6344.

Chapter 4

Shape tuneable synthesis of perovskite DyCrO_3 at a low temperature by varying primary reaction conditions



Outline

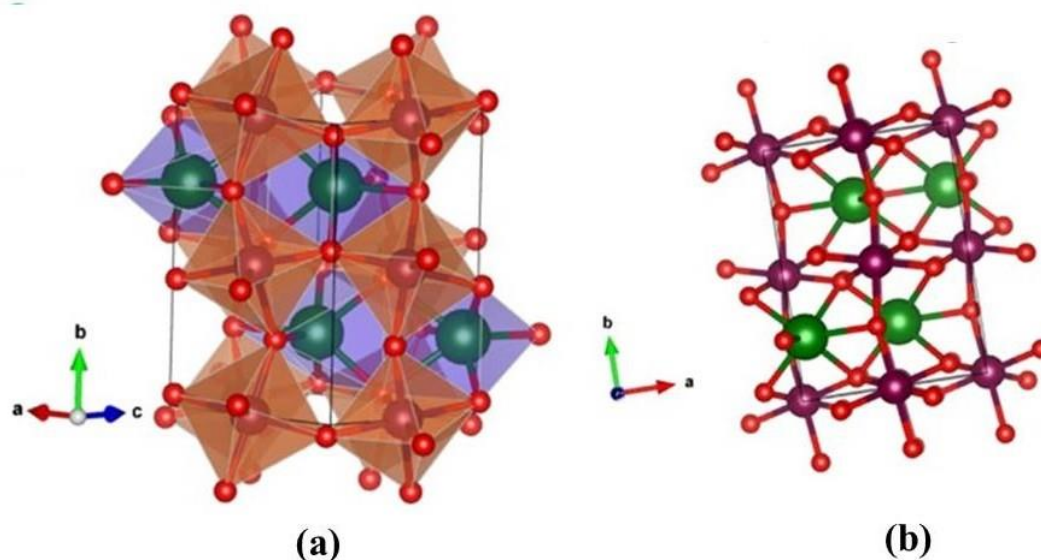
Rare-earth chromites (RCrO_3) with a perovskite structure are a fascinating class of materials widely used in many fields. Various methods have produced this family of materials; however, most of them only produce polycrystalline ceramics and need high-temperature crystallization processes exceeding $800\text{ }^\circ\text{C}$. Herein, uniformly sized perovskite DyCrO_3 was produced for 7 days of crystal growth duration at low temperatures (as low as $280\text{ }^\circ\text{C}$) using a mild hydrothermal method. The synthesis parameters, such as the amount of KOH, crystal growth duration, reaction temperature, precursor change, and effect of surfactant, were extensively investigated. The XRD pattern reveals the orthorhombic single-phase DyCrO_3 for the ideal reaction condition observed and stated in this work. The morphology of the DyCrO_3 was also studied for performed reaction conditions. The presence of surfactants like CTAB and PVA was investigated to examine the morphological alteration.

4.1 Introduction:

Orthorhombic perovskite rare-earth chromites (RCrO_3) have attracted a lot of interest in the fields of materials science, physics, and chemistry in recent years due to their electrical, magnetic, and structural properties.¹⁻⁵ Perovskite RCrO_3 is a class of *p-type* semiconductors that was employed as material of electronic sensing for ethanol and propylene¹ as well as catalytic agent in the methanol² and the hydrocarbon reaction oxidation⁶. LaCrO_3 sintered ceramics with A-site doping have minimal thermal expansion behavior, stability in reducing conditions, and good electrical conductivity. These properties make them ideal components in solid oxide fuel cells as interconnecting materials.³ Perovskite RCrO_3 is thought to be a new class of multiferroics and has been found to display ferroelectric (FE) and antiferromagnetic (AFM) properties at relatively low temperatures.⁷ This family is of great interest for future data storage applications because of the magnetoelectric coupling in between the rare-earth (R^{3+}) and chromium (Cr^{3+}) cations in theoretical prediction and the multiferroic properties derived from experimental observation.⁵ Due to their potential use as multifunctional materials, perovskite RCrO_3 compounds from the rare-earth family are currently piquing the interest of researchers. Evidently, perovskite RCrO_3 research is quite promising.⁸

In solid oxide fuel cells as an interconnecting material operating at intermediate temperatures, DyCrO_3 polycrystalline material can be coated over ferritic stainless steel. This coating dramatically reduces the stainless steel's oxidation rate.⁹ New magnetic and dielectric transitions have reportedly been observed in the DyCrO_3 and HoCrO_3 .¹⁰ According to studies of their dielectric and pyroelectric characteristics, two chromites shows FE.¹¹ In our group previously, Gupta et al. discovered that the surface chemistry as well as morphology could alter dynamic and static magnetic behavior while synthesizing DyCrO_3 using a hydrolytic sol-gel technique based on citric acid and oxalic acid.¹² At the magnetic ordering transition temperature, the high magnetic moments of Dy^{3+} cation (10.63 μB) cause their oxides to exhibit

a significant magnetocaloric effect (MCE), which could be advantageous for magnetic refrigeration. This finding implies that the strong magnetic moments of Dy^{3+} could enhance coupling between magnetic-ferroelectric via exchange interactions ($4f-3d$) as well as lattice distortions brought on by variation of cation size.¹³ Orthorhombic perovskite DyCrO_3 's crystal structure is depicted in **Scheme 4.1(a)** and **(b)**. With the help of CIF-COD ID: 1008154, the DyCrO_3 structure was created using the VESTA software (version 3.1.0). In DyCrO_3 , the Cr ion is octahedrally associated with six O ions, while two Cr cations, four Dy cations, and 12 O anions work together to coordinate the O anions. The standard description of the perovskite structure is a 3D cubic lattice of corner-sharing CrO_6 octahedra.¹⁴



Scheme 4.1: Crystal structure of orthorhombic perovskite DyCrO_3 plotted using VESTA software (3.1.0 version) using CIF – COD ID: 1008154. (a) The basic unit of the perovskite structure is the CrO_6 octahedra (the Cr atom is situated at the center of an orange octahedron). (b) The green, magenta, and red spheres represented Dy, Cr, and O atoms.

It is typically possible to tailor magnetic & multiferroic properties in RCrO_3 by doping into the crystal lattice $\text{Fe}^{3+}(3d^5)$ and $\text{Mn}^{3+}(3d^4)$, because of the before unheard-of $\text{Fe}^{3+}/\text{Mn}^{3+}$ -O- Cr^{3+} linkages which are partially ordered in novel mixed lattice. This will increase number of

ferromagnetic (FM) exchange interactions of additional spins as well as the lattice distortion.^{15, 16, 17, 18} The CrO_6 octahedral tilting degree, which significantly impacts magnetic as well as polarisation behaviors, is affected by the order and size of the A-site atoms in $RCrO_3$ and hence determines the crystal lattice distortion.^{19, 20} By using a supercritical hydrothermal method, Walton et al.²¹ had already reported magnetic behavior of $La_xSm_{1-x}CrO_3$, having an A-site composition-dependence, which demonstrates a decrease in Neel's transition temperature (T_N) followed by a reduction in the average size of A-site cation with raising the Sm doping level.²¹ Many intriguing physical characteristics of $RCrO_3$ have been observed, including magnetization reversal, photoinduced magnetic transition in $ErCrO_3$ ²² and exchange bias in $TmCrO_3$ as well as $SmCrO_3$ ^{23, 24}. Also, magnetic-field as well as temperature-induced magnetization switching and exchange bias in $YbCrO_3$,^{25, 26} and bi-ferroic and $LuCrO_3$ magnetodielectric effects.^{27, 28} According to Bertaut notation, the magnetic structure of $RCrO_3$ typically exhibits three types of AFM configurations of G-type with Γ_1 ($A_x G_y C_z$), Γ_2 ($F_x C_y G_z$), & Γ_4 ($G_x A_y F_z$).²⁹

The main technique used to create $RCrO_3$ materials is the high-temperature solid-state method, which involves repeatedly grinding and sintering the material above 1000 °C.³⁰ There are potentially several other methods. However, many synthetic procedures rely on solution chemistry, including combustion route³¹, self-propagating synthesis³², sol-gel³³, Pechini method³⁴, gel casting process³⁵, and standard flux method for forming $RCrO_3$ single crystals.³⁶ The preparation of the perovskite phase from the methods mentioned above required at least one high-temperature treatment step. Because of powder X-ray diffraction's low detection limit for a impurity phases in small portion, $RCrO_3$ materials made using these synthesis methods was prone to overoxidized phases forming near the sample surface.¹² Additionally, it is possible to synthesize $RCrO_3$ using a microwave-assisted technique, which requires 1300 °C for sintering to produce high-purity materials.³⁷ Nanostructures of $RCrO_3$ has been produced by a

hydrothermal procedure employing an ethylene glycol precursor that must be calcined at 800–1000 °C.³⁸ In $\text{PbF}_2\text{PbOB}_2\text{O}_3$ at synthesis temperature of 1240 °C for ten days duration with gradual rate of cooling (34 °C/h), YbCrO_3 single crystals was produced using the flux technique.³⁹ However, high-temperature/-pressure methods should be used to synthesize the majority of perovskite samples with tiny A-site ionic-sized elements. ScCrO_3 and InCrO_3 must be synthesized, for instance, with a pressure of up to 6 GPa and 1500 K temperature.⁴⁰

The hydrothermal process, on the other hand, is quite gentle. The hydrothermal process is also quick, easy, safe, and scalable, which can influence particle crystallization and offer control over the end product's structures and morphologies. The creation of functional solids with well-defined morphologies using the synthetic hydrothermal technique, a solution-based approach, involved a traditional nucleation-growth strategy in crystallization processes. RCrO_3 can crystallize under hydrothermal conditions with relatively lower reaction temperatures⁴¹. Yoshimura et al. produced LaCrO_3 crystals in 1982 using a hydrothermal technique at 400 °C.⁴² Ca-doped LaCrO_3 was created by Rivas Vazquez et al. (2004) at a temperature of around 400 °C.⁴³ LaCrO_3 was synthesized at temperature of 260 °C with heavy proportion of KOH in 1999, according to Zheng et al.⁴⁴. Walton et al. described a thorough procedure for crystallizing metal hydroxide precursors at temperatures between 320 °C and 380 °C to synthesize RCrO_3 hydrothermally. However, the crystallites produced with this approach aggregate.⁴⁵ They also showed that the hydrothermal method is superior to the high-temperature calcination method for creating a mixed A-site cations uniform distribution at an atomic-scale.⁴⁶ According to Xu et al.,⁴⁷ constant supercritical flow hydrothermally approach to produced LaCrO_3 nanoparticles can be used to fabricate this family of materials continuously. In a recent publication, hydrothermal preparation of mixed-metal hydroxides (amorphous) at reaction temperature 370 °C for growth duration 48 h was also required to synthesize a series of $\text{La}_{1-x}\text{Sm}_x\text{CrO}_3$ ($x = 0, 0.25, 0.5, 0.62, 0.75, 0.87, \text{ and } 1.0$).⁴⁸ Nevertheless,

Ref.45 states that two phases were involved in the hydrothermal synthesis of PrCrO_3 . PrCrO_3 was produced following the preparation of two amorphous hydroxides, $\text{Pr}(\text{OH})_3$ and $\text{Cr}(\text{OH})_3$, which underwent a hydrothermal reaction at high temperatures after getting washed and then dried for two days. Similar to this, Ref. 49 also required two steps to produce PrCrO_3 hydrothermally. Before crystallization, the amorphous PrCrO_3 was first synthesized under certain hydrothermal conditions. Then the product was obtained following annealing in an environment of N_2 at 400 °C. High temperatures and specialized high-temperature-resistant equipment were required for these procedures. In moderate hydrothermal conditions, it is more challenging to synthesize single crystals of perovskite chromite with smaller rare-earth occupied A-sites. As a result, even though many papers have focused on the creation and use of perovskite RCrO_3 , the primary synthetic method frequently entails a high-temperature process that results in polycrystalline products. It is crucial to develop a broad, moderate way to produce RCrO_3 with crystal size as well as shape uniformly for the applications related to single crystal orthochromites. The one-step hydrothermal approach has made complex oxides, including perovskites,⁵⁰ garnets,⁵¹ pyrochlores,⁵² and other valuable materials.⁵³

This study offers a low-temperature hydrothermal synthesis method for producing micro-sized single-phase perovskite DyCrO_3 , which is helpful for future research on chromites applications and low-temperature crystal growth. Herein, the critical points of the hydrothermal reactions, such as the addition of KOH amount, growth temperature, crystal growth duration, precursor change, and effect of surfactant addition, were intensively investigated. Also, the reaction addition route was reinvestigated in the present work. Further, the morphology change in the single-phase DyCrO_3 for different reaction conditions was thoroughly studied. Lastly, the room-temperature Raman spectra were analyzed for the single-phase DyCrO_3 .

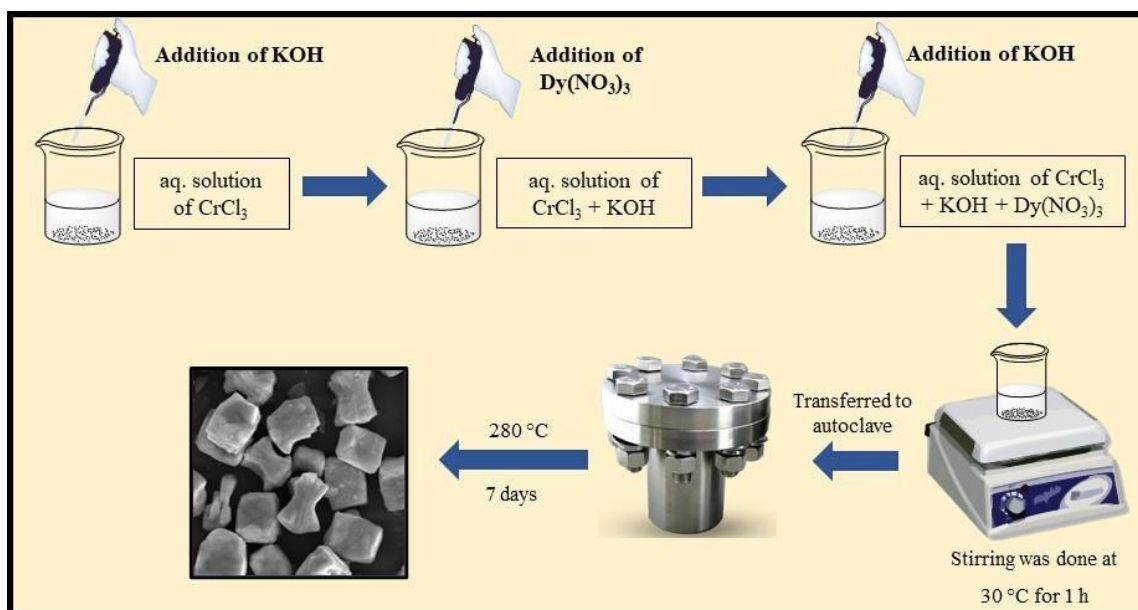
4.2 Experimental

4.2.1 Sample preparation

The single-phase orthorhombic perovskite DyCrO_3 were synthesized at low temperature hydrothermally. The starting materials of dysprosium (III) nitrate hydrate ($\text{Dy}(\text{NO}_3)_3 \cdot x\text{H}_2\text{O}$, Aldrich, 99.9% metal basis), chromium chloride hexahydrate ($\text{CrCl}_3 \cdot 6\text{H}_2\text{O}$, Aldrich, 98.0%), chromium nitrate ($\text{Cr}(\text{NO}_3)_3$, Aldrich, 99.9%), potassium hydroxide (KOH, Merck), Cetyl trimethyl ammonium bromide (CTAB, Aldrich), Polyvinyl alcohol (PVA, Thomas baker,) were used.

The reaction started with the dissolution of CrCl_3 in distilled water at room temperature with continuous stirring. Then 1.5 g to 2 g of KOH in the solid form was added to the stirring solution. Adding KOH made the solution viscous with a color change. Now, stir the solution for ~10 minutes so that heat gets released due to KOH dissolution and the reaction solution cools down to room temperature. The further reaction was going on by adding an aqueous solution of $\text{Dy}(\text{NO}_3)_3$ with continuous magnetic stirring. Again, wait for ~10 minutes before adding the second part of the KOH portion. Secondly, 0.25 g to 4g of KOH was added to the agitated solution to keep the mineralizer concentration high enough for the hydroxide mixture to dehydrate and crystallize into perovskites.⁵⁴ Then, the mixture was stirred for ~ 30 minutes to form a homogeneous solution. After that, the mixture was poured into a Teflon liner (in a stainless-steel autoclave) and transferred to the furnace. The reaction was carried out at a particular temperature and for days to get the single phase of the DyCrO_3 . Then the autoclave permits it to cool down naturally at room temperature. The obtained material was washed with distilled water several times and dried at 80 °C. As discussed, **Scheme 4.2** shows the reaction sequence followed in the hydrothermal synthesis of DyCrO_3 . The concentration of Dy: Cr was taken as 1:1. Further, various reaction conditions were studied to obtain the single-phase of DyCrO_3 as (i) with different KOH amounts in the two-step addition, (ii) with different reaction

temperatures, (iii) with different crystal growth duration, (iv) with two types of chromium precursors, and (v) with the addition of surfactants.



Scheme 4.2: Schematic showing the sequence of the addition of precursors in the reactions, temperature maintained during the reaction, and crystal growth duration.

4.2.2. Characterisation techniques

The single phase with the crystallinity of orthorhombic perovskite DyCrO₃ was confirmed using a PANalytical X'PERT PRO X-ray diffraction (XRD) instrument. The XRD instrument was equipped with the iron-filtered Cu K α radiation with a wavelength of 1.54 Å in the 2 θ range of 10°–80° with a step size of 0.013°. Raman spectra were recorded at room temperature from HR-800 Raman spectrophotometer made of Jobin Yvon-Horiba, France, having He-Ne laser of wavelength 633 nm, operated at 20 mW. The Raman instrument was equipped with a thermoelectrically cooled (with Peltier junctions), multi-channel, spectroscopic-grade CCD detector (1024×256 pixels of 26 microns). An objective of 50 XLD magnification was used to focus and collect the signal from the powder sample dispersed on a glass slide. Field Emission Scanning Electron Microscopy (FESEM: Hitachi S-4200) was performed to analyze the shape and size of the samples in different reaction conditions. The

morphology was characterized using an FEI Tecnai T20 transmission electron microscopy (TEM) equipped with a super twin lens (s-twin) operated at 200 keV accelerating voltage. The powders obtained were dispersed in ethanol and then drop-casted on a carbon-coated copper TEM grid with 200 mesh and loaded in a single-tilt sample holder.

4.3. Results and discussion

4.3.1. Reaction mechanism

Hydrothermal crystallization of orthorhombic perovskite DyCrO_3 involved two steps: (i) Mixed double metal hydroxide precursors were created in the first stage, and (ii) the second phase includes dehydrating the hydroxide precursor to initiate and advance crystal formation using a similar polymerization process.⁵⁴ The key factors to be taken into account while hydrothermally synthesizing perovskite rare earth chromites are the mineralizer's dehydration processes in the right concentration and regulated manner, temperature maintained during a reaction, and crystal development time. The reactant's addition followed a specific pattern to obtain a single-phase perovskite DyCrO_3 during the reaction, as shown in Scheme 4.2. The alteration in the sequence results in different products discussed in the coming section.

If the $\text{Dy}(\text{NO}_3)_3$ is added for the first time and then KOH, it leads to a precursor dehydration process forming $\text{DyO}(\text{OH})$ and $\text{Dy}(\text{OH})_3$. So, there will be no change in the precursor with further addition of CrCl_3 as it developed $\text{Cr}(\text{OH})_4$. If directly added the precursors $\text{Dy}(\text{NO}_3)_3$ and then CrCl_3 in a one step, $\text{Dy}(\text{OH})\text{-CrO}_4$ formed, which is difficult to form perovskite phase. So, considering amphoteric nature of Cr^{+3} , the KOH must be added in two steps in the reaction. KOH was added in the first step work for Cr^{+3} precipitation and in second step for nucleation of perovskite chromites by supplying enough concentration of mineralizer. The reaction was carried out with the different steps of adding KOH. KOH first step addition leads to the formation of only rare-earth hydroxide. In contrast, the last step addition of KOH was reported with the appearance of the rare-earth hydroxide crystallites

along with chromium-oxygen clusters. The proper concentration of KOH only provides the precipitation and nucleation of the perovskite phase. The different reaction conditions were studied by considering the critical point of the hydrothermal reaction as listed above. The results of these additional conditions were discussed as follows:

4.3.1.1 With identical KOH amounts but different reaction temperatures

The KOH amount in the reaction was taken as 2 g in the first step and 4 g in the second step, as mentioned in the published literature^{54, 55, 56}. The hydrothermal reaction temperature varied from 240 °C to 280 °C in an interval of 20 °C, with a crystal growth duration of 7 days for all temperatures. The recorded XRD graphs show the formation of Dy(OH)₃, which matches the JCPDS file no. [83-2039] of Dy(OH)₃, for all temperatures, as shown in **Figure 4.1**. So, the concluding remarks from overall reactions in this section offer that the KOH addition in the 2 g, and 4 g combination was not suitable for forming single-phase perovskite DyCrO₃. **Table 4.1** shows the phases observed for the given reaction conditions, and highlighted portion depicts the change in reaction temperature.

4.3.1.2 With different KOH amounts added in two steps during the reaction

The reactions were studied with the changing KOH amount to obtain the single-phase orthorhombic DyCrO₃. The amount of KOH gradually decreases in both steps compared to the reactions studied in the first section with the KOH combinations of 2 g + 4 g, by taking all other reaction parameters, i.e., reaction temperature, crystal growth duration, and used precursors, was constant. The first reaction started with a decrease in the KOH amount in the first step from 2 g to 1.5 g, and in the second step, from 4 g to 2 g, at 280 °C for 7 days reaction duration, which resulted in the formation of DyCrO₃ along with Dy(OH)₃ confirmed by the XRD graphs shown in **Figure 4.2**. Considering the DyCrO₃ appearance, the KOH amount in the first step was maintained at 1.5 g and altered in the second step by gradually decreasing it

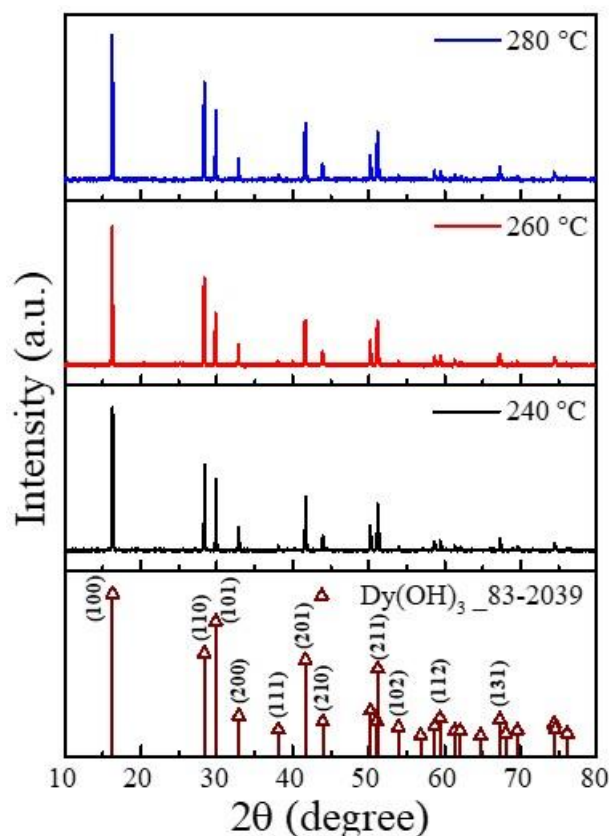


Figure 4.1: XRD patterns showing the graphs of synthesized materials with the KOH amount added of 2 g + 4 g in two steps for different reaction temperatures 240 °C, 260 °C, and 280 °C having the same crystal growth duration of 7 days. The recorded data matched the reported JCPDS file of $\text{Dy}(\text{OH})_3$ [File No. 83-2039].

KOH added during the reaction (g)	Reaction temperature (°C) ± 5 °C	Reaction duration (days)	Precursors used	Phase obtained
2 + 4	240	7	CrCl_3 , $\text{Dy}(\text{NO}_3)_3$	$\text{Dy}(\text{OH})_3$
2 + 4	260	7	CrCl_3 , $\text{Dy}(\text{NO}_3)_3$	$\text{Dy}(\text{OH})_3$
2 + 4	280	7	CrCl_3 , $\text{Dy}(\text{NO}_3)_3$	$\text{Dy}(\text{OH})_3$

Table 4.1: Tabulated reactions results at different temperatures 240 °C, 260 °C, and 280 °C for the KOH amount of 2 g + 4 g, with the same synthesis duration of 7 days. The highlighted column shows the change in the reaction temperature.

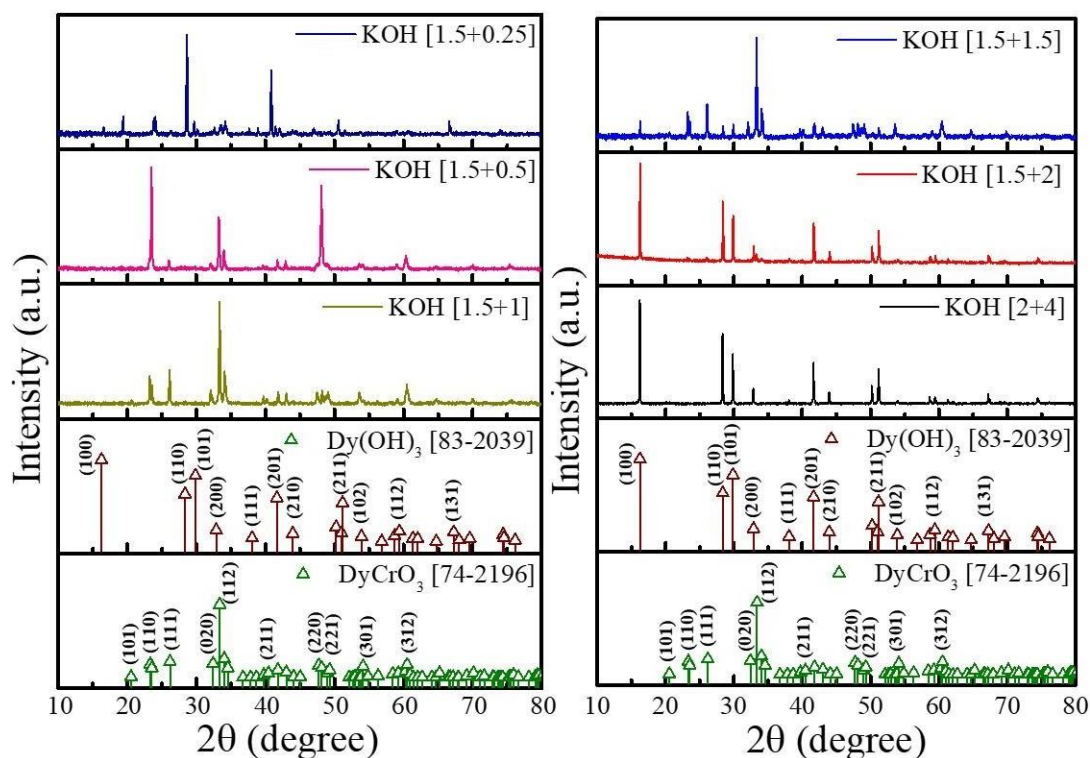


Figure 4.2: XRD patterns obtained for reactions conducted with change in adding KOH amount in both the steps for the reaction temperature 280 °C and crystal growth duration of 7 days. Only for KOH combinations of 1.5 g + 1 g and 1.5 g + 0.5 g, single phase DyCrO_3 was observed; otherwise, it resulted in DyCrO_3 along with Dy(OH)_3 or only Dy(OH)_3 . The phases obtained were matched with the reported JCPDS files of DyCrO_3 and Dy(OH)_3 of File nos. [74-2196] and [83-2039], respectively.

to 1.5 g, 1 g, 0.5 g, and 0.25 g. The phases obtained after these reactions were examined by XRD (Figure 4.2) as well as listed out in Table 4.2. The highlighted column in Table 4.2 depicts the gradual decrease in the KOH amount in the reaction. So, from the observed results, only KOH combinations of 1.5 g + 1 g and 1.5 g + 0.5 g gave a single-phase DyCrO_3 . Whereas for other KOH combinations, the reactions resulted in DyCrO_3 along with the impurity phase of Dy(OH)_3 . So, the correct KOH concentrations for crystallization of single-phase DyCrO_3 were concluded as 1.5 g in the first step and 1g or 0.5 g in the second step. The reaction

conditions in the upcoming sections were studied by considering the ideal KOH amount as 1.5 g + 1 g in the two-step addition.

KOH added during the reaction (g)	Reaction temperature (°C) \pm 5 °C	Reaction duration (days)	Precursors used	Phase obtained
2 + 4	280	7	CrCl ₃ , Dy(NO ₃) ₃	Dy(OH) ₃
1.5 + 2	280	7	CrCl ₃ , Dy(NO ₃) ₃	Dy(OH) ₃ + DyCrO ₃
1.5 + 1.5	280	7	CrCl ₃ , Dy(NO ₃) ₃	Dy(OH) ₃ + DyCrO ₃
1.5 + 1	280	7	CrCl ₃ , Dy(NO ₃) ₃	DyCrO ₃
1.5 + 0.5	280	7	CrCl ₃ , Dy(NO ₃) ₃	DyCrO ₃
1.5 + 0.25	280	7	CrCl ₃ , Dy(NO ₃) ₃	Dy(OH) ₃ + DyCrO ₃

Table 4.2: List of the phases observed from the reactions with decreasing KOH amount gradually from 2 g to 1.5 g in the first step and from 4 g to 2 g, 1.5 g, 1 g, 0.5 g, and 0.25 g in the second step with the other reaction parameters keeping constant. The highlighted portion in the table shows the change in the amount of KOH added during the reaction.

Further, the morphology of the single-phase DyCrO₃ was observed in the FESEM. The KOH combinations of 1.5 g + 1 g and 1.5 g + 0.5 g resulted in the same phase formation of perovskite DyCrO₃, but the morphology of both the reactions product was different.

The DyCrO₃ synthesized in KOH amount of 1.5 g in the first step and 1 g in the second step revealed the bone-like structure from the side perspective and rectangular shape particle from an upper standpoint (**Figure 4.3(a)**). The **Figure 4.3(a)** inset gives the zoomed-in view of a particle at 3 μ m scale. Considering the 30-particle calculation, the particle histogram was plotted, which gives an average particle size of almost \sim 3.6 μ m (**Figure 4.3(b)**). Further, the decrease in KOH amount for the second step from 1 g to 0.5 g, keeping the first step of 1.5 g constant, made a difference in the particle morphology.

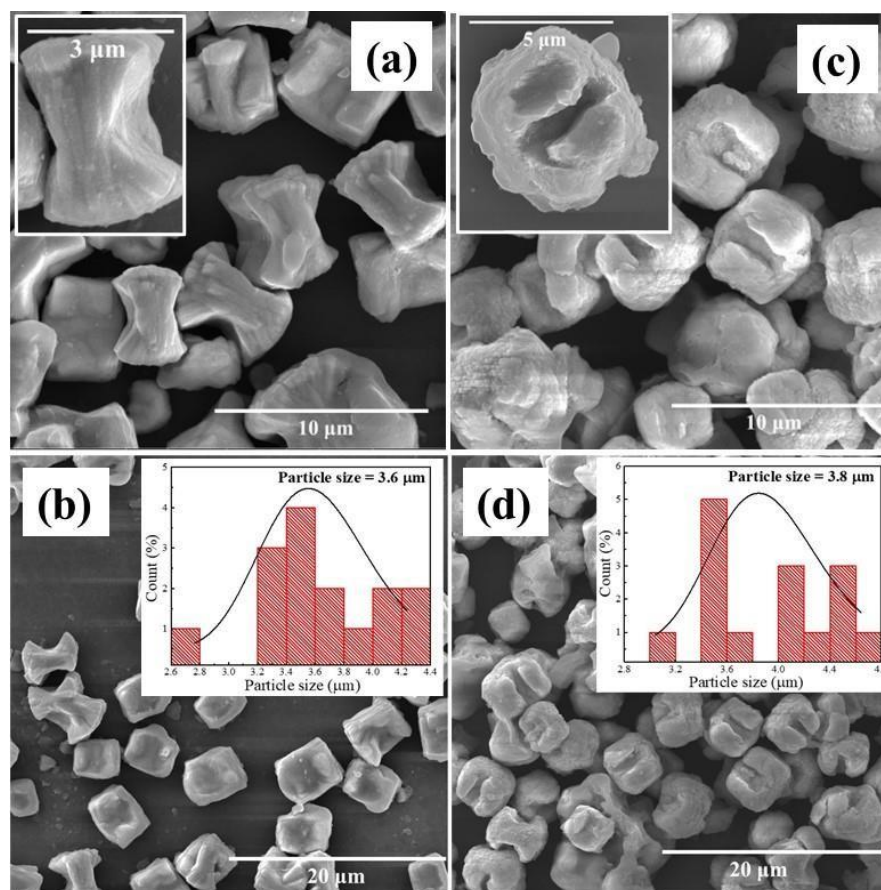


Figure 4.3: FESEM images showing the morphology of the synthesized single-phase DyCrO₃ with change in the addition of KOH amount, while other reaction parameters like reaction temperature (280 ° C) and reaction duration (7 days) keeping constant. Adding KOH amount in 1.5 g + 1 g shows (a) rectangular morphology from the upper perspective, inset: the single particle with 3 μm scale. (b) particle size histogram shows the average particle size of ~ 3.6 μm. While adding the KOH amount in 1.5 g + 0.5 g shows (c) round edges to the rectangular morphology with a mouth-like opening at the center on one side, the inset shows a zoomed-in view of a single particle in the scale of 5 μm. (d) the histogram shows the average particle size of ~ 3.8 μm.

The shape of the particle looks like round edges to the rectangular particle with a mouth opening on one side central part (**Figure 4.3(c)**). The single particle with a zoomed-in view is shown in **Figure 4.3(c) inset** with a measurement scale of 5 μm. However, the calculated

particle histogram for 30 particles gives an average particle size of nearly 3.8 μm for the synthesized single-phase DyCrO_3 (**Figure 4.3(d)**).

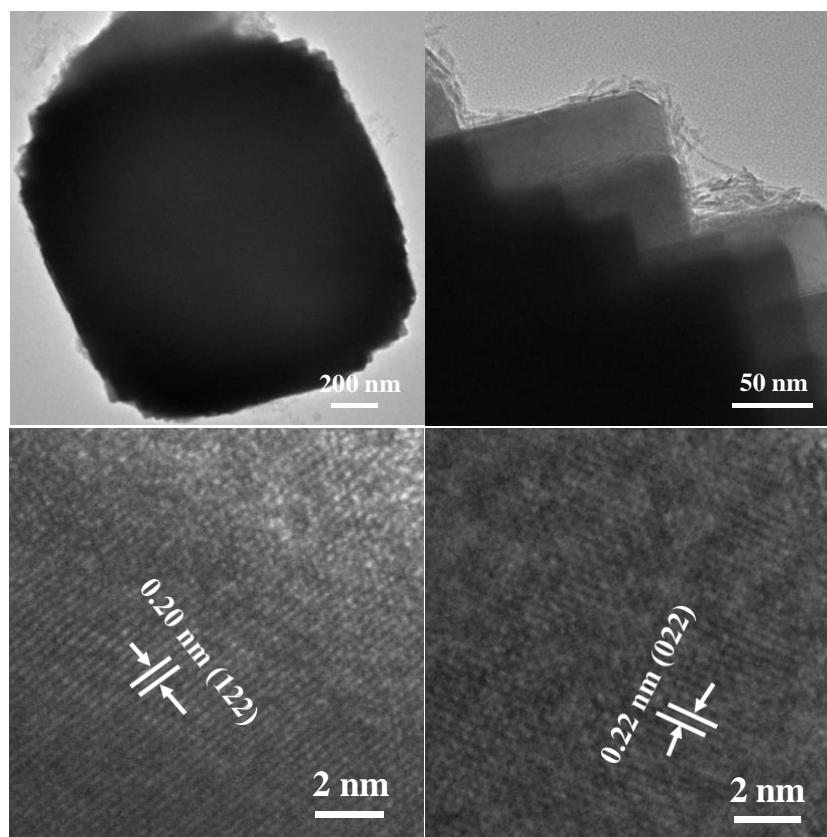


Figure 4.4: TEM images for the single-phase DyCrO_3 synthesized with the KOH amount of 1.5 g and 1 g in two-step addition, at 280 $^{\circ}\text{C}$ for 7 days, showing the rectangular morphology. The lattice fringes show the crystalline nature of the DyCrO_3 .

The single-phase DyCrO_3 , synthesized in the reaction condition containing KOH amount in 1.5 g + 1 g, at 280 $^{\circ}\text{C}$ for 7 days crystal growth duration, was again studied by TEM imaging to confirm the morphology. The images were recorded at 200 nm and 50 nm scales, as shown in **Figure 4.4**. The image recorded at 200 nm scale shows the rectangular shape morphology, but due to the crystal's thickness, which is significantly greater than 100 nm and makes it impossible for electrons to pass through the crystal, and hence in the center part shows an entirely black image. So, the image was recorded at 50 nm (zoomed-in view) and focused

on the edges of the rectangular morphology, which shows the steps. The steps from this image concluded that the rectangular particle of the single-phase DyCrO_3 . The d-spacing in the DyCrO_3 was measured with the Digital Micrograph software. The d-spacing for the single-phase DyCrO_3 is ~ 0.20 nm and ~ 0.22 nm corresponding to (122) and (022) planes, as shown in **Figure 4.4**.

4.3.1.3 With different crystal growth duration

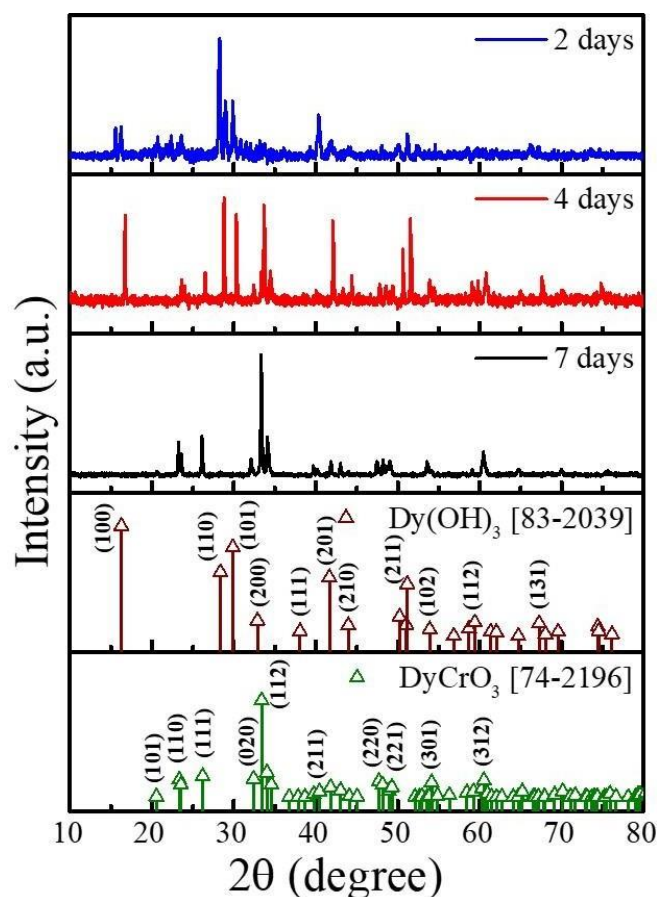


Figure 4.5: XRD patterns showing the phases obtained for different crystal growth durations by considering other parameters such as added KOH amount and reaction temperature constant and also matched with the reported JCPDS files of Dy(OH)_3 -[83-2039] and DyCrO_3 -[74-2196]. Only for 7 days, reactions resulted in single-phase DyCrO_3 ; otherwise, the formation of Dy(OH)_3 and impurity phases also occurred.

The third important point for hydrothermal synthesis was the duration of crystal growth. The results of the phase formation were investigated by altering crystal growth duration while keeping other parameters constant in the reactions. The time of the reactions varies for 7 days, 4 days, and 2 days by considering other reaction parameters stable as KOH amount 1.5 g in the first step and 1 g in the second step, at a reaction temperature of 280 °C. The recorded XRD patterns reveal the phases formed by changing the duration of crystal growth.

The single phase DyCrO₃ was obtained by keeping the reaction up to 7 days as confirmed by the XRD pattern shown in **Figure 4.5**. Less than that results in the developing Dy(OH)₃ and other impurities along with DyCrO₃. So, 7 days was the suitable crystal growth duration for forming single-phase DyCrO₃. Also, the results of the reaction are listed in **Table 4.4**.

KOH added during the reaction (g)	Reaction temperature (°C) ± 5 °C	Reaction duration (days)	Precursors used	Phase obtained
1.5 + 1	280	7	CrCl ₃ , Dy(NO ₃) ₃	DyCrO ₃
1.5 + 1	280	4	CrCl ₃ , Dy(NO ₃) ₃	Dy(OH) ₃ + DyCrO ₃
1.5 + 1	280	2	CrCl ₃ , Dy(NO ₃) ₃	Dy(OH) ₃ + DyCrO ₃ + impurity

Table 4.4: Lists of phases obtained for different reaction durations keeping other reaction parameters constant. The highlighted portion shows the change in the crystal growth duration in the table.

4.3.1.4 With different Chromium precursors

After investigating the basic conditions of the hydrothermal reactions, other parameters were also studied. The precursors may change the reaction morphology or phase crystallization temperatures; hence, the reaction was investigated with different chromium (Cr) precursors.

The two precursors of Chromium salts, i.e., CrCl_3 and $\text{Cr}(\text{NO}_3)_3$, were used to obtain the single-phase DyCrO_3 . The phases obtained with the different precursors were listed and shown in the XRD graphs. Both the Cr-precursors crystallized the single-phase DyCrO_3 at a reaction temperature of $280\text{ }^\circ\text{C}$ with the KOH concentration of $1.5\text{ g} + 1\text{ g}$ in two steps, confirmed by the XRD patterns shown in **Figure 4.6**, which was well matched with the reported JCPDS file no. [74-2196].

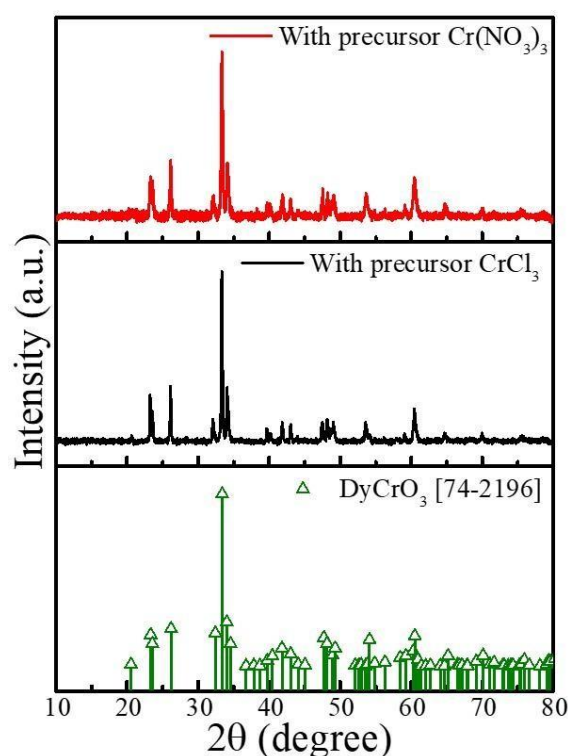


Figure 4.6: shows XRD graphs for single-phase DyCrO_3 with different chromium precursors in the reaction conditions matched with the JCPDS file no. [74-2196] correlated with the DyCrO_3 phase.

There was no difference in the crystallization of DyCrO_3 by differing the precursors. The morphology of the single-phase DyCrO_3 prepared using different Cr-precursors was further studied using FESEM. The CrCl_3 and $\text{Cr}(\text{NO}_3)_3$ precursors give the rectangular shape particles, as shown in **Figure 4.7(a) and (c)**. The morphology made with the CrCl_3 precursor was clean, but for $\text{Cr}(\text{NO}_3)_3$, particles did not show clean edges. The particle histogram shows

a larger average particle size of $\sim 3.8 \mu\text{m}$ for $\text{Cr}(\text{NO}_3)_3$ than for CrCl_3 ($\sim 3.6 \mu\text{m}$) (**Figure 4.7 (c) and (d)**). So, both Cr-precursors resulted in the same morphology with different particle sizes.

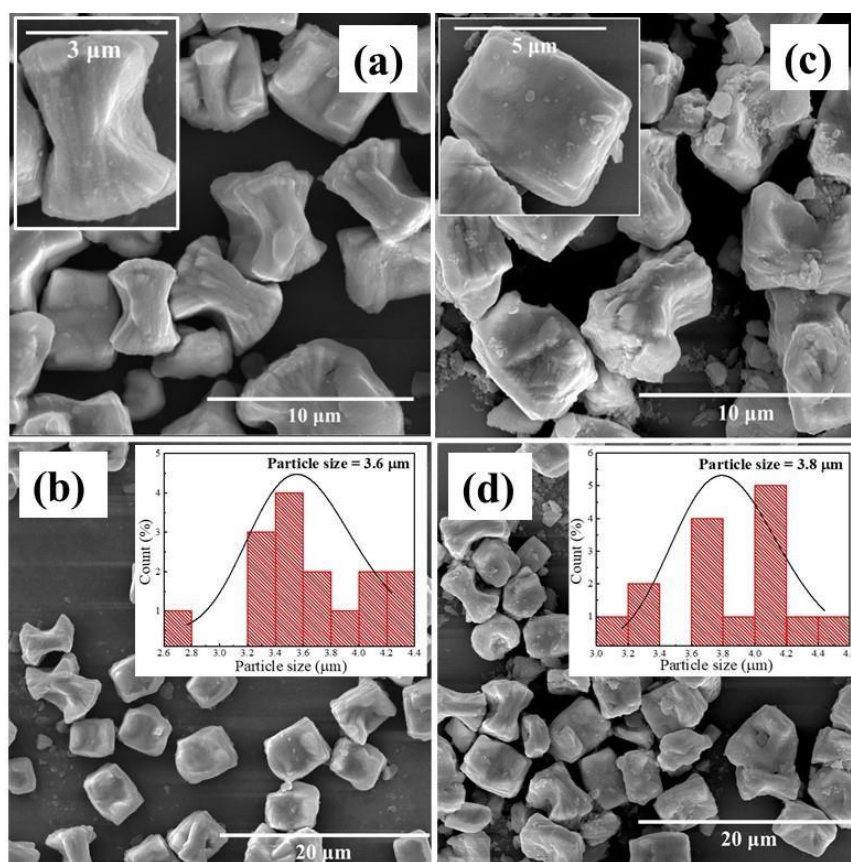


Figure 4.7: FESEM images showing rectangular particles for both the reactions in which (a) CrCl_3 and (b) $\text{Cr}(\text{NO}_3)_3$ were used as Cr-precursors at 280°C , for KOH amount of 1.5 g+ 1 g with 7 days duration. (c) and (d) show the histogram calculated for single-phase DyCrO_3 synthesized with CrCl_3 and $\text{Cr}(\text{NO}_3)_3$.

4.3.1.5 With the addition of surfactants CTAB and PVA

The hydrothermal synthesis of orthorhombic DyCrO_3 was further investigated using surfactants such as cetyltrimethylammonium bromide (CTAB) and Polyvinyl alcohol (PVA), as shown in **Figure 4.8**. The surfactant was added after the addition of the second step KOH (refer to **scheme 4.1**), stirred well to make a homogeneous solution, and transferred to the autoclave. The single-phase DyCrO_3 obtained in XRD patterns are shown in **Figure 4.9**.

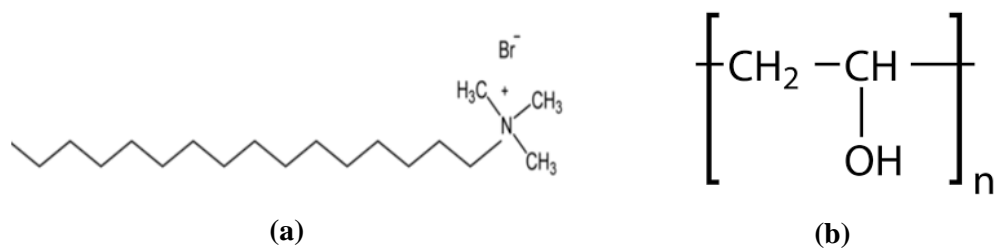


Figure 4.8: Surfactant used in the synthesis process of perovskite DyCrO_3 : (a) cetyltrimethylammonium bromide (CTAB) and (b) Polyvinyl alcohol (PVA).^{57, 58}

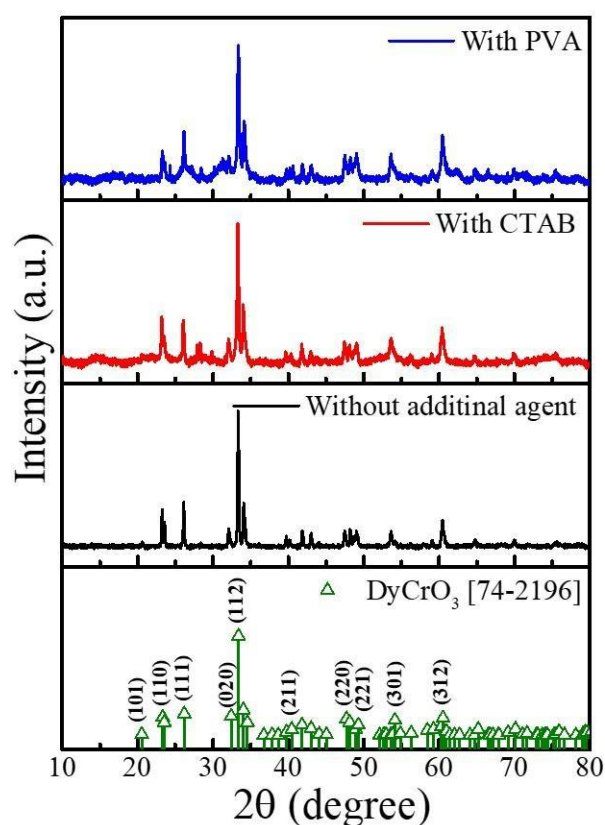


Figure 4.9: XRD patterns of the single phase DyCrO_3 obtained from the ideal reaction conditions of KOH amount 1.5 g + 1 g, at 280 °C for 7 days reaction duration using different surfactants such as CTAB and PVA and matched with the reported JCPDS File No. [74-2196].

So, with the surfactant, the DyCrO_3 phase formed in the ideal reaction condition of KOH amount 1.5 g + 1 g, at 280 °C for 7 days reaction duration as mentioned above. In the solution process, surfactants are frequently used to regulate the crystal structure, morphology, and

particle size¹⁹. Hence the reactions were further investigated using FESEM for the morphology change. Cationic surfactants include CTAB. CTAB will ionize into Br^- and CTA^+ when dissolved in ethanol or water. A lengthy hydrophobic tail and a tetrahedral head characterize CTA^+ , which is positively charged. At low surfactant concentrations, conventional surfactants, such as CTAB, often produce micelles with spherical shapes. **Figure 4.10(a)** illustrates CTAB aggregates into spherical micelles in an aqueous solution when its concentration is between 0.1 - 0.5 M. However, at high CTAB concentrations, CTAB aggregation in aqueous solutions produces rod-like micelles that act as soft templates.^{59, 60} In order to give particles stability and regulate their morphologies, CTAB has been an extensively utilized reagent.

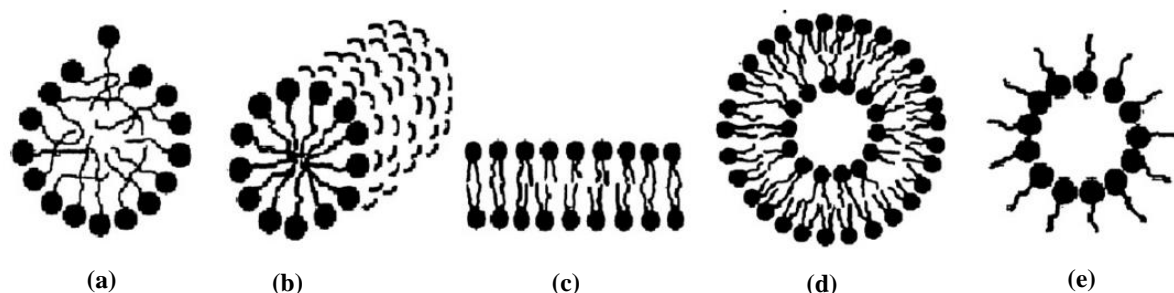


Figure 4.10: Typical aggregate morphology of CTAB in solution: (a) spherical micelle, (b) worm-like micelle, (c) bilayer phase, (d) vesicle, and (e) inverted micelle.⁵⁹

By more firmly or selectively adhering to different developing crystal facets, CTAB may retain particle size and form.⁶⁰ It was found from the CTAB-assisted hydrothermal process explained elsewhere, CTA^+ forms ion pairs with negatively charged hydroxides of Cr and Dy by electrostatic interaction. The CTAB could accelerate the ionization of these hydroxides as it was a strong-acid-weak base salt. And due to low concentration of CTAB it gives the spherical dumbbell shape to the particles as discussed in the FESEM image.

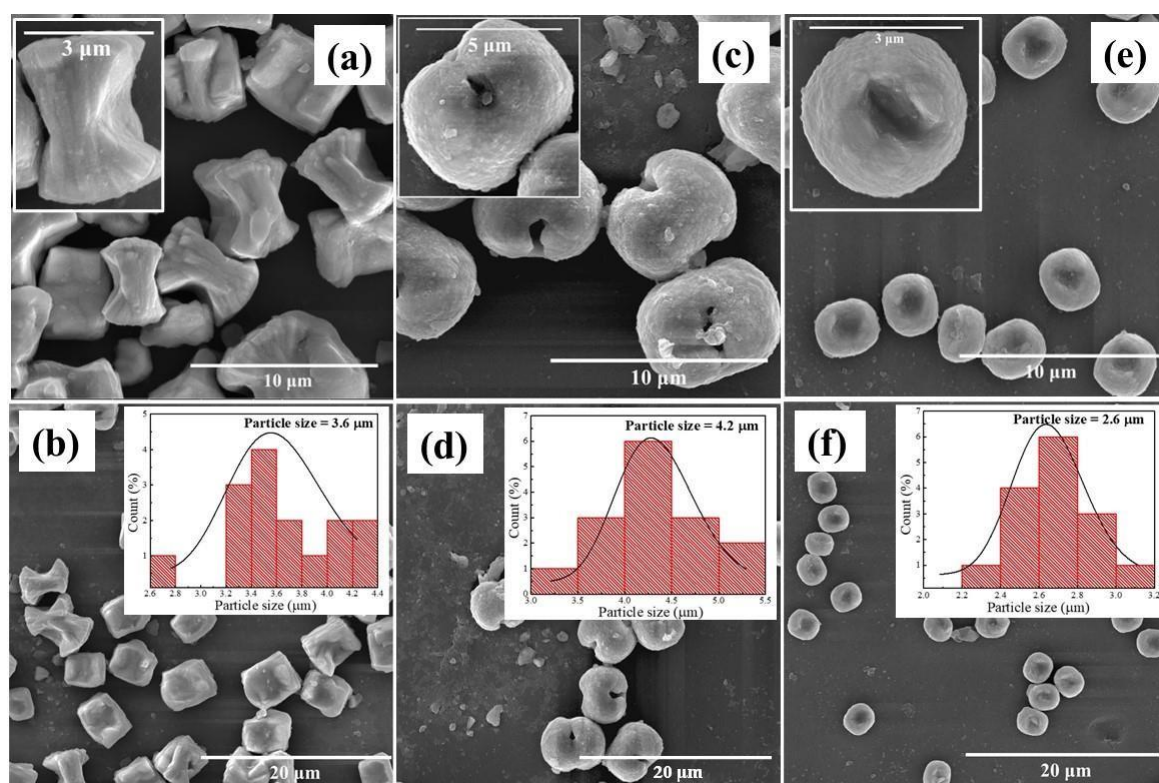


Figure 4.11: FESEM images recorded for synthesized single-phase DyCrO_3 in ideal reaction conditions of KOH amount 1.5 g + 1 g, at 280 °C for 7 days (a) without surfactant, (c) CTAB-assisted, and (e) PVA-assisted. Insets of (a), (c), (e) show the single particle morphology in the reactions. (b), (d) and (f) depict the histogram for DyCrO_3 without surfactant, with CTAB, and with PVA, respectively.

PVA was employed to scatter particles and regulate size throughout the hydrothermal synthesis. The distinctive structure of PVA allowed for the consistent distribution of nanoparticles throughout the chain. To prevent cation mobility, PVA offers a polymeric network, which preserves the local stoichiometry & reduces the precipitation of undesirable phases. As a result, the likely impurity phases are so uncommon that they do not fall inside the XRD detection accuracy limitations. Additionally, the PVA chains' hydroxyl groups can form hydrogen bonds with a variety of anions, increasing the metal salt's solubility in the PVA-containing solution. PVA is a polymer that acts as an emulsifying agent. It reduces the interfacial tension that exists between the organic and aqueous phases and contributes to the

formation of smaller spherical structure during the emulsification process. Moreover, PVA can form a film that surrounds droplets, avoiding coalescence during the evaporation of the organic solvent, thus preventing aggregation of the formed NPs.^{61, 62, 63, 64}

The FESEM images in **Figure 4.11(a)**, **(c)**, and **(e)** depict the morphology of the synthesized DyCrO_3 without surfactant, with CTAB, and with PVA, respectively. The reactions with the ideal conditions of KOH amount 1.5 g + 1 g, at 280 °C for 7 days, without surfactant, give the rectangular morphology. The Inset of **Figure 4.11(a)** shows the single particle morphology at the measurement scale of 3 μm . However, the morphology change occurred with surfactant CTAB and PVA, which was recorded in FESEM. The CTAB-assisted reaction gives the spherical morphology with the dumb-bell shape appearance. Here, in the reaction, the CTAB concentration used was 0.1 M, which comes under the low concentration category, giving spherical micelles structure as shown in **Figure 4.10(a)**. The single particle morphology can be seen in **Figure 4.11(c)** inset, which was recorded at 5 μm scale.

The PVA-assisted reaction shows smaller particles with an oval shape (**Figure 4.11(e)**). The Inset of **Figure 4.11(e)** shows the single particle morphology at the measurement scale of 3 μm . The average particle size histogram for the single-phase DyCrO_3 was calculated by considering 30 particles shown in **Figures 4.11(b)**, **(d)**, and **(f)** for reactions without surfactant, CTAB-assisted, and PVA-assisted, respectively. So, the average particle sizes for reaction with ideal conditions without surfactant, CTAB-assisted, and PVA-assisted gives $\sim 3.6 \mu\text{m}$, $\sim 4.2 \mu\text{m}$, and $\sim 2.6 \mu\text{m}$, respectively. The PVA-assisted morphology gives the smaller particle size. It appears that the presence of surfactant lowers the solution's surface tension, reducing the energy required to produce a phase.^{64, 65}

Figure 4.12(a)-(f) shows the TEM images for the prepared DyCrO_3 samples. The photos appear dark as the electron beam cannot pass through the sample due to more thickness

than 100 nm. The particle shape can be seen in **Figure 4.12(a)**, **(c)**, and **(e)** for the prepared DyCrO₃ particle in ideal conditions of KOH amount 1.5 g + 1 g, at 280 °C for 7 days without surfactant, CTAB-assisted, and PVA-assisted, respectively. In **Figure 4.12(b)**, the particle edges are readily visible, which shows 2D sheets layered on each other. **Figures 4.12 (d)** and **(f)** show the round edges for the CTAB-assisted and PVA-assisted single-phase DyCrO₃.

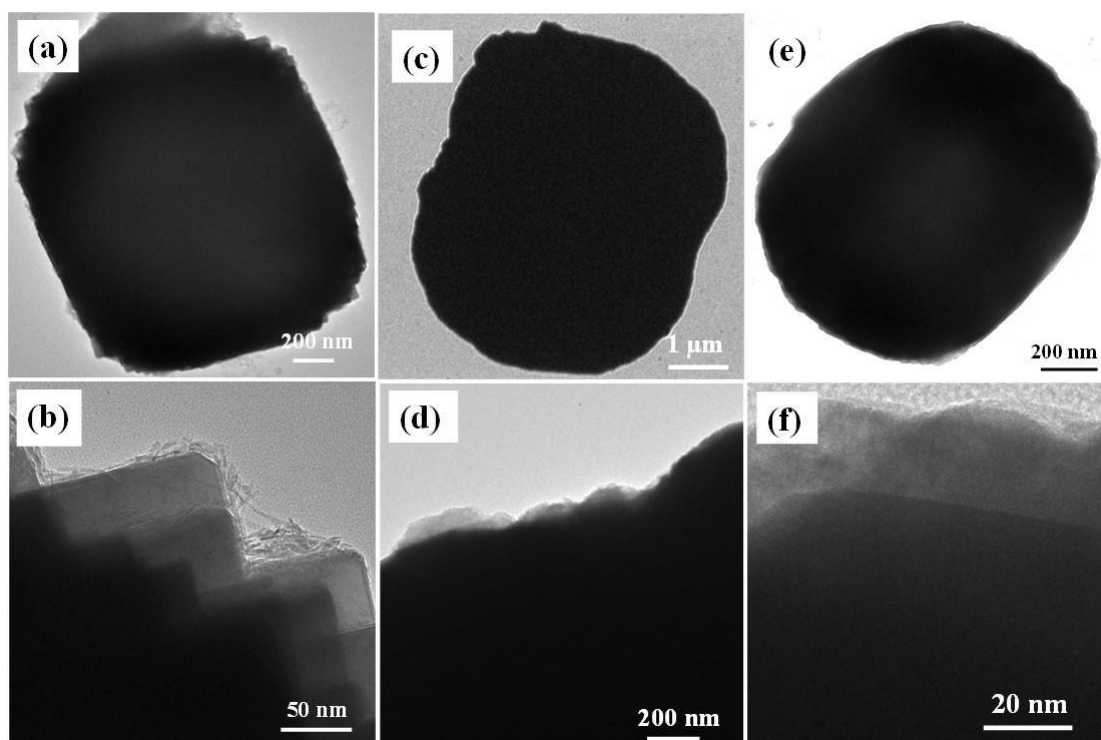


Figure 4.12: TEM images recorded for synthesized single-phase DyCrO₃ in ideal reaction condition of KOH amount 1.5 g + 1 g, at 280 °C for 7 days: (a)-(b) without surfactant, (c)-(d) CTAB-assisted, and (e)-(f) PVA-assisted.

From the overall studied reaction conditions, we got the single-phase perovskite DyCrO₃ for the five conditions shown in **Figure 4.13**. The refinement of the XRD graphs also shows the single phase of DyCrO₃ obtained in studied conditions.

Further, the crystallite size (d) for the single-phase orthorhombic perovskite DyCrO₃ was calculated using the Debye-Scherrer equation (1) for the highest intensity (112) plane tabulated in **Table 4.5**. The formula and procedure used to determine the crystallite size across the hkl plane is discussed in the chapter 2 thoroughly.

The larger crystallite sizes were observed in the sample prepared with ideal reaction conditions with KOH of 1.5 g + 1 g. However, the decrease in the KOH amount in the second step from 1g to 0.5 g also decreases the crystallite size of the DyCrO₃ particle. Comparing precursors for single-phase DyCrO₃ prepared with Cr(NO₃)₃, the calculated particle size was smaller than the sample prepared using CrCl₃. Again, surfactant plays an essential role in the crystallite size change. The reactions without surfactant have larger crystallite sizes.

While with a surfactant, the crystallite size decreases. But, on comparing CTAB-assisted and PVA-assisted DyCrO₃, PVA-assisted synthesized particles have larger crystallite size as compared to CTAB-assisted because PVA addition may be associated with the metal salt's improved solubility in PVA solution as a result of hydrogen bonding between anions

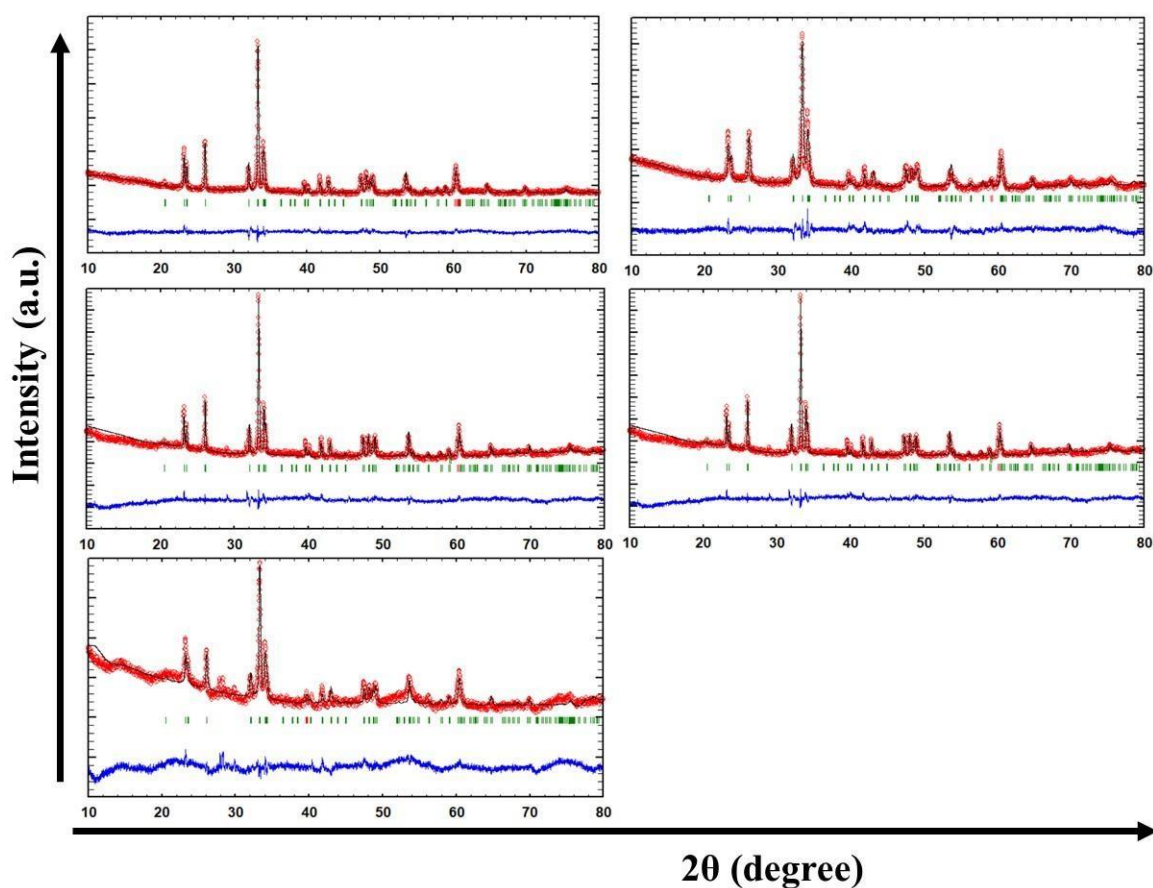


Figure 4.13: XRD refinement data for the reaction conditions. The observed and calculated peaks are denoted in red marks and solid lines (black), respectively. The vertical lines in the middle (green color) show Bragg reflection positions. The line in the blue color in the lower part of the graph reveals the difference in the calculated and observed intensities.

inside the sol⁶⁴, which quickens the reaction's kinetics. As a result, the crystals grow during the hydrothermal treatment for a longer period of time because they form at relatively short hydrothermal treatment durations.

DyCrO ₃ with a different condition	Crystallite size along (112) plane (nm)
KOH-1.5+1; 7days, 280 °C; CrCl ₃	96 ± 10
KOH-1.5+0.5; 7days, 280 °C; CrCl ₃	36 ± 3
KOH-1.5+1; 7days, 280 °C; Cr(NO ₃) ₃	46 ± 3
KOH-1.5+1; 7days, 280 °C; CrCl ₃ ; CTAB	36 ± 3
KOH-1.5+1; 7days, 280 °C; CrCl ₃ ; PVA	46 ± 3

Table 4.5: Tabulated crystallite size for the single-phase DyCrO₃ prepared in different reaction conditions.

4. 4 Raman Study of single phase DyCrO₃

Orthorhombic perovskite chromites theoretically exhibit 24 Raman active modes. Therefore, the active Raman modes are 7 A_{1g}, 5 B_{3g}, 5 B_{1g}, and 7 B_{2g}. These modes were produced via structural distortion, which was identified in the Raman vibrational spectra as CrO₆ octahedral distortion in two orientations, A-site distortion and Jahn-teller distortion in the ideal perovskite position. Raman modes were categorized as follows: (i) symmetric modes, B_{1g} and A_g; (ii) antisymmetric octahedral stretching modes, 2 B_{2g}, and 2 B_{3g}; (iii) bending modes, A_g, B_{3g}, and 2 B_{2g}; (iv) tilt or rotation modes of octahedral, 2 A_g, 2 B_{2g}, B_{3g}, , B_{1g}; and (v) rare-

earth cation moment resulted in modes, 3 A_g , 3 B_{1g} , B_{2g} , B_{3g} . This space group contains the remaining 3 acoustic modes, along with 25 optical modes.^{54, 55, 56} However, all of the modes were not apparent in the samples created through experimental synthesis. The vibrational spectra for single-phase $DyCrO_3$ produced hydrothermally at 280 °C with 1.5 g + 1 g of KOH in two steps for 7 days are shown in **Figure 4.14** under ideal reaction conditions.

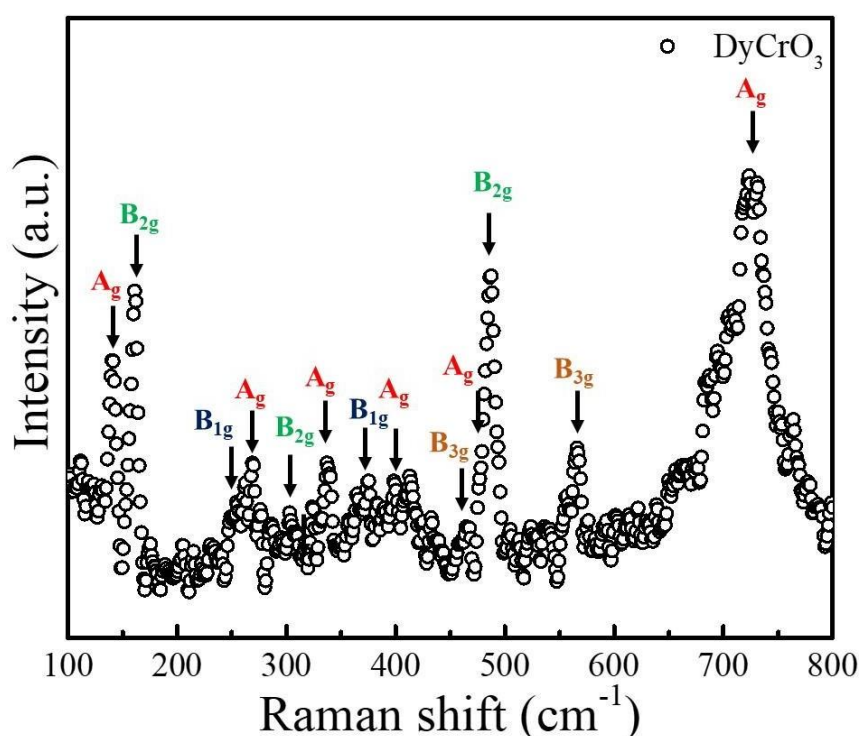


Figure 4.14. Room temperature Raman spectra of hydrothermally synthesized $DyCrO_3$ in ideal KOH 1.5 g in the first step and 1 g in the second step at 280 °C of crystal growth temperature in 7 days.

In an experiment, the hydrothermally synthesized $DyCrO_3$'s Raman spectra showed 13 modes in the ideal reaction conditions shown in **Table 4.6**, with the Raman frequencies and shown in **Figure 4.14**. The Raman spectra's scattered spots reveal the precise location of the modes in the material. The vibration of Dy^{3+} ions is connected to the bands A_g and B_{2g} , at 141 cm^{-1} and 161 cm^{-1} , respectively. Peaks of B_{1g} at 375 cm^{-1} were associated with an A-site (Dy^{3+}) and O1 z -direction mode of reverse motion. Additionally, A_g (403 cm^{-1}) and B_{2g} (303 cm^{-1}) are

relevant modes for the synergetic motion of Dy^{3+} and O1. A_g , A_g , and B_{2g} , which are positioned at 473, 724, and 487 cm^{-1} , respectively, are three modes that emerge from the motion of CrO_6 and are related to out-of-phase x rotations, bendings, and bendings of CrO_6 . Mode A_g , which is positioned at 403 cm^{-1} , is activated by the synergistic interaction of Jahn–Teller distortion and rotation along [010], which causes CrO_6 in-phase y rotations. Along with this mode inconsistency with the A-site rare-earth cations, there is an unidentified mode discrepancy.^{54, 55, 56}

Raman Frequency (cm^{-1})	Raman modes
141	A_g
161	B_{2g}
255	B_{1g}
270	A_g
303	B_{2g}
337	A_g
375	B_{1g}
403	A_g
464	B_{3g}
473	A_g
487	B_{2g}
566	B_{3g}
724	A_g

Table 4.6: Raman modes with the assigned frequencies were listed in the table.

4.5 Conclusion

In conclusion, using a hydrothermal technique at a temperature as lower as $280\text{ }^\circ\text{C}$, we have effectively synthesised homogenous single-phase $DyCrO_3$ in micrometer-sized particles. We compared the primary reaction conditions to investigate the synthesis limitations of $DyCrO_3$ such as KOH amount, reaction temperature, crystal growth duration, surfactants effect, precursor change, and reactant addition routes. The synthesized $DyCrO_3$ shows higher crystallinity and homogeneous particle size. KOH and surfactant play essential roles in the formation of different morphology of the products. Rectangular morphology

comprises 2D sheets stacked on each other with the KOH amount of 1.5 g + 1 g at 280 °C for 7 days (called ideal reaction condition).

In contrast, rectangular particles with round edges have mouth-like openings at the center form with the change in ideal reaction condition only at the amount of KOH, i.e., 1.5 g + 0.5 g. During hydrothermal synthesis, no perovskite phase might be produced below 280 °C and for 7 days. With carefully monitored mineralizer concentrations in every step and a crystallisation temperature of 280 °C, single-phase DyCrO₃ could be produced. The primary impurity for reactions occurring at low temperatures was Dy(OH)₃. The CTAB-assisted and PVA-assisted reactions show the dumbbell shape and oval shape morphology for the synthesized DyCrO₃ phase. The synthetic method described here demonstrated the lower temperature reaction with different shapes for preparing perovskite DyCrO₃. Raman spectra recorded at room temperature show characteristic vibration states of Dy³⁺ local structure and CrO₆ clusters. Our research provides a simple method for producing high-quality rare-earth chromite single - crystalline at low temperatures, that might also supply single crystals for numerous commercial and technical uses.

4.5 References

1. M. Siemons and U. Simon, *Sens. Actuators B.* (2007), 126, 181–186.
2. T. Arakawa, S. Tsuchi-ya and J. Shiokawa, *Mater. Res. Bull.* (1981), 16, 97–103.
3. (a) J. W. Fergus, *Solid State Ionics* (2004), 171, 1–15; (b) A. Atkinson, S. Barnett, R. J. Gorte, J. T. S. Irvine, A. J. Mcevoy, M. Mogensen, S. C. Singhal and J. Vohs, *Nat. Mater.*, (2004), 3, 17–27.
4. J. Suntivich, H. A. Gasteiger, N. Yabuuchi, H. Nakanishi, J. B. Goodenough and Y. Shao-Horn, *Nat. Chem.* (2011), 3, 546–550.
5. (a) J. R. Sahu, C. R. Serrao, N. Ray, U. V. Waghmare and C. N. R. Rao, *J. Mater. Chem.* (2007), 17, 42–44; (b) R. Saha, A. Sundaresan and C. N. R. Rao, *Mater. Horiz.* (2014), 1,

20–31.

6. J. Beckers, G. Rothenberg, “Hot spot” hydrocarbon oxidation catalysed by doped perovskites – towards cleaner diesel powers, *ChemPhysChem* (2005), 6, 223–225.
7. S. Rana, A. Sundaresan and C. N. R. Rao, *Mater. Horiz.* (2014), 1, 20–31.
8. K. Sardar, M.R. Lees, R.J. Kashtiban, J. Sloan, R.I. Walton, Direct hydrothermal synthesis and physical properties of rare-earth and yttrium orthochromite perovskites, *Chem. Mater.* (2011), 23, 48–56.
9. Z. J. Feng, Y. X. Xu and C. L. Zeng, *J. Power Sources* (2013), 235, 54–61.
10. G. V. Subba Rao, B. M. Wanklyn and C. N. R. Rao, *J. Phys. Chem. Solids* (1971), 32, 345–358.
11. H. B. Lal, R. D. Dwivedi and K. Gaur, *J. Mater. Sci.: Mater. Electron.* (1996), 7, 35–38.
12. P. Gupta, R. Bhargava, R. Das and P. Poddar, *RSC Adv.* (2013), 3, 26427–26432.
13. A. McDannald, L. Kuna and M. Jain, *J. Appl. Phys.* (2013), 114, 113904.
14. Aleksandrov, K. S.; Bartolome, *J. Phase Transitions* (2006), 74, 255.
15. Yuan, L.; Huang, K.; Hou, C.; Feng, W.; Wang, S.; Zhou, C.; Feng, S., *New J. Chem.* (2014), 38, 1168–1172.
16. Wang, S.; Wu, X.; Yuan, L.; Zhang, C.; Cui, X.; Lu, D., *CrystEngComm* (2018), 20, 3034–3042.
17. Qiao, Y.; Zhou, Y.; Wang, S.; Yuan, L.; Du, Y.; Lu, D.; Che, G.; Che, H., *Dalton Trans.* (2017), 46, 5930–5937.
18. Das, N., Singh, S., Joshi, A. G., Thirumal, M., Reddy, V. R., Gupta, L. C., Ganguli, A. K., *Inorg. Chem.* (2017), 56, 12712–12718.
19. Zhang, R., Abbett, B. M., Read, G., Lang, F., Lancaster, T., Tran, T. T., Halasyamani, P. S., Blundell, S. J., Benedek, N. A., Hayward, M. A., *Inorg. Chem.* (2016), 55, 8951–8960.
20. Yin, L. H., Yang, J., Tong, P., Luo, X., Park, C. B., Shin, K. W., Song, W. H., Dai, J. M., Kim, K. H., Zhu, X. B., Sun, Y. P., *J. Mater. Chem. C* (2016), 4, 11198–11204.

-
21. Daniels, L. M., Weber, M. C., Lees, M. R.; Guennou, M., Kashtiban, R. J., Sloan, J., Kreisel, J., Walton, R. I., *Inorg. Chem.* (2013), 52, 12161–12169.
 22. Kurita, S., Toyokawa, K., Tsushima, T., Sugano, S., *Solid State Commun.* (1981), 38, 235–239.
 23. Yoshii, K., *Mater. Res. Bull.* (2012), 47, 3243–3248.
 24. Wang, L., Rao, G. H., Zhang, X., Zhang, L. L., Wang, S. W., Yao, Q. R., *Ceram. Int.* (2016), 42, 10171–10174.
 25. Gupta, P., Poddar, P., *Inorg. Chem.* (2015), 54, 9509–9516.
 26. Wang, L., Wang, S. W., Zhang, X., Zhang, L. L., Yao, R., Rao, G. H., *J. Alloys Compd.* (2016), 662, 268–271.
 27. Duran, A., Meza, F. C.; Mora´n, E., Alario-Franco, M. A., Ostos,´ C., *Mater. Chem. Phys.* (2014), 143, 1222–1227.
 28. Preethi Meher, K. R. S., Wahl, A., Maignan, A., Martin, C., Lebedev, O. I., *Phys. Rev. B: Condens. Matter Mater. Phys.* (2014), 89, 144401.
 29. Bertaut, E. F., *Acta Crystallogr., Sect. A: Cryst. Phys., Diffr., Theor. Gen. Crystallogr.* (1968), A24, 217–231.
 30. Neumeier, J. J., Terashita, H., *Phys. Rev. B: Condens. Matter Mater. Phys.* (2004), 70, 214435.
 31. Manoharan, S. S., Patil, K. C., *J. Solid State Chem.* (1993), 102, 267–276.
 32. Kuznetsov, M. V., *Parkin, I. P, Polyhedron* (1998), 17, 4443–4450.
 33. Liu, X. M., Su, W. H., Lu, Z., *J. Phys. Chem. Solids* (2001), 62, 1919–1921.
 34. M. Mori and N. M. Sammes, *Solid State Ionics* (2002), 146, 301–312.
 35. S. P. Jiang, L. Zhang and Y. Zhang, *J. Mater. Chem.* (2007), 17, 2627–2635.
 36. B. M. Wanklyn, *J. Cryst. Growth* (1969), 5, 323–328.
 37. Prado-Gonjal, J., Schmidt, R., Romero, J.-J., Ávila, D., Amador, U., Moran, E., *Inorg. Chem.* (2013), 52, 313–320.
-

-
38. Lei, S., Liu, L., Wang, C., Wang, C., Guo, D., Zeng, S., Cheng, B., Xiao, Y., Zhou, L., *J. Mater. Chem. A* (2013), 1, 11982–11991.
 39. Kotru, P. N., Ā azdan, A. K., Wanklyn, B. M., *J. Mater. Sci.* (1989), 24, 2401–2407.
 40. Belik, A. A., Matsushita, Y., Tanaka, M., TakayamaMuromachi, E., *Chem. Mater.* (2012), 24, 2197–2203.
 41. Craig I. Hiley and Richard I. Walton, *CrystEngComm* (2016), 18, 7656-7670.
 42. M. Yoshimura, S.-tai Song and S. Somiya, *J. Ceram. Assoc. Jpn.* (1982), 90, 91–95.
 43. L. P. Rivas-Vazquez, J. C. Rendon-Angeles, J. L. Rodriguez Galicia, K. Zhu and K. J. Yanagisawa, *Solid State Ionics* (2004), 172, 389–392.
 44. W. Zheng, W. Pang, G. Meng and D. Peng, *J. Mater. Chem.* (1999), 9, 2833–2836.
 45. K. Sardar, M. R. Lees, R. J. Kashtiban, J. Sloan and R. I. Walton, *Chem. Mater.* (2011), 23, 48–56.
 46. Daniels, L. M.; Kashtiban, R. J.; Kepaptsoglou, D.; Ramasse, Q. M.; Sloan, J.; Walton, R. I, *Chem. - Eur. J.* (2016), 22, 18362–18367.
 47. Xu, Y.; Pirou, S.; Zielke, P.; Simonsen, S. B.; Norby, P.; Hendriksen, P. V.; Kiebach, R. *Ind. Eng. Chem. Res.* (2018), 57, 2123–2130.
 48. L. M. Daniels, M. C. Weber, M. R. Lees, M. Guennou, R. J. Kashtiban, J. Sloan, J. Kreisel and R. I. Walton, *Inorg. Chem.* (2013), 52, 12161–12169.
 49. S. Lei, L. Liu, C. Wang, C. Wang, D. Guo, S. Zeng, B. Cheng, Y. Xiao, L. Zhou, *J. Mater. Chem. A* (2013) 11982.
 50. Y. Chen, H. Yuan, Ge Tian, G. Zhang and S. Feng, *J. Solid State Chem.* (2007), 180, 167–172.
 51. 18 Li Guo, K. Huang, Y. Chen, G. Li, L. Yuan, W. Peng, H. Yuan and S. Feng, *J. Solid State Chem.* (2011), 184, 1048– 1053.
 52. Y. Mao, G. Li, W. Xu and S. Feng, *J. Mater. Chem.* (2000), 10, 479–482.
-

-
53. S. Feng and R. Xu, *Acc. Chem. Res.* (2001), 34(3), 239–247.
 54. Shan Wang, Xiaofeng Wu, Tiesheng Wang, Jiaqi Zhang, Chenyang Zhang, Long Yuan, Xiaoqiang Cui, and Dayong Lu, *Inorg. Chem.* (2019), 58, 2315–232.
 55. Shan Wang, Keke Huang, Changmin Hou, Long Yuan, Xiaofeng Wub and Dayong Lu, *Dalton Trans.* (2015), 44, 17201–17208.
 56. Shan Wang, Changmin Hou, Long Yuan, Mingyang Qu, Bo Zouc and Dayong Lu, *Dalton Trans.* (2016), 45, 17593–17597.
 57. https://en.wikipedia.org/wiki/Cetrimonium_bromide.
 58. https://en.wikipedia.org/wiki/Polyvinyl_alcohol.
 59. Yan-Xiang Wang, Jian Sun, XueYun Fan, Xi Yu, *Cer. Inter.* (2011), 37, 3431–3436.
 60. Sook Young Moon, Takafumi Kusunose, Tohru Sekino, *Materials Letters* (2009), 63, 2038–2040.
 61. N. Moumen, M.P. Pileni, *Chem. Mater.* (1996), 8, 1128–1134.
 62. Q. Shi, C. Jiang, Y. Wang, W. Yang, C. Yang, *Appl. Surf. Sci.* (2013), 273, 769–775.
 63. M. Jalalian, S. M. Mirkazemi, S. Alamolhoda, *J. Magn. Magn. Mater.* (2016), vol 419, 363–367.
 64. N. A.M. Barakat, S. J. Park, M. S. Khil, H. Y. Kim, *Mater. Sci. Eng. B* (2009), 162, 205–208.
 65. O. Yalçın, H. Bayrakdar, S. Özüm, *J. Magn. Magn. Mater.* (2013), 343, 157–162.

Chapter 5

Summary and Future Scope

Outline

This chapter summarised the research presented in the thesis and suggested potential areas for more study.

5.1 Summary of the thesis:

The R-Cr-O system has unique structural and physical features as a component of ternary metal oxides. We get the two significant structures, RCrO_3 and RCrO_4 , from the R-Cr-O combination. The R element involved in the phase determines the diverse crystal structures of RCrO_4 , including zircon-type and monazite-type structures. Due to different *R-O* and *Cr-O* distances, each phase has unique electric and magnetic characteristics in RCrO_4 . The unstable valence state of Cr, i.e., Cr^{5+} is also crucial in determining these features. As both of the sublattices, R and Cr, order at low temperatures, it is a perfect system for studying the *3d-4f* interaction and helps us to obtain the MCE effect at low temperatures.

The physical characteristics of the compounds were altered due to change in shape, size, and different chemical environments. The synthesis method used to produce a particular phase is also crucial during the investigation. Understanding the material's characteristics was simple because of the thorough knowledge of the formation mechanism used during the synthesis. Furthermore, the compounds' confirmed single phase gives credibility to the researched features. Choosing the proper synthesis technique is necessary for these. One can only regulate the pure compound by thoroughly understanding the material's formation process.

Chapter 1 covered the fundamental information regarding the various types of magnetism, its discovery, and its history. Even though the magnetism of metal elements was well established, the magnetic properties of compounds were a little more challenging to comprehend. The use of exchange interaction was attempted to explain the nature of magnetism in the various compounds. In-depth explanations of the multiple forms of exchange interaction were provided using examples. The conversation also covered the principles of other physical characteristics, including the ferroelectric and magnetocaloric effects. In this chapter, the RCrO_4 and RCrO_3 compounds are also discussed. The graphic illustrating the basic units was used to thoroughly explore the crystalline RCrO_4 structures such as tetragonal zircon-type,

monoclinic monazite-type, and tetragonal scheelite-type as well as orthorhombic perovskites RCrO_3 . This chapter described the phase transition in RCrO_4 compounds from zircon and monazite-type to scheelite-type under external pressure and from zircon and monazite-type to perovskites under external temperature. Additionally, a review of the published literature for RCrO_4 and RCrO_3 compounds were also included. The importance of R-Cr-O compounds in terms of their fundamental and technological implications is discussed in this chapter. The thesis' scope is the subject of the final discussion.

Our first experiment used a hydrolytic sol-gel synthesis to synthesize zircon-type DyCrO_4 discussed in **Chapter 2**. It was thoroughly explained how DyCrO_4 is synthesized in both acidic (using oxalic acid) and basic (using ammonium solution) media. According to TGA's findings, Cr_2O_3 and Dy_2O_3 are present in the sol-gel gelation step of the formation mechanism. The formation of nanocrystalline DyCrO_4 from Cr_2O_3 and Dy_2O_3 after sintering supports the benefit of sol-gel over solid-state reaction. When ammonia solution alone was used to create the gel, the DyCrO_4 phase crystallized at 500 °C and then changed to the DyCrO_3 phase at 800 °C. The gel that forms when oxalic acid alone and oxalic acid with a pH of 10 is combined crystallizes to DyCrO_4 at the same temperature of 500 °C. EDTA's acidic medium gel crystallized DyCrO_4 at 600 °C, but EDTA with a pH of 10 produces DyCrO_4 at 500 °C, which is lower than the acidic medium. At a sintering temperature of 500 °C, citric acid has crystalline DyCrO_4 and Cr_2O_3 as an impurity in both the acidic and the basic medium. For all complexing agents at higher sintering temperatures, the DyCrO_4 phase disintegrated into DyCrO_3 . It was observed that the DyCrO_4 crystallite size generated with oxalic acid and EDTA at pH 10 was ~ 55 nm. The morphology of the DyCrO_4 samples is hydrocathrus-like, as seen by TEM. Due to the differing environments of the complexing agents utilized in the acidic and basic media during the sol-gel synthesis, the valence state of the elements present in DyCrO_4 has distinct binding energies. The magnetic measurements of single-phase DyCrO_4 produced

by solid-state oxalic acid synthesis at pH 10 revealed ferromagnetic nature below the transition temperature of 21 K, which is lower than the bulk DyCrO₄ previously reported by that method. As a result, the nanocrystalline DyCrO₄ produced at a lower sintering temperature (500 °C) and for a shorter period of time (2 h) can be used for cryogenic applications such as hydrogen liquefaction due to its lower transition temperature of 21 K.

We continue our study on this in **Chapter 3** after learning more about the structures of RCrO₄ molecules. The hydrolytic sol-gel process created the whole series of compounds, RCrO₄ (R = La, Pr, Nd, Sm, Gd, Dy, Ho, Er, Tm, Yb), and YCrO₄. While LaCrO₄ formed as monazite-type, RCrO₄ (R = Nd, Sm, Gd, Dy, Ho, Er, Tm, Yb) and YCrO₄ crystallized as zircon-type. On the other hand, PrCrO₄ demonstrated the coexistence of both polymorphs, i.e., structures of the zircon-type and those of the monazite-type, at 600 °C. According to the results of the Raman analysis of zircon-type RCrO₄ compounds, the external Raman modes T(B_g) and T(E_g) shifted from Nd-Yb to a lower frequency. However, as the atomic radius reduced and the atomic number increased from Nd-Yb, R(E_g) and internal modes shifted to higher energies. Comparing DyCrO₄, LaCrO₄ (rare-earth), and YCrO₄ (non-rare earth), it can be shown that YCrO₄ has a lower frequency of the ν_1 (A_{1g}) mode than the other two substances. The structural comparison shows that the monazite-type structure has a lower frequency of the ν_1 (A_{1g}) mode than the zircon-type structure. The internal Raman modes ((ν_2 (B_{1g}), ν_2 (A_{1g}), ν_4 (B_{1g}), ν_3 , ν_1 (A_{1g})) in the DyCrO₄ host were moved to the lower frequency range by the substitution of Sm. In contrast to the lower frequency shift that counteracts lanthanide contraction in samples transitioning from Nd-Yb in the RCrO₄ system, the shift toward the higher frequency is attributed to the mass effect.

There was also research done on the second structure from the R-Cr-O pairings. As we already noted, it crystallized as the perovskite RCrO₃ structure. **Chapter 4** discussed the hydrothermal synthesis method for synthesizing perovskites DyCrO₃ at low temperatures.

Compared to particle size and shape, low-temperature synthesis offers significant benefits. An extensive investigation of the reaction chain is conducted first in the study. Analyzing the end products allowed us to monitor the impact of several precursor additions closely made sequentially, along with KOH, to modify the reaction. It was determined that this was the best sequential method after obtaining the desired product of single-phase DyCrO_3 from a particular sequential addition of precursors.

The research was also expanded by changing reaction parameters such as synthesis time, temperature, and amount of KOH. The adding KOH in the amounts of 1.5 g + 1g in two steps to obtain single-phase DyCrO_3 at the synthesis temperature of 280 °C for 7 days. Consequently, this is regarded as the optimal circumstance for producing single-phase DyCrO_3 . The morphology of the produced particles, which resemble rectangular sheets stacks on each other, is seen in the microscopy images of FESEM as well as HRTEM. However, the variation in KOH amount for both steps resulted in the formation of Dy(OH)_3 individually or along with DyCrO_3 .

Additionally, single-phase DyCrO_3 was formed with a different morphology than the optimal condition of adding 1.5 g + 0.5 g KOH. This morphology was round edges to the rectangular shape particle. As a result, the ideal reaction was investigated by adding complexing agents like CTAB and PVA. This interests us to pursue this research further for other particle shapes. As a response, adding CTAB at low concentration causes the change in morphology to look like dumbbells, but adding PVA causes the morphology to change to a oval-like shape with smaller particle sizes.

5.2. Future scope

The synthesis of rare earth complex oxides with excellent control over particle morphology is quite challenging. We have synthesized the single-phase RCrO_4 compounds using hydrolytic sol-gel synthesis. We have obtained hydrocathrous-like morphology for the DyCrO_4 in nanoscale, which differs in the transition temperature to 21 K from the previously reported bulk sample (23 K). So, there will be a need to synthesize the RCrO_4 phases at low temperatures to control these compounds' shape and size as the particles' shape and size significantly impact the material's physical properties. There is an open problem to be addressed in the future.

The ferroelectric effect is another significant feature of this work. RCrO_4 compounds have recently emerged as a new class of multiferroic materials. Ferroelectric materials offer various practical physical properties, but only a few combinations were investigated for ferroelectricity in the RCrO_4 system. They include: 1) high dielectric constants that make them useful for electrical capacitors; 2) high piezoelectric constants that make them suitable for sensors, actuators, and RF filters; 3) ferroelectric hysteresis that makes it possible to create non-volatile memories; 4) more excellent pyroelectric characteristics for infrared detectors and thermistors; and 5) potent electro-optic effects that are employed in optical switches and data storage, among other applications. Hence, there is a need to explore these materials near future for ferroelectric applications.

Furthermore, in my current thesis study, we synthesized orthochromites at low temperatures and again obtained various morphologies. In great detail, it is necessary to investigate shape and size-dependent features in orthochromites since particle size and morphology significantly impact the material's physical characteristics. The multiferroic characteristics of these orthochromites, which are also extensively investigated, make them commonly regarded as insulators. However, catalytic research might take advantage of it. This

calls for more investigation into another rare earth chromite property that must be done soon. Rare earth chromites' optical characteristics have not yet been extensively discussed in the literature. In order to better understand their catalytic activity, it is required to look at their optical characteristics, band gap, etc. Additionally, their uses in water-splitting-based hydrogen production have not yet been thoroughly investigated.

ABSTRACT

Name of the Student: Supriya Prabhakar Ughade

Registration No.: 10PP17A26047

Faculty of Study: Physical Sciences

Year of Submission: 2023

CSIR Lab: NCL, Pune

Name of the Supervisor: Dr. Pankaj Poddar

Title of the Thesis: Structural and Physical Properties of Rare-earth Chromium Oxides

This thesis focuses on the rare-earth chromates (RCrO_4) and chromites (RCrO_3), two compounds produced by the R-Cr-O combination in ternary metal oxide systems. These compounds' varied structural configurations and the presence of rare earth elements give them a variety of physical characteristics. Different oxidation states of chromium (Cr) in both structures have an impact on the material's final characteristics. **Chapter 1** of this thesis introduces the fundamentals of magnetism, the role of exchange interaction, and the many different physical features. The RCrO_4 and RCrO_3 structures, their phase transitions, and an overview of the studied properties are included. This chapter discusses the importance of R-Cr-O compounds in terms of their scientific and technological applicability. **Chapter 2** investigates and proposes the formation mechanism for the hydrolytic sol-gel synthesis of DyCrO_4 in acidic and basic environments after carefully reviewing the intermediate samples obtained throughout the reaction processes. The effect of complexing agents was also examined in order to establish the crystallization temperature for single-phase DyCrO_4 with the least amount of impurities. The magnetic properties of DyCrO_4 made in a basic solution with oxalic acid were then examined. In the same vein, **Chapter 3** discussed the effects of changing rare earth elements on the structural phase transition in RCrO_4 compounds from monazite to zircon-type using Raman scattering. Sol-gel synthesis has been used to create single-phase polycrystalline monazite-type LaCrO_4 , intermediate PrCrO_4 , zircon-type RCrO_4 (R = Nd, Sm, Gd, Dy, Ho, Er, Tm, and Yb), and YCrO_4 . By contrasting Raman modes for various crystal structures, rare-earth (Dy, La), and non-rare-earth (Y) elements, the investigation's scope is further broadened. In order to create perovskites DyCrO_3 , **Chapter 4** describes a low-temperature synthesis hydrothermally. The reaction mechanism was also thoroughly studied while reaction variables like synthesis time, temperature, and amount of KOH were changed. The purpose and outcomes of adding the precursors in order have also been discussed. The investigations mentioned in the thesis and the scope of this work are summarised in **Chapter 5**.

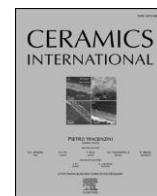
List of Publication(s) in SCI Journal(s) Emanating from the Thesis Work

1. **Supriya Ughade**, Bhavana Joshi, Pankaj Poddar, Formation of zircon-type DyCrO₄ and its magnetic properties, *Ceramics International* 48 (2022) 24666–24676. DOI: <https://doi.org/10.1016/j.ceramint.2022.05.113>
2. **Supriya Ughade**, Pankaj Poddar, A systematic study of rare-earth ions size-dependent structural phase transition from monazite to zircon-type in rare earth chromates using Raman spectroscopy, *Journal of Raman Spectroscopy* (2023) 1-9, DOI: [10.1002/jrs.6542](https://doi.org/10.1002/jrs.6542)

List of papers with abstract presented (oral or poster) at national or international conferences /seminars

Science Day Celebration

1. CSIR-NCL, 2021 (Presented poster titled “A comprehensive study of the formation of DyCrO₄ and its magnetic properties”)
2. CSIR-NCL, 2023 (Presented poster titled “A systematic study of rare-earth ions size-dependent structural phase transition from monazite to zircon-type in rare earth chromates using Raman spectroscopy”)



Formation of zircon-type DyCrO₄ and its magnetic properties

Supriya Ughade^{a,b}, Bhavana Joshi^a, Pankaj Poddar^{a,b,*}

^a Physical & Materials Chemistry Division, CSIR-National Chemical Laboratory, Pune, 411008, India

^b Academy of Scientific and Innovative Research (AcSIR), Sector 19, Kamla Nehru Nagar, Ghaziabad, Uttar Pradesh, 201 002, India

ARTICLE INFO

Keywords:

Hydrolytic sol-gel method
DyCrO₄
Formation mechanism
Complexing agent
pH

ABSTRACT

The formation mechanism of hydrolytic sol-gel synthesized DyCrO₄ with a complexing agent in acidic and basic mediums is thoroughly studied. The role of complexing agents and pH on phase formation temperature is also intensively investigated. The formation temperature for DyCrO₄ is ~500 °C in the absence and presence of complexing agents such as oxalic acid and ethylenediaminetetraacetic acid (EDTA) at pH 10. When citric acid is used, the DyCrO₄ forms with Cr₂O₃ impurity. The crystallite size in the presence of a complexing agent in the basic medium is ~55 nm which is small as compared to only ammonia solution. The various reaction modes lead to tetragonal zircon-type DyCrO₄ at ~500 °C, transforming into orthorhombic perovskite DyCrO₃ at 800 °C. The magnetization curve shows the ferromagnetic behavior of DyCrO₄ below transition temperature T_c ~21 K. This low T_c makes nanocrystalline DyCrO₄ a potential material for cryogenic applications.

1. Introduction

The mixed-metal oxides such as chromites, manganites, and ferrites have gained tremendous attention due to their large-scale structural, magnetic, and transport properties, potentially being used in optoelectronic and magnetoelectric devices [1–6]. The R-Cr-O (R = rare earth element) combination in mixed-metal oxides was crystallized in chromates (RCrO₄) and chromites (RCrO₃). The RCrO₄ compounds were found in a tetragonal zircon-type structure (for R = Pr, Nd, Sm, Eu, Gd, Tb, Dy, Ho, Er, Tm, Yb, Lu) with space group *I*₄*1*/*amd* and monoclinic monazite-type structure (for R = La, Ce) with space group *P*2₁/*n*, while R = Pr shows both types of structures [7–17]. The RCrO₄ compounds were sensitive to external parameters like temperature and pressure. On the application of external pressure, the zircon-type RCrO₄ structure changes to another tetragonal scheelite-type structure with space group *I*₄/*a*. This irreversible phase transition exhibits a volume contraction of close to 10%, denoting first-order phase transition. This phase transition results in volume change without changing the basic units of the parent structure [18–23]. The difference in crystal structure directly affects the properties of RCrO₄. Hence, selecting an appropriate synthesis process for RCrO₄ becomes very important.

The magnetic interaction in RCrO₄ compounds depends on R³⁺-R³⁺ interchain spacing. In RCrO₄, when R = Nd, Sm, Eu, Yb, Lu shows antiferromagnetic (AFM) ordering, whereas R = Gd, Er, Tm, Dy, Ho settled for ferromagnetic (FM) ordering because of the shortening of the R³⁺

-R³⁺ inter-chain distances [8–15]. As pointed out by the Anderson-Goodenough-Kanemori (AGK) empirical rules, the super-exchange interaction results in AFM ordering for ~180° interaction and FM for 90° interaction [24–26]. Morales-Sanchez et al. reported the Sm-Sm distance for the SmCrO₄ was ~7.248 Å, larger than that along the *c*-axis, with the most favorable angle Sm-O-Cr of 180° that will enhance the interactions along the *a*-axis [10]. So, SmCrO₄ shows AFM nature. The RCrO₄ structures are also ideal for studying the *3d-4f* spin interaction. The magnetism shown by these structures was due to the interplay of spin interactions in rare-earth and transition metal-sublattices. This interplay generates one exciting property in the material, namely the magnetocaloric effect (MCE). This technology is not related to any harmful chemicals, and that's why environment friendly. Initially, MCE was only used for cryogenic refrigeration, but now it is used in applications where cryogenic temperatures are required, such as hydrogen liquefaction, magnetic measurements, etc. [27–29].

Among RCrO₄ compounds, zircon-type DyCrO₄ was studied for their unusual meta-magnetism driven by coexisting ferromagnetic and anti-ferromagnetic interactions [6]. The large angular momentum of Dy³⁺ plays a significant role in tuning the magnetic properties of RCrO₄. Schemes S1(a) and (b) shows the crystal structure for zircon-type DyCrO₄. The DyCrO₄ structure was drawn with the VESTA software (version: 3.1.0) using CIF-COD ID: 1008138. The DyCrO₄ structure consists of two basic units, namely CrO₄ tetrahedra and DyO₈

* Corresponding author. Physical & Materials Chemistry Division, CSIR-National Chemical Laboratory, Pune, 411008, India.

E-mail address: p.poddar@ncl.res.in (P. Poddar).

<https://doi.org/10.1016/j.ceramint.2022.05.113>

Received 9 March 2022; Received in revised form 25 April 2022; Accepted 10 May 2022

Available online 16 May 2022

0272-8842/© 2022 Elsevier Ltd and Techna Group S.r.l. All rights reserved.

bidisphenoid polyhedra. DyO₈ polyhedra connect along the two crystallographic axes sharing O–O edges along the x-axis and y-axis, whereas it alternatively aligns with the CrO₄ tetrahedra along the third direction (z-axis). So CrO₄ tetrahedra were spatially isolated by DyO₈ polyhedra. It provides the superexchange pathways between Dy⁺³ ions through the direct linkage of polyhedra (Dy⁺³–O^{2–}–Dy⁺³) or the CrO₄ tetrahedra (Dy⁺³–O^{2–}–Cr⁺³–O^{2–}–Dy⁺³), which was responsible for the magnetic properties in these compounds [6]. The rare-earth sublattices of Dy⁺³ were ordered antiferromagnetically at low temperatures (<25 K), whereas transition metal Cr⁺³ was ordered at relatively high temperatures [4–6]. The low-temperature ordering in the Dy sublattices was due to the complex orbital configuration of *f*-electrons compared to transition metal *d*-electrons and magnetic interactions between *f*-*f* and *d*-*f* electrons [8].

In tetragonal zircon-type DyCrO₄ (*I*₄/*amd*), both Cr and Dy sublattices are ordered collinearly and simultaneously at a common transition temperature (24 K), making the magnetocaloric effect possible at low temperatures [8]. MCE is related to the magnetic entropy change in the adiabatic process when applying a magnetic field. This entropy change is associated with the angular momentum 'J'. The J value for a rare and unstable Cr⁺⁵ (3d¹4s⁰) is large enough in RCrO₄ compared to the other isostructural RXO₄ (X = P, As, V) compounds. Such a large J value of Cr⁺⁵ may be responsible for the large entropy change near the transition temperature of these compounds [19,30–33]. On the other hand, Cr⁺³ in orthorhombic perovskite DyCrO₃ (*Pbmm*) hardly contributes to the magnetocaloric effect at low temperatures due to the different ordering temperatures of Dy⁺³ and Cr⁺³ [5].

The synthesis of DyCrO₄ compounds was consistently reported by the solid-state methods [34,35]. However, materials synthesized by the solid-state technique are bulk and have poor control over particle size, crystallinity, and morphology. The solid-state synthesis involves the multiple sintering sequences for a longer time (~4–11 h) in an oxygen environment to achieve the single-phase of the RCrO₄ compound [9–12, 14]. Whereas, the solution-based sol-gel method offers good control over morphology and particle size. It produces complex inorganic ternary and quaternary oxides at comparatively lower sintering temperatures and in a shorter synthesis time than the solid-state method. The aqueous hydrolysis chemistry of the metal ions in the sol-gel synthesis can be modified by complexing agents. This modification gives pure phases and nanoparticles that can tune magnetic properties [36,37].

In this work, the nanocrystalline DyCrO₄ synthesis was carried out using sol-gel and complexing agents. Further, the formation mechanism involved in the hydrolytic sol-gel process was intensively investigated and proposed for the first time in zircon-type DyCrO₄. These samples were synthesized in two different mediums; acidic (in oxalic acid) and basic (in ammonia solution), and the formation mechanism was carried out thoroughly by analyzing the intermediate samples collected in between the reactions. The steps consisting of the formation of complex, gel, and specific structures at sintering temperatures were discussed. It was observed that complexing agents like oxalic acid, citric acid, and EDTA affects the crystallization temperature of zircon-type DyCrO₄. The comparative study between the complexing agent for different mediums (acidic and basic) was done to understand which suitable complexing agent with a reaction medium will form the single phase of DyCrO₄ with minimal impurity. To the best of our knowledge, the sol-gel method for synthesizing DyCrO₄ is rarely reported, and not much information is available on the formation mechanism. Further, morphology changes and surface valence state of the Dy, Cr, and O with the used reaction mediums for different complexing agents were investigated. The magnetic properties of sol-gel synthesized DyCrO₄ in oxalic acid were also studied and compared to the earlier reported solid-state prepared bulk DyCrO₄.

2. Experimental

2.1. Sample preparation

A hydrolytic sol-gel method was used to synthesize the polycrystalline zircon-type DyCrO₄. The reaction sequence is explained in Scheme S2. The mechanism of phase formation was studied by (i) changing the reaction medium, i.e., acidic and basic (depending on the pH of the precursor solution in the reaction), and (ii) in the absence and presence of a complexing agent. Oxalic acid (H₂C₂O₄·2H₂O, Merck, 99.5%), citric acid (C₆H₈O₇, Merck, 99.5%), and EDTA (C₁₀H₁₆N₂O₈, Thomas Baker, 99.0%) were used as complexing agents. The homogeneous solution was prepared for two different reaction mediums, acidic (A) and basic (B).

The dysprosium (III) nitrate hydrate (Dy(NO₃)₃·xH₂O, Aldrich, 99.9% metal basis), chromium trioxide (CrO₃, Thomas Baker, 99.9%) were dissolved in deionized water in the molar ratio- Dy: Cr = 1.3: 1, without using any complexing agent called hereafter as precursor solution. The precursor solution was kept on stirring for 3h at ~30 °C, which resulted in a sol formation. The pH of the precursor solution was observed to be ~0.4. Further, without adjusting the pH, the precursor solution, when heated at 80 °C, resulted in sticky gel adhering to the beaker's bottom that was difficult to collect and use for the calcination. For comparison, sol was formed by adding 30% ammonia solution dropwise to adjust the pH to ~10. The obtained sol with pH 10 was heated at 80 °C, which initially forms a gel, and then dried powder can be collected for further calcination process and denoted as DyCrO₄(B).

The formation mechanism was studied using the intermediate samples between the reactions in acidic (in the presence of oxalic acid) and basic (in ammonia solution) mediums for characterization. At the same time, the effect of a complexing agent was also studied by adding an aqueous solution of oxalic acid to the precursor solution. The pH of the precursor solution with oxalic acid was ~0.24. As mentioned earlier, the acidic sol was heated and dried to collect the powder. Also, for basic sol with oxalic acid, the pH was adjusted to 10 by the dropwise addition of 30% ammonia solution and dried to collect the powder. The oxalic acid derived acidic and basic powders were named DyCrO₄(OA) and DyCrO₄(OB), respectively.

Further, the powders were calcined at 500 °C, 600 °C, 700 °C, and 800 °C for 2h to find the accurate crystallization temperature of the phases. Citric acid and EDTA were also used as complexing agents in the other two reactions. The whole reaction was carried out with citric acid, and EDTA using the same reaction sequence mentioned for oxalic acid in acidic and basic medium and denoted as DyCrO₄(CA), DyCrO₄(CB), DyCrO₄(EA), DyCrO₄(EB). (C = citric acid, E = EDTA, A = acidic and B = basic)

2.2. Characterization techniques

Powder X-ray diffraction (XRD) patterns of the synthesized samples were recorded using a PANalytical X'PERT PRO instrument in the 2θ range of 10°–80° with iron-filtered Cu Kα radiation (λ = 1.54 Å) and step size of 0.013°. HR-800 Raman spectrophotometer (Jobin Yvon-HORIBA, France) was used for bond analysis equipped with He-Ne laser (633 nm), operated at 20 mW with the accuracy of ±1 cm⁻¹. The Raman spectra were recorded with thermoelectrically cooled (with Peltier junctions), multichannel, spectroscopic grade CCD detector (1024 × 256 pixels of 26 μm). An objective of 50 XLD magnification was used to focus and collect the signal from the powder sample dispersed on a glass slide. The thermal decomposition study was done using the thermogravimetric analysis (TGA) model DTG-60H of Shimadzu instrument at a heating rate of 10 °C/min in an air atmosphere. Transmission Electron Microscope (TEM) (FEI Tecnai T20) was used to characterize the morphology and particle size at an accelerating voltage of 200 keV. Field emission scanning electron microscopy (FESEM: Hitachi S-4200) was used to analyze the particle size. Also, Energy Dispersive X-ray Analysis (EDAX)

(a) Acidic medium (in presence of oxalic acid):

1. $\text{CrO}_3 + \text{H}_2\text{O} \rightarrow \text{H}_2\text{CrO}_4$
2. $\text{Dy}(\text{NO}_3)_3 + \text{H}_2\text{O} \rightarrow \text{Dy}^{3+} + (\text{NO}_3)^{3-}$
3. $\text{H}_2\text{CrO}_4 + \text{Dy}^{3+} + (\text{NO}_3)^{3-} + (\text{COOH})_2 \rightarrow \text{Dy}_2(\text{C}_2\text{O}_4)_3 \cdot \text{H}_2\text{O} + \text{H}_2\text{CrO}_4$
4. $2 \text{H}_2\text{CrO}_4 \rightarrow 2 \text{CrO}_3 + 2 \text{H}_2\text{O} \uparrow \rightarrow \text{Cr}_2\text{O}_5 + \frac{1}{2} \text{O}_2 \uparrow \rightarrow \text{Cr}_2\text{O}_3 + \text{O}_2 \uparrow$
5. $2 \text{Dy}_2(\text{C}_2\text{O}_4)_3 \cdot \text{H}_2\text{O} \rightarrow 2 \text{Dy}_2(\text{C}_2\text{O}_4)_3 + \text{H}_2\text{O} \uparrow \rightarrow 2 \text{Dy}_2\text{O}_3 + 6 \text{CO}_2 \uparrow + 6 \text{CO} \uparrow$
6. $\text{Cr}_2\text{O}_3 + \text{Dy}_2\text{O}_3 + \text{O}_2 \rightarrow 2 \text{DyCrO}_4$
7. $2 \text{DyCrO}_4 \rightarrow 2 \text{DyCrO}_3 + \text{O}_2 \uparrow$

(b) Basic medium (in presence of ammonium solution only):

8. $\text{H}_2\text{CrO}_4 + \text{Dy}^{3+} + (\text{NO}_3)^{3-} + \text{NH}_4\text{OH} \rightarrow (\text{NH}_4)_2\text{CrO}_4 + (\text{NH}_4)_2\text{Cr}_2\text{O}_7 + \text{Dy}(\text{OH})_3 + \text{NH}_4(\text{NO}_3)$
9. $2 (\text{NH}_4)_2\text{CrO}_4 \rightarrow (\text{NH}_4)_2\text{Cr}_2\text{O}_7 + 2 \text{NH}_3 \uparrow + \text{H}_2\text{O} \uparrow$
10. $3 (\text{NH}_4)_2\text{Cr}_2\text{O}_7 \rightarrow 3 (\text{Cr}_2\text{O}_5 \cdot \text{NH}_3) + \text{N}_2 \uparrow + 6 \text{H}_2\text{O} \uparrow + \text{NH}_3 \uparrow \rightarrow [(\text{CrO}_2)_6(\text{H}_2\text{O})] + \text{N}_2 \uparrow + 2 \text{H}_2\text{O} \uparrow + \text{NH}_3 \uparrow \rightarrow 6 \text{CrO}_2 + \text{H}_2\text{O} \uparrow \rightarrow 3 \text{Cr}_2\text{O}_3 + 2 \text{O}_2 \uparrow$
11. $\text{Dy}(\text{OH})_3 \rightarrow \text{DyOOH} + \text{H}_2\text{O} \uparrow$
12. $2 \text{DyOOH} \rightarrow \text{Dy}_2\text{O}_3 + \text{H}_2\text{O} \uparrow$

Scheme 1. Proposed formation mechanism of the DyCrO_4 compound in (a) acidic (in presence of oxalic acid) and (b) basic (in presence of ammonia solution) mediums.

was done to determine the elemental composition of synthesized samples. The X-ray Photoelectron spectra for Dy, Cr, and O were recorded on Thermo Fisher Scientific X-ray Photoelectron Spectrometer (XPS) K-Alpha+. The monochromatic Al K α ($h\nu=1486.6$ eV) as the X-ray source was operated with a beam current of 6 mA and voltage of 12 kV coupled with a Physical Electronics O4-548 dual Mg/Al anode and in an ultra-high vacuum system with a base pressure of $\leq 5 \times 10^{-9}$ Torr. The spot size of 400 μm was used during the XPS measurement. The recorded XPS data were deconvoluted using XPS PEAK 4.123. The XPS measurements were done on the exposed surface of the nanoparticles (NPs) prepared with a different complexing agent for acidic and basic pH without any surface treatment. All measurements mentioned above were performed at a laboratory temperature of ~ 30 °C. A superconducting quantum interference device-based vibrating sample magnetometer (SQUID-VSM, Quantum Design) was used to measure the magnetic properties of DyCrO_4 . The precisely weighed powder sample was taken and packed inside a plastic sample holder. It was fitted into a brass specimen holder

provided by Quantum Design Inc., contributing to an overall magnetic signal. The magnetization *versus* magnetic field (M-H) loops was collected at a different temperature in a field sweep 60 kOe. The magnetization *versus* temperature (M-T) measurements at standard field-cooled (FC) and zero-field cooled (ZFC) sequences was performed at a temperature sweep from 5 to 300 K in a field of 100 Oe.

3. Results and discussion**3.1. Formation mechanism**

In order to study the effect of acidic and basic mediums on the phase formation temperature of DyCrO_4 , the formation mechanism of the sol-gel reaction was intensively examined by collecting intermediate samples. The details involved in the mechanism were discussed in this work.

3.1.1. Acidic medium

The DyCrO_4 was synthesized using oxalic acid (pH ~ 0.24) using the hydrolytic sol-gel method. The dissolution of CrO_3 in water resulted in the formation of chromic acid (H_2CrO_4) and $\text{Dy}(\text{NO}_3)_3$ in the aqueous medium dissociated in Dy^{3+} and $(\text{NO}_3)^{3-}$ ions (Scheme 1(1, 2)). So, at 30 °C, the precursor solution contains H_2CrO_4 , Dy^{3+} , and $(\text{NO}_3)^{3-}$. The addition of oxalic acid in the precursor solution made the complex with Dy^{3+} , resulting in dysprosium oxalate hydrate ($\text{Dy}_2(\text{C}_2\text{O}_4)_3 \cdot \text{H}_2\text{O}$) (Scheme 1(3)) as seen in the powder XRD pattern (JCPDS card number 21-0315, Fig. 1a(i)) and Raman spectra (Fig. 1b(iv)). Whereas the highlighted portions of the Raman spectra in Fig. 1b at ~ 890 cm^{-1} and 365 cm^{-1} also gave the presence of CrO_4 unit for the chromic acid solution and < 200 cm^{-1} (denoted by *) confirming the presence of Dy-O [38–40]. At 80 °C, after 1h, the XRD peaks of dysprosium oxalate hydrate disappeared due to its conversion from crystalline to an amorphous form, as observed in Fig. 1a(i & ii). The Raman spectra also showed changes in the bonding at 80 °C compared to the precursor solution at 30 °C (Fig. 1b(v)). After the complete gelation, the XRD in Fig. 1a(iii) revealed the traces of crystalline dysprosium oxalate hydrate. Fig. 1b(vi) shows a slight shift in peak at ~ 890 cm^{-1} of Raman spectra supporting linkage formation in the gel. The peaks at ~ 890 cm^{-1} and ~ 357 cm^{-1} gave evidence for CrO_4 unit, which was also present in the single phase of DyCrO_4 (Fig. 1b(vii)) [38–40].

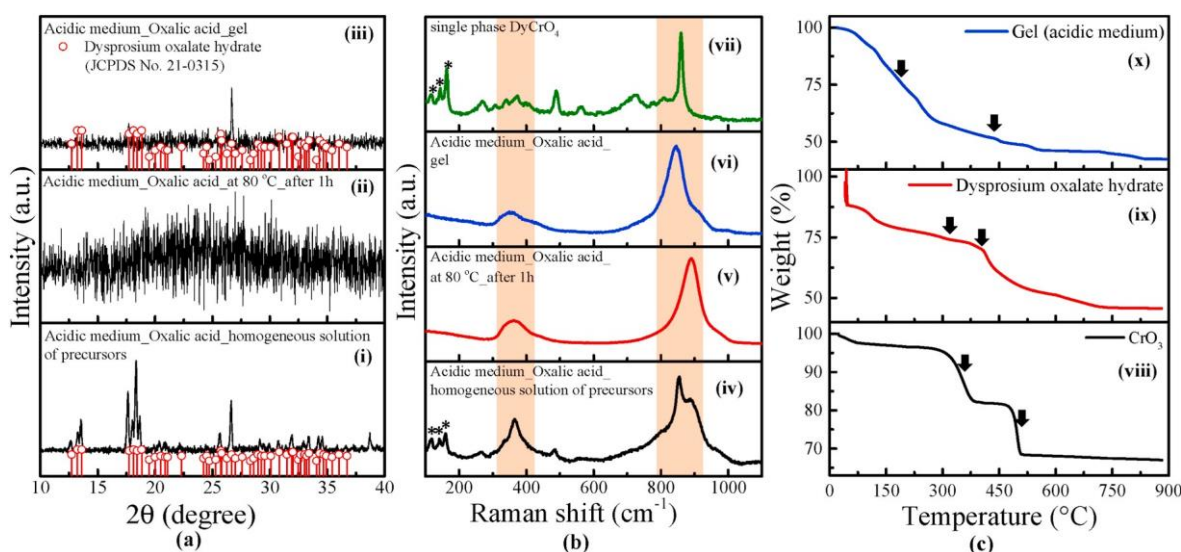


Fig. 1. (a) XRD patterns (b) Raman spectra for the samples taken during the reaction in acidic medium for oxalic acid. (i) & (iv) Crystallinity and bonding for the homogeneous solution of precursors at 30 °C. (ii) & (v) Amorphous nature and bonding at 80 °C after 1h. (iii) & (vi) crystallinity and bonds in the gel form. (vii) The structural bonding in single-phase DyCrO_4 . The highlighted portion in the Raman graphs shows the presence of CrO_4 unit (~ 890 cm^{-1} and ~ 365 cm^{-1}). In comparison, < 200 cm^{-1} , asterisks show the presence of Dy. (c) The TGA plots of (viii) CrO_3 precursor, (ix) synthesized dysprosium oxalate hydrate (x) dried gel in air. The arrows in the graphs denote the decomposition point in the corresponding compounds.

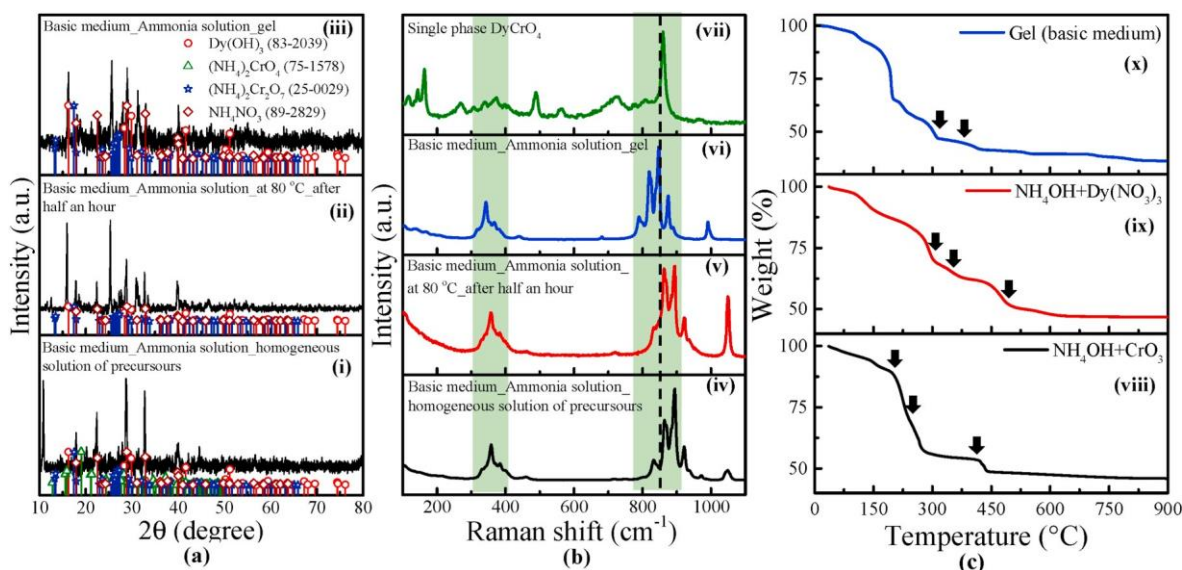


Fig. 2. (a) XRD patterns and (b) Raman spectra for the samples taken during the reaction for basic medium (ammonia solution): (i, iv) homogeneous solution of precursors at 30 °C, (ii, v) sample taken at 80 °C after 1h, (iii, vi) gel form, where, XRD revealed the presence of $(\text{NH}_4)_2\text{Cr}_2\text{O}_7$, NH_4NO_3 and $\text{Dy}(\text{OH})_3$. (vii) Raman bonding in single-phase DyCrO_4 . The highlighted portion and dotted line in the Raman spectra show the peak at $\sim 358 \text{ cm}^{-1}$ and $\sim 860 \text{ cm}^{-1}$ denoted the presence of the CrO_4 unit. (c) Thermal decomposition curve in presence of air (viii) CrO_3 and (ix) $\text{Dy}(\text{NO}_3)_3$ precursors mixed with 30% ammonia solution, (x) dried gel of the sample. Decomposition points for the corresponding compounds are denoted by arrows.

The phase transformation of dysprosium oxalate hydrate and chromic acid from dried gel to crystalline DyCrO_4 during the sintering from 30 °C to 500 °C was also studied by TGA. Initially, TGA of precursor CrO_3 and dysprosium oxalate hydrate synthesized for reaction were studied individually to identify the decomposition temperature. The TGA curve of only the CrO_3 precursor depicts the decomposition at $\sim 357 \text{ °C}$ for the pyrolysis of CrO_3 forming Cr_2O_5 (Fig. 1c(viii)). The second decomposition step shows the conversion of Cr_2O_5 to Cr_2O_3 at $\sim 499 \text{ °C}$. The steps for converting CrO_3 to Cr_2O_3 well matched with the reported data studied in N_2 and O_2 that had shown similar results in both the atmosphere [41]. The thermal decomposition of only dysprosium oxalate hydrate shows a loss of water at $\sim 112 \text{ °C}$. The formation of anhydrous oxalate can be traced by weight loss occurring between

$\sim 112 \text{ °C}$ and 304 °C . Further, the anhydrous oxalate rapidly decomposes to give Dy_2O_3 at $\sim 416 \text{ °C}$, as shown in Fig. 1c(ix); the arrows in the plot show the decomposition temperatures [42]. The thermal decomposition of gel containing dysprosium oxalate hydrate and chromic acid exhibits similar transition temperatures starting from the evaporation of water molecule at $\sim 82 \text{ °C}$ along with the conversion of chromic acid to CrO_3 (Fig. 1c(x)). Further, the CrO_3 loses oxygen to form Cr_2O_5 at $\sim 238 \text{ °C}$ and Cr_2O_3 at $\sim 450 \text{ °C}$, as shown in Scheme 1(4) [41]. The gel's transition temperatures are lower for Cr_2O_5 and Cr_2O_3 than the individual transition temperature of CrO_3 to Cr_2O_3 , as the gel also contains dysprosium oxalate hydrate. The second component of the gel form, dysprosium oxalate hydrate ($\text{Dy}_2(\text{C}_2\text{O}_4)_3 \cdot \text{H}_2\text{O}$), transforms to anhydrous oxalate ($\text{Dy}_2(\text{C}_2\text{O}_4)_3$) in the first step between 133 °C and 283 °C ,

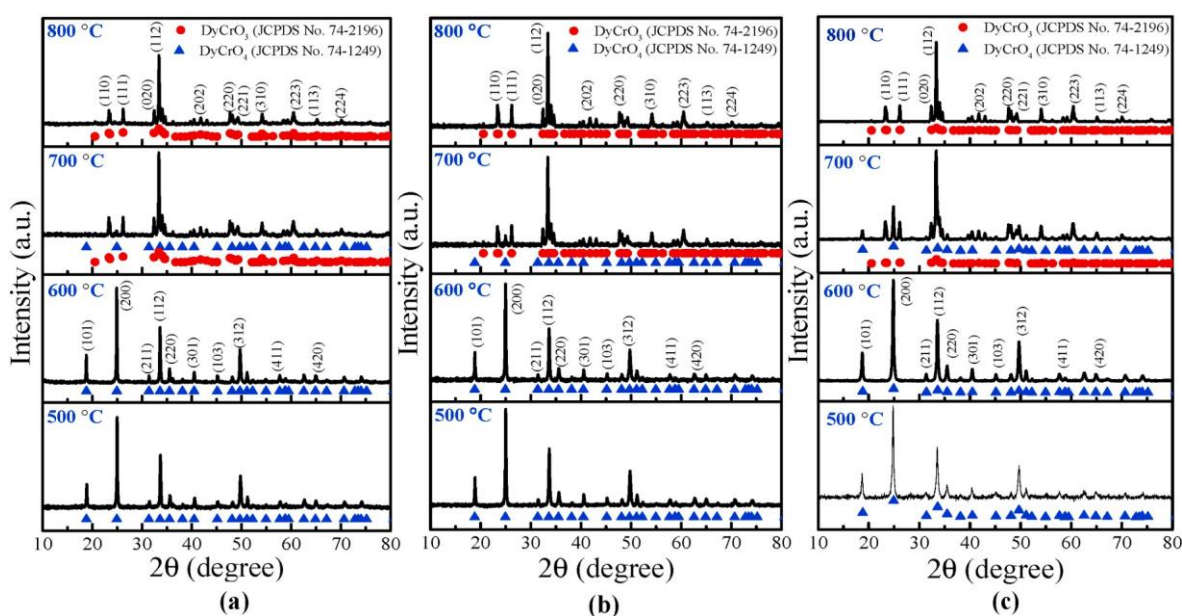


Fig. 3. The phase transformation of DyCrO_4 to DyCrO_3 with increasing temperatures from 500 °C to 800 °C when any of these conditions are met: (a) in ammonia solution, (b) in oxalic acid (acidic medium), and (c) in oxalic acid (basic medium).

and rapidly decomposes to Dy_2O_3 between 283 °C and 450 °C in the second step, as the anhydrous oxalate was very unstable (Scheme 1(5)) [42]. So, in the temperature range of 400 °C–450 °C, the Cr_2O_3 and Dy_2O_3 phases are present during the gel sintering process, which further converts to DyCrO_4 at ~500 °C as confirmed by XRD presented later (Fig. 3b). The DyCrO_4 then decomposes to DyCrO_3 at ~700 °C as observed by slight weight loss in TGA Fig. 1c(x). The same reactions are also presented in Scheme 1(6,7). The similar formation mechanism might also apply to the citric acid and EDTA.

3.1.2. Basic medium

In order to carry out the reaction in the basic medium, the 30% ammonia solution (NH_4OH) was added to the precursor solution containing chromic acid (H_2CrO_4), Dy^{3+} , and $(\text{NO}_3)^{3-}$ ions (Scheme 1(1, 2)). After the addition of NH_4OH in the precursor solution, it resulted in ammonium chromate ($(\text{NH}_4)_2\text{CrO}_4$ (JCPDS card number [75–1578]), ammonium dichromate ($(\text{NH}_4)_2\text{Cr}_2\text{O}_7$ (JCPDS card number [25–0029]), and NH_4NO_3 (JCPDS card number [89–2829]), as shown in Fig. 2a(i) and Scheme 1(8). The Raman peak at ~860 cm^{-1} showed a CrO_4 unit, as reported for single-phase DyCrO_4 (Fig. 2b(iv & vii)) [38]. The shift in CrO_4 frequency from 890 cm^{-1} (acidic medium -(H_2CrO_4)) to 860 cm^{-1} (basic medium) confirms the formation of the complex $(\text{NH}_4)_2\text{CrO}_4$ due to the addition of NH_4OH . The shift to the lower frequency is due to the higher mass of $(\text{NH}_4)_2\text{CrO}_4$ compared to H_2CrO_4 . The highlighted portion in Fig. 2b shows the bending of CrO_4 at ~358 cm^{-1} [40]. For the gel formation, the homogeneous solution was heated at 80 °C. The intermediate sample was collected after 1h at 80 °C, which shows the presence of $(\text{NH}_4)_2\text{Cr}_2\text{O}_7$, NH_4NO_3 , and $\text{Dy}(\text{OH})_3$ (JCPDS card number [83–2039]) as shown in XRD pattern Fig. 2a(ii) and Scheme 1(9) [43]. After the formation of gel, the phases remain consistent, as confirmed by XRD (Fig. 2a(iii)). The bonding in Raman spectra (Fig. 2b(v and vi)) also remains unchanged.

The phases formed during the sintering temperature were investigated by thermal decomposition using TGA of the dried gel obtained in the reaction; further phases were confirmed by thermal decomposition of CrO_3 and $\text{Dy}(\text{NO}_3)_3$ mixed with 30% ammonia solution separately. The CrO_3 mixed with 30% ammonia solution, when dried at 80 °C, forms $(\text{NH}_4)_2\text{Cr}_2\text{O}_7$. The TGA investigated this ammonium dichromate, as shown in Fig. 2c(viii). The decomposition steps were observed at ~224 °C (conversion of Cr(VI) to Cr(V) with the partial loss of ammonia), ~253 °C–265 °C (approached Cr(IV) from Cr(V), with the loss of rest of ammonia) and at ~430 °C (complete decomposition to Cr_2O_3) (Scheme 1(10)) [44]. The thermal decomposition of NH_4NO_3 and $\text{Dy}(\text{OH})_3$ formed as a product of a mixture of $\text{Dy}(\text{NO}_3)_3$ with 30% ammonia was also studied using TGA (Fig. 2c(ix)). The decomposition of the mixture observed at ~292 °C reveals the presence of DyOOH , which converts to Dy_2O_3 at 345 °C–474 °C (Scheme 1(11,12)) [45]. In the same temperature range, the NH_4NO_3 decomposed to gases, as reported by Chaturvedi et al. [46] Further, in Fig. 2c(x), the TGA of gel containing $(\text{NH}_4)_2\text{Cr}_2\text{O}_7$, NH_4NO_3 , and $\text{Dy}(\text{OH})_3$ were also investigated. The decomposition temperatures of gel observed to be: ~110 °C, ~227 °C, ~253 °C, ~306 °C–411 °C corresponds to the loss of water; transformation of Cr(VI) to Cr(V), with loss of half of the ammonia; conversion of Cr(V) to Cr(IV) followed by the formation of Cr_2O_3 , respectively (Scheme 1(10)) [44]. The remaining two components of the gel NH_4NO_3 and $\text{Dy}(\text{OH})_3$ were decomposed in the gases and formed DyOOH from $\text{Dy}(\text{OH})_3$ at ~306 °C. Further, Dy_2O_3 formation occurs at ~411 °C [45, 46]. Based on the comparison of decomposition of only ammonium dichromate and $\text{Dy}(\text{OH})_3$, it can be concluded that in sintered gel, Cr_2O_3 and Dy_2O_3 both are present at an altered temperature of ~411 °C that can be further converted to DyCrO_4 at ~500 °C (Scheme 1(5)) as confirmed by XRD (Fig. 3a). The proposed scheme suggests the formation of Cr_2O_3 and Dy_2O_3 . However, the phase formation could not be observed in XRD and Raman but can be illustrated by TGA. The DyCrO_4 was transformed to DyCrO_3 above ~700 °C by removing oxygen, as shown in Scheme 1(5).

The same reactions were carried out using the complexing agents (oxalic acid, citric acid, and EDTA), followed by adding ammonia solution to increase the solution's pH by ~10. The oxalic acid reacts with Dy^{3+} to form Dy-oxalate hydrate, and further addition of $(\text{NH}_4)_2\text{OH}$ forms $(\text{NH}_4)_2\text{CrO}_4$. These complex molecules may form Dy_2O_3 and Cr_2O_3 via the intermediate reactions as discussed by the proposed mechanism in acidic and basic mediums during the sintering process. Further, sintering of Dy_2O_3 and Cr_2O_3 up to 600 °C forms single-phase DyCrO_4 . Similar reactions can also elaborate the formation mechanism when citric acid and EDTA are used with ammonia solution. The advantages of the sol-gel reactions carried out in this work suggest the formation of Dy_2O_3 and Cr_2O_3 via intermediate steps. These Dy_2O_3 and Cr_2O_3 forms nano-sized DyCrO_4 during the sintering process (as confirmed from XRD). Such controls over the size are difficult to achieve in the solid-state reaction, which is generally used for DyCrO_4 synthesis.

3.2. X-ray diffraction study

The gel form of DyCrO_4 precursors synthesized using only a complexing agent (acidic medium), only ammonia solution (basic medium), and complexing agents with the ammonia solution (pH~10) were sintered at different temperatures 500 °C–800 °C. Further, the XRD measurements were carried out to understand the role of the complexing agent in altering the sintering temperature and achieving single-phase DyCrO_4 and its transformation to DyCrO_3 , as discussed below.

3.2.1. Ammonia solution (NH_4OH)

The zircon-type $\text{DyCrO}_{4(\text{NB})}$ was obtained by sintering the intermediate gel forms of Dy, and Cr precursors formed using only NH_4OH . The phase formation is studied by XRD at different temperatures to get DyCrO_4 and DyCrO_3 . Fig. 3a revealed zircon-type DyCrO_4 , obtained at 500 °C and 600 °C, that decomposes to DyCrO_3 at 700 °C and 800 °C by the removal of the oxygen from DyCrO_4 . The phases well matched the reported JCPDS card numbers [74–1249] and [74–2196] of zircon-type DyCrO_4 and perovskite DyCrO_3 compounds, respectively.

3.2.2. Oxalic acid ($\text{C}_2\text{H}_2\text{O}_4$)

Oxalic acid (bidentate ligand) crystallized the phases for both acidic ($\text{DyCrO}_{4(\text{OA})}$) and basic ($\text{DyCrO}_{4(\text{OB})}$) mediums at 500 °C, similar to phases crystallized for $\text{DyCrO}_{4(\text{NB})}$, as shown in Fig. 3b and (c). In acidic and basic mediums, at 500 °C and 600 °C, the zircon-type DyCrO_4 phase was obtained and well-matched with the JCPDS card number [74–1249]. Further, calcination at higher temperatures of 700 °C and 800 °C, the DyCrO_4 phase started to deform in the DyCrO_3 perovskite phase with the removal of oxygen from the structure. The phase obtained at 800 °C was well-matched with the JCPDS card number [74–2196]. At 700 °C, both phases, DyCrO_4 and DyCrO_3 , were observed. The same trend for the phase formation temperature was noticed in $\text{DyCrO}_{4(\text{OA})}$ and $\text{DyCrO}_{4(\text{OB})}$, as oxalic acid controls the decomposition profile of the nitrates to form pure phase DyCrO_4 in basic and acidic mediums [38].

3.2.3. Citric acid ($\text{C}_6\text{H}_8\text{O}_7$)

The tridentate ligand, citric acid, decomposes the phases differently from other ligands. The citrate sol-gel method is more popular for the synthesis of nanoparticles of the perovskites like DyCrO_3 , SmCrO_3 , and YbCrO_3 . The pH-dependent homogeneity and stability of metal citrate solutions were studied previously [5]. The present work observed that the citrate sol-gel method decomposes the phases differently over the calcination in acidic and basic mediums. $\text{DyCrO}_{4(\text{CA})}$ shows the DyCrO_4 phase at 500 °C and 600 °C with some impurities in an acidic medium. The phase was not entirely crystallized over the temperature range up to 600 °C. It was converted to DyCrO_3 perovskite phase at 700 °C and 800 °C. The hump near 30° in the XRD graphs shown in Fig. S1(a) for 600 °C heating temperature may be due to the individual hydroxide in the sample. However, in the basic medium (Fig. S1(b)) for $\text{DyCrO}_{4(\text{CB})}$, at

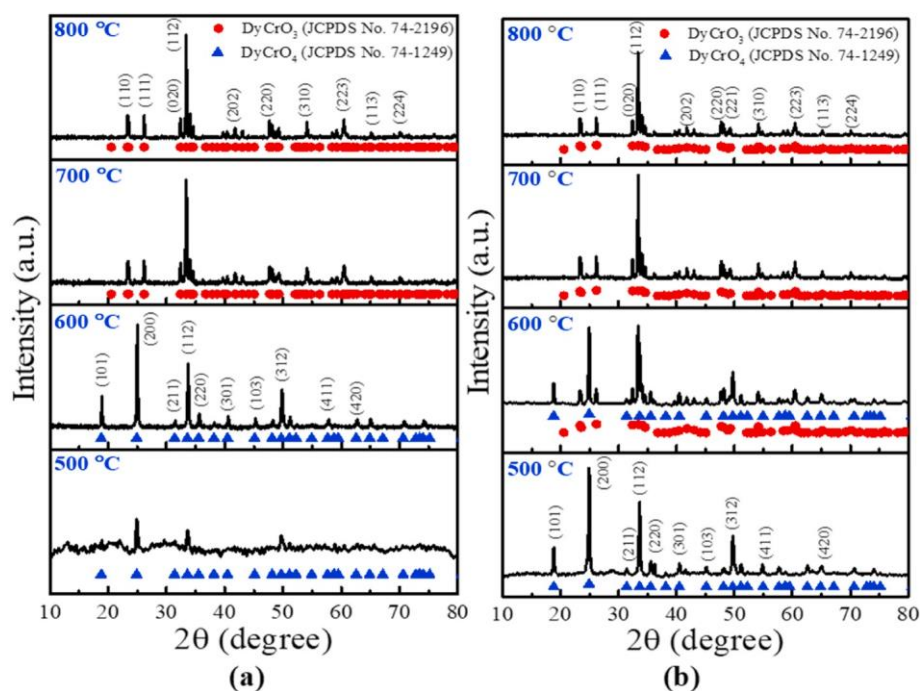


Fig. 4. The XRD patterns of dysprosium chromium oxide system in the presence of EDTA over the heating temperature range 500 °C–800 °C when the reaction is performed at (a) lower pH (acidic), (b) higher pH ~10 (basic).

Table 1

The phases of the dysprosium chromium oxide system with increasing temperatures in different complexing agents in lower (acidic) and higher (basic) pH.

Reaction mediums	Reaction temperature (°C)	Ammonia Solution	Complexing agents		
			Oxalic acid	Citric acid	EDTA
Acidic (pH not adjusted)	500	–	DyCrO ₄	DyCrO ₄	DyCrO ₄
	600	–	DyCrO ₄	Impurity + DyCrO ₄	DyCrO ₄
	700	–	DyCrO ₄ +DyCrO ₃	DyCrO ₃	DyCrO ₃
	800	–	DyCrO ₃	DyCrO ₃	DyCrO ₃
Basic (pH~10 adjusted using ammonia solution)	500	DyCrO ₄	DyCrO ₄	Cr ₂ O ₃	DyCrO ₄
	600	DyCrO ₄	DyCrO ₄	Cr ₂ O ₃ + DyCrO ₄	DyCrO ₄ + DyCrO ₃
	700	DyCrO ₃ + DyCrO ₄	DyCrO ₃ + DyCrO ₄	Cr ₂ O ₃ + DyCrO ₃	DyCrO ₃
	800	DyCrO ₃	DyCrO ₃	DyCrO ₃	DyCrO ₃

500 °C found, the presence of Cr₂O₃ with the hump at 30°. DyCrO₄(CB) shows the presence of DyCrO₄ at 600 °C with Cr₂O₃ impurity phase, and over the heating temperature of 700 °C and 800 °C, the phase decomposed to DyCrO₃. It was observed that the citrate sol-gel method did not give the single phase of DyCrO₄ in the basic condition at pH 10, which means it favors the formation of Cr⁺³ ionic state to form the DyCrO₃.

3.2.4. EDTA (C₁₀H₁₆N₂O₈)

EDTA (hexadentate ligand) crystallized the phases relatively at a lower temperature in the basic medium (DyCrO₄(EB)) as compared to the acidic medium (DyCrO₄(EA)), as shown in Fig. 4(a) and (b). The DyCrO₄ phase was obtained for calcination temperatures of 500 °C and 600 °C in a basic medium, whereas DyCrO₄(EA) was found at 600 °C. At 700 °C and 800 °C, a DyCrO₃ was obtained for DyCrO₄(EA) and DyCrO₄(EB). At calcination of 600 °C, DyCrO₄(EB) exhibits mix phase of DyCrO₄ and DyCrO₃. Comparing the two reaction mediums for EDTA, the basic medium completes the hydrolysis process earlier than the acidic. Hence, the DyCrO₄ phase was crystallized at a lower temperature in a basic medium than in an acidic medium. The early completion of hydrolysis steps provides more condensation sites; thus, the phase was formed at a lower temperature [38].

Based on the overall XRD analysis of the phases obtained at different heating temperatures with various complexing agents in acidic and basic

mediums, oxalic acid and EDTA formed the single DyCrO₄ phase, as shown in Table 1. The crystallite size (*d*) for the single-phase DyCrO₄ prepared using a complexing agent in different reaction mediums depending on the solution's pH was calculated using the Debye-Scherrer equation (1) for the highest intensity (200) plane tabulated in Table S1. The formula used to calculate the crystallite size along the hkl plane (hkl are the Miller indices of the plane) from the measured width of their diffraction curves are given as:

$$d = K\lambda / B \cos \theta \text{ -----} \quad (1)$$

Here, B represents the width of the diffraction curve at an intensity equal to half the maximum intensity called full width at half maxima (FWHM), measured in radians. The λ is the wavelength of the incident X-rays of source Cu K α ($\lambda \sim 1.54 \text{ \AA}$), θ is the Bragg angle associated with hkl plane, and K is the numerical constant, considered as 0.94 since the shape of particles is random as observed in FESEM. Without taking the B values directly from peak broadening, it is corrected from standard data using equation (2).

$$B^2 = B_M^2 - B_S^2 \text{ -----} \quad (2)$$

B_M and B_S are the measured widths (FWHM) of the diffraction peaks of synthesized materials and standard samples, resulting in deducting the instrumental errors from the peak broadening.

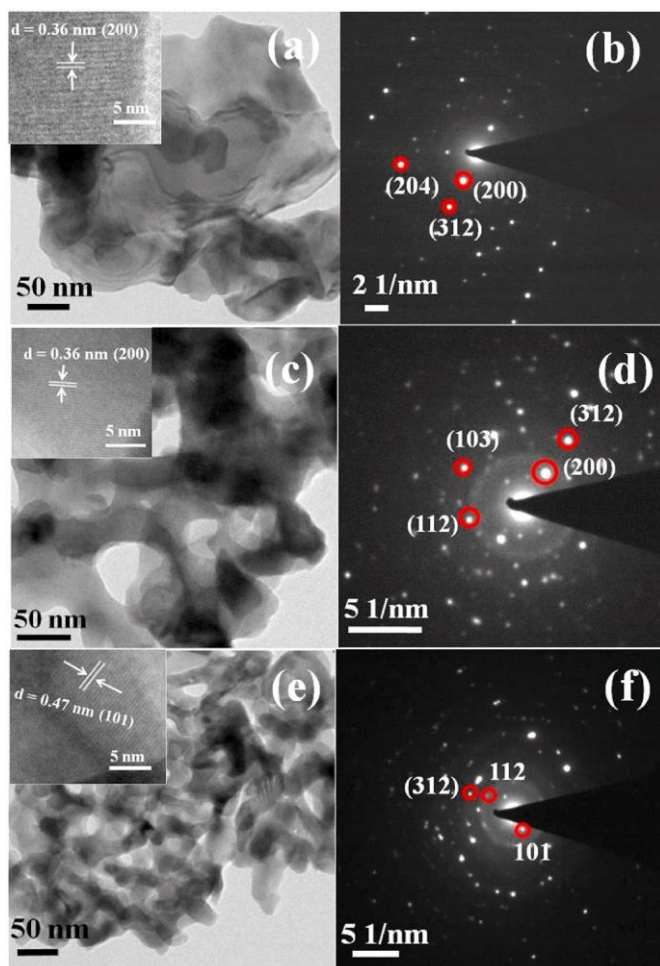


Fig. 5. TEM data of DyCrO_4 : (a) Extended sheet-like morphology for basic medium in ammonia solution with the d-spacing of 0.36 nm (200) (inset of (a)). (b) Crystalline nature in SAED. (c) and (e) show hydrocathrus-like morphology in acidic and basic mediums for oxalic acid, respectively. Inset of (c) shows the lattice fringes spacing of 0.36 nm corresponds to the (200) plane. Inset (e): d-spacing of 0.47 nm represent (101) plane. (d) and (f) SAED pattern reveals the level of crystallinity.

The $\text{DyCrO}_{4(\text{OA})}$ and $\text{DyCrO}_{4(\text{EA})}$ has crystallite size of ~ 63 nm and ~ 77 nm, respectively. However, in the basic medium, the crystallite size was reduced to ~ 56 nm ($\text{DyCrO}_{4(\text{OB})}$) and ~ 54 nm ($\text{DyCrO}_{4(\text{EB})}$), which was nearly the same for both the complexing agent. The crystallite size of ~ 218 nm was observed for $\text{DyCrO}_{4(\text{NB})}$. It was concluded from the calculation that the DyCrO_4 synthesized with the complexing agent in basic medium favor the synthesis of smaller crystallite size. The crystallite size for $\text{DyCrO}_{4(\text{CA})}$ and $\text{DyCrO}_{4(\text{CB})}$ was not calculated, as the single-phase DyCrO_4 was not obtained.

3.3. Electron microscopy imaging and diffraction study

The morphology of the DyCrO_4 samples for different reaction mediums in the presence of a complexing agent was investigated using TEM. The TEM images show the hydrocathrus-like morphology with unevenly sized holes for the DyCrO_4 phase synthesized using a complexing agent and extended sheet-like structure in the absence of a complexing agent. The bright-field (BF) TEM image in Fig. 5a reveals the extended sheet-like structure for $\text{DyCrO}_{4(\text{NB})}$. The size of morphology well corresponds to the listed crystallite size of $\text{DyCrO}_{4(\text{NB})}$. BF-images Fig. 5c and (e) shows the TEM images for $\text{DyCrO}_{4(\text{OA})}$ and $\text{DyCrO}_{4(\text{OB})}$. The acidic medium has a hydrocathrus-like morphology with larger

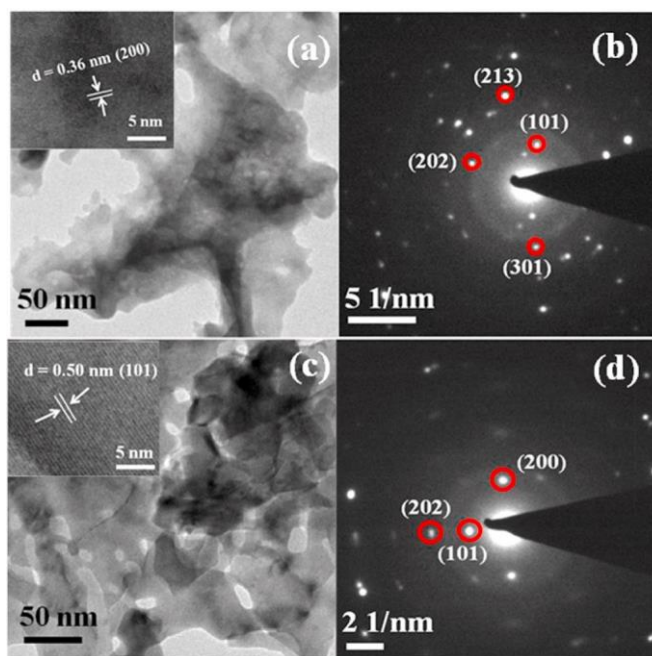


Fig. 6. (a) and (c) BF-TEM images show the hydrocathrus-like morphology for DyCrO_4 prepared using EDTA in both acidic and basic mediums. The lattice fringes spacing of 0.36 nm corresponds to (200) plane (inset (a)) and 0.50 nm present (101) plane (inset (c)). (b) and (d) DF-TEM images reveal the SAED patterns showing crystalline nature of DyCrO_4 in acidic and basic mediums with EDTA, respectively. (BF-bright field and DF- dark field).

holes but connected sheets. Whereas, in the basic medium the sheet like morphology has smaller particles and comparatively smaller holes than that of the acidic medium. Following the same trend, the calculated crystallite size was smaller in basic medium. Inset of Fig. 5a, (c), and 5(e) shows the lattice fringes spacing of 0.36 nm for (200) plane of $\text{DyCrO}_{4(\text{NB})}$ and, $\text{DyCrO}_{4(\text{OA})}$ whereas 0.47 nm for (101) plane of $\text{DyCrO}_{4(\text{OB})}$. Darkfield images (DF) in Fig. 5b, (d), and 5(f), shows the selected area electron diffraction (SAED) pattern, confirmed the crystalline nature of the synthesized $\text{DyCrO}_{4(\text{NB})}$, $\text{DyCrO}_{4(\text{OA})}$, $\text{DyCrO}_{4(\text{OB})}$ respectively. The $\text{DyCrO}_{4(\text{CA})}$ shows the hydrocathrus-like morphology having larger holes (Fig. S2(a)) with a d-spacing of 0.32 nm (inset Fig. S2(a)). The crystalline nature of the prepared $\text{DyCrO}_{4(\text{CA})}$ was confirmed by the SAED pattern, as shown in Fig. S2(b). The TEM-image and SAED pattern of $\text{DyCrO}_{4(\text{CB})}$ heated at 600°C was shown in Figs. S2(c) and S2(d). At 600°C , $\text{DyCrO}_{4(\text{CB})}$ sample attains the DyCrO_4 phase with the impurity of Cr_2O_3 . The d-spacing of 0.25 nm is shown in inset Fig. S2(c) may correspond to the (220) plane of the Cr_2O_3 phase. The sample's crystallinity was again confirmed from the SAED pattern in Fig. S2(d).

The $\text{DyCrO}_{4(\text{EA})}$ and, $\text{DyCrO}_{4(\text{EB})}$ show the same morphology as that of $\text{DyCrO}_{4(\text{OA})}$ and, $\text{DyCrO}_{4(\text{OB})}$, as presented in Fig. 6a, (c). SAED pattern shows the crystalline nature of the $\text{DyCrO}_{4(\text{EA})}$ and $\text{DyCrO}_{4(\text{EB})}$ samples in Fig. 7(b) and (d). Inset of Fig. 6a and (c) shows the lattice fringes spacing of 0.36 nm ($\text{DyCrO}_{4(\text{EA})}$) and 0.50 nm ($\text{DyCrO}_{4(\text{EB})}$). The size of morphology in TEM images are consistent with the calculated crystallite size of synthesized DyCrO_4 using a complexing agent in the different reaction mediums from XRD measurements.

After sintering, the FESEM measurements were done for the single-phase DyCrO_4 to calculate the particle size. All the FESEM images show the random morphology of DyCrO_4 particles suggesting their crystallization. The histogram was calculated for 30 particles in each case. Fig. S3 shows the FESEM images with the calculated histogram. The particle size is in nm, as mentioned in Fig. S3. Further, the EDAX analysis was done as presented in Table S2, which confirms the presence of Dy, Cr, and O in sintered single-phase DyCrO_4 samples.

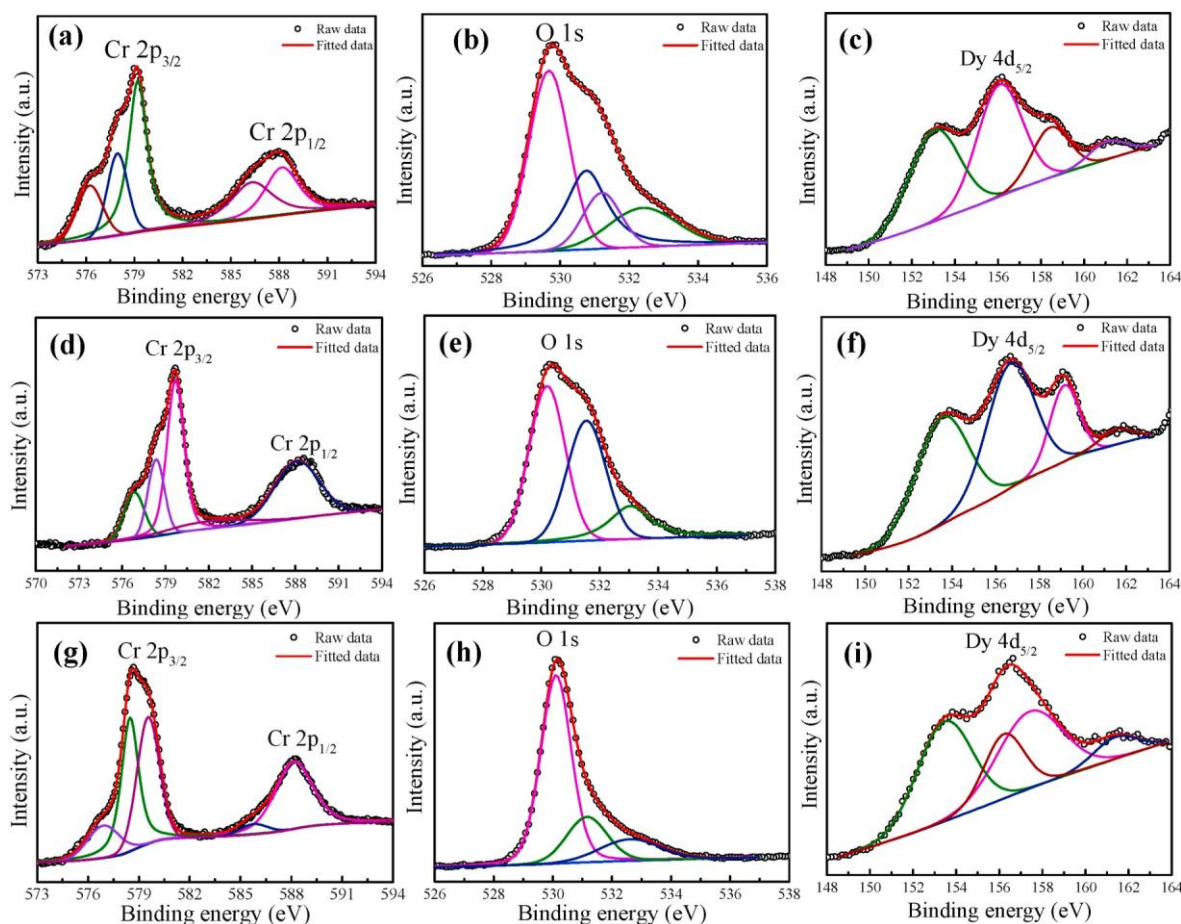


Fig. 7. XPS derived Cr 2p, O 1s, Dy 4d core levels electron binding energy spectra for DyCrO₄ synthesized in the absence of small molecule in basic medium ((a)–(c)), in the presence of oxalic acid in acidic medium ((d)–(f)), and oxalic acid in basic medium ((g)–(i)) to conclude the valence state of elements.

3.4. X-ray photoelectron spectroscopy analysis

XPS spectra for the DyCrO₄ synthesized using a complexing agent at different reaction mediums were recorded at room temperature to reveal the surface valence states of the Dy, Cr, and O atoms. The core-level binding energy was aligned with the carbon binding energy of ~284.8 eV. Fig. 7a represents the XPS spectra of DyCrO_{4(NB)} without a complexing agent. The Cr 2p_{3/2} peak for DyCrO_{4(NB)} resolved into three peaks at ~576 eV, ~578 eV, ~579 eV corresponding to Cr⁺³, Cr⁺⁵, and Cr⁺⁶. At the same time, the Cr 2p_{1/2} resolved into two peaks, ~586 eV and 588 eV [47,48]. Fig. 7d and (g) show the Cr 2p XPS binding energy spectra for DyCrO_{4(OA)} and DyCrO_{4(OB)}, respectively. The spectra contain two spin-orbit split peaks of 2p_{1/2} and 2p_{3/2} were located at ~588 and 580 eV for DyCrO_{4(OA)}, whereas for DyCrO_{4(OB)} at ~588 and 579 eV. The deconvolution of peaks further resolved the Cr 2p_{3/2} peak of DyCrO_{4(OA)} in three peaks situated at ~577 eV (Cr⁺³), ~578 eV (Cr⁺⁵), ~580 eV (Cr⁺⁶) [47,48]. However, the Cr 2p_{1/2} peak divides into ~582 and 588 eV. It is well known that the binding energy of Cr⁺⁶ and Cr⁺⁵ has nearly the same value, so it is difficult to distinguish them. Cr is in a +5-oxidation state that contains one unpaired electron in its valence band, contributing to the different valency states of Cr. The XPS spectra of Cr 2p_{3/2} for DyCrO_{4(OB)} fitted peaks show the three peaks at ~577 eV (Cr⁺³), ~578 eV (Cr⁺⁵), ~579 eV (Cr⁺⁶), and Cr 2p_{1/2} at ~585, and 588 eV. The binding energy for the surface elements present in DyCrO_{4(OA)} and DyCrO_{4(OB)} was nearly the same. It contains 3+, 5, and +6 valence states of Cr.

The fixed spherical size of the oxygen ion is approximated, but in reality, the valence electronic shell of the oxygen ion is no longer uniform but polarized when placed between covalent cations. The O1s

spectra of DyCrO_{4(NB)} (Fig. 7b) fitted with four peaks ~529 eV (Cr–O, metal oxide), ~530 eV (O¹⁻), ~531 eV (surface absorbed oxygen in –OH form), ~532 eV (chemically absorbed oxygen in the form of water) [49, 50]. Fig. 7e and (h) also show the similar deconvolution peaks of O1s spectra for DyCrO_{4(OA)} and DyCrO_{4(OB)}. Thus, the XPS spectra of oxygen indicate the carboxyl and hydroxyl groups of the oxalic acid.

Fig. 7f and (i) shows the deconvoluted Dy 4d core-level spectra for DyCrO_{4(OA)} and, DyCrO_{4(OB)}, respectively. The Dy 4d spectra have the four peaks at ~153 eV, ~156 eV, ~159 eV, ~161 eV for DyCrO_{4(OA)} and ~153 eV, ~156 eV, ~157 eV, ~161 eV for DyCrO_{4(OB)}. The peaks at ~153 eV correspond to the Dy–Cr bond. The Dy–O-related peak was positioned at ~156 and 157 eV. In contrast, the highest binding energy peaks at ~161 eV of Dy 4d were revealed for the Dy³⁺ ionic state [51–57]. The same correspondence for the peak binding energy was also observed in DyCrO_{4(NB)}, with the peaks at ~153 eV (Dy–Cr), ~156 eV (Dy–O), ~158, and 161 eV (Dy³⁺) in Fig. 7c.

The surface valence state of DyCrO_{4(EA)} and DyCrO_{4(EB)} was also studied. The Cr 2p, O 1s, and Dy 4d core-level XPS spectra for DyCrO₄ synthesized using EDTA were shown in Fig. S4(a)–(c) for acidic medium and S4(d)–(f) for basic medium. The deconvoluted peaks positioned at ~576 eV, ~578 eV, ~579 eV in both DyCrO_{4(EA)} and DyCrO_{4(EB)} corresponds to Cr 2p_{3/2}. The peaks related to Cr⁺³ ionic states were positioned at ~576 eV. While ~578 eV reveals Cr⁺⁵, and ~579 eV shows the presence of Cr⁺⁶ ionic form [47,48]. Peaks at ~586 and 588 eV show Cr 2p_{1/2} for DyCrO₄ prepared in the presence of EDTA only and EDTA at pH 10. The deconvoluted O 1s spectra resolved into three peaks in both the mediums located at ~530 eV (Cr–O, due to metal oxide), ~531 eV (surface absorbed oxygen), and ~533 eV (chemically absorbed oxygen in the form of water) for DyCrO_{4(EA)} and DyCrO_{4(EB)} [49,50]. The

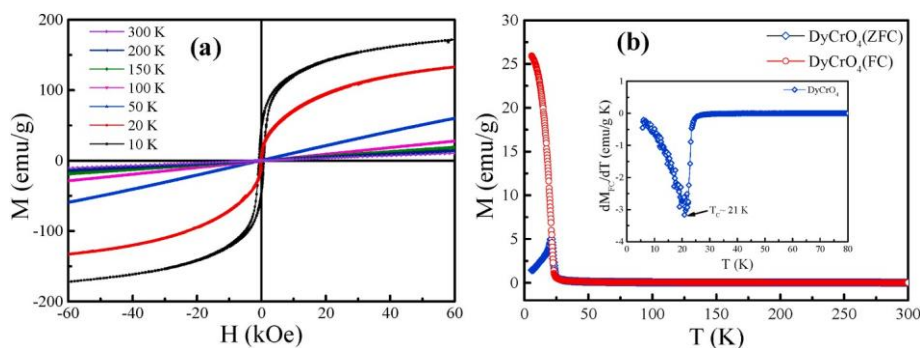


Fig. 8. Magnetic nature of the DyCrO_4 synthesized using oxalic acid in a basic (pH~10) medium. (a) The magnetization versus magnetic field behavior of the sample over the temperature range 10 K–300 K. At 300 K, DyCrO_4 shows a paramagnetic nature, whereas at 10 K, the DyCrO_4 shows a soft ferromagnetic nature. (b) Field-cooled and zero-field cooled measurements for the DyCrO_4 at a magnetic field of 100 Oe. Inset shows dM_{FC}/dT curve to conclude the transition temperature at ~ 21 K.

core-level XPS spectrum of Dy 4d shows the presence of Dy^{3+} , Dy–Cr, and Dy–O. The peaks at ~ 152 and 159 eV of $\text{DyCrO}_{4(\text{EA})}$ correspond to Dy^{3+} . The same binding energy peak was observed in $\text{DyCrO}_{4(\text{EB})}$ at ~ 159 eV. The peak at ~ 153 and 156 eV reveals Dy–Cr and, Dy–O bonds, respectively, for $\text{DyCrO}_{4(\text{EA})}$ and $\text{DyCrO}_{4(\text{EB})}$ [51–57]. The XPS spectra for the samples prepared with citric acid in both the pH condition $\text{pH} < 7$ and $\text{pH} > 7$ were not recorded as the phases got for these reaction conditions have some impurity of Cr_2O_3 . So, the XPS spectra reveal the chemical composition and state of the surface atoms in all synthesized samples under different reaction conditions.

3.5. Magnetic measurements

The magnetic measurement was carried out only for $\text{DyCrO}_{4(\text{OB})}$, as both the mediums crystallized the zircon phase at the same temperature of 500°C . The $M - H$ measurements resulted in the straight line passing through origin without any hysteresis for temperatures 300 K–50 K, corresponding to the paramagnetic (PM) state (Fig. 8a) of $\text{DyCrO}_{4(\text{OB})}$. Whereas, for 20 K and 10 K, the curve shows the hysteresis loop was depicting the soft ferromagnetic nature of $\text{DyCrO}_{4(\text{OB})}$, as shown in Fig. S5 (zoom view). At 10 K, the $M - H$ curve shows the coercivity ~ 752 Oe and remanence ~ 40 emu/g; however, the values are smaller than permanent magnetic materials such as ferrites and magnetic alloys [58,59]. The soft ferromagnetic behavior at low temperature in the DyCrO_4 was due to the $f-f$ orbital superexchange interactions, as f orbitals have complex interactions. A similar, soft ferromagnetic curve was also observed in the case of solid-state derived DyCrO_4 due to the involvement of f -orbitals [6,8].

Fig. 8b shows the temperature dependence of zero-field-cooled (ZFC) and field-cooled (FC) magnetization measured at a field of 100 Oe for the determination of transition temperature (T_c) of $\text{DyCrO}_{4(\text{OB})}$. The ZFC and FC curve does not separate in the paramagnetic state and increases monotonically with decreasing temperature (T). It was observed that in the ZFC curve of $\text{DyCrO}_{4(\text{OB})}$, the magnetization value sharply increases as the temperature goes to ~ 21 K (T_c) due to paramagnetic-ferromagnetic (PM-FM) transition. A similar PM-FM transition was reported by Long et al. in solid-state derived bulk DyCrO_4 at 23 K [6]. For bulk DyCrO_4 , the neutron diffraction study also shows the transition temperature at 23 K [8]. The ZFC and FC magnetization vs temperature curves separation shows the domain wall pinning effect. The domain can align along the external field direction or in a local anisotropy field direction if the sample is cooled down from the high temperature with or without field. Inset of Fig. 8b shows the derivative of FC magnetization concerning temperature reveals the transition temperature T_c of ~ 21 K, which is lower than the reported for the solid-state synthesized bulk DyCrO_4 [27,60]. The lowering in the transition temperature in sol-gel synthesized nanocrystalline DyCrO_4 was related to the small size effect of the particles; as the particle size decreases, the surface-to-volume ratio increases, which results in a larger number of surface electron

spins per unit volume. The electron spin fluctuations became more prominent in nanocrystalline particles, causing disordered spin alignments, leading to the reduction in transition temperature as well as magnetization [61].

4. Conclusion

The process involved in the synthesis of zircon-type DyCrO_4 by hydrolytic sol-gel method in acidic (using oxalic acid) and basic (using ammonium solution) mediums was thoroughly discussed. The formation mechanism shows the presence of Cr_2O_3 and Dy_2O_3 in the gelation step of sol-gel as concluded by TGA. After sintering, this Cr_2O_3 and Dy_2O_3 form nanocrystalline DyCrO_4 , validating the advantage of sol-gel over solid-state reaction. When only ammonia solution was used for gel formation, the DyCrO_4 phase crystallized at 500°C , which further converted to the DyCrO_3 at 800°C . The gel formed with only oxalic acid and oxalic acid with pH 10 crystallizes to DyCrO_4 at the same temperature of 500°C . In the case of EDTA, the acidic medium gel crystallized the DyCrO_4 at 600°C , whereas EDTA with pH 10 forms DyCrO_4 at 500°C , which is lower than that of the acidic medium. The citric acid in the acidic as well as in the basic medium gives crystalline DyCrO_4 along with Cr_2O_3 as an impurity at a sintering temperature of 500°C . The DyCrO_4 phase decomposed to the DyCrO_3 for all complexing agents with increased sintering temperature. The crystallite size of DyCrO_4 formed using oxalic acid and EDTA at pH 10 was determined to be ~ 55 nm. TEM shows the hydrocathrus-like morphology for the DyCrO_4 samples. The binding energy of the valence state of elements present in the DyCrO_4 differs due to the different surroundings of complexing agents used in the acidic and basic mediums during the sol-gel synthesis. The magnetic measurements of single-phase DyCrO_4 synthesized using oxalic acid at pH 10 showed ferromagnetic nature below the transition temperature of 21 K, which is less than the previously reported bulk DyCrO_4 by solid-state synthesis. Thus, the nanocrystalline DyCrO_4 synthesized at a lower sintering temperature (500°C) and in a shorter duration (2 h), can be suitable for cryogenic applications such as hydrogen liquefaction owing to its lower transition temperature of 21 K.

Notes

The authors declare no competing financial interest.

Declaration of competing interest

The authors declare that they have no known competing financial interests or personal relationships that could have appeared to influence the work reported in this paper.

- [46] S. Chaturvedi, P.N. Dave, Review on thermal decomposition of ammonium nitrate, *J. Energetic Mater.* 31 (2013) 1–26, <https://doi.org/10.1080/07370652.2011.573523>.
- [47] K. Jagannathan, A. Srinivasan, C.N.R. Rao, An XPS study of the surface oxidation states of metals in some oxide catalysts, *J. Catal.* 69 (1981) 418–427, [https://doi.org/10.1016/0021-9517\(81\)90177-9](https://doi.org/10.1016/0021-9517(81)90177-9).
- [48] D.L. Hoang, A. Dittmar, M. Schneider, A. Trunschke, H. Lieske, K.W. Brzezinkab, K. Witke, Evidence of lanthanum-chromium mixed oxides formed in CrO_x/La₂O₃ model catalysts, *Thermochim. Acta* 400 (2003) 153–163, [https://doi.org/10.1016/S0040-6031\(02\)00491-4](https://doi.org/10.1016/S0040-6031(02)00491-4).
- [49] D.A. Pawlak, M. Ito, M. Oku, K. Shimamura, T. Fukuda, Interpretation of XPS O (1s) in mixed oxides proved on mixed perovskite crystals, *J. Phys. Chem. B* 106 (2002) 504–507, <https://doi.org/10.1021/jp012040a>.
- [50] L.Q. Wu, Y.C. Li, S.Q. Li, Z.Z. Li, G.D. Tang, W.H. Qi, L.C. Xue, X.S. Ge, L.L. Ding, Method for estimating ionicities of oxides using O1s photoelectron spectra, *AIP Adv.* 5 (2015), <https://doi.org/10.1063/1.4931996>.
- [51] P. Wu, C. Cai, The solid state electrochemistry of dysprosium(III) hexacyanoferrate (II), *Electroanalysis* 17 (2005) 1583–1588, <https://doi.org/10.1002/elan.200403260>.
- [52] Y.T. Tsai, T.C. Chang, W.L. Huang, C.W. Huang, Y.E. Syu, S.C. Chen, S.M. Sze, M. J. Tsai, T.Y. Tseng, Investigation for coexistence of dual resistive switching characteristics in DyMn₂O₇ memory devices, *Appl. Phys. Lett.* 99 (2011), <https://doi.org/10.1063/1.3629788>, 2009–2012.
- [53] K. Thirumalai, M. Shanthi, M. Swaminathan, Hydrothermal fabrication of natural sun light active Dy₂WO₆ doped ZnO and its enhanced photo-electrocatalytic activity and self-cleaning properties, *RSC Adv.* 7 (2017) 7509–7518, <https://doi.org/10.1039/c6ra24843h>.
- [54] R. Tholkappian, K. Vishista, Synthesis, structural, magnetic and xps studies of garnet type-dysprosium iron oxides by glycine-assisted combustion method, *Nanosci. Nanotechnol. Lett.* 7 (2015) 469–475, <https://doi.org/10.1166/nl.2015.1967>.
- [55] D. Barreca, A. Gasparotto, A. Milanov, E. Tondello, A. Devi, R.A. Fischer, Nanostructured Dy₂O₃ films: an XPS investigation, *Surf. Sci. Spectra* 14 (2007) 52–59, <https://doi.org/10.1116/11.20080702>.
- [56] A.P. Milanov, R.W. Seidel, D. Barreca, A. Gasparotto, M. Winter, J. Feydt, S. Irsen, H.W. Becker, A. Devi, Malonate complexes of dysprosium: synthesis, characterization and application for LI-MOCVD of dysprosium containing thin films, *Dalton Trans.* 40 (2011) 62–78, <https://doi.org/10.1039/c0dt00455c>.
- [57] F. Zhang, M. Wen, M. Cheng, Q. Wu, X. Meng, Inducing nanolayers-assembly of FePtDy 1D superstructure and its induced visible light photocatalysis effect for TiO₂, *J. Mater. Chem.* 20 (2010) 7661–7668, <https://doi.org/10.1039/c0jm00481b>.
- [58] Asuka Namai, Marie Yoshikiyo, Kana Yamada, Shunsuke Sakurai, Takashi Goto, Takayuki Yoshida, Tatsuro Miyazaki, Makoto Nakajima, Tohru Suemoto, Hiroko Tokoro, Shin-ic, Hard magnetic ferrite with a gigantic coercivity and high frequency millimetre wave rotation, *Nat. Commun.* 3 (2012) 1–6, <https://doi.org/10.1038/ncomms2038>, 1035.
- [59] Pratap K. Deheri, Viswanathan Swaminathan, Shekhar D. Bhamre, Zhongwu Liu, Raju V. Ramanujan, Sol-gel based chemical synthesis of Nd₂Fe₁₄B hard magnetic nanoparticles, *Chem. Mater.* (2010) 6509–6517, <https://doi.org/10.1021/cm103148n>.
- [60] G.A. Stewart, J.M. Cadogan, W.D. Hutchison, D.H. Ryan, A Mössbauer study of DyCrO₄ and ErCrO₄, *AIP Adv.* 9 (2019), <https://doi.org/10.1063/1.5079989>.
- [61] Bashar Issa, Ihab M. Obaidat, Borhan A. Albiss, Yousef Haik, Magnetic nanoparticles: surface effects and properties related to biomedicine applications, *Int. J. Mol. Sci.* 14 (2013) 21266–21305, <https://doi.org/10.3390/ijms141121266>.



EDINBURGH
INSTRUMENTS



SCAN ME

RAMAN AND BEYOND...

- + Multi-modal Confocal Microscopy
- + Raman & Photoluminescence Mapping
- + Fluorescence & Phosphorescence Lifetime Imaging (FLIM/PLIM)



MANUFACTURED
WITH PRIDE IN THE
UNITED KINGDOM

edinst.com

A systematic study of rare-earth ions size-dependent structural phase transition from monazite to zircon-type in rare earth chromates using Raman spectroscopy

Supriya Ughade^{1,2} | Pankaj Poddar^{1,2} 

¹Physical and Materials Chemistry Division, CSIR-National Chemical Laboratory, Pune, India

²Academy of Scientific and Innovative Research (AcSIR), Ghaziabad, Uttar Pradesh, India

Correspondence

Pankaj Poddar, Academy of Scientific and Innovative Research (AcSIR), Sector 19, Kamla Nehru Nagar, Ghaziabad, Uttar Pradesh 201 002, India.
Email: p.poddar@ncl.res.in

Funding information

DST-INSPIRE FELLOWSHIP, India

Abstract

Rare earth chromates (RCrO_4) undergo monazite to zircon-type structural phase transition due to a decreased rare-earth ion size. They also exhibit an intermediate mixed phase. However, there is no systematic study on the influence of structural distortion on their phononic behavior, which is quite sensitive to subtle environmental variations. A change in the room temperature phononic spectrum was studied in the family of RCrO_4 compounds, where R was varied from La to Yb using Raman modes. With an increase in the atomic number from Nd to Yb for zircon-type phases, the external translational and rotational modes were observed to shift towards lower and higher wavenumbers, respectively. At the same time, all internal vibrational modes shifted towards higher phonon energies. A comparison between Raman modes for monazite, intermediate, and zircon-type RCrO_4 phases showed a gradual shift in the internal modes towards a higher wavenumber. The confirmation of the change in Raman modes with the decreasing radius was found by comparing the rare-earth elements in DyCrO_4 and LaCrO_4 with non-rare-earth elements in YCrO_4 .

KEYWORDS

monazite-type, Raman spectroscopy, rare earth chromates (RCrO_4), YCrO_4 , zircon type

1 | INTRODUCTION

The development of new experimental methodologies is frequently the main impetus for scientific advancement. One of the few experimental methods that can identify coexisting domains with sizes comparable to the lattice constant is Raman spectroscopy. This is because the occurrence of structural non-uniformity in the material significantly impacts the intensity, shape, and Raman peak positions. These include structural abnormalities like dislocations or grain boundaries and point defects like vacancies, interstitials, and anti-sites. For several materials, it is possible to see distinct variations in

Raman spectrum characteristics due to changes in composition and doping.^{1,2}

In this work, the Raman measurements were investigated thoroughly by considering the rare earth chromate system. Rare earth chromates (RCrO_4 , where R = rare earth element) was crystallized in two different polymorphs depending on the R involved in the crystal structure. With the increasing lanthanide radius, the first R element "La" formed a monazite-type structure with monoclinic symmetry belonging to space group $\text{P2}_1/\text{n}$ (C^5h). The monazite-type structure has four molecules per unit cell ($Z = 4$). The other R elements, such as Nd, Sm, Eu, Gd, Tb, Dy, Ho, Tm, Yb, and Lu, crystallized in a tetragonal zircon-type structure

with space group $I4_1/amd$ (Dh^{19} , $Z = 4$). R = Pr exhibits both monazite-type and zircon-type structures for the $PrCrO_4$ compound. Many groups tried to obtain $PrCrO_4$ in any single-phase form; however, crystallization of $PrCrO_4$ in any single phase was very difficult.³⁻⁶ The phase stability of rare earth chromates depends on the radius of the R element in the crystal structure.⁴

The crystal structure of monazite-type has two basic units: RO_9 edge-shared polyhedra and CrO_4 tetrahedra. In contrast, a tetragonal zircon-type structure has been observed with basic units of RO_8 dodecahedra or polyhedra and CrO_4 tetrahedra.⁵⁻⁹ The crystal structures for both monazite-type and zircon-type $RCrO_4$ are shown in Figure S1A,B, drawn using VESTA software (version: 3.1.0). The monoclinic monazite-type structure had a higher oxygen coordination number of 9 than the tetragonal zircon-type structure, with an oxygen coordination number of 8.¹⁰⁻¹⁷ Monazite and zircon-type structures were observed to have strong sensitivity towards the externally applied pressure and temperature. With external pressure, the zircon-type structure deforms into other tetragonal scheelite-type structures having larger density and lower symmetry. The zircon to scheelite transition only involved a noticeable change in the bond angles. However, with the application of external temperature, an orthorhombic perovskite structure was formed for both the monazite and zircon-type structures.³

The physical and chemical properties of the materials mainly depend on the inherent crystallographic structure, which results in the importance of phase control of the materials. An extensive investigation of the magnetic properties of most of the $RCrO_4$ was studied by considering the rare valence state of chromium “+5.”^{3-5,10,11,15,18-20} The $RCrO_4$ compounds were good candidates to study $3d-4f$ interaction and magnetocaloric effect (MCE) at low temperatures, as both the sublattices are ordered at this temperature.³⁻⁷ The co-structural compounds such as RPO_4 and RVO_4 were studied for the structural changes using Raman modes at room temperature and with pressure variation. First, the RPO_4 compounds were studied for the lattice vibration in the structure. The structural packing of $(PO_4)^{3-}$ ions was observed in these compounds for the lanthanide series. However, the same closer packing of $(VO_4)^{3-}$ ion was also studied in the RVO_4 compounds.^{21,22} Aoki et al.¹³ conducted the initial Raman study at room temperature with $LaCrO_4$ and $NdCrO_4$. $LaCrO_4$ has a monoclinic monazite-type structure, and $NdCrO_4$ has a tetragonal zircon-type structure. The vibrational structures of these compounds were analyzed using Raman spectroscopy, which was affected due to the CrO_4 tetrahedra symmetry. Further, with pressure-dependent Raman spectra, Long et al.²³ reported the Raman study at room temperature for $DyCrO_4$ and $NdCrO_4$. They observed eight Raman

modes in their work. The phase transition from zircon to the scheelite-type structure was investigated with Raman modes. The rest of the $RCrO_4$ compounds (except R = La, Nd, and Dy) have not been studied yet. The R-site element in $RCrO_4$ compounds determines the crystallization structure. So the different R-site elements create structural changes in these compounds, which have not been investigated so far. The reported synthesis method for these compounds was a solid-state reaction method with the drawback of having an impurity phase in the obtained mixture. Thus, there is a need to synthesize the single-phase $RCrO_4$ compounds and re-investigate their physical and chemical properties.^{3,6,7,24,25}

The present study shows the room-temperature Raman spectra for monoclinic monazite-type $LaCrO_4$, intermediate $PrCrO_4$, and tetragonal zircon-type $RCrO_4$ (R = Nd, Sm, Gd, Dy, Ho, Er, Tm, and Yb) phases. The effect of R-site element size on the Raman modes of $RCrO_4$ was investigated, as it gives the structural phase transition from monazite to zircon-type structure with an increase in the size of rare earth elements. The comparative study for the Raman spectra of different structures as well as Dy, La as rare earth elements, and Y as non-rare earth elements present at the R-site in $RCrO_4$ compounds was also observed. Y is the next adjacent element to lanthanide from the d -block (group 3). It has similar chemical properties as that of lanthanides, but the radius contraction may differ in this element. So $YCrO_4$ was introduced in the Raman study along with the $RCrO_4$ system to determine the contraction effect on the structure.

Further, the Raman study extended to changes in the Raman modes of $DyCrO_4$ by substituting Dy with Sm in some percentages forming the $Sm_xDy_{1.3-x}CrO_4$ system. The Sm has a larger atomic radius and smaller atomic number than Dy. So the effect of a larger atomic radius element substitution in place of a smaller one was investigated in this system.

2 | EXPERIMENT

2.1 | Sample preparation

The polycrystalline samples of the monazite-type $LaCrO_4$ and zircon-type $RCrO_4$ (R = Nd, Sm, Gd, Dy, Ho, Er, Tm, Yb) and $YCrO_4$ were synthesized using a hydrolytic sol-gel synthesis method. As mentioned in our previous work, the reaction sequence was followed to prepare $RCrO_4$ compounds.²⁶ The starting materials of R (III) nitrate hydrate (R $[NO_3]_3 \cdot H_2O$, Aldrich, 99.9% metal basis), chromium nitrate (Cr $[NO_3]_3$, Aldrich, 99.9%), and oxalic acid ($H_2C_2O_4 \cdot 2H_2O$, Merck, 99.5%) were used. The ratio of the precursors was taken as R: Cr = 1:1 except

for R = Dy. The DyCrO₄ single phase was found with a higher concentration of Dy (NO₃)₃ as compared to other R elements. First, to synthesize LaCrO₄, the precursor's La (NO₃)₃, Cr (NO₃)₃, and oxalic acid were dissolved in de-ionized water separately. The homogeneous solution was obtained by stirring all three aqueous solutions in one beaker. The pH of the homogeneous solution was raised to ~10 by adding 30% ammonia solution drop-wise. The mixture was then stirred at ~30°C for 3 h, which resulted in a sol formation. The obtained sol was heated at 80°C and formed the gel. The gel form of the sample is heated, so the water gets evaporated and converted into the dried gel. The dried gel was sintered at 600°C for 2 h to obtain the expected phase. The same procedure was repeated to prepare zircon-type RCrO₄ (R = Nd, Sm, Gd, Dy, Ho, Er, Tm, Yb) and YCrO₄, intermediate PrCrO₄ and Sm_xDy_{1.3-x}CrO₄ system by taking respective precursor salts. Further, to observe the effect of the longer atomic radius of Sm in place of the smaller atomic radius of Dy on Raman scattering, the samples were prepared by substituting Sm in place of Dy in DyCrO₄. Sm concentration was taken as x = 0.3, 0.7, and 1 for the replacement of Dy in Sm_xDy_{1.3-x}CrO₄, as the single-phase of DyCrO₄ was obtained with a molar ratio of 1.3:1 (Dy:Cr).

2.2 | Characterization techniques

The crystallinity and phase purity of the samples were confirmed by X-ray diffraction (XRD) using a PANalytical X'PERT PRO instrument. The X-ray source was the iron-filtered Cu K α radiation of wavelength 1.54 Å with a diffraction angle (2 θ) varied in the range of 10–80° with a step size of 0.013°. Room-temperature Raman spectra were obtained from HR-800 Raman spectrophotometer (Jobin Yvon-Horiba, France) with a He-Ne laser of wavelength 633 nm, of 20 mW power. The Raman instrument was equipped with a thermoelectrically cooled (with Peltier junctions), multi-channel, spectroscopic-grade CCD detector (1,024 × 256 pixels of 26 μ m). An objective of 50 XLD magnification was used to focus and collect the signal from the powder sample dispersed on a glass slide.

3 | RESULTS AND DISCUSSION

3.1 | X-ray diffraction analysis

The XRD patterns show that at a sintering temperature of 600°C, LaCrO₄ crystallized in a monazite-type structure, as shown in Figure S2 (JCPDS card number [89-0448]). However, PrCrO₄ (sintered at 600°C) shows the coexistence of both zircon [JCPDS card number

74-1243] and monazite [JCPDS card number 35-1289] phases (Figure S2), with the zircon phase forming the major fraction. Even after optimization of reaction conditions, the efforts to obtain the single-phase PrCrO₄ did not get success with the hydrolytic sol-gel method. The other RCrO₄ phases (R = Nd, Sm, Gd, Dy, Ho, Er, Tm, Yb) and YCrO₄ crystallized in the zircon-type after sintering at 600°C (Figure S2). The Rietveld refinement using FullProf software confirms the single phase, as shown in Figure S3. When the JCPDS data of the zircon-type structures of RCrO₄ compounds were piled together, it showed a systematic shift in the 2 θ position (Figure S4A) towards higher angles while going from NdCrO₄ to YbCrO₄, which shows the decrease in the lattice parameters. A similar shift in the 2 θ position was also observed in XRD data of as-synthesized samples, as shown in Figure S4B. The shift in the 2 θ towards the higher values shows the contraction in the lattice.^{27,28} The lattice gets contracted with the increasing atomic number and decreasing atomic size (radius). The RCrO₄ structure is affected by changing the R-site from Nd to Yb in the zircon-type structure. The powder XRD measurements on Sm_xDy_{1.3-x}CrO₄ series, with x = 0.3, 0.7, and 1 (Figure S6), show that no structural phase transition was observed when the ratio Sm/Dy was altered from the parent structures (SmCrO₄ and DyCrO₄), which both crystallize in the zircon-type structure.

3.2 | Room temperature Raman spectra

According to group theory analysis, the monoclinic monazite-type structure exhibits 69 optical modes represented as^{29,30}

$$\Gamma \frac{1}{4} 16B_u \mid 17A_u \mid 18A_g \mid 18B_g:$$

Among that, 36 modes are Raman active, and 33 modes are IR-active:

$$\Gamma \frac{1}{4} 18A_g \mid 18B_g,$$

$$\Gamma \frac{1}{4} 16B_u \mid 17A_u:$$

The tetragonal zircon-type structure has 33 optical modes from group theory prediction. Among these 33 optical modes, 12 are Raman active.^{21–23,29,31}

$$\Gamma \frac{1}{4} A_{1g} \delta v_1, v_2 \mid B_{1g} \delta 2T, v_3, v_4 \mid B_{2g} \delta v_2 \mid E_g \delta 2T, R, v_3, v_4:$$

The vibrational spectra of the monazite-type and zircon-type structures were divided into two modes:

(1) internal modes (ν_1 – ν_4), which are associated with CrO_4 tetrahedron and can be further divided into bending and stretching modes, and (2) external modes can be classified as translational (T)- and rotational (R)-like modes that involve the movement of both R element and CrO_4 ions.^{29,30}

Recorded room-temperature Raman spectra show the different modes correlated with the structural change, illustrating the structural phase transition in RCrO_4 compounds from monazite to zircon-type structure as the rare-earth ions radius decreases from Lu to Yb, as observed in the XRD measurements. In this experiment, 11 modes with measurable intensity were observed in the Raman spectra of the monazite-type LaCrO_4 (Figure 1). Out of the 11 modes listed in Table S1, 10 modes were correlated with the previously reported LaCrO_4 .^{13,29} The absence of other Raman modes could be due to their small Raman scattering cross-section and the overlapping of many A_g and B_g modes. The intermediate zircon and monazite-type PrCrO_4 show 14 measurable intensity peaks, but only eight vibrational modes were correlated

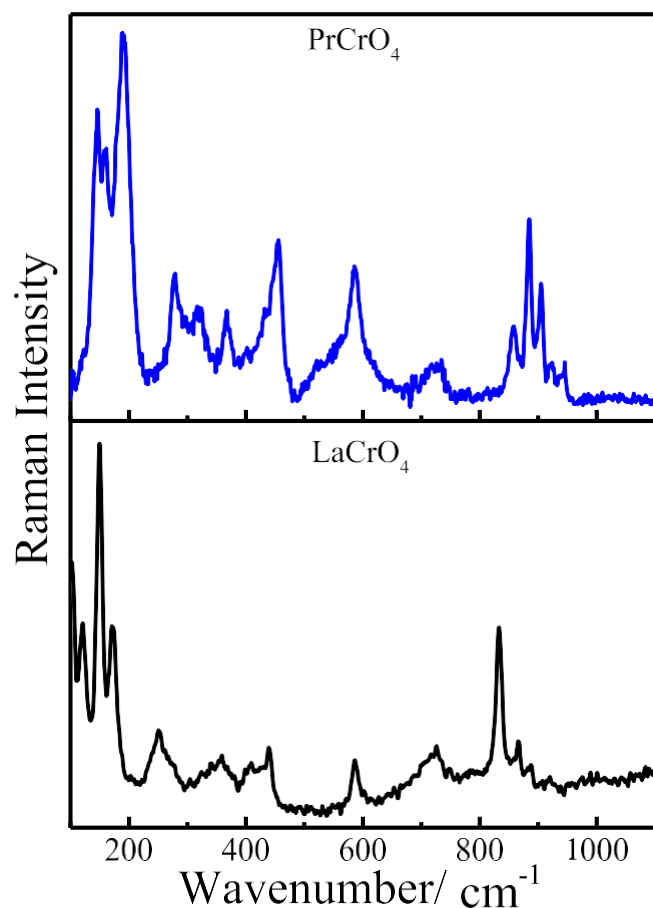


FIGURE 1 The room temperature Raman spectra for monazite-type LaCrO_4 , mixed monazite, and zircon-type PrCrO_4 in the frequency range 100–1,100 cm^{-1}

with the reported constructs (Figure 1).³⁰ These assigned modes show the zircon-type as well as the monazite-type structure of PrCrO_4 . The maximum modes were related to the zircon-type structure, which means the zircon phase was the major one in the mixture of PrCrO_4 . One external (R [E_g]) and five internal (ν_2 [B_{1g}], ν_2 [A_{1g}], ν_4 [B_1], ν_3 [B_{1g}], and ν_1 [A_{1g}]) modes were observed for the zircon-type PrCrO_4 ; at the same time, four A_g modes were listed in the monazite-type PrCrO_4 . The Raman wavenumbers assigned with the modes for LaCrO_4 and PrCrO_4 are listed in Table S1.

Figure 2A shows room temperature Raman spectra for zircon-type RCrO_4 (R = Nd, Sm, Gd, Dy, Ho, Er, Tm, and Yb) compounds from 100–1,100 cm^{-1} wavenumber range. The external modes for zircon-type RCrO_4 were reported from the 100–200 cm^{-1} wavenumber range. Three external modes were observed in this lower wavenumber region, as shown in Figure 2B. The external translational (T [E_g]) and rotational (R [E_g]) modes split into two separate modes as the atomic radius of the R (r_R) decreased in zircon-type RCrO_4 . The two translational T (B_g) and T (E_g) modes shifted to lower wavenumber towards the left side as the atomic radius decreased and the atomic number increased from Nd–Yb. This tendency was ostensibly compensated for as a mass effect (harmonic approximation remains valid). In comparison, the R (E_g) mode shifted to the higher energy related to the lanthanide contraction.^{21,22} The shift in the external modes was denoted by the dotted line in Figure 2B; as even the atomic number rises, the energy of the R-atomic ion's orbital drops. Consequently, the stronger the interaction force constant between R and CrO_4 is, the smaller the energy difference is, which accounts for the shift in frequency of the internal modes and the decline in the R–O bond distance.^{21,22}

The internal vibrational modes for the RCrO_4 were recorded from 200 to 1,000 cm^{-1} . In the first two internal modes, ν_2 (B_{2g}) and ν_2 (A_{1g}), symmetric bending modes were observed in the wavenumber range of 200–400 cm^{-1} (Figure 3A). The antisymmetric bending mode ν_4 (B_{1g}) was located at ~ 456 cm^{-1} for the NdCrO_4 , which was shifted to the right towards a higher wavenumber region with the increasing atomic number and decreasing atomic radius, as shown in Figure 3B. The antisymmetric stretching (ν_3 [B_{1g}] and ν_3 [E_g]) with symmetric stretching (ν_1 [A_{1g}]) modes were observed in the higher wavenumber region from 700–1,000 cm^{-1} , shown in Figure 3B. All observed internal modes in zircon-type RCrO_4 compounds were shifted to a higher wavenumber (right shift) as the atomic number increased (r_R decreases) from Nd to Yb (shown in the dotted line in Figure 3). This tendency was attributed to the lanthanide contraction, which causes the lanthanide atomic radii to shrink as the

FIGURE 2 (A) The Raman spectra at room temperature from the frequency range 100–1,100 cm^{-1} and (B) external vibrational modes of Raman spectra for zircon-type RCrO_4 compounds ($R = \text{Nd, Sm, Gd, Dy, Ho, Er, Tm, Yb}$) in 100–200 cm^{-1} frequency range. The dotted line shows the shift in the Raman modes.

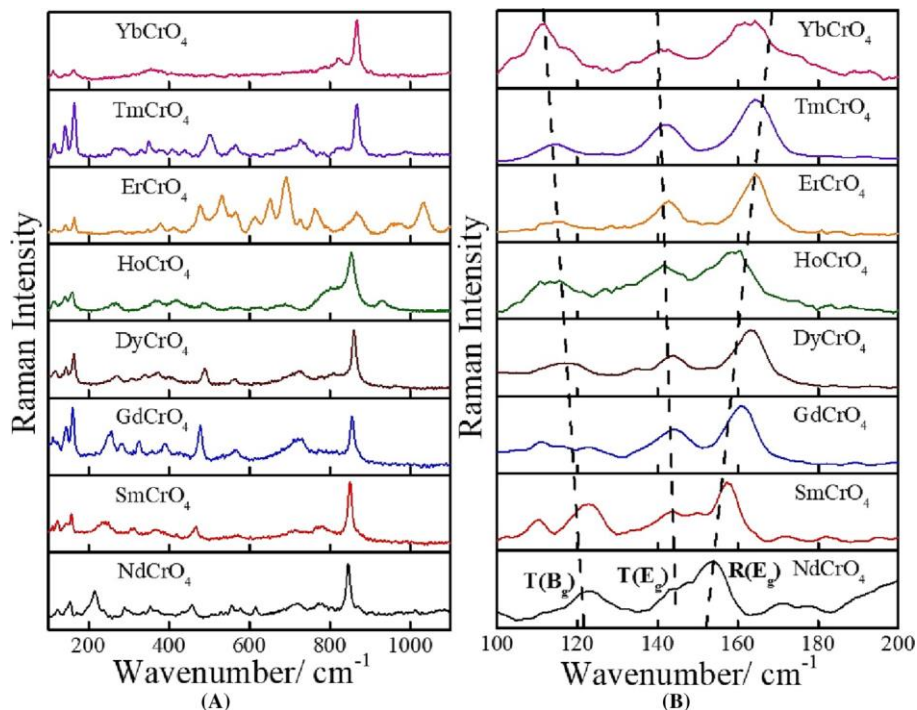
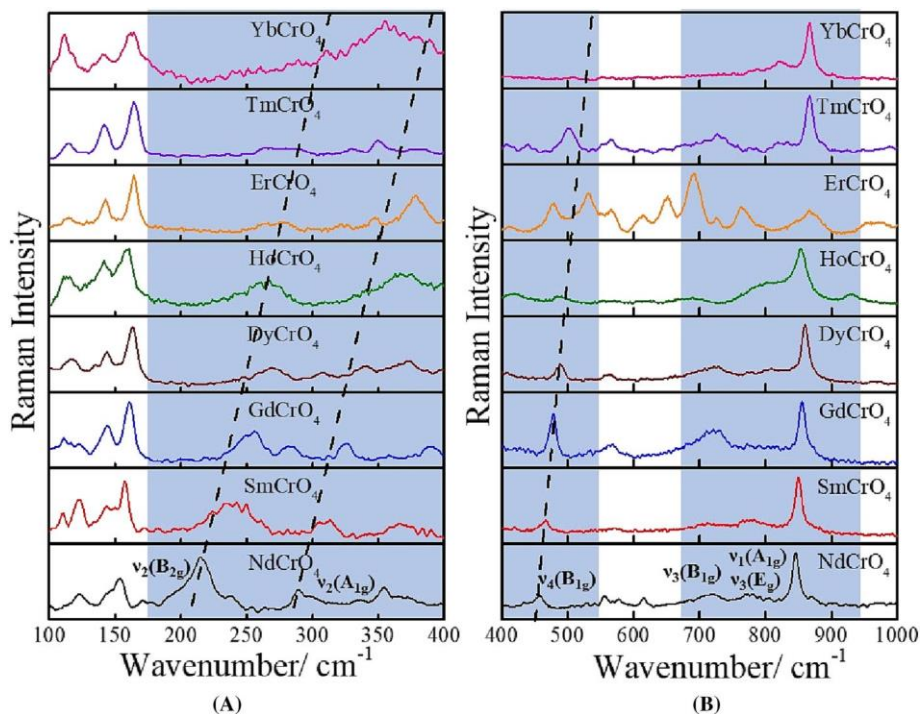


FIGURE 3 Internal vibrational modes of Raman spectra recorded at room temperature in zircon-type RCrO_4 ($R = \text{Nd, Sm, Gd, Dy, Ho, Er, Tm, Yb}$) compounds in the frequency range (A) 100–400 cm^{-1} and (B) 400–1,000 cm^{-1} . The shaded portion and dotted line reveal the Raman frequencies and shift in the Raman modes.



lanthanide atomic number grows and the energy of the atomic orbital drops, starting with Nd–Yb. The interaction force constant across R and CrO_4 is correlated with this energy differential. The stronger interaction force constant is produced as a result of the lower energy differential. Additionally, this causes the R – O bond length to decrease and the wavenumber of an internal mode to increase.^{21,22} The RCrO_4 shows many peaks in the

Raman spectra. The modes were assigned to RCrO_4 combinations by correlating with the reported vibrational spectra of RVO_4 and RPO_4 . This work observed 9, 10, 8, 8, 8, 4, 6, and 5 Raman modes for NdCrO_4 , SmCrO_4 , GdCrO_4 , DyCrO_4 , HoCrO_4 , ErCrO_4 , TmCrO_4 , and YbCrO_4 , respectively. In addition, some weak modes probably overlapped in the compounds, which is why we cannot discern them in our work. The modes observed

TABLE 1 At room temperature, internal and external Raman modes are listed for zircon-type RCrO_4 ($R = \text{Nd, Sm, Gd, Dy, Ho, Er, Tm, and Yb}$) and YCrO_4 .

Compounds	External modes (cm^{-1})					Internal modes (cm^{-1})						
	E_g	B_{1g}	E_g	E_g	B_{1g}	$\nu_2(B_{2g})$	$\nu_2(A_{1g})$	$\nu_4(B_{1g})$	$\nu_3(B_{1g})$	$\nu_2(B_{1g})$	$\nu_3(E_g)$	$\nu_1(A_{1g})$
NdCrO_4	-	123	144	152	-	215	289	456	717	-	776	846
SmCrO_4	110	122	143	157	-	238	311	466	712	-	780	850
GdCrO_4	111	-	142	160	-	255	326	478	720	-	-	855
DyCrO_4	-	117	142	163	-	268	340	489	810	-	-	860
HoCrO_4	-	114	141	158	-	266	367	489	805	-	-	853
ErCrO_4	-	114	141	163	-	-	377	-	-	-	-	-
TmCrO_4	-	114	142	165	-	-	-	501	826	-	-	868
YbCrO_4	-	111	141	161	-	-	-	-	821	-	-	867
YCrO_4	-	150	186	278	-	-	337	488	805	-	-	856

for ErCrO_4 in the higher wavenumber region from 200 to $1,000 \text{ cm}^{-1}$ cannot be assigned as the peaks are not matched with the reported data. Table 1 shows the Raman wavenumbers assigned with the modes for zircon-type RCrO_4 ($R = \text{Nd, Sm, Gd, Dy, Ho, Er, Tm, Yb}$) and YCrO_4 .

It is interesting to show how the Raman modes of zircon-type RCrO_4 ($R = \text{Nd, Sm, Gd, Dy, Ho, Er, Tm, Yb}$) vary as a function of the radii of the lanthanide ion (r_R) to classify the data logically. Figure S5A,B presents the graphs of detected external and internal modes versus radii of R^{3+} lanthanide ions, respectively. The obtained external modes show the random increase or decrease in the Raman modes with increasing r_R , as shown in Figure S5A. However, Figure S5B shows the general trend of decreasing wavenumbers with rising r_R in the internal modes correlated with the rise of bond lengths. As can be observed, each Raman mode has a considerably different r_R -dependent shift in wavenumber.

The R^{3+} ions inside the RO_8 dodecahedron gradually shrink from Pr^{3+} to Yb^{3+} as the size of the rare earth decreases. The size of a CrO_4 tetrahedra also grows concurrently. As a result, as the RCrO_4 series of oxides grow, the Cr-O bond length expands, and the bonds weaken. The stronger bonds, on the other hand, have a more acidic Lewis character and a greater attraction for electrons since the R-O bond length decreases during the series. Due to the lanthanide contraction in zircon-type RCrO_4 compounds, the ionic radii of the rare earth are reduced from Pr to Yb, which causes a linear decline in the a and c lattice parameters of these phases.^{10,11,32}

The Raman measurements further extend to the comparative study between rare-earth (Dy and La) and non-rare earth (Y) elements in RCrO_4 at R-site and for different structures such as zircon, monazite, and mixed

RCrO_4 compounds. The comparison between rare-earth and Y in RCrO_4 combinations shows the shift in the Raman peaks, as shown in Figure 4A. The highlighted portion in Figure 4A shows the peak position for $\nu_1(A_{1g})$ mode. The intense high rise of symmetric stretching mode $\nu_1(A_{1g})$ (internal mode related to motion in CrO_4 tetrahedra) for zircon-type DyCrO_4 is located at $\sim 860 \text{ cm}^{-1}$. The exact mode was positioned at $\sim 832 \text{ cm}^{-1}$ for monazite-type LaCrO_4 and $\sim 856 \text{ cm}^{-1}$ for zircon-type YCrO_4 . So, comparing the Dy and La (rare earth) and Y (non-rare earth) elements in the structure, the highest intensity mode $\nu_1(A_{1g})$ is located at a lower wavenumber in YCrO_4 due to the larger Y-O bond length than Dy-O in the zircon-type DyCrO_4 structure. In contrast, $\nu_1(A_{1g})$ mode in the LaCrO_4 is located at the middle position as that of DyCrO_4 and YCrO_4 , as the crystal structure changes the wavenumber of Raman modes.

Figure 4B compares the Raman modes in the different crystal structures. The $\nu_1(A_{1g})$ mode of monazite-type LaCrO_4 (at $\sim 832 \text{ cm}^{-1}$) is lower than that of zircon-type NdCrO_4 (at $\sim 846 \text{ cm}^{-1}$). The $\nu_1(A_{1g})$ mode relates to the CrO_4 unit in monazite-type and zircon-type crystal structures. The comparison between the common modes gives us the distortion in the structure related to the R-O bond distance. The PrCrO_4 containing monazite and zircon-type structures shows various modes in the $800\text{--}1,000 \text{ cm}^{-1}$ frequency range associated with the CrO_4 bonding.^{29,30}

Based on group theory analysis, the internal modes at lower wavenumber range were apparently associated to the Sm or Dy motion, in which a simplified zircon-type structure is thought to be formed of two sublattices of Sm or Dy and CrO_4 "molecules."^{29,30} In comparison, CrO_4 motion was connected to the latter modes at a greater wavenumber range (external modes). Raman

FIGURE 4 Raman spectra for (A) rare-earth-based RCrO_4 ($R = \text{Dy}, \text{La}$) and non-rare earth-based YCrO_4 compounds and (B) rare-earth-based RCrO_4 compounds with the different crystal structures (zircon-type and monazite-type). Highlighted portion in both figures shows the peak position of $\nu_1(\text{A}_{1g})$ mode.

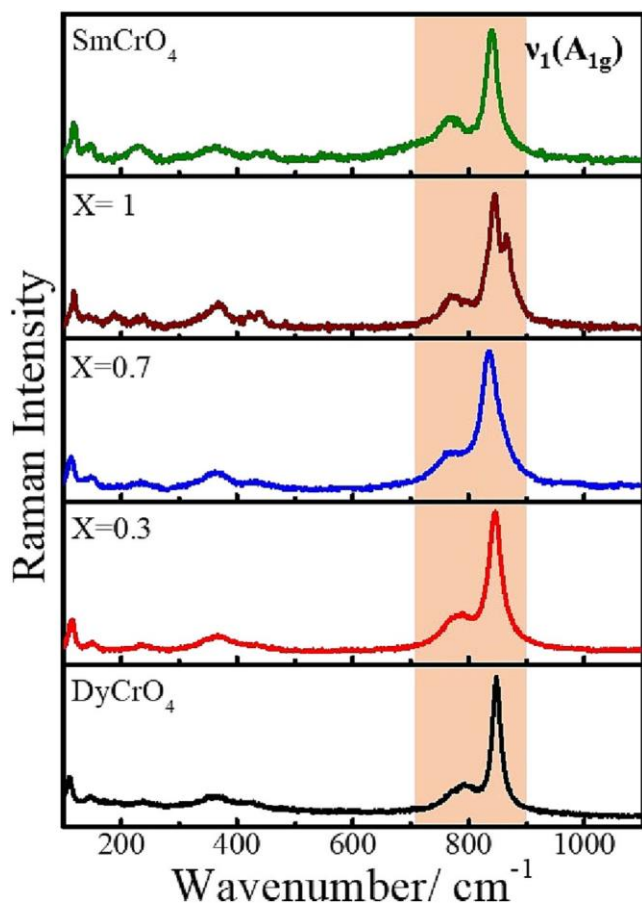
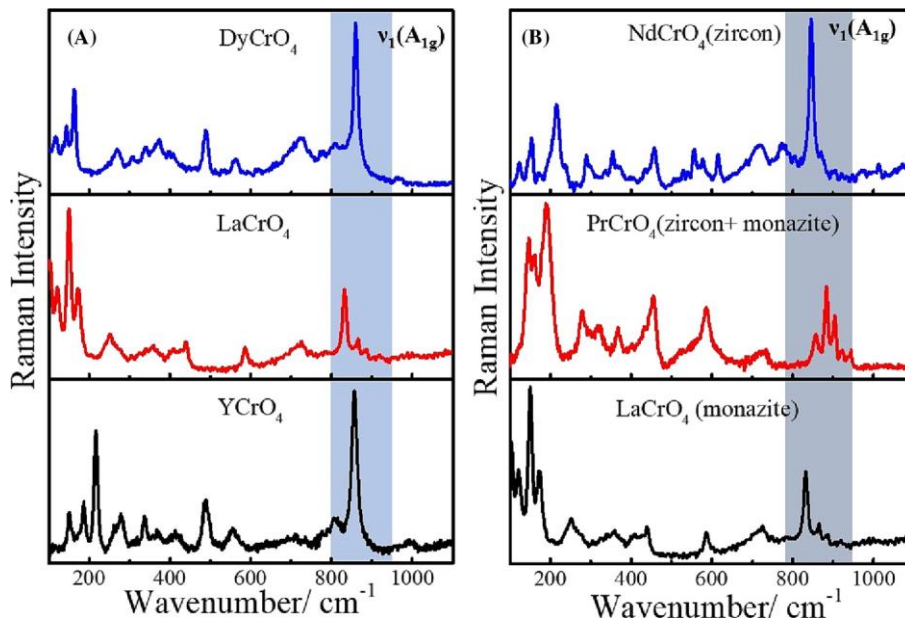


FIGURE 5 A comparison between recorded Raman spectra for zircon-type $\text{Sm}_x\text{Dy}_{1.3-x}\text{CrO}_4$ ($x = 0, 0.3, 0.7, 1$). The shaded portion shows the Raman shift for $\nu_1(\text{A}_{1g})$ mode

spectroscopy is a useful instrument for examining the consequences of structural abnormalities, as was already

mentioned. A perfect crystal's first-order Raman phonon spectrum is composed of small lines that correlate to the Raman-allowed zone center and follow specific polarization selection rules. However, in the case of disordered crystals, the phonon spectrum is expected to exhibit the following characteristics: (i) a broadening of the first-order Raman lines; (ii) the activation of prohibited Raman phonons; (iii) the emergence of broad Raman bands indicating the phonon density of states; and (iv) frequency shifting of certain peaks proportional to the amount of the dopant element (i.e., one-phonon-like and two-phonon-like behavior).³³

In this study, the newly synthesized materials were studied using Raman measurements. The Dy was substituted with Sm in zircon-type DyCrO_4 , and the effect of substitution was studied using Raman spectra (Figure 5). The zircon-type DyCrO_4 was substituted with $x = 0.3, 0.7, 1$ and compared with single-phase DyCrO_4 and SmCrO_4 . The intensity of the Raman peaks in the samples $x = 0.3$ and 0.7 was greater as compared to the other samples. The Raman spectra observed extra peaks for $x = 0.3$ and 0.7 . The most intense $\nu_1(\text{A}_g)$ peak for pure DyCrO_4 was found at $\sim 847 \text{ cm}^{-1}$, which is somewhat at the lowest wavenumber as the previously measured DyCrO_4 . The peak position shift was observed when Dy was substituted in zircon-type DyCrO_4 by Sm. The intense peak $\nu_1(\text{A}_g)$ shifted to a lower wavenumber for $\text{Sm}_x\text{Dy}_{1.3-x}\text{CrO}_4$ ($x = 0.7$), with a broadening in the line width. However, for $x = 1$, the $\nu_1(\text{A}_g)$ mode splits into two peaks. The peak position may relate to the single-phase SmCrO_4 and DyCrO_4 , which reveals the vibration of the CrO_4 group in both structures, indicating two phonons-like behavior. The substitution of Sm with

$x = 0.3$ and $x = 1$ shows the lower shift in the $\nu_1(A_g)$ mode compared to the Sm substitution with $x = 0.7$. The broadening of the Raman peaks was observed in the $Sm_xDy_{1.3-x}CrO_4$ system as the percentage of Sm substitution was raised. And that is why it is difficult to record the phonon frequency of the samples accurately. Internal $\nu_2(B_g)$, $\nu_4(B_g)$, $\nu_1(A_g)$, and ν_3 modes shifted to lower wavenumber because of the effects of lanthanide contraction as discussed for the zircon-type $RCrO_4$. At the same time, the external mode $T(B_{1g})$ shifted to a higher wavenumber, whereas $T(E_g)$ shows randomly increased and decreased Raman wavenumber. The shifting in the higher wavenumber confirmed the mass effect—validation of harmonic approximation.^{21,22} The same trend for external and internal modes was observed with the zircon-type $RCrO_4$ changing with the R-site from Nd–Yb. The wavenumbers assigned to the Raman modes are listed in Table S2.

4 | CONCLUSION

The entire series of compounds $RCrO_4$ ($R = La, Pr, Nd, Sm, Gd, Dy, Ho, Er, Tm, Yb$) and $YCrO_4$ were synthesized using the hydrolytic sol–gel method. The $RCrO_4$ ($R = Nd, Sm, Gd, Dy, Ho, Er, Tm, Yb$) and $YCrO_4$ crystallized in zircon-type, while $LaCrO_4$ forms monazite type. On the other hand, $PrCrO_4$ showed the coexistence of both the polymorphs, that is, zircon-type and monazite-type structures at $600^\circ C$. So these compounds experience the structural phase transition from monazite to zircon-type because of decreased lanthanide ion size from La to Lu. Again, the room-temperature Raman spectra of $RCrO_4$ also show the structural phase transition with different Raman modes correlated with the structural change. The Raman study of zircon-type $RCrO_4$ compounds concludes that the external Raman modes $T(B_g)$ and $T(E_g)$ shifted to a lower wavenumber from Nd–Yb. However, $R(E_g)$ and internal modes moved to higher energy as the atomic radius decreased and the atomic number increased from Nd–Yb. The radii-dependent wavenumber study of zircon-type $RCrO_4$ compounds shows a decrease in the Raman wavenumbers with increased r_R . A comparison between $DyCrO_4$, $LaCrO_4$ (rare-earth) and $YCrO_4$ (non-rare earth) shows the lower wavenumber of $\nu_1(A_{1g})$ mode for $YCrO_4$ compared to the other two compounds. The structural comparison reveals the $\nu_1(A_{1g})$ mode at a lower wavenumber in the monazite-type structure than in the zircon-type structure. The substitution of Sm in the $DyCrO_4$ host shifted the internal Raman modes ($\nu_2[B_{1g}]$, $\nu_2[A_{1g}]$, $\nu_4[B_{1g}]$, ν_3 , and $\nu_1[A_{1g}]$) to the lower wavenumber region. The shift towards the higher wavenumber is related to

the mass effect, whereas the lower wavenumber shift counters the lanthanide contraction in the samples going from Nd–Yb in the $RCrO_4$ system.

ACKNOWLEDGMENTS

S. U. acknowledges the support from the DST-INSPIRE FELLOWSHIP, India, for providing the Senior Research Fellowship (SRF).

CONFLICT OF INTEREST STATEMENT

The authors declare no conflict of interest.

ORCID

Pankaj Poddar  <https://orcid.org/0000-0002-2273-588X>

REFERENCES

- [1] E. Z. Stutz, S. Escobar Steinvall, A. P. Litvinchuk, J. B. Leran, M. Zamani, R. Paul, A. Fontcuberta, I. Morral, M. Dimitrievska, *Nanotechnology* 2021, 32, 085704.
- [2] N. Kazemi-Zanjani, E. Kergrene, L. Liu, T. K. Sham, F. Lagugné-Labarthe, *Sensors (Switzerland)* 2013, 13, 12744.
- [3] A. Indra, K. Dey, J. K. Dey, S. Majumdar, U. Rütt, O. Gutowski, M. V. Zimmermann, S. Giri, *Phys. Rev. B* 2018, 98, 14408.
- [4] Y. Long, Q. Liu, Y. Lv, R. Yu, C. Jin, *Phys. Rev. B - Condens. Matter Mater. Phys.* 2011, 83, 4.
- [5] Y. Aoki, H. Konno, H. Tachikawa, *J. Mater. Chem.* 2001, 11, 1214.
- [6] A. Midya, N. Khan, D. Bhoi, P. Mandal, *J. Appl. Phys.* 2014, 115, 2012.
- [7] A. Midya, N. Khan, D. Bhoi, P. Mandal, *Appl. Phys. Lett.* 2013, 103, 092402.
- [8] A. Ray, T. Maitra, *J. Phys. Condens. Matter* 2015, 27, 105501.
- [9] A. Morales-Sánchez, F. Fernández, R. Sáez-Puche, *J. Alloys Compd.* 1993, 201, 161.
- [10] R. Sáez-Puche, E. Jiménez, J. Isasi, M. T. Fernández-Díaz, J. L. García-Muñoz, *J. Solid State Chem.* 2003, 171, 161.
- [11] E. Jiménez, J. Isasi, R. Sáez-Puche, *J. Solid State Chem.* 2002, 164, 313.
- [12] S. G. Manca, E. J. Baran, *J. Appl. Cryst.* 1982, 15, 102.
- [13] Y. Aoki, H. Konno, H. Tachikawa, M. Inagaki, *Bull. Chem. Soc. Jpn.* 2000, 73, 1197.
- [14] H. Konno, H. Tachikawa, A. Furusaki, R. Furuichi, *Anal. Sci.* 1992, 8, 641.
- [15] S. G. Manca, E. J. Baran, *J. Phys. Chem. Solid* 1981, 42, 923.
- [16] N. Clavier, R. Podor, N. Dacheux, *J. Eur. Ceram. Soc.* 2011, 31, 941.
- [17] D. Errandonea, *Phys. Status Solidi Basic Res.* 2017, 254, 1700016.
- [18] E. Jimenez-Melero, N. H. van Dijk, W. H. Kraan, P. C. M. Gubbens, J. Isasi, R. Saez-Puche, *J. Magn. Magn. Mater.* 2005, 288, 1.
- [19] E. Climent-Pascual, J. Romero de Paz, J. M. Gallardo-Amores, R. Sáez-Puche, *Solid State Sci.* 2007, 9, 574.
- [20] K. Tezuka, Y. Hinatsu, *J. Solid State Chem.* 2001, 160, 362.
- [21] C. C. Santos, E. N. Silva, A. P. Ayala, I. Guedes, P. S. Pizani, C. K. Loong, L. A. Boatner, *J. Appl. Phys.* 2007, 101, 053511.

- [22] G. M. Begun, G. W. Beall, L. A. Boatner, W. J. Gregor, *J. Raman Spectrosc.* 1981, *11*, 273.
- [23] Y. W. Long, L. X. Yang, Y. Yu, F. Y. Li, Y. X. Lu, R. C. Yu, Y. L. Liu, C. Q. Jin, *J. Appl. Phys.* 2008, *103*, 093542.
- [24] E. Palacios, C. Tomasi, R. Sáez-Puche, A. J. Dos Santos-García, F. Fernández-Martínez, R. Burriel, *Phys. Rev. B* 2016, *93*, 1.
- [25] Q. Y. Dong, Y. Ma, Y. J. Ke, X. Q. Zhang, L. C. Wang, B. G. Shen, J. R. Sun, Z. H. Cheng, *Mater. Lett.* 2015, *161*, 669.
- [26] S. Ughade, B. Joshi, P. Poddar, *Ceram. Int.* 2022, *48*, 24666.
- [27] P. Barpanda, N. Recham, J. N. Chotard, K. Djellab, W. Walker, M. Armand, J. M. Tarascon, *J. Mater. Chem.* 2010, *20*, 1659.
- [28] M. Ginting, S. Taslima, K. Sebayang, D. Aryanto, T. Sudiro, P. Sebayang, *AIP Conf. Proc.* 2017, *1862*, 030062.
- [29] X. Cheng, D. Guo, S. Feng, K. Yang, Y. Wang, Y. Ren, Y. Song, *Opt. Mater. (Amst)*. 2015, *49*, 32.
- [30] E. N. Silva, A. P. Ayala, I. Guedes, C. W. A. Paschoal, R. L. Moreira, C. K. Loong, L. A. Boatner, *Opt. Mater. (Amst)*. 2006, *29*, 224.
- [31] I. Guedes, Y. Hirano, M. Grimsditch, N. Wakabayashi, C. K. Loong, L. A. Boatner, *J. Appl. Phys.* 2001, *90*, 1843.
- [32] Y. W. Long, L. X. Yang, Y. Yu, F. Y. Li, R. C. Yu, C. Q. Jin, *Phys. Rev. B - Condens. Matter Mater. Phys.* 2007, *75*, 104402.
- [33] M. R. Moura, A. P. Ayala, I. Guedes, C. K. Loong, L. A. Boatner, *J. Appl. Phys.* 2004, *96*, 6344.

SUPPORTING INFORMATION

Additional supporting information can be found online in the Supporting Information section at the end of this article.

How to cite this article: S. Ughade, P. Poddar, *J Raman Spectrosc* 2023, *1*. <https://doi.org/10.1002/jrs.6542>